

Dissertation der Fakultät für Physik  
der  
Ludwig-Maximilians-Universität München

**Searches for Heavy Charged Long-Lived Particles  
with the ATLAS Detector**

vorgelegt von

**Michael Adersberger**

geboren in Prien am Chiemsee

München, den 12. November 2018



Erstgutachterin: Prof. Dr. Dorothee Schaile

Zweitgutachter: Prof. Dr. Martin Faessler

Tag der mündlichen Prüfung: 20. Dezember 2018

## Zusammenfassung

In dieser Arbeit wird eine Suche nach schweren langlebigen geladenen Teilchen mit dem ATLAS Detektor am Large Hadron Collider vorgestellt. Diese Suche analysiert einen Datensatz von  $36.1 \text{ fb}^{-1}$  Proton-Proton-Kollisionen. Die erwartete Signatur solcher schwerer langlebiger geladener Teilchen im Detektor ist ähnlich der eines Myons, jedoch haben diese hypothetischen Teilchen eine höhere Masse. Dies hat zur Folge, dass diese Teilchen mit einer deutlich niedrigeren Geschwindigkeit erzeugt werden als hochenergetischen Standard-Modell-Teilchen. Des Weiteren führt die niedrige Geschwindigkeit der Teilchen zu Ionisations-Energieverlusten deutlich über denen von Myonen, welche den Hauptuntergrund für diese Suche darstellen. Schwere langlebige Teilchen können sowohl elektrisch- also auch farbgeladen sein. Farbgeladene schwere langlebige Teilchen hadronisieren zusammen mit Quarks zu sogenannten  $R$ -Hadronen. Diese können durch den Austausch der Quarks in hadronischen Interaktionen ihre Gesamtladung ändern.

Zur Identifikation von schweren geladenen langlebigen Teilchen, werden Messungen des Ionisations-Energieverlust im Pixel Detektor sowie Flugzeitmessungen im Tile-Kalorimeter, in den Monitored-Drift-Tubes und in den Resistive-Plate-Chambers, verwendet. Die Suche ist mit dedizierten Signal Regionen, sowohl für farbgeladene langlebige Teilchen als auch für paar-produzierte langlebige Teilchen die nur elektrisch geladen sind, ausgestattet. Da kein signifikanter Überschuss an Daten über der erwarteten Anzahl an Ereignissen gefunden wurde, können die Ergebnisse verwendet werden um Ausschlussgrenzen auf den Wirkungsquerschnitt und die Masse der Teilchen zu bestimmen. Paar-produzierte Stotom, Stop oder Gluino  $R$ -hadronen können bis zu einer Masse von 1250 GeV, 1340 GeV beziehungsweise 2000 GeV ausgeschlossen werden. Für farbneutrale paar-produzierte langlebige Teilchen können Massen bis 430 GeV für Staus und 1090 GeV für Charginos ausgeschlossen werden.



## Abstract

In this thesis a search for Heavy Charged Long-Lived Particles (HCLLPs) in a dataset of  $36.1 \text{ fb}^{-1}$  of proton–proton collisions with the ATLAS detector at the Large Hadron Collider is presented. HCLLPs manifest in the detector by signatures of heavy muon-like particles and are expected to be produced with velocities, significantly lower than the speed of light. Accordingly they are also expected to have an ionisation energy loss larger than that of muons, which are the main background for this search. Beside their electrical charge, HCLLPs can also be colour charged and hadronise together with Standard Model quarks to so called *R*-hadrons. Those *R*-hadrons can have a very special signature as they are able to change their overall charge through the exchange of the Standard Model quarks in hadronic interactions.

The observables used to identify HCLLPs in this analysis are a  $dE/dx$  estimate with the pixel detector and time-of-flight measurements with the Tile Calorimeter, the Monitored Drift Tubes and the Resistive Plate Chambers. The signal regions are designed to cover signatures of colour-charged particles that can undergo a change of charge as well as pair-produced colour singlets that are charged throughout the whole detector. No significant excess over the estimated background was observed and the results are used to set upper limits on the production cross section as well as lower mass limits for several models. The obtained lower mass limits for sbottom, stop and gluino *R*-hadrons are 1250 GeV, 1340 GeV and 2000 GeV, respectively, while for colour singlets such as staus and charginos 430 GeV and 1090 GeV are obtained.



# Contents

|          |   |           |
|----------|---|-----------|
| <b>1</b> | <b>Introduction</b>   | <b>3</b>  |
| <b>2</b> | <b>Theory</b>   | <b>5</b>  |
| 2.1      | Standard Model . . . . .                                    | 5         |
| 2.1.1    | Particle Content . . . . .                                  | 5         |
| 2.1.2    | Interactions . . . . .                                      | 6         |
| 2.1.3    | Lifetime . . . . .  | 10        |
| 2.1.4    | Motivation for a Theory Beyond the Standard Model . . . . . | 13        |
| 2.2      | Heavy Charged Long-Lived Particles . . . . .                | 16        |
| 2.2.1    | Theories extending the Standard Model . . . . .             | 16        |
| 2.2.2    | Cosmological Impact and Constraints . . . . .               | 20        |
| 2.3      | Summary . . . . .   | 26        |
| <b>3</b> | <b>Experiment</b>   | <b>27</b> |
| 3.1      | Large Hadron Collider . . . . .                             | 27        |
| 3.2      | ATLAS detector . . . . .                                    | 31        |
| 3.2.1    | Inner Detector . . . . .                                    | 33        |
| 3.2.2    | Calorimeters . . . . .                                      | 36        |
| 3.2.3    | Muon Spectrometer . . . . .                                 | 41        |
| 3.2.4    | Trigger system . . . . .                                    | 44        |
| 3.3      | Data preparation . . . . .                                  | 45        |
| <b>4</b> | <b>Heavy Charged Long-Lived Particles at Colliders</b>      | <b>47</b> |
| 4.1      | Production . . . . .  | 47        |
| 4.2      | Hadronisation . . . . .                                     | 49        |
| 4.3      | Velocity . . . . .  | 51        |
| 4.4      | Energy Loss . . . . .                                       | 53        |

|          |  |           |
|----------|--|-----------|
| 4.5      | Hadronic Interaction . . . . .                           | 56        |
| 4.6      | Lifetime . . . . .                                       | 64        |
| 4.7      | Summary . . . . .  | 65        |
| <b>5</b> | <b>Search for Heavy Charged Long-lived Particles</b>     | <b>67</b> |
| 5.1      | Analysis Strategy . . . . .                              | 67        |
| 5.2      | Previous Searches . . . . .                              | 70        |
| 5.3      | Data and Simulation . . . . .                            | 72        |
| 5.4      | Object reconstruction . . . . .                          | 77        |
| 5.4.1    | Inner Detector Track with Calorimeter Hits . . . . .     | 77        |
| 5.4.2    | SlowMuon . . . . .                                       | 83        |
| 5.5      | Identifying heavy charged long-lived particles . . . . . | 86        |
| 5.5.1    | Pixel dE/dx . . . . .                                    | 86        |
| 5.5.2    | Time-of-flight Tile Calorimeter . . . . .                | 91        |
| 5.5.3    | Time-of-flight Muon Spectrometer . . . . .               | 120       |
| 5.5.4    | Combination of time-of-flight measurements . . . . .     | 125       |
| 5.6      | Event Selection . . . . .                                | 129       |
| 5.6.1    | Missing-transverse-energy trigger . . . . .              | 129       |
| 5.6.2    | Single-muon trigger . . . . .                            | 132       |
| 5.6.3    | Event cleaning . . . . .                                 | 134       |
| 5.7      | Candidate Selection . . . . .                            | 135       |
| 5.7.1    | Common track selection . . . . .                         | 136       |
| 5.7.2    | ID+Calo candidates . . . . .                             | 138       |
| 5.7.3    | Full-detector candidates . . . . .                       | 141       |
| 5.8      | Signal selection and optimisation . . . . .              | 147       |
| 5.8.1    | Signal regions . . . . .                                 | 147       |
| 5.8.2    | Optimisation . . . . .                                   | 150       |
| 5.9      | Background Estimation . . . . .                          | 154       |
| 5.10     | Systematic uncertainties . . . . .                       | 167       |
| 5.10.1   | Theoretical cross section . . . . .                      | 167       |
| 5.10.2   | Signal efficiency . . . . .                              | 168       |
| 5.10.3   | Luminosity . . . . .                                     | 174       |
| 5.10.4   | Background estimation . . . . .                          | 174       |
| 5.11     | Results . . . . .  | 178       |
| 5.11.1   | Statistical method . . . . .                             | 178       |
| 5.11.2   | Results and interpretation . . . . .                     | 180       |

|  |            |
|--|------------|
| 5.11.3 Re-interpretation Long-Lived Multi-Charged Particles . . . . .    | 196        |
| 5.12 Ideas for the future . . . . .                                      | 198        |
| <b>6 Summary and Conclusion</b>  | <b>205</b> |
| <b>A Search for Heavy Charged Long-lived Particles</b>                   | <b>211</b> |
| A.1 Time-of-flight measurement in the Liquid Argon calorimeter . . . . . | 211        |
| A.2 Pre-selection Optimisation . . . . .                                 | 212        |
| A.3 Templates . . . . .  | 216        |
| A.4 Signal contamination in templates . . . . .                          | 218        |
| A.5 Signal contamination background estimate . . . . .                   | 219        |
| A.6 Background estimate from $\eta$ template . . . . .                   | 222        |
| A.7 Re-interpretation Long-Lived Multi-Charged Particles . . . . .       | 224        |



# Chapter 1

## Introduction

Modern particle physics appears to be currently in a way pointing period. In 2012, with the discovery of the Higgs boson [1, 2], the last missing piece of the Standard Model of Particle Physics (SM) was found. However the SM is known to be limited in several ways, as for example an implementation of a coherent description of gravity is missing. Another limitation of the SM is, that it does not offer a good candidate for dark matter, a new type of matter proposed to explain astrophysical and cosmological observations, such as gravitational lensing effects [3] or the observed power spectrum of the cosmic microwave background [4]. A variety of theories Beyond the Standard Model (BSM), that are able to solve one or the other problem of the SM, are suggested, but there is currently no one-fits-all solution available. For experimental particle physics this encourages open-mindedness in the searches for new physics to exploit the full potential of the experiments. At particle colliders, beside the majority of searches looking for prompt SM particles also unconventional searches, that are for example targeting new types of long-lived particles, are conducted. The mechanisms in the SM resulting in long lifetimes for some of the particles can, in a similar way, lead to significant lifetimes for particles in a BSM theory. A possible explanation why those new types of particles have not been observed so far, is that they are too heavy to be produced in significant amounts. Heavy long-lived particles can be targeted in two different ways depending on their nature. If they interact with the detector material and are long-lived enough they can be directly reconstructed in the event. If they are not able to interact with the detector they can be targeted with searches looking for their decay products, as long as the decays happen within the detector volume and with a resolvable displacement from the primary interactions. For both cases very distinct signatures, with basically no SM backgrounds, are expected.

The main target of the search described in this thesis are HCLLPs that are decaying outside of the detector. Those particles are expected to be produced at the Large Hadron Collider (LHC) with velocities significantly lower than the speed-of-light, due to their high masses and have a heavy-muon-like signature in the detector. Furthermore their low velocities lead to ionisation energy losses that are significantly larger than those of muons. Both velocities estimated from time-of-flight measurements as well as ionisation energy loss measurements are used as observables to identify HCLLPs. There are no SM particles that are heavy and long-lived enough to serve as HCLLP candidates, the only background for this search are muons with outliers in the energy loss and time-of-flight measurements. Very specific features are expected for colour-charged heavy long-lived particles as they hadronise with SM quarks to so called  $R$ -hadrons. Those  $R$ -hadrons can change their charge through hadronic interactions in the detector, leading to signatures where  $R$ -hadrons are only visible in some parts of the detector.

The thesis is structured as follows. In the second chapter the theoretical motivation is given. This includes a short summary of the SM and its limitations. The mechanisms leading to longevity in the SM are used to explain the long lifetimes of particles predicted in BSM theories. Also the impact of HCLLPs on the early universe and the corresponding constraints on their lifetimes and masses are discussed. In the third chapter the experimental setup with the ATLAS detector at the LHC is presented. A particular focus is on the subsystems that are used for ionisation energy loss measurements and time-of-flight measurements to identify HCLLPs. In the subsequent chapter the expected signatures of HCLLPs at colliders are discussed in detail. This involves a description of the impact of the production mechanisms on the kinematics of HCLLPs as well as their expected velocity and energy loss. A particular focus is placed on the hadronisation and the hadronic interactions of  $R$ -hadrons. In addition the range of lifetimes relevant for the search described in this thesis are discussed. In the fifth chapter the search for HCLLPs using a data sample of  $36.1 \text{ fb}^{-1}$  proton-proton collisions collected with the ATLAS experiment [5] will be discussed as the main part of this thesis. This involves the estimation and calibration of the main observables used for the identification of HCLLPs as well as the analysis search strategy and the estimation of the backgrounds, which is conducted in a fully data-driven manner. The chapter is concluded with a discussion of the results. In the final chapter a summary as well as an outlook for the search for HCLLPs is given.

# Chapter 2

## Theory

### 2.1 Standard Model

The SM is one of the best experimentally validated theories so far. Nevertheless history teaches us, there was always a next, more general theory spanning a wider range of validity. In the first part of this chapter a brief introduction of the SM particle content and the basic interactions is given. This is followed by a general discussion of the reasons for longevity in the SM. Those can serve as a guideline to detect the relevant phase space of theories BSM with long-lived particles. In the last section the need for such a BSM theory will be motivated. This section is inspired by Reference [6], which gives a comprehensive introduction to the SM.

#### 2.1.1 Particle Content

The particle content of the SM is composed of fermions (half-integer spin) and bosons (integer spin): Fermions are leptons and quarks, which are in our current understanding the fundamental bricks of matter and organised in three generations, where each higher generation is a high mass copy of the former. There are two types of bosons: gauge and scalar bosons. Gauge bosons are the mediators of the forces, while the scalar boson is giving the particles their masses. For leptons each generation is composed of an electrically charged lepton and a respective neutral neutrino. The first generation is formed by the electron ( $e^-$ ) and the electron-neutrino ( $\nu_{e^-}$ ), the second by the muon ( $\mu^-$ ) and the muon-neutrino ( $\nu_{\mu^-}$ ) and the third by the tau ( $\tau^-$ ) and tau-neutrino ( $\nu_{\tau^-}$ ). Also in the quark sector each generation of quarks is composed of an up-type and a down-type quark, where the up-type quark carries an electric-charge of  $2/3$  and the down-type quark an electric-charge of  $-1/3$ . Quarks also carry a colour-

charge and therefore also interact over the strong force. The first generation is composed of the up- ( $u$ ) and down-quark ( $d$ ), the second of the charm- ( $c$ ) and strange-quark ( $s$ ) and the third of the top- ( $t$ ) and bottom-quark ( $b$ ). For each of the fermions also an anti-particle exists, which has the same mass and spin as the particle, but inverted charge-like quantum numbers. Additionally quarks and leptons have a right- and left-handed eigenstate, due to the chiral nature of the weak interaction. This means that the weak interaction only couples to left-handed fermions and right-handed anti-fermions.

Gauge bosons are the mediators of the forces. The mediator for the Electromagnetic (EM)-interaction is the massless photon ( $\gamma^0$ ), while the weak interaction is mediated by the neutral  $Z^0$ - and the charged  $W^\pm$ -bosons. The strong interaction is mediated by gluons ( $g$ ) carrying a colour and an anti-colour. The last piece of the SM, and also the latest elementary particle being discovered, is the scalar Higgs boson ( $H^0$ ) [1, 2], the quantum excitation of the underlying Higgs-field. The Higgs-field gives masses to  $W^\pm$ - and  $Z^0$ -bosons via the Higgs mechanism and to quarks and leptons via Yukawa-couplings [8]. The particle content of the SM is summarised in Table 2.1 including mass, spin and colour-/electric-charge.

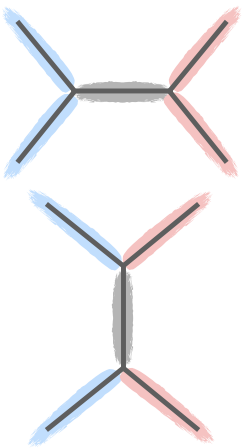


Figure 2.1: Schematic drawing of the lowest order Feynman-diagramms (tree-level). The interacting particles (in-coming) are on a blue background while the produced particles (out-going) are on a red one. The internal line (gray background) corresponds to a virtual internal particle propagator. The interaction points between different lines are called vertices and contribute to the matrix-element with the corresponding coupling constant.

### 2.1.2 Interactions

The SM describes three of the four, so far known, fundamental interactions. While the interactions of the EM, the weak and strong interactions are covered, an implementation of gravity is still missing, which will be discussed in more detail in Section 2.1.4. The SM is expressed in a mathematical framework called Quantum Field Theory (QFT). In this framework particles are understood as excitations of the underlying fields. Their interactions are treated by interaction terms of the corresponding fields. There are three probes for the interactions of elementary particles: bound states, decay and scattering. The key ingredients to calculate lifetimes (decay) or cross sections (scattering) are the matrix element of the underlying processes and the available phase space. The matrix element is calculated by evaluating Feynman diagrams, which are the graphical representations of the underlying processes (e.g. Figure 2.1). This means that all dynamics end up there. The phase space in contrast depends on the momenta and masses of the involved particles, so it is purely kinematic.

Toy lowest order Feynman-diagramms are drawn in Figure 2.1. They only differ by a rotation and hence by the in-coming and out-going particles.

| name                           | label          | mass [MeV]          | el. charge [e] | colour             |
|--------------------------------|----------------|---------------------|----------------|--------------------|
| <b>leptons (spin = 1/2)</b>    |                |                     |                |                    |
| electron                       | $e^-$          | 0.511               | -1             | -                  |
| electron-neutrino              | $\nu_{e^-}$    | $< 2 \cdot 10^{-6}$ | 0              | -                  |
| muon                           | $\mu^-$        | 105.66              | -1             | -                  |
| muon-neutrino                  | $\nu_{\mu^-}$  | $< 0.2$             | 0              | -                  |
| tau                            | $\tau^-$       | 1776                | -1             | -                  |
| tau-neutrino                   | $\nu_{\tau^-}$ | $< 18$              | 0              | -                  |
| <b>quarks (spin = 1/2)</b>     |                |                     |                |                    |
| up                             | $u$            | 2                   | 2/3            | r,g,b              |
| down                           | $d$            | 5                   | -1/3           | r,g,b              |
| charm                          | $c$            | 1275                | 2/3            | r,g,b              |
| strange                        | $s$            | 95                  | -1/3           | r,g,b              |
| top                            | $t$            | $173 \cdot 10^3$    | 2/3            | r,g,b              |
| bottom                         | $b$            | $4 \cdot 10^3$      | -1/3           | r,g,b              |
| <b>gauge bosons (spin = 1)</b> |                |                     |                |                    |
| gluon                          | $g$            | 0                   | 0              | (r,g,b) $\times 2$ |
| photon                         | $\gamma^0$     | 0                   | 0              | -                  |
| W-boson                        | $W^\pm$        | 80385               | $\pm 1$        | -                  |
| Z-boson                        | $Z^0$          | 91188               | 0              | -                  |
| <b>Higgs boson (spin = 0)</b>  |                |                     |                |                    |
| Higgs                          | $H^0$          | $126 \cdot 10^3$    | 0              | -                  |

Table 2.1: Summary of the particle content of the SM with spin, mass, colour- and electric-charge of the respective particles [7].

They have four external lines, which correspond to visible particles and one internal line corresponding to a virtual particle, that can not be observed. In contrast to the observable particles, the virtual particle can have any mass due to the uncertainty principle. A virtual particle with a mass different to its rest-mass is called off-shell. The larger the difference to the rest-mass the less likely the process. Also direct four-point interactions are possible but are allowed only for interactions where exclusively gluons or vector-bosons participate. Predominantly three-point interaction vertices are the fundamental bricks all higher-order diagrams are made of. Each of those vertices introduces a factor  $\sqrt{\alpha_x}$ , with  $\alpha$  being the coupling constant of  $x$ : em (electromagnetic), w (weak) or s (strong) interaction. Depending on the strength of the coupling higher order diagrams with more vertices can be almost negligible or important.

### Electromagnetic Interaction

The EM-interaction is described by the quantum electrodynamics (QED) which is a gauge theory with a  $U(1)$  symmetry group. The mediator particle of the EM-interaction is the photon. The photon couples to the electric-charge which means that it couples to quarks and charged leptons as well as charged composed particles. In principle also the coupling to  $W$ -bosons is possible, but these processes are very rare. The fundamental vertex associated with the EM-interaction is shown in Figure 2.2. It describes the interaction of a charged particle ( $c$ ) with a photon. In this version the emission or absorption of a  $\gamma^0$  is shown. The vertex can also be rotated, which means that the in- and outgoing-particles are exchanged. The rotated diagram corresponds to a pair-creation or an annihilation reaction of two charged particles. The coupling constant for the EM-interaction is  $\alpha_{em}$  ( $\sim 1/137$  [7]).

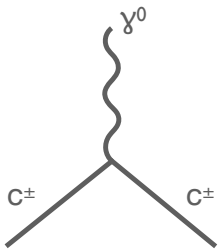


Figure 2.2: Feynman diagram showing the emission or absorption of a  $\gamma^0$  by a charged particle ( $c$ ).

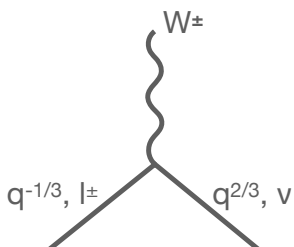


Figure 2.3: Feynman diagram showing the fundamental charged weak vertex, involving both the coupling to leptons or quarks.

### Weak Interaction

The weak interaction, as the name suggests, is significantly weaker than the other interactions described in the SM. The corresponding mediator particles are the  $W^\pm$ - and  $Z^0$ -bosons, which couple to the weak isospin. All leptons and quarks interact over the weak interaction. In particular also neutrinos, which are electrically neutral and have no colour charge, only interact weakly.

The fundamental vertices associated with the weak interaction can be split into neutral vertices ( $Z^0$ -boson) and charged vertices ( $W^\pm$ -boson).

The neutral vertices are basically the same as the ones for the  $\gamma^0$ , Figure 2.2, where the  $\gamma^0$  is replaced by a  $Z^0$ -boson. The main difference, besides the significantly weaker coupling, is, that also a direct coupling to neutrinos is allowed. The fundamental charged vertex is shown in Figure 2.3. For the leptons it corresponds to a lepton converting into a neutrino of same lepton flavour or backwards. Also the fundamental charged vertex involving quarks changes the quark type (up- to down-type or vice versa). Besides generation-saving processes also those changing between the generations were observed. This was understood by the weak force coupling not to the mass eigenstates (physical particles), but to the weak eigenstates. For the down-type quarks those weak eigenstates are a linear combination of the mass eigenstates. The weak eigenstates are connected to the mass eigenstates by the CKM matrix [9], which is slightly off-diagonal and therefore allows for a conversion of a down-type quark to an up-type quark of a different generation or vice-versa. For completeness also vertices involving a  $Z^0$  coupling to two  $W^\pm$  bosons and 4-boson interactions are possible.

The weak interaction can be unified with the EM-interaction in the electroweak theory, which is accomplished in a  $SU(2)\times U(1)$  gauge group. The unification of the two forces implies that above a certain unification energy scale the weak and the EM-force merge into a single electroweak force [10, 11, 12].

### Strong Interaction

The strong interaction is described by quantum chromo dynamics (QCD), which is a  $SU(3)$  gauge group theory. Adding this to the electroweak gauge group one obtains the SM gauge group as  $SU(3) \times SU(2) \times U(1)$ . The mediator of the strong interaction is the gluon, which couples to the colour charge and is, in contrast to the photon, colour charged itself. It is therefore also able to couple to itself. Besides the gluon, only quarks carry a colour charge. Quarks are singly colour charged forming a colour triplet while gluons carry a colour and an anti-colour forming a colour octet. The fundamental vertices for QCD are shown in Figures 2.4, 2.5 and 2.6. The first is showing the interaction of a quark with a gluon, while the latter two are showing self-interactions of gluons.

In contrast to the EM interaction the coupling constant for the strong interaction  $\alpha_s \approx 1$ , which means that higher order diagrams are important. But this is not the coupling that is actually observed in experiments, as vacuum polarisations are able to screen the charge seen by the particles.

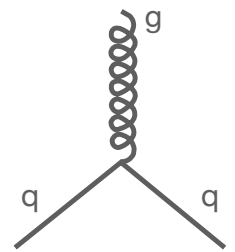


Figure 2.4: Fundamental QCD vertex involving two quarks and a gluon.

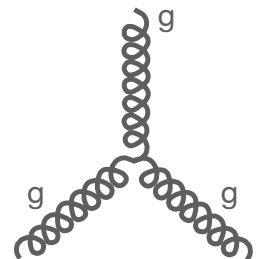


Figure 2.5: Gluon three-point interaction vertex.

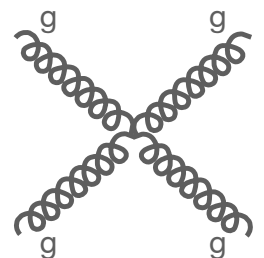


Figure 2.6: Gluon four-point interaction vertex.

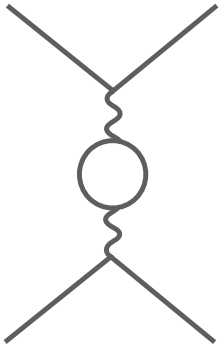


Figure 2.7: Exemplaric diagram showing a particle interaction involving an additional particle loop.

An illustrative description of this screening can be given in QED. Imagine e.g. the external lines in Figure 2.7 being electrons and the mediating photon pair-producing and annihilating an electron-positron pair, as sketched with the loop. The electron-positron pair can be understood as a dipole, screening the charge of the external electrons. This results in a change of the effective coupling between them. These screening effects are rather weak in QED but very important in QCD due to the strong coupling. Estimating the effects of all loop corrections results in the effective coupling constant being momentum transfer dependent, which can be also interpreted as a distance dependence due to the uncertainty principle. For QED the effective coupling increases at short distances, whereas for larger distances it decreases. The inverted behaviour was found for QCD, so for short distances the quarks get asymptotically free, while the coupling gets strong for larger distances. This behaviour of the strong interaction has important consequences: Colour charged particles do not exist isolated, but only in overall colourless states, known as quark confinement. Quarks are bound into hadrons which are either mesons (quark-anti-quark pairs) or baryons (bound states of three quarks/anti-quarks). For gluons also glueballs, states only built from gluons, would be possible but have not been observed so far. A further important consequence is that the further colour charged particles are pushed apart the more energy is transferred to the colour field between them. It can get energetically favourable that a new quark-anti-quark pair is produced out of the vacuum. If the colour charged particles are produced with high energies e.g. at colliders, this creation of new particles occurs until the energy in the movement apart is no longer sufficient to produce new particles. Then the coloured partons combine to form colour neutral hadrons. This process is called hadronisation. The signature of colour charged particles in a high-energy collider are therefore several hadrons flying in approximately the same direction, called a jet.

### 2.1.3 Lifetime

In the context of QFT, lifetime is not a discrete value associated to a particle type, but has an intrinsic random element. Correspondingly, the parameter of interest is not the lifetime, as no direct prediction on the decay of a given particle is possible, but a mean lifetime that can be used for a statistical prediction on the number of decaying particles in the limit of large samples. The number of remaining particles follows an exponential decay law with the decay rate being the reciprocal of the mean lifetime.

Most of the particles do not have only a single possible decay channel, but several with different decay products. Hence the overall decay rate for a particle is given as the sum over all decay rates for the allowed decays. The decay rates or mean lifetimes can be calculated from the matrix element and an integration over the allowed phase space.

From the theoretical perspective there are three potential sources for a prolongation of the particle lifetimes: Number of decay channels, matrix element and phase space. If the particle has no allowed decay channels, e.g. as it is the lightest particle with a conserved quantum number, the particle has a long or infinite lifetime depending on the quantum number being strictly or almost conserved. Having a low number of allowed particle decay channels is a key feature for long-lived particles, as this minimises the probability for non-suppressed decay modes. For particles with allowed decay channels to become long-lived, those have to be suppressed through a small matrix element, a small phase space or both. One reason for a small matrix element can be the virtuality of an intermediate particle, e.g. the  $W$ -boson in Figure 2.8. As introduced in Section 2.1.2, intermediate particles can have masses different to their restmass, but those processes are suppressed the larger the difference. Decay modes via heavy mediators are significantly suppressed. Another reason for a suppression of the matrix element can be soft couplings. For example, if the decay of a particle is only feasible via the gravitational force, it is significantly suppressed compared to a decay e.g. involving solely strong interactions. An additional scenario suppressing the decay rate is, if the tree-level processes are not allowed and hence the particle decay is only feasible at higher order, with each vertex suppressing the decay by the corresponding coupling constant. Last but not least the available phase space can be a reason for a low decay rate. For a particle decay the available phase space is given by the mass difference between the decaying particle and the sum over the mass of the decay products. This is typically realised, if the particle is almost mass degenerated with the lightest particle with a (almost) conserved quantum number.

For most of the known cases, long lifetimes do not occur due to a single of the previously discussed reasons, but rather due to a combination of them. Overall, one ends up with the following list, which can serve as a guideline to identify particles with significant lifetimes in the SM as well as in theories extending the SM:

- number of decay modes
  - lightest particle with a (almost) conserved quantum number

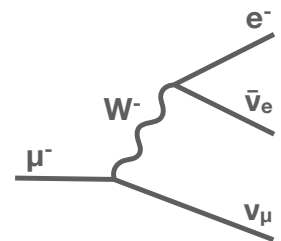


Figure 2.8: Feynman diagram for the muon decay to an electron, anti-electron-neutrino and muon-neutrino.

- few decay channels
- matrix element
  - off-shell intermediate particles
  - soft couplings
  - forbidden tree-level decay
- phase space
  - mass degenerated with lightest particle with a (almost) conserved quantum number

| <b>electron/proton</b> |   |
|------------------------|---|
| conserved quantumn.    | ✓ |
| few decay channels     | X |
| off-shell particle     | X |
| soft coupling          | X |
| forbidden tree-level   | X |
| mass degenerated       | X |

Table 2.2: Reasons for longevity for the SM electron/proton.

This recipe for the identification of particles with significant lifetimes will be verified for some examples in the SM in the following.

The simplest examples in the SM are the electron and the proton. Both particles are stable as they are the lightest particles with a conserved quantum number. The electron is the lightest particle carrying a lepton number, while the proton (uud) is the lightest baryon and thus stable due to baryon number conservation.

A further example for a particle with significant lifetime in the SM is the muon. The only allowed tree-level decay of the muon is shown in Figure 2.8. All higher-level diagrams are based on the tree-level decay with some additional radiations, which are suppressed due to the additional vertices. The muon is the second-to-lightest charged lepton, hence only the decay to an electron is allowed. The decay is mediated by the weak force which has two implications: First the decay involves two weak vertices leading to a soft coupling and second the mediator particle, the W-boson, is suppressing the process due to its high mass (Table 2.1). The arguments for the muon getting a substantial lifetime are summarised in Table 2.3.

The meta-stable particle with the longest lifetime in the SM is the neutron, which is the second lightest particle carrying a baryon number. The only allowed tree-level decay is the beta-decay to an electron-anti-electron-neutrino pair and a proton, where a down quark converts into an up quark. Also for the case of the neutron only the decay via the weak interaction is possible, hence both the off-shell mediator and the soft coupling argument hold for the neutron. Besides those arguments, the neutron is also almost mass degenerated with the proton. The mass difference between the proton (938.3 MeV) [7] and the neutron (939.6 MeV) [7] is only 1.3 MeV, which results in a very small available phase space for the decay. This leads to a significant elongation of the mean lifetime (880.1 s) [7]

| <b>muon</b>          |   |
|----------------------|---|
| conserved quantumn.  | X |
| few decay channels   | ✓ |
| off-shell particle   | ✓ |
| soft coupling        | ✓ |
| forbidden tree-level | X |
| mass degenerated     | X |

Table 2.3: Reasons for longevity for the SM muon.

| <b>neutron</b>       |   |
|----------------------|---|
| conserved quantumn.  | X |
| few decay channels   | ✓ |
| off-shell particle   | ✓ |
| soft coupling        | ✓ |
| forbidden tree-level | X |
| mass degenerated     | ✓ |

Table 2.4: Reasons for longevity for the SM neutron.

compared to the muon ( $2.2 \cdot 10^{-6}$  s) [7], which has in principle a similar decay mode. The reasons for the longevity of the neutron are summarised in Table 2.4

The last example discussed here is the B0 meson, which is composed of a down- and an anti-bottom-quark. Also the B0 meson can only decay via the weak-interaction, but due to the high mass many possible decay modes are allowed. The decay of the bottom-quark to a top-quark is forbidden due to the higher mass of the top-quark, hence the decays always involve vertices with small couplings due to the off-diagonal elements in the CKM matrix  $V_{cb} = (40.5 \pm 1.5) \times 10^{-3}$  and  $V_{ub} = (4.09 \pm 0.39) \times 10^{-3}$  [7]. Decays to e.g. pairs of leptons are even further suppressed as no flavour changing neutral currents are allowed at tree-level, and only decays with a high vertex multiplicity involving off-diagonal CKM couplings are possible. This results in a mean lifetime for the B0 meson of  $(1.519 \pm 0.007) \times 10^{-12}$  s [7], which corresponds to a resolvable decay distance at collider experiments. The arguments for the B0 meson getting a substantial lifetime are summarised in Table 2.5.

| B0-meson             |   |
|----------------------|---|
| conserved quantumn.  | X |
| few decay channels   | X |
| off-shell particle   | ✓ |
| soft coupling        | ✓ |
| forbidden tree-level | ✓ |
| mass degenerated     | X |

Table 2.5: Reasons for longevity for the SM B0-meson.

### 2.1.4 Motivation for a Theory Beyond the Standard Model

The SM represents one of the best experimentally proven theories, but has still some open questions and issues. These issues can be split into two categories, problems that are understood as mathematically inelegant and hence disturb the beauty of the theory, and problems that need to be solved to understand the fundamental principles of Nature. So problems that should be solved and problems that have to be solved. Some issues belonging to the first category are summarised under the naturalness argument of a theory, which requires the ratios between the free parameters of a theory to be roughly of  $O(1)$ . One example for an unnatural behaviour of the SM is the hierarchy problem. The Higgs mechanism relates the Higgs mass to the masses of the gauge bosons and hence sets the scale of the electroweak interaction. Therefore a Higgs mass of  $O(100 \text{ GeV})$  was needed and also observed. In QFT loop corrections are able to screen the bare quantities as already introduced in Section 2.1.2. For the Higgs mass the correction to the bare mass by fermion loops is given as

$$\Delta m_h^2 = -\frac{|\lambda_f|^2}{8\pi^2} \Lambda^2 + \dots, \quad (2.1)$$

with the Yukawa coupling to the Higgs field ( $\lambda_f$ ) and the cut-off scale ( $\Lambda$ ). The cut-off scale is the energy where the validity of the theory breaks down. For the SM often the Planck scale  $O(10^{19}$  GeV) is assumed as there gravitation is definitely no longer negligible and hence a new theory is for sure needed. To get the Higgs mass to the observed value the bare Higgs mass and the contributions due to loop corrections have to be fine-tuned up to 16 digits, which feels unnatural. Also the number of free parameters in the SM (19) is rather large, which supports the idea of a more fundamental theory with less free parameters.

A further "should be solved" problem is the absence of a striking argument for why exactly three generations of fermions have been observed and also why the EM-charge is quantised the way it is. One solution to those problems would be a Grand Unified Theory (GUT), which is also a very mathematically elegant idea. In a GUT theory at a high energy scale (GUT scale  $O(10^{16}$  GeV)) the electroweak and strong couplings are merged into a single coupling, that is characterised by a larger simple symmetry, which is broken to the SM at lower energy scales. This implies that the coupling constants of EM-, weak- and strong-interaction have to intersect at the GUT scale. An extrapolation from the SM to the GUT scale does not result in such an intersection. Hence, for a GUT to be realised in Nature, new physics between the weak scale and the GUT scale is mandatory. Also a further unification of the couplings with gravitation might be realised, often referred to as Theory of Everything. The quantisation of the EM-charge can be explained within a GUT by putting quarks and leptons in the same multiplet. An important probe for GUTs in the measurable energy range is the, so far not observed, decay of the proton, as they imply that the lepton and baryon numbers are not conserved.

One problem of the SM that "has to be solved" is that until now no consistent formulation of a quantum gravity was possible. The theory of the large scales (general relativity) and the theory of the small scales (SM) can not be consistently treated in an overarching theory so far.

A further issue of the SM that has to be solved is the matter-anti-matter asymmetry seen in the observable Universe. One well motivated and accepted assumption of the Big Bang theory is that equal amounts of matter and anti-matter were produced. The SM does not explain what has happened to the anti-matter as everything we see is made out of matter. There are two different attempts to solve this issue: It is thought that there might be regions where anti-matter is dominant though this would lead to a, not yet observed, "burning horizon" in the regions where

anti-matter- and matter-dominated regions intersect. Another possible solution is that the observed asymmetry would be realised by a mechanism transforming anti-matter to matter. The conditions that have to be fulfilled for such a mechanism were formulated by Sakharov [13] as: baryon/lepton-number violation, out of thermal equilibrium, and CP-violation. The baryon/lepton-number violation is allowing processes where matter is produced from anti-matter and vice versa, but in a thermal equilibrium backwards process would have the same rate cancelling the net matter anti-matter transfer. Also the CP-conjugated processes have the same rates as long as no CP-violation is present. Hence, both requirements, being out-of thermal equilibrium and the presence of CP-violation are necessary to produce a net anti-matter to matter conversion. The out-of-thermal-equilibrium conditions should be fulfilled through the cooling of the Universe due to its expansion. Solutions for the baryon- or lepton-number violation would be e.g. a GUT which allows for such processes. The CP-violation, that is further needed, can be seen in the SM through small complex terms in the CKM matrix, but the amount of CP-violation is orders of magnitudes too small to explain the observed asymmetry. So additional sources for CP-violation are needed to answer the question about the missing anti-matter.

Last but not least there is the outstanding question about the origin of Dark Matter and Dark Energy. It was observed that the expansion of the Universe is accelerating. This is accounted for in the standard model of cosmology with a cosmological constant which is interpreted as a dark energy permeating all of space and driving the acceleration. Gravitational lenses and deviations from the expected rotation curves of galaxies are examples for observations that can not be explained with visible matter only. The most commonly accepted solution is Dark Matter, dark means that it has no QED and QCD interactions and is hence not directly detectable with telescopes. It is only detectable over its influence on ordinary/visible matter via the gravitational force. One possible type of Dark Matter candidates are weakly interacting massive particles, which could be in a mass range where they can be produced at colliders. The standard model of cosmology includes both Dark Energy and Dark Matter and can be used to simulate the cosmic microwave background, which is nicely agreeing with the observed distribution. A fit to the observed data allows for a prediction of the abundances of Dark Energy, Dark Matter and ordinary matter, shown in Figure 2.9. This means that only about 5% of the Universe is made out of ordinary, well known matter, while only little is

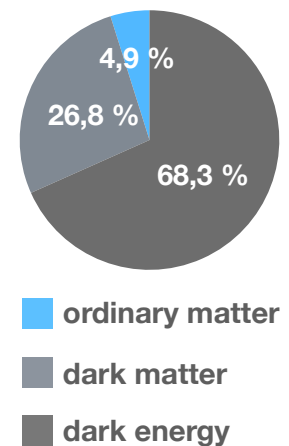


Figure 2.9: The abundances of ordinary matter, Dark Matter and Dark Energy in the Universe today [7].

known about the nature of the rest.

Summarising this section, the SM has some open questions. The majority of theories that are targeting some of the discussed issues are coming with additional particles. Those additional particles can be in a mass range where they are producible at the LHC. But as there is currently no one-fits-all theory that is solving all the discussed issues, it is important to have searches that are as model independent as possible to ensure that nothing substantial is missed. One target for model independent search strategies are heavy charged long-lived particles, which will be discussed in the following.

## 2.2 Heavy Charged Long-Lived Particles

One potential type of new particles that can be targeted with detector searches are HCLLPs. Heavy in this context means that the masses are higher than the ones of SM particles, so roughly starting at 200 GeV. Those particles have to be electrically or colour charged, or both to allow for direct interactions with the detector, which is a key feature of the signature targeted with the search described in this work. In the first part of this section theories extending the SM providing HCLLP candidates are introduced. This is followed by a discussion of the cosmological constraints on HCLLPs as their life-time might be sufficient to have a significant impact on the formation of the Universe.

### 2.2.1 Theories extending the Standard Model

As discussed in Section 2.1.4, there is a need for theories extending the SM. It is natural to believe that those theories are similar to the SM and hence also scenarios leading to long-lived particles are thinkable. Therefore the hints for longevity, discussed in Section 2.1.3, can be used to detect parameter spaces in theories extending the SM, which provide charged long-lived particle candidates. Some examples will be discussed in the following.

#### **Supersymmetry**

One extension of the SM is the introduction of a new space-time symmetry, called Supersymmetry (SUSY), which is mapping fermions on bosons and vice versa. This would predict a fermionic super-partner for each boson and a bosonic super-partner for each fermion. The nomenclature for

the super-partners is an *s*- in front of the bosonic super-partners (e.g. selectron, squark) and an *-ino* behind the names of the fermionic super-partners (e.g. gluino, wino).

A pure supersymmetric theory would allow for both lepton- and baryon-number being violated, which would imply a rather rapid decay of the proton. Such decays are largely restricted by experiments (lifetime proton  $> 2.1 \times 10^{29}$  years [7]). The most common solution is to require *R*-parity conservation, with *R*-parity being a multiplicative quantum number, that is +1 for the SM particles and -1 for the super-partners. Besides the stability of the proton the *R*-parity conservation also implies that the lightest supersymmetric particle is stable, and hence can serve as a Dark Matter candidate. A further consequence would be that supersymmetric particles would only be produced in pairs.

In a perfect "unbroken" SUSY the masses of the SM-particles and their respective super-partners would be the same. Loop corrections to the Higgs mass are of opposite sign for fermions and bosons. As the SM particles are paired with sparticles those correction would perfectly cancel for an unbroken SUSY and hence solve the hierarchy problem. But as such particles have not been observed, SUSY has to be broken to introduce masses for the super-partners high enough to be not yet observable at colliders. But still, if the mass difference is not too large between particles and sparticles, SUSY would remain an elegant solution to the hierarchy problem.

As SUSY was not observed so far, nothing is known about the potential mechanism of supersymmetry-breaking. From the phenomenological side the most straight forward approach is to introduce the minimal number of allowed (gauge and poincare invariance) supersymmetry-breaking terms in the theory, that do not reintroduce the hierarchy problem. The corresponding model is called Minimal Supersymmetric Standard Model and has to deal with overall  $O(100)$  free parameters, which is an enormous freedom and can hardly be used as a guideline for searches for new particles. Attempts to lower the degrees of freedom are done by introducing mechanisms for the supersymmetry-breaking (e.g. Gauge Mediated Supersymmetry Breaking (GMSB)) or by choosing other constraints on the parameters (e.g. Split SUSY).

In GMSB models [14] typically the gravitino is the lightest supersymmetric particle. The next-to-lightest supersymmetric particle can get long-lived, as for those models *R*-parity is conserved and therefore only the decay to the gravitino, suppressed by the softness of the gravitational coupling,

| <b>stau (GMSB)</b>   |   |
|----------------------|---|
| conserved quantumn.  | X |
| few decay channels   | ✓ |
| off-shell particle   | X |
| soft coupling        | ✓ |
| forbidden tree-level | X |
| mass degenerated     | X |

Table 2.6: Reasons for longevity for the stau in GMSB models.

| <b>chargino (AMSB)</b> |   |
|------------------------|---|
| conserved quantumn.    | X |
| few decay channels     | ✓ |
| off-shell particle     | X |
| soft coupling          | ✓ |
| forbidden tree-level   | X |
| mass degenerated       | ✓ |

Table 2.7: Reasons for longevity for the chargino in GMSB models.

| <b>gluino (split-SUSY)</b> |     |
|----------------------------|-----|
| conserved quantumn.        | (✓) |
| few decay channels         | ✓   |
| off-shell particle         | ✓   |
| soft coupling              | X   |
| forbidden tree-level       | X   |
| mass degenerated           | X   |

Table 2.8: Reasons for longevity for the gluino in Split-SUSY models.

is allowed. Besides gauginos, and for a small parameter space sneutrinos, also staus can be the next-to-lightest supersymmetric particle and therefore candidates for a heavy charged long-lived particle. GMSB models also serve regions of parameter space where the other sleptons are almost mass-degenerated with the stau and hence can be long-lived as well.

In models with Anomaly Mediated Supersymmetry-breaking (AMSB) [15] typically the lightest chargino and neutralino are almost mass degenerated. For some regions of parameter space the neutralino is the lightest supersymmetric particle and hence stable. The decay of the chargino to the neutralino is suppressed due to the small available phase space. So those models serve a Dark Matter candidate, the neutralino, and a charged long-lived particle, the chargino. In other regions of the AMSB parameter-space the stau is the lightest supersymmetric particle and hence stable, but as this region is less favourable as it does not serve a good electrically-neutral Dark Matter candidate.

Further interesting scenarios are the so called Split-SUSY models. The masses of the gauginos and higgsinos are roughly at the weak scale while the scalars have very large masses. A nice side-effect of this constellation is that the decay of the proton, which has to involve an internal squark, is heavily suppressed due to the off-shellness of the super-heavy squarks. Independent of whether or not  $R$ -parity is conserved the only possible decays for gluinos are the decays over the super-heavy squarks or the decay to a gravitino suppressed by the soft coupling. Hence Split-SUSY models serve long-lived gluinos, which are colour-charged and hence could give very distinct signatures in the detector, which will be discussed in more detail in Section 4.5.

The parameter space of supersymmetric models is very broad and hence many further scenarios leading to longevity for charged particles are possible. In principle all charged sparticles can be long-lived for some supersymmetric parameter space. The searches should be therefore performed as generic as possible in order to cover as large regions of the parameter space as possible.

### Universal Extra Dimensions

Further models resulting in similar scenarios for heavy charged long-lived particles are models with universal extra dimensions [16]. In those models all SM particles are allowed to propagate in the extra dimensions. The models are constructed in a way that the 4-dimensional SM, which

is perfectly describing the low-energy-scale physics, is a low-energy effective theory of an underlying N-dimensional theory. As we live in a 4-dimensional world, the additional dimensions have to be somehow hidden. The simplest way of such a compactification would be that the extra-dimension is wrapped to a circle with radius  $R$ , as shown in Figure 2.10. If a plane wave-function is able to propagate into the extra dimension, one gets the following form:  $\Psi(t, \vec{x}, y) = \exp(-i(Et - \vec{p}\vec{x} - p_y y))$  with  $E$  being the Energy,  $t$  the time,  $\vec{x}$  and  $\vec{p}$  the coordinate and momentum in the ordinary dimension and  $y$  and  $p_y$  being the coordinate and momentum in the extra dimension. As the additional dimension is wrapped the wave in the extra-dimension is the same after a full circle:  $\Psi(t, \vec{x}, y) = \Psi(t, \vec{x}, y + 2\pi R)$ . This is called the periodicity condition. By inserting the plane wave in the periodicity condition one gets  $2\pi p_y R = 2\pi n$  where  $n$  is an integer. This means that momentum in the extra dimension would be quantised  $p_y = n/R$ , which can be interpreted as excitations of the SM particles with masses  $\sqrt{m^2 + n^2/R^2}$ . This method can be extended to more dimensions leading to similar results. The new particles are excitation (Kaluza-Klein (KK)) modes, where the zero mode corresponds to the SM. The corresponding KK particles of the excitation modes would be stable for the case of strict momentum conservation in the extra dimensions. The particles would have a conserved KK quantum-number. One difficulty is to obtain the exact SM as a 4D effective theory. This is achieved e.g. in Reference [17], by breaking the momentum conservation in the extra dimension on loop-level, resulting in a breaking of the KK quantum-number to a KK parity. Only the odd KK numbers are charged under this parity and hence the lightest KK particle of the first mode is stable, leading to a very similar particle spectrum as in super-symmetry.

For the simplest cases, the lightest particles would be, similarly as in the SM, also long-lived for the first KK mode. This means that one can get e.g. long-lived charged KK-gluons or KK-electrons. By including the graviton as lightest KK parity charged particle one can get similar signatures as for the GMSB models with e.g. a next to lightest long-lived KK-tau [18]. Universal extra dimensions can serve good Dark Matter candidates if the lightest KK particle is neutral and stable.

### Multi-charged long-lived particles

HCLLPs are not limited to  $|q| = 1e$  and a variety of theories extending the SM is predicting them with higher charges [19, 20]. One further example is a Yang-Mills-Higgs model constructed from an almost-commutative

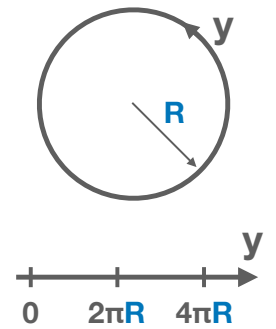


Figure 2.10: Schematic drawing of one extra-dimension wrapped to a circle with radius  $R$ . The direction along the boundary is chosen as coordinate ( $y$ ).

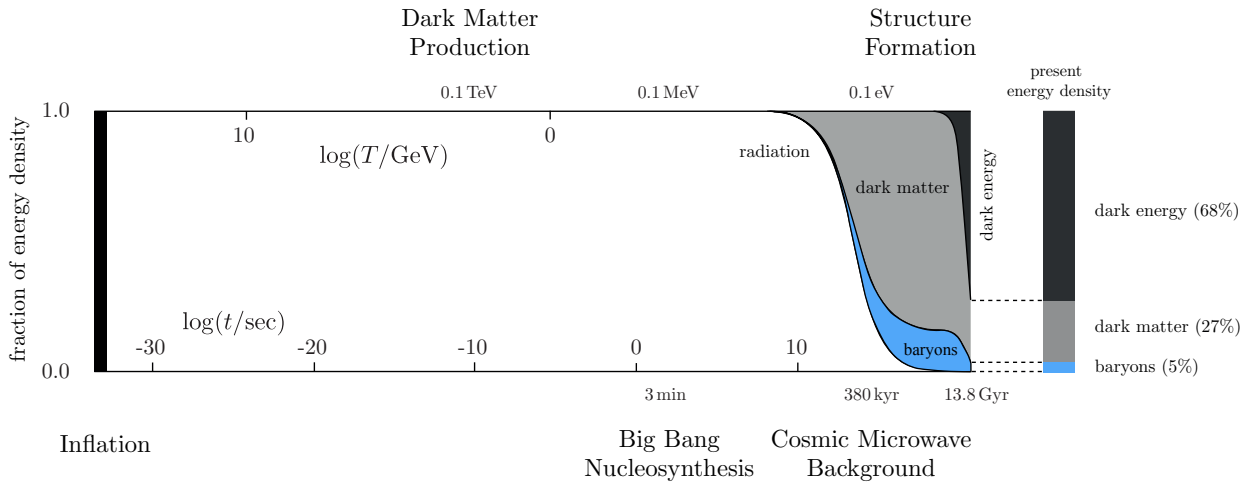


Figure 2.11: Diagram showing the current understanding of the Big Bang and the different epochs of the Universe together with the evolution of energy density composition of the Universe [22].

geometry [21]. In this model a pair of electroweak singlets with opposite electric charge is added to the SM. The hypercharge of the corresponding fermions can be any non-zero fractional number and, as the particles are not charged under any other gauge charge of the SM, they are expected to behave like heavy stable (multi-) charged leptons. It is also speculated that those particles could form electrically neutral bound states, which could be a candidate for composite dark matter.

### 2.2.2 Cosmological Impact and Constraints

Heavy charged long-lived particles can have significant impact on the evolution of the Universe after the Big Bang depending on their lifetimes and possible interactions. They can be either themselves Dark Matter candidates or co-existing with an additional dark matter candidate. As it is hard to construct a theory leading to the dark nature (not interacting with light) for the former, in the following it will be mostly focused on the co-existing candidates. Comparing the expected impact of heavy charged long-lived particles with observations gives rather stringent limits on the densities and interactions, which will be discussed in the following. A very comprehensive introduction to the current understanding of the evolution of the Universe can be found in Reference [22] and an elaborated summary of cosmological constraints on HCLLPs can be found in [23].

The evolution of the Universe together with its energy density composition is shown in Figure 2.11. The Big Bang is expected to be followed by an epoch of accelerated expansion, called inflation. In the first minutes the

energy was mostly present in the form of radiation. During this era interactions were frequent, highly energetic and out of thermal equilibrium. Particles that are produced therefore annihilate shortly afterwards. The rate of interactions is much higher than the expansion rate of the Universe, but as the Universe is cooling down the interaction rate decreases faster than the expansion rate leading to a decoupling of the particles. As the masses and interactions of different particles are distinct they decouple at different times. Dark Matter as well as co-existing heavy charged massive particles, if massive, are expected to decouple rather early in the Universe, as indicated in Figure 2.11. A few minutes after the Big Bang the Universe is cold enough that light nuclei such as e.g. Hydrogen, Helium or Lithium can form and not immediately disintegrate. This period is called Big Bang nucleosynthesis. Roughly 400.000 years later the Universe has sufficiently cooled down, that the plasma of protons and electrons recombines forming Hydrogen atoms. The Universe gets transparent for photons as no free charges are present anymore. These photons from the beginning of the Universe are still detectable in the form of the Cosmic Microwave Background. After this the structure formation begins leading 13.8 Gyr later to the Universe observed today.

Constraints from non-collider physics on HCLLPs can be categorised into constraints from the impact on the evolution of the early Universe, constraints from indirect measurements on the interaction of new types of matter, and direct measurements of interaction with SM particles.

- impact on formation of the Universe
  - gravitational impact on evolution
  - impact on Big Bang nucleosynthesis
  - Dark Matter relic density
- decay products
  - highly energetic photons
  - distortion in Cosmic Microwave Background
- direct detection
  - scattering with SM particles
  - anomalous isotopes

Constraints from the gravitational impact of HCLLPs on the evolution of the Universe can be explained as follows. An over-production of matter particles in the early Universe would lead to a faster termination of the radiation dominated epoch. Which means that the Universe would be younger. Strong limits can be obtained comparing the corresponding age of the Universe with the age of the oldest observed objects, e.g. globular clusters [24].

A further important source of constraints for HCLLPs is their impact on the Big Bang nucleosynthesis. The abundances of the light elements estimated from simulations of the Big Bang nucleosynthesis are in good agreement with the abundances measured in regions of the Universe without significant processing in stars. The only deviation was found for the  ${}^7\text{Li}$  abundance, where the simulations predict a roughly three times larger abundance than the ones observed [25]. HCLLPs produced at the beginning of the Universe are expected to have mostly highly energetic decay products, due to the energy available from the mass of the HCLLPs. If the lifetime of the particles is sufficient to decay in significant amounts during Big Bang nucleosynthesis they could inject highly energetic particles into the plasma. This can have significant impact on the relative abundances, as those particles could be able to disintegrate e.g. Helium nuclei. In particular hadronic injections such as highly energetic protons are problematic, but also induced photodissociation processes by highly energetic non hadronic particles can lead to effects, that are in conflict with the observations. But it was also shown for example in Reference [26], that HCLLPs could explain the lower  ${}^7\text{Li}$  abundances. They are able to form bound states with nuclei which have, due to their high mass, cross sections in the order of nuclei and not of the order of atoms. Such bound states are able to induce reactions which increase the  ${}^6\text{Li}$ , but decrease the  ${}^7\text{Li}$  abundance. If the HCLLPs are partners to electrons or muons (e.g. selectron or smuon in SUSY), regions in phase space can be found where the right abundances for both  ${}^6\text{Li}$  and  ${}^7\text{Li}$  can be achieved. A possible way to get around highly energetic decay products disintegrating the light atoms are models where long lifetimes are achieved by a mass degeneration between the HCLLP and the Dark Matter candidate. For those scenarios most of the energy is carried away by the Dark Matter candidate, and only very soft SM particles are injected into the plasma. For those cases also partners to the tau (e.g. staus) can lead to the right abundances of the light elements [27].

Another important constraint is that the correct relic densities for Dark

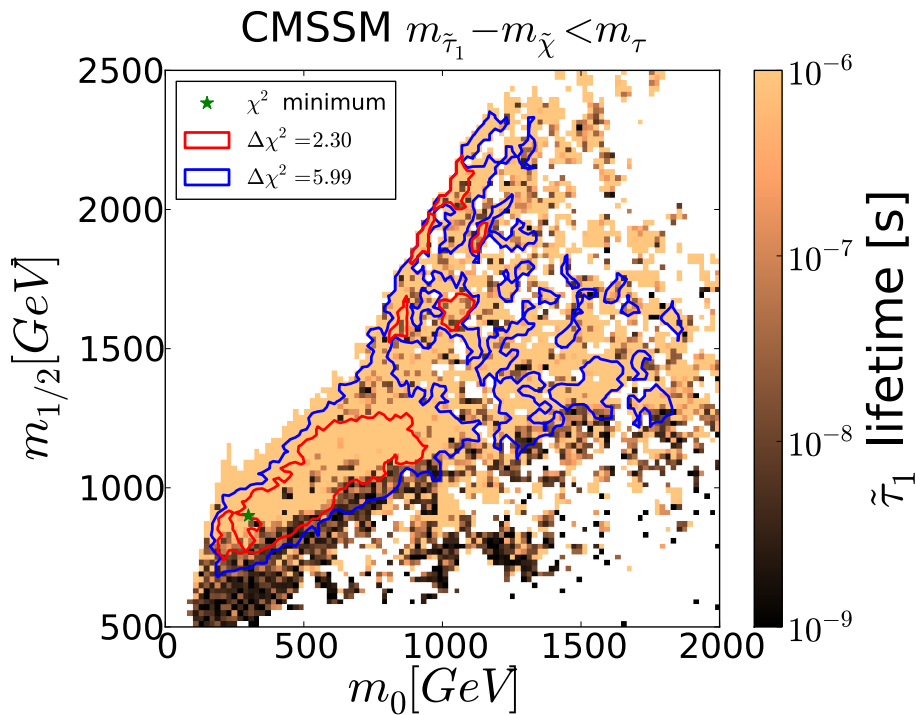


Figure 2.12: Plot showing 10,000 CMSSM points with the mass-difference between the chargino and stau being smaller than the tau mass, leading to long-lived staus. The best result from the CMSSM fit is shown with a green star, the 68% and 95% CLs regions are drawn in red and blue respectively. The colour code is indicating the lifetime of the stau for the respective model point [29].

Matter have to be achieved as measured e.g. by the Wilkinson Microwave Anisotropy Probe (WMAP) [28]. The related constraints are of course largely model dependent as they need knowledge about the interactions of Dark Matter candidates and potentially also the related HCLLPs. Studies were carried out e.g. in Reference [29] scanning the Constrained Supersymmetric Standard Model (CMSSM) [30] parameter-space for the correct relic Dark Matter density, incorporating results from searches at the LHC. Low supersymmetry-breaking mass parameters are mostly ruled out by direct searches. The high mass region not yet excluded by the searches typically gives to large relic Dark Matter densities [31]. Interesting regions for high mass parameters are hence regions where the Dark Matter candidate co-exists with an almost mass degenerated stau. The mass degeneration results in rather long lifetimes for the staus, which hence are able to annihilate with the Dark Matter candidates, in this case the lightest neutralino, to effectively lower the relic Dark Matter density. The results of the CMSSM fit are shown in Figure 2.12. It can be seen that most of the interesting regions and in particular the best fit result is estimated for staus with lifetimes in the region 100 ns-1000 ns. These lifetimes are sufficiently large for particles produced at the LHC (velocities close to the speed-of-light) to travel  $O(100$  m). Which are distances sufficient to pass the full ATLAS detector.

Problematic for charged long-lived particles are also constraints from indirect observations, such as decay products in the form of highly energetic photons. Highly energetic photons from the decays of HCLLPs would be visible today, for particles decaying after the recombination of protons and electrons. The corresponding spectrum, including the effects of photon scattering and redshift, are calculated and compared with the observed diffuse gamma-ray background in Reference [32] to place limits depending on mass, relic density, lifetime and branching fraction to photons. Relics with reasonable branching fractions can be ruled out for lifetimes of the order  $10^{-4}$  times the age of the Universe.

Decay products in the form of highly energetic photons can also be problematic for the Cosmic Microwave Background. For lifetimes lower than the ones problematic for the diffuse gamma-ray background the produced highly energetic particles would be injected into the thermalisation of the blackbody spectrum of the Cosmic Microwave Background. The limits on spectral distortion can be used to place limits similar to the ones from the diffuse gamma-ray background, but for smaller lifetimes [33].

The Dark Matter density near the earth can be estimated through rotation curves of the Milky Way, hence over the gravitational impact. Using this as input the cross section of Dark Matter particles interacting with SM particles can be measured by experiments looking for momentum exchange between Dark Matter particles and nuclei. The current upper cross section limits are  $10^{-44}$  cm<sup>2</sup> and lower for scattering of Dark Matter candidates with masses between 1 GeV – 1 TeV with a nucleon [7]. This rules out by far Dark Matter candidates, that interact over the SM electromagnetic or strong force, which means that HCLLPs can not be Dark Matter candidates themselves.

For very long lifetimes the HCLLPs would still be present today in significant amounts. Hence they could also be present on earth. Searches were carried out looking for bound states, such as heavy hydrogen, or if colour-charged heavy isotopes. For the heavy isotopes searches deep-sea water was analysed using mass spectroscopy as e.g. in Reference [34]. For the strongly interacting massive particles as probes, different types of nuclei e.g. Au or Fe were exposed e.g. on the earth surface or to heavy ion collisions [35]. Nothing was observed and strong limits on the concentration of HCLLPs on earth are set [7], which rules out most models with very long lifetimes.

In Reference [36] the relic abundance for gluinos was calculated in Split-SUSY models and compared to the constraints discussed before. The life-

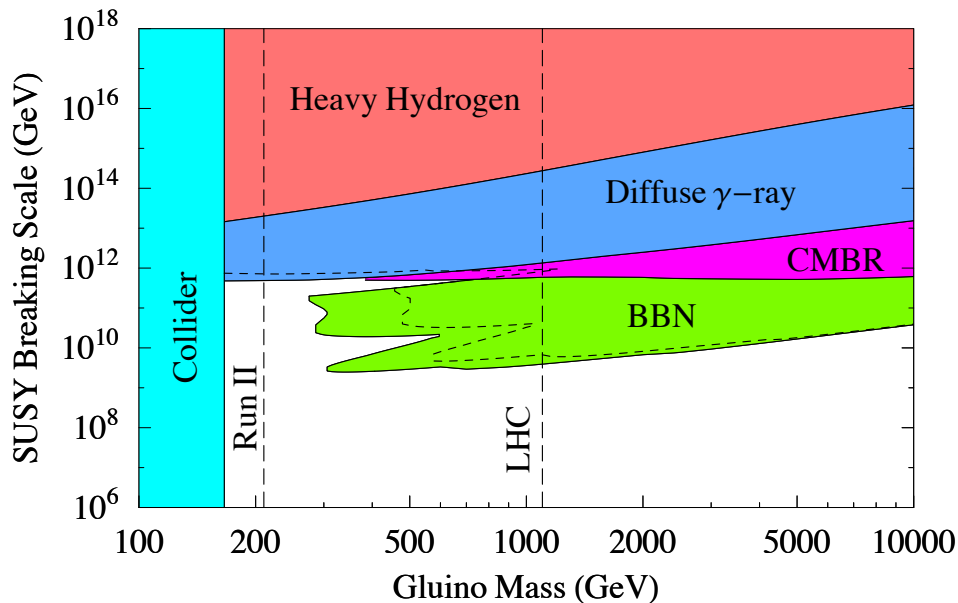


Figure 2.13: Regions that are ruled out by different direct or cosmological constraints are shown in the respective colours. Red: Searches for heavy hydrogen. Blue: Measurements of the diffuse gamma ray background. Purple: Black body spectrum of Cosmic Microwave Background. Green: light element abundances due to Big Bang nucleosynthesis. Turquoise: direct detector searches. Conservative as limits from mono-jet searches are used for cases where  $R$ -hadrons are produced solely electrically neutral. If some fraction is produced charged limits are significantly stronger. The figure is taken from [36]

time in those models is roughly given by Equation 2.2 [37].

$$\tau \approx 4 \text{ s} \left( \frac{m_S}{10^9 \text{ GeV}} \right)^4 \left( \frac{1 \text{ TeV}}{m_{\tilde{g}}} \right)^5 \quad (2.2)$$

With  $m_S$  being the supersymmetry breaking scale. The constraints for these models are shown in Figure 2.13. As expected, the longer the lifetime, the later the epoch of the Universe the constraints come from. For very long lifetimes models are excluded via the searches for heavy hydrogen, while for smaller lifetimes the decay products, in form of highly energetic photons, are in conflict with the diffuse gamma-ray background or the measured Cosmic Microwave Background. The lower edge of the Big Bang nucleosynthesis exclusion curve is roughly at 100 s, which is still sufficient for HCLLPs to be detector stable.

At least to first order HCLLPs are ruled out as Dark Matter candidates itself, but e.g. composite Dark Matter could still be interesting, potentially with additional forces between the new particles [38]. For models where the HCLLPs are coexisting with Dark Matter the most stringent constraints come from highly energetic decay products. The constraints become much weaker for compressed scenarios between the HCLLP and the dark matter candidate. In those compressed scenarios only very soft decay products and hence less troublesome particles are generated in

the decay. Those cases can also imply that co-existing HCLLPs lower the relic density of Dark Matter through co-annihilation and also solve the  ${}^7\text{Li}$  overproduction in Big Bang nucleosynthesis simulations. So scenarios with HCLLPs might be the last corners of phase space for theories with simple Dark Matter such as SUSY and are hence a well motivated target for detector searches.

## 2.3 Summary

The SM is a very successful theory that has passed decades of precision testing. Nevertheless there are several hints that point towards a more fundamental theory. An example would be the missing understanding of the nature of Dark Matter or Dark Energy. There is a large variety of theories extending the SM that try to solve one or the other issue, but so far no one-fits-all solution was discovered. Many of those theories have in common, that they allow for long-lived particles for reasons similar to the ones leading to longevity in the SM. In this work the main focus lies on HCLLPs which could, due to their significant lifetimes, have had an impact on the formation of the universe. This on the one hand rules out large regions of lifetimes and particle masses, but on the other hand they could also solve some cosmological questions like for example the  ${}^7\text{Li}$  abundance after the Big Bang nucleosynthesis. The interesting lifetimes are in a range, where the particles are able to interact with the detector and hence are a theoretical motivation for generic searches for HCLLPs at colliders.

## Chapter 3

# Experiment

In this chapter the experimental setup will be discussed. First, a brief introduction of the LHC will be given, including the relevant details about bunch structure and luminosity. This is followed by a description of the ATLAS detector. For the ATLAS detector the main focus is on the detector components which are in particular relevant for the identification of HCLLPs.

### 3.1 Large Hadron Collider

The LHC [39] is currently the largest and also most powerful particle accelerator in the world and situated near Geneva (Switzerland) at CERN. It is installed in a 26.7 km tunnel with an average depth of roughly one hundred meters below surface. The LHC is designed to accelerate hadrons, like protons or heavy ions. For protons the design value for the maximum beam energy is 7 TeV, which corresponds to a maximum centre-of-mass energy of 14 TeV for the collisions. The beams are brought to collision at the four interaction points, where the large LHC experiments are located. Those are ATLAS, CMS [40], LHCb [41] and ALICE [42]. LHCb is primarily designed for physics involving bottom-quarks, while ALICE is mainly focused on heavy ion physics. In contrast to those specialised detector designs, ATLAS and CMS are general purpose detectors.

To achieve such high energies the LHC is equipped with an injector chain subsequently increasing the energy of the hadron beams. A schematic drawing of the CERN acceleration complex is shown in Figure 3.1. For proton-proton collisions the primary acceleration to 50 MeV is carried out by LINAC2. The next acceleration stage is reached with the Proton Synchrotron Booster, producing protons with 1.4 GeV. From there the pro-

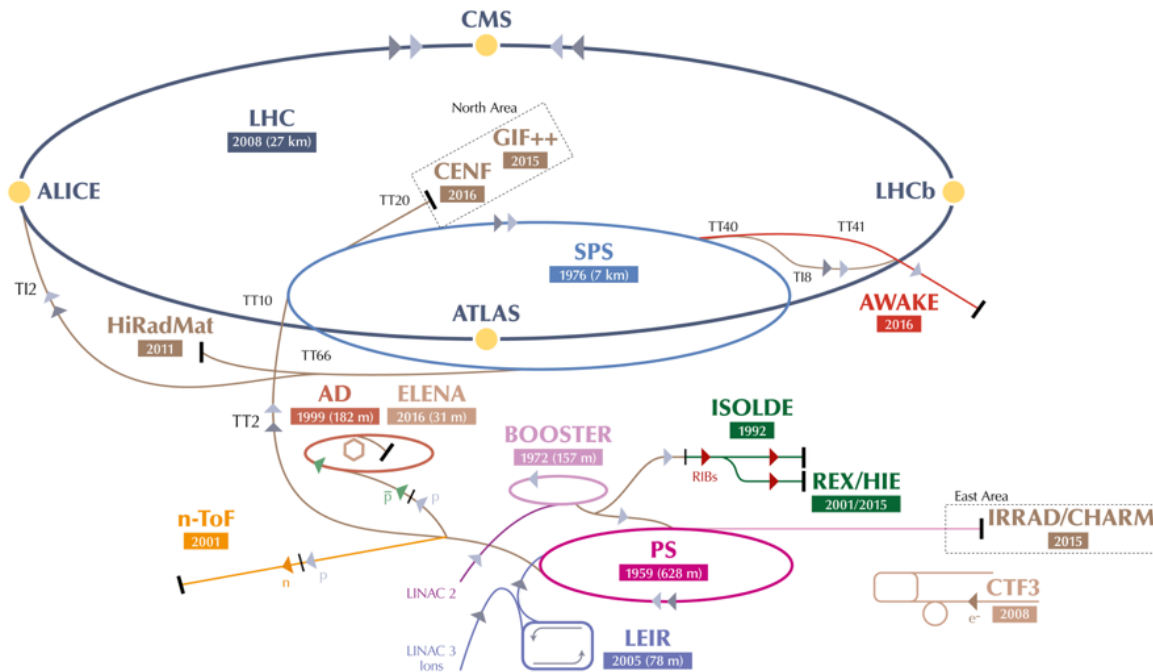


Figure 3.1: The CERN accelerator complex. The large blue circle illustrates the LHC, with the four large experiments ATLAS, CMS, LHCb and ALICE indicated by yellow markers [43]

tons are injected into the Proton Synchrotron and accelerated to 26 GeV. Finally the last acceleration stage before the LHC is the Super Proton Synchrotron producing 450 GeV protons, which are then injected into the LHC. A summary of the LHC pre-injector chain can be found in [44].

The LHC main accelerator ring is situated in the tunnel built for the previous Large Electron-Positron Collider (LEP) experiment [45]. It is equipped with about 10,000 superconducting magnets to bend the particle path and focus the beams of the two counter running beamlines. Among them are 1,232 dipole magnets, which are used to bend the particles on the circular path. The dipole magnets are designed to produce a magnetic field of up to 8.33 T. The other magnets are quadrupole or higher-multipole-order magnets with the purpose to focus the beams. For the acceleration of the beams the LHC is equipped with a 400 MHz radio frequency superconducting cavity system. The LHC beams are hence not constant but a series of proton bunches. In principle the 400 MHz system would allow for buckets every 2.5 ns, but only every tenth gets filled by the kicker magnets [46], which are injecting the protons. It has therefore a bunch spacing of 25 ns. Due to imperfections of the kicker magnet, also the intermediate buckets get filled but with significantly lower numbers of

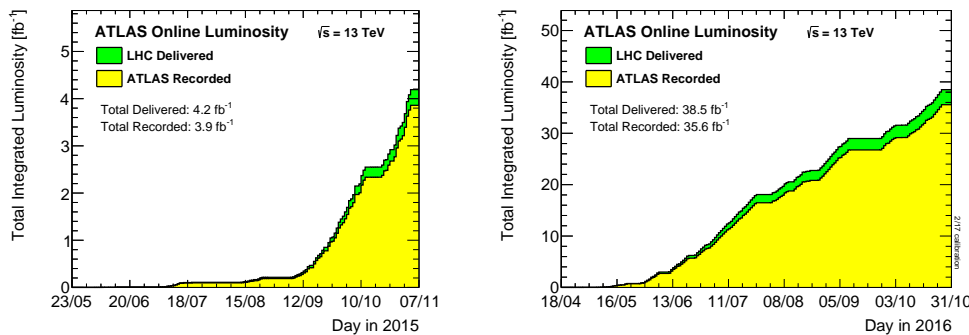


Figure 3.2: The total integrated luminosity over time delivered by LHC or recorded by ATLAS, respectively for 2015 (left) and 2016 (right). The figures are taken from [47]

protons. The bunches are organised in trains, with larger gaps of empty buckets between the trains.

Each of the colliding bunches contains roughly  $10^{11}$  protons, which lead to roughly 25 simultaneous inelastic proton-proton collisions per bunch crossing in 2015 and 2016, where the data for the search described in this thesis were recorded. A high number of simultaneous collisions on the one hand increases the probability for interesting collisions with high momentum transfer, but on the other hand also crowd the detector, which can be problematic for the reconstruction of the particles. Those additional collisions in the same bunch-crossing are called in-time pileup. Whereas particles from so called out-of-time pileup originate from the previous or following bunch crossings. Also out-of-time pile-up can be problematic for the reconstruction of the events, which can be understood by following gedankenexperiment: Assuming a detector with roughly 20 m distance to be traversed by the particles. For speed-of-light particles this results in a time to reach the end of the detector of roughly 60 ns. Comparing this with the bunch spacing of 25 ns means that particles from about two-three bunch crossings are simultaneously in the detector. The measurements can hence be corrupted by particles traversing the same detector components.

The measure for the rate of collisions in scattering physics is the luminosity ( $\mathcal{L}$ ), which is defined as the number of particles passing a unit area per time unit. By knowing the cross-section ( $\sigma$ ) of the process the number of events per unit time can be calculated as

$$\frac{dN}{dt} = \sigma \mathcal{L}. \quad (3.1)$$

The total amount of accumulated collisions is accordingly given by the in-

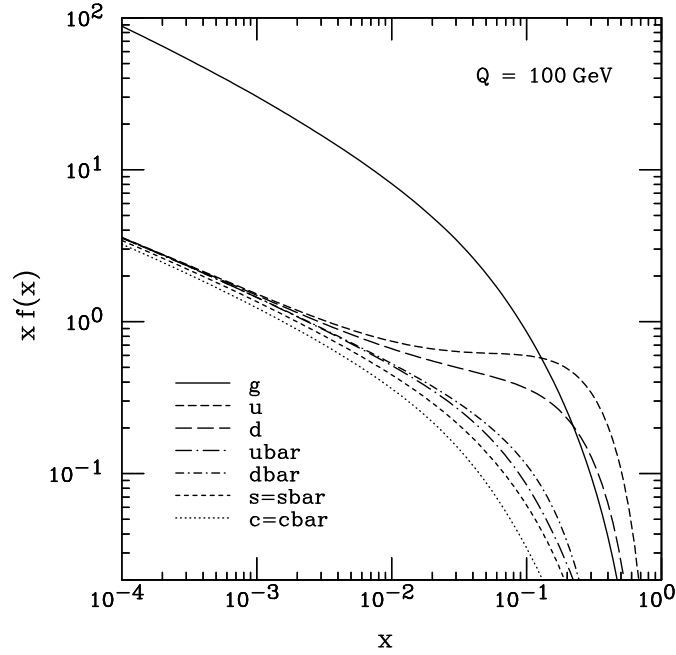


Figure 3.3: The PDF's for different partons at a momentum transfer  $Q=200$  GeV, with  $x$  being the momentum fraction of the the total proton momentum. [48]

egrated luminosity  $\mathcal{L}_{\text{int}} = \int \mathcal{L} dt$ . The integrated luminosity delivered by the LHC and recorded in ATLAS is shown in Figures 3.2 for the data-taking periods considered in this thesis.

In a proton-proton collider the initial-state particles are composed from so called partons. The longitudinal momentum of the parton involved in the hard process is unknown. Instead only the probability for having a given fraction of the total momentum ( $x$ ) can be determined, represented by the Parton Density Functions (PDF)'s as shown in Figure 3.3. Besides the valence quarks (up-, up-, down-quark for a proton), also gluons as exchange particles of the strong interaction are present in the proton. Furthermore a sea of additional quarks is part of the proton, from pair-production and immediate annihilation. From Figure 3.3 it can be seen that low momentum fraction  $x$  is most likely carried by gluons, while for high  $x$  the valence quarks take over. The probability for an up-quark is larger than for the down-quark, as the proton is made from two up- and only one down-quark. The colliding partons, and hence the initial state for the production, can be both gluons or quarks, even the ones not present as valence quarks. As the exact longitudinal momentum of the colliding partons is unknown at hadron colliders several useful variables are defined in the transverse plane as e.g. the transverse momentum ( $p_T$ ). Also the missing transverse energy  $\cancel{E}_T$  is an important quantity, and is defined as the inverted sum of the transverse momenta of the reconstructed parti-

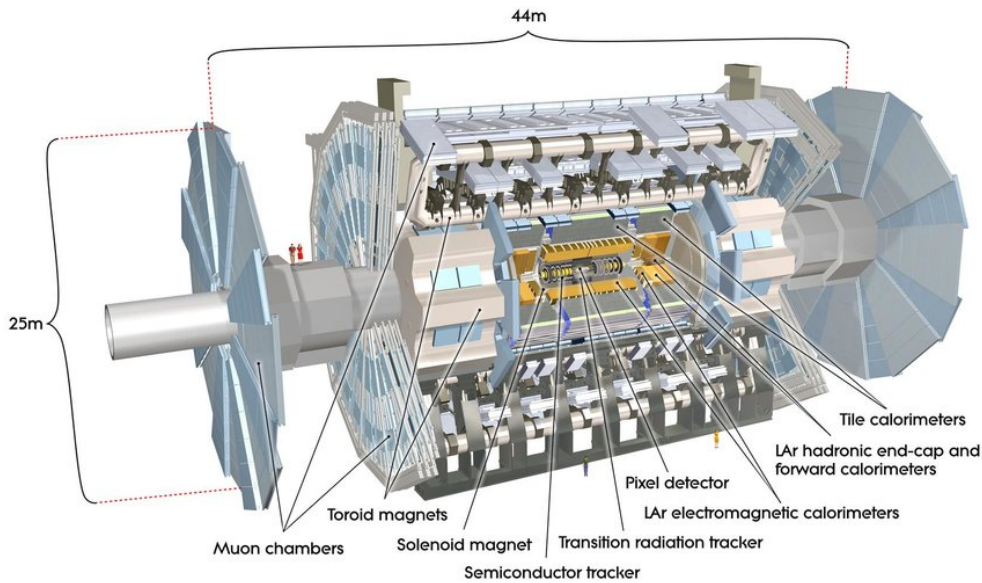


Figure 3.4: A schematic drawing of the ATLAS detector with its different sub-systems. The figure is taken from [49].

cles. The  $\cancel{E}_T$  is a way to find undetected particles, as the momenta of the colliding partons are solely in the longitudinal direction and hence due to momentum conservation, the transverse momenta should add to zero.

## 3.2 ATLAS detector

The ATLAS detector is one of the two multipurpose detectors at the LHC. It is used to identify particles produced in the collisions of protons delivered from the LHC. It hence has to deal with the challenge of enormous rates and identify relevant particles in a dense environment of soft QCD background.

A schematic drawing of the ATLAS detector with the different sub-systems is shown in Figure 3.4. The ATLAS detector has an onion-shaped structure, comparable to other multipurpose detectors. In the barrel region this is achieved by concentric cylindrical detector layers, while both sides are closed by layers of disks, called end-caps, to achieve close-to  $4\pi$  coverage. The total size of the ATLAS detector is roughly 44 m along the beam axis and about 25 m in diameter. The innermost part of the ATLAS detector, called Inner Detector (ID), is a tracking system composed of a pixel detector, a Semiconductor Tracker (SCT) and a Transition Radiation Tracker (TRT) immersed in a solenoidal magnetic field of 2 T [50] to allow for a precision momentum measurement of charged particles. The ID is followed by the calorimeters. For the electromagnetic calorime-

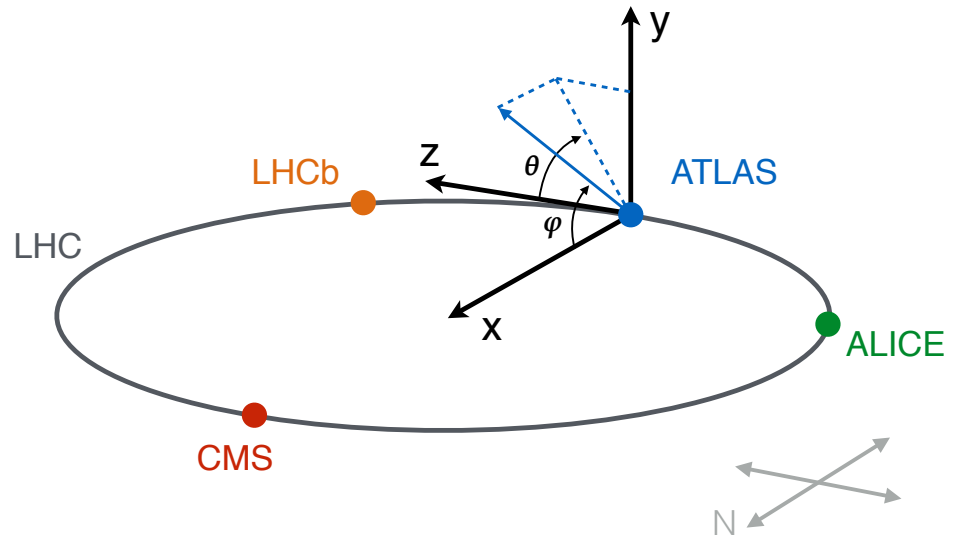


Figure 3.5: A schematic drawing of the ATLAS coordinate system.

ters both in the barrel and in the end-caps Liquid Argon (LAr) detectors are used. The hadronic calorimeter in the barrel region is a tile calorimeter, while the hadronic end-cap calorimeters use the LAr technology. Also the three layers of forward calorimeters (one electromagnetic and two hadronic calorimeters) are based on the LAr technology. The outermost part of the ATLAS detector is the Muon Spectrometer (MS), which is embedded in a 4 T toroidal magnetic field [51, 52] and used for the identification and precision momentum measurement of muons, the only charged SM particles able to pass the calorimeters. In the barrel it is equipped with Monitored Drift Tubes (MDTs) and Resistive Plate Chambers (RPCs), while in the end-caps MDTs and Thin Gap Chambers (TGCs) are used. In the very forward region Cathode Strip Chambers (CSCs) are installed. The different subsystems and their functionality will be explained in more detail in the following sections. The ATLAS detector is equipped with a two level trigger system to reduce the information to a level that is recordable, which will be discussed in the last section. A detailed description of the ATLAS detector can be found in Reference [53].

The coordinate system used in the ATLAS detector is illustrated in Figure 3.5. A right-handed coordinate system with the Interaction Point (IP) as origin is chosen. The  $x$ -axis pointing towards the centre of the LHC, the  $y$ -axis pointing to the surface and the  $z$ -axis oriented along the beamline. The azimuthal angle  $\phi$  is measured in the  $x$ - $y$ -plane with respect to the positive  $x$ -axis, while the polar angle  $\theta$  is measured with respect to the positive  $z$ -axis in the  $r$ - $z$ -plane, with  $r$  being the radial distance. In scattering experiments the pseudorapidity  $\eta$  is typically used instead of the polar

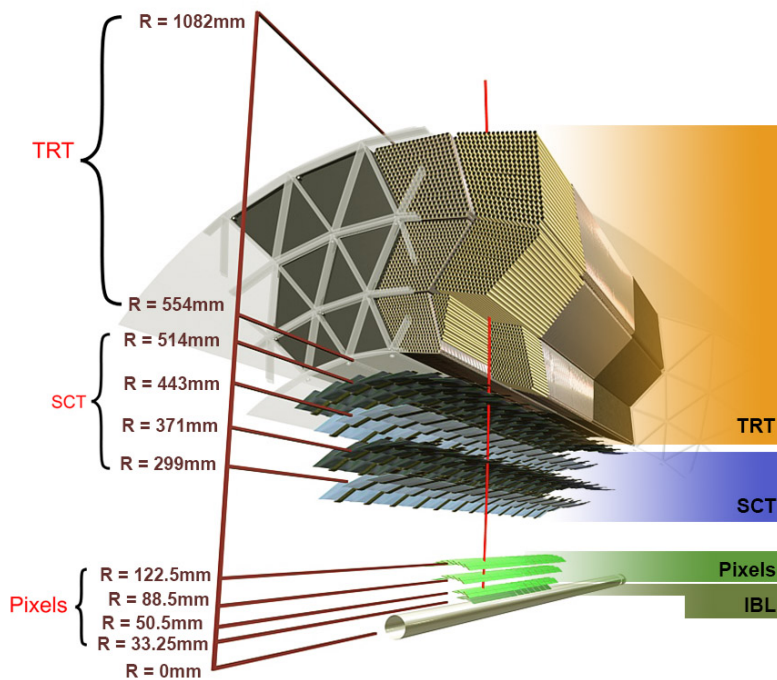


Figure 3.7: Schematic cut-away drawing of the ATLAS ID including the different subsystems. Also the radii for the different layers (pixel detector, SCT) or the size of the TRT are given, respectively. The figure is taken from Reference [54].

angle. The pseudorapidity is the same as the rapidity in the limit of negligible particle rest masses compared to the momentum of the particles. One advantage of the rapidity is, that differences in rapidity are Lorentz invariant for boosts along the longitudinal-axis. While the rapidity is energy dependent the pseudorapidity is only dependent on the angle and can be calculated from  $\theta$  as

$$\eta = -\ln \left[ \tan \left( \frac{\theta}{2} \right) \right]. \quad (3.2)$$

Some random values of the pseudorapidity and the respective  $\theta$ -angles are shown in Figure 3.6. It can be seen, that for a forward direction (along  $z$ -axis)  $\eta$  goes to infinity, while for a central direction at  $\theta = 90^\circ$  the pseudorapidity declines to zero. A further advantage of the pseudorapidity is that the particle production rate as a function  $\eta$  is roughly constant for a hadron collider.

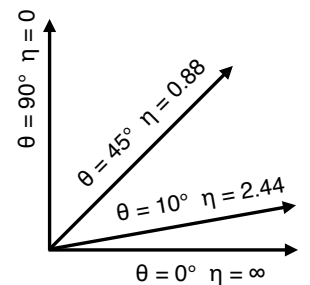


Figure 3.6: The values of the pseudorapidity for some  $\theta$ -angles.

### 3.2.1 Inner Detector

The ATLAS ID has the main task to measure the momenta of charged particles. High-precision position hit information can be combined to reconstruct particle trajectories (tracks), which can be used to determine the momentum and the sign of the charge of particles via the curvature of

the track in the magnetic field. The ID covers the  $|\eta|$  range up to 2.5 and is composed of three types of detectors, a pixel detector, a SCT and a TRT. A schematic drawing of the ATLAS ID is shown in Figure 3.7. Besides momentum and charge determination a further main task of the ATLAS ID is to identify primary and secondary vertices and associate the tracks to them. The association of charged particles to the primary vertices is in particular important to clean the events from particles originating from pile-up collisions. The secondary vertex reconstruction can be used to identify meta-stable particles with resolvable lifetimes. The ID is designed to give a momentum resolution of

$$\sigma_{p_T}/p_T = 0.05\%p_T [\text{GeV}] \oplus 1\% \quad (3.3)$$

for particles with a minimum  $p_T$  of 400 MeV. A detailed description of the different subsystems will be given in the following.

### Pixel Detector

The innermost part of the ATLAS inner tracking system is the silicon pixel detector [55]. The pixel detector consists of four concentric detector layers in the barrel region at 33.25 mm, 50.5 mm, 88.5 mm and 122.5 mm covering the  $|\eta|$  range up to 1.7. The innermost layer, called Insertable B-Layer (IBL) [56], was not part of the original design but installed in May 2014. The IBL was installed as close to the beamline as possible and improves the vertexing significantly, due to the location at a small radius. The typical pixel size used in the IBL is  $50 \mu\text{m} \times 250 \mu\text{m}$  with a thickness of  $200 \mu\text{m}$ , whereas for the other layers a typical pixel has a size of  $50 \mu\text{m} \times 400 \mu\text{m}$  in the transverse and longitudinal direction respectively with a thickness of  $250 \mu\text{m}$ . Furthermore the IBL gives an additional high precision hit, which is improving the tracking. In the end-caps the pixel detector is equipped with three disks perpendicular to the beam pipe on each side, covering the region  $1.7 < |\eta| < 2.5$ . The disks are placed at 495 mm, 580 mm and 650 mm in  $|z|$ . Overall the pixel detector is equipped with  $73.2 \times 10^6$  pixels in the four barrel layers and  $13.2 \times 10^6$  pixels in the end-caps, which gives in total  $86.4 \times 10^6$  pixels. In the barrel a position resolution accuracy of  $10 \mu\text{m}$  in  $\phi$  and  $115 \mu\text{m}$  in  $z$  is achieved. Besides the precision position information the pixel detector is also capable of measuring the charge collected via a time-over-threshold [57] measurement. The time-over-threshold is the time for which a signal in a pixel exceeds a certain value. It is measured in units of bunch crossings.

The time-over-threshold is proportional to the energy deposit in the pixel and hence can serve as a measure for it. The IBL signal is read out with a 4-bit resolution, while the other pixel layers are read out with an 8-bit accuracy. Problems for the energy deposit measurements can occur due to saturation effects. For the outer pixel layers about 8.5 times the energy released by a minimum ionising particle is causing a saturation in a pixel. The IBL pixels however already saturate at 1.5 times the expected energy deposit of a minimum ionising particle. The IBL is therefore equipped with an additional bit indicating if a given pixel is in saturation.

### **Semiconductor Tracker**

The second layer of the inner tracking system is the SCT, a silicon-based detector similar to the pixel detector. In the barrel the SCT consists of four double layers of silicon strip detectors, with a typical strip length of 126 mm and a pitch of  $80 \mu\text{m}$ . The strips on the outer of the double layers are tilted under a small stereo angle of 40 mrad to get an information in the non-precision direction along the strips ( $z$ -direction). A spatial resolution of  $580 \mu\text{m}$  along the  $z$ -axis is achieved, while in the precision direction in the  $\phi$ -plane an accuracy of  $16 \mu\text{m}$  is accomplished. The SCT end-caps consist of nine disks on each side covering the  $|\eta|$  range up to 2.5. In contrast to the pixel detector, the SCT does not provide any information about the energy deposit in the strips.

### **Transition Radiation Tracker**

The outermost part of the ATLAS inner tracking system is the TRT [58]. The TRT consists of thin-walled proportional drift tubes called straw tubes with a diameter of 4 mm. A gold-plated tungsten wire with a diameter of  $30 \mu\text{m}$  is placed in the centre of the straw tubes and serves as anode. The cathode is the straw itself and made of to wound films of capton coated by a thin layer of aluminium on the inner side. The straws are mechanically supported by four carbon-fibre strands. In the barrel region the TRT is composed of 52,544 straw tubes with a length of 144 cm oriented along the beamline. In each of the two end-caps 122,880 straw tubes are installed with a length of 37 cm. There the straw tubes are oriented radially with respect to the beamline. The TRT in contrast to the other two inner tracking systems covers only the  $|\eta|$  range up to 2.0. In the  $r$ - $z$  plane the TRT barrel covers the volume between -712 mm and 712 mm in  $z$  and 563 mm-1066 mm in  $r$  and the end-caps the region between 848 mm and

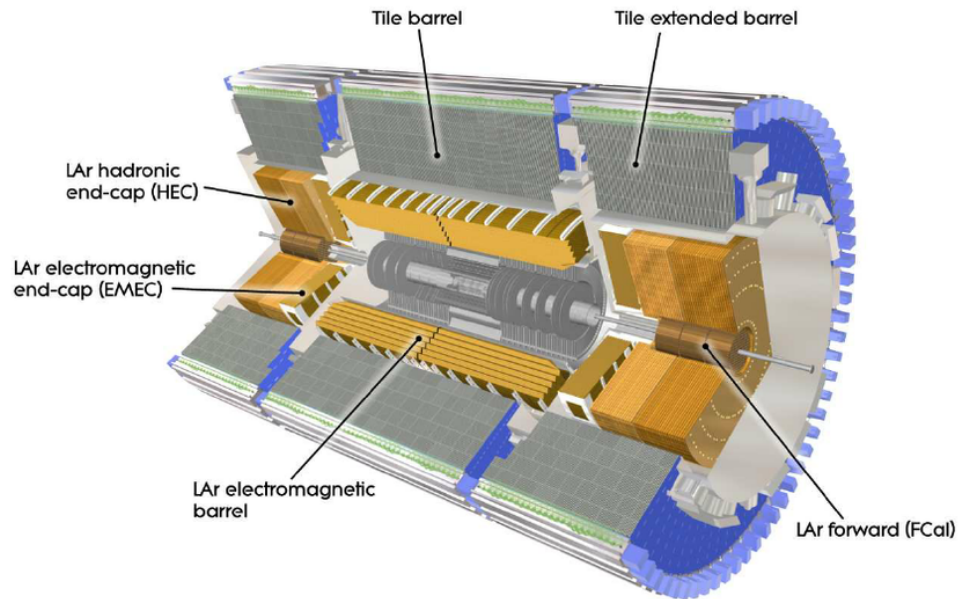


Figure 3.8: Schematic cut-away drawing of the ATLAS calorimeters including the different subsystems. The figure is taken from Reference [59].

2710 mm in  $z$  and 644 mm - 1004 mm in  $r$ . The volume between the straw tubes is filled with polypropylene fibres to identify highly boosted particles through transition radiation produced at the fibre surfaces. Due to this technology, a separation between electrons and e.g. the heavier pions is possible. The straw tubes are filled with 70% Xe, 27% CO<sub>2</sub> and 3% O<sub>2</sub>, where the large fraction of Xe is chosen due to its x-ray absorption capability of the transition radiation photons. The individual straws in the barrel are split into two channels read out on both sides, while the straws tubes in the end-caps are read out on the outer side. Each channel provides a drift circle measurement with a spatial resolution of 170 $\mu$ m and low and high threshold bits to differentiate between normal tracking hits and transition radiation hits.

### 3.2.2 Calorimeters

The main purpose of the ATLAS calorimeters is to measure the energy of particles through their electromagnetic or hadronic particle showers, respectively. The ATLAS detector is therefore equipped with EM calorimeters to stop electrons and photons and hadronic calorimeters to stop hadrons. The only charged SM particles able to escape the calorimeters are the muons. The ATLAS calorimeters are all sampling calorimeters with independent active and absorber material. A schematic drawing of the ATLAS calorimeters with the different subsystems is shown in Figure 3.8.

## Electromagnetic Calorimeters

Highly energetic photons undergo pair creation in the presence of nuclei, while electrons and positrons emit photons via bremsstrahlung. These two alternating effects lead to EM showers when highly energetic photons, electrons or positrons enter dense material. Those showers die out when the energy of the produced particles falls below a critical energy at which ionisation energy loss takes over for electrons/positrons. The shower depth is characterised in multiples of the radiation length, which corresponds to the distance where the energy has been reduced to  $1/e$ . The ATLAS EM calorimeter [60] is designed to measure the full showers also for highly energetic electrons or photons and has therefore a minimum thickness of 22 radiation lengths. The LAr calorimeter in the barrel covers the  $|\eta|$  range up to 1.475 and extends radially from roughly 1.4 m to 2.0 m, while the end-caps have an acceptance window of  $1.375 < |\eta| < 3.2$ . The end-cap EM calorimeters consist of two co-axial wheels covering  $1.375 < |\eta| < 2.5$  and  $2.5 < |\eta| < 3.2$ , respectively. In the very forward region three concentric layers of LAr calorimeters are placed to cover the region  $3.1 < |\eta| < 4.9$ , where the first layer is mostly aiming for EM showers. The first module is therefore equipped with copper as absorber, while the other two use the more dense tungsten to also absorb hadronic showers. The barrel and end-cap EM calorimeters use lead as absorber material and LAr as active medium. As electrodes copper coated kapton is used. The different layers are arranged in an accordion shaped geometry, as shown in Figure 3.9, to allow for a crackless design in the  $\phi$ -direction. The LAr calorimeter in the barrel is composed of three detector layers with an additional thin pre-sampler that allows for corrections of the already traversed material. The LAr calorimeter is equipped with a fine granularity of e.g.  $\Delta\eta \times \Delta\phi = 0.025 \times 0.0245$  in the second detector layer as can be seen in Figure 3.10. With this fine granularity a precise measurement of the shower shape and also of the pointing of electrons or in particular the trackless photons is possible.

In the LAr calorimeters each read-out channel is digitised with a set of five subsequent samplings separated by 25 ns. This is done for three different gains (Low, Medium, High) to enable a large dynamic range. The charge collected in each channel as well as the timing of the measurement can be reconstructed from the different samplings using the Optimal Filtering Algorithm (OFA) [61]. The design energy resolution for the EM barrel



Figure 3.9: Image showing a section of the ATLAS EM LAr calorimeter with the characteristic accordion structure. The picture is provided by CERN.

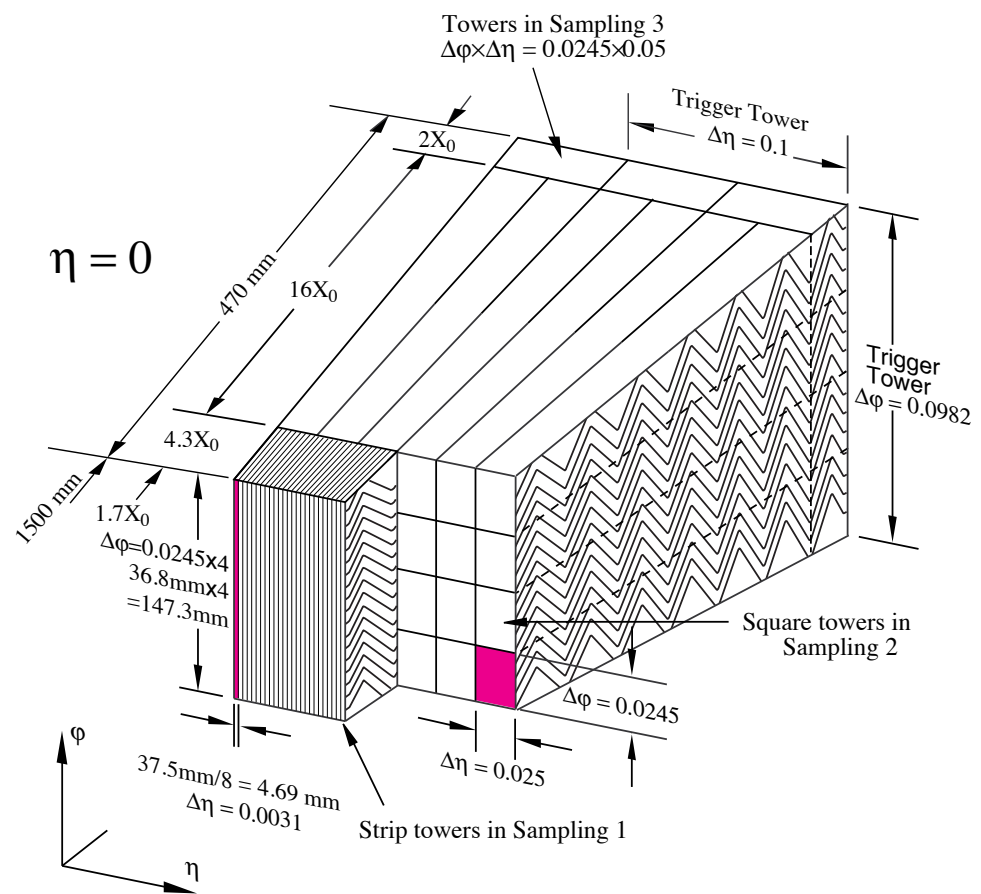


Figure 3.10: Sketch of a segment from the ATLAS LAr calorimeter. The Figure is taken from Reference [60].

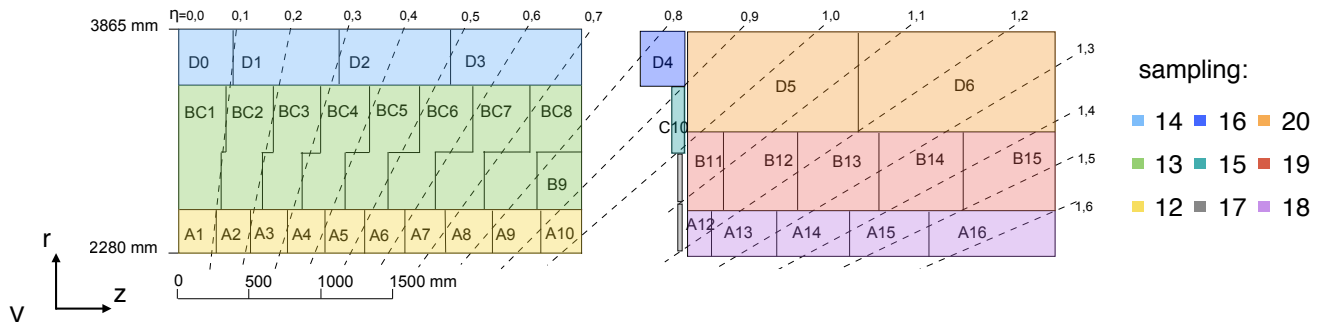


Figure 3.11: Layout and labelling of the ATLAS Tile calorimeter cells. The design is symmetric in  $z$ , the labelling in the other half is with a minus sign. The Figure is adapted from Reference [63].

calorimeter is

$$\frac{\sigma_E}{E} = \frac{10\%}{\sqrt{E [\text{GeV}]}} \oplus 0.7\% [49]. \quad (3.4)$$

Testbeam studies have shown that with 245 GeV electrons a timing resolution of 163 ps can be achieved. The timing resolution during normal LHC/ATLAS operation is limited to 256 ps (299 ps) for High (Medium) gain [62], mainly due to the bunch-spread along the beam axis<sup>1</sup>. These numbers give the resolution in the limit of large energy deposit, while for small energy deposits the resolution can be significantly worse.

<sup>1</sup>An intrinsic time uncertainty originates from time the bunches overlap as collisions can occur at any time they pass through each other.

### Hadronic Calorimeters

Similar to highly energetic electrons and photons also hadrons produce particles showers traversing dense material. But the processes responsible for the hadronic showers are different. Important processes are hadron production, nuclear de-excitations and pion/muon decays. A hadronic shower has typically a longer penetration depth than EM showers and hence an additional more dense hadronic calorimeter is needed to absorb the particle showers of highly energetic hadrons or jets. The hadronic shower depth is characterised by the hadronic interaction length.

The ATLAS hadronic calorimeters have an average thickness of 11 interaction lengths. The barrel hadronic calorimeter is a Tile calorimeter [64], while the end-cap and forward calorimeters are LAr calorimeters. The hadronic end-cap calorimeters utilise lead as absorber and cover the range  $1.5 < |\eta| < 3.2$ . The forward calorimeters span the range from 3.1 up to 4.9 in  $|\eta|$ , which leads to close-to  $4\pi$  coverage.

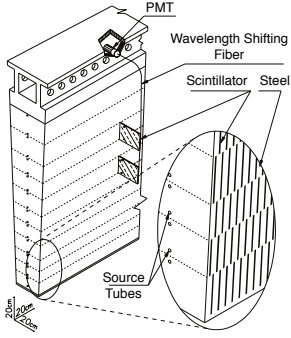


Figure 3.12: Sketch of a segment from the ATLAS LAr calorimeter. [60].

The Tile Calorimeter is segmented into a barrel and two extended barrels on each side. It covers the  $|\eta|$  region up to 1.65 and has inner and outer radii of 2280 mm and 3865 mm, respectively. Each barrel consists of 64 wedges, each with a size of 0.1 rad in  $\phi$ , as shown in Figure 3.12. In the  $r$ - $z$ -plane the Tile Calorimeter is segmented into cells with an  $\eta$  coverage of 0.1 for the two inner layers of the barrel, while cells in the third layer of the barrel and in the two inner layers of the extended barrel are covering a range of 0.2 in  $\eta$ . The coverage for the cells in the outer layer of the extended barrel is 0.25 in  $\eta$ . The shape as well as the labelling of the cells is shown in Figure 3.11. The different layers in the barrel and extended barrel are labeled as samplings 12 – 20. The size of the Tile Calorimeter cells varies significantly. While the innermost cell A1 has a size of roughly 25 cm  $\times$  25 cm, the outermost cell D6 has a size of roughly 1.5 m  $\times$  1 m. The different shape of the cells in sampling 13 is chosen to enable a quasi-projective geometry.

The Tile calorimeter uses alternating plates of steel as passive and scintillating tiles as active material. The plates are staggered in  $r$ -direction and periodic in  $z$ -direction, as can be seen in Figure 3.12. The scintillating tiles are read out on both sides in  $\phi$  via wavelength shifting fibres. Those fibres are routed to photo multipliers, with each cell being read out by one photo multiplier for each side. The front-end electronics produce a low- and a high- gain pulse. The low-gain signal is used if the high-gain signal is in saturation. With this splitting both a good signal-to-noise ratio for small signals and a large dynamic range can be achieved. The signals get digitised similar to the LAr calorimeter using samplings separated by 25 ns. In contrast to the LAr calorimeter, seven samplings are used for the Tile Calorimeter. The samplings are synchronised with the system clock in a way, that the fourth sampling corresponds to the point in time where a particle travelling at the speed-of-light and produced at the IP arrives at the center of the cell. Also for the Tile Calorimeter the OFA [65] is used to reconstruct the energy deposit and the timing, whereby the timing is measured with respect to the fourth sampling and hereafter denoted as  $t_0$ . The design energy resolution for the hadronic barrel and end-cap calorimeters is

$$\frac{\sigma_E}{E} = \frac{50\%}{\sqrt{E [\text{GeV}]} } \oplus 3\% [49], \quad (3.5)$$

while for the forward calorimeters the design energy resolution is given

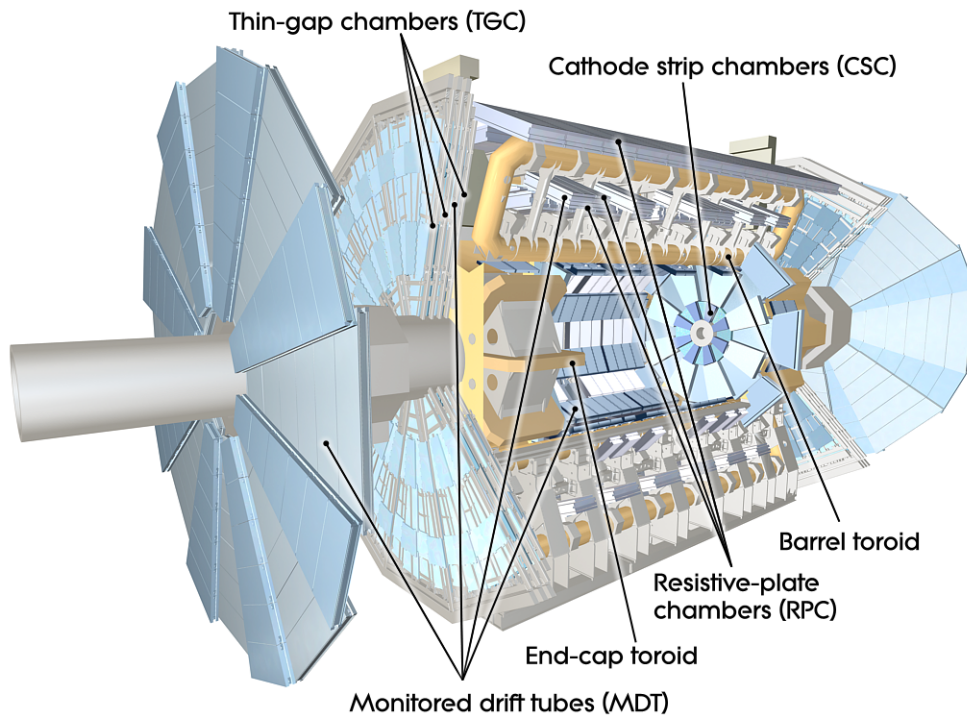


Figure 3.13: Schematic cut-away drawing of the ATLAS Muon Spectrometer including the different subsystems. [67].

by

$$\frac{\sigma_E}{E} = \frac{100\%}{\sqrt{E [\text{GeV}]}} \oplus 10\% [49]. \quad (3.6)$$

The timing resolution measured with jets in the limit of high-energy deposits is 272 ns (316 ns) for high-(low-)gain [66].

### 3.2.3 Muon Spectrometer

The outermost component of the ATLAS detector is the MS [68], which has two main tasks: Accurate momentum measurement and fast trigger signals for muons, the only charged SM particles able to traverse the calorimeters without getting absorbed. The MS is therefore immersed in a toroidal magnetic field and equipped with four different detector types: MDT's, RPC's, TGC's and CSC's. The subdetectors are arranged in three concentric layers in the barrel region. In the end-cap region on each side three wheels are installed, one small and two large wheels. A schematic drawing of the ATLAS MS is shown in Figure 3.13. The design resolution for the standalone tracking in the MS is

$$\sigma_{p_T}/p_T = 10\% [49] \quad (3.7)$$

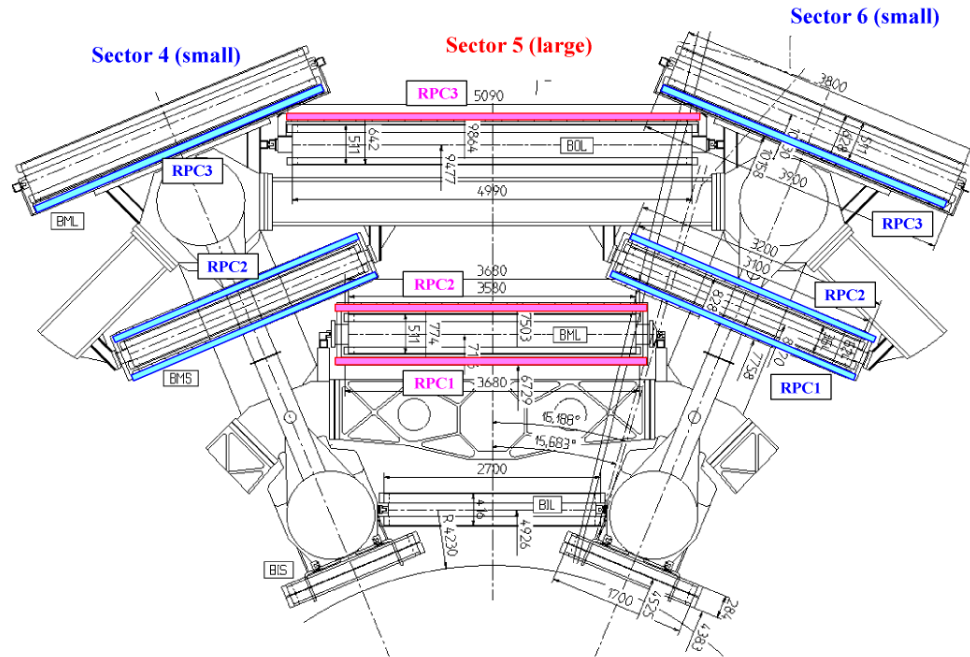


Figure 3.14: A cut-through of the upper part of the MS in the barrel. The RPC chambers are highlighted in colours. [49].

for muons with a transverse momentum of 1 TeV. The different subsystems will be introduced in the following.

### Monitored Drift Tubes

MDT's are installed in the barrel as well as in the end-cap wheels covering the  $|\eta|$  range up to 2.7. Similar to the TRT, the MDT uses proportional drift tubes, but with a larger diameter of roughly 30 mm. Overall about 354 000 drift tubes are installed in the ATLAS detector. The drift tubes are filled with 93% Argon and 7% CO<sub>2</sub> and a gold coated tungsten-rhenium wire is placed in the centre, serving as anode. The length of the drift tubes is up to 6 m. A muon traversing the drift tubes ionises the gas. The produced ions and electrons get accelerated in the electric field between the wire and the tube. From the signal a drift time and, by knowing the drift velocity, a drift circle can be reconstructed and used to determine the trajectories of the muon. For a single tube an average resolution of 80  $\mu\text{m}$  is achieved.

### Resistive Plate Chambers

RPC's are used as trigger chambers in the barrel for  $|\eta| < 1.05$ . They also complement the space point from the MDTs with a coarse position in-

formation in  $\phi$ -direction. Two layers are located on the inner and outer side of the middle layer and additional chambers are placed on the outer side of the larger chambers and on the inner side of the small chambers in the third layer as shown in Figure 3.14. Each RPC unit consists of two independent detector layers with precision directions along  $\eta$  and  $\phi$ , respectively. The detectors consist of two resistive plates separated by a distance of 2 mm. The gap in between is filled with a gas mixture based on  $C_2H_2F_4$ . Metallic strips glued to the outer surface are used for the read out of the signal. The typical size of the strips is 3 cm and they are separated by 2 mm. The electrons, produced via ionisation by the muons traversing the gas, initiate an avalanche in the high electric field of about 4.5 kV/mm. The spacial resolution for the RPC's is roughly 1 cm while for timing resolution approximately 1 ns is achieved [49].

### Thin Gap Chambers

TGCs are placed on the inner and middle end-cap wheel and used for triggering and for the measurement of the azimuthal coordinate along the drift tubes of the MDT's. The TGC's cover the  $|\eta|$  range from 1.05 to 2.7, but only up to 2.4 for triggering. On the inner wheel two layers of TGC's are installed while the middle wheel is complemented by seven TGC layers. TGC's are multi-wire proportional chambers, where gold-coated tungsten wires are used as anodes separated by 1.8 mm. The wires are placed in the centre between two thin graphite cathode layers supported by 1.6 mm G-10. Behind the G-10 layer copper strips with a width of 1.46–4.91 cm are located radially to the wires to give position information in the radial direction. One characteristic of the TGC's is the small wire-to-cathode distance of 1.4 mm, which ensures a fast signal. The signal is read out on both wire-groups and strips to determine a 3D space point. The wire-groups are formed by 4 to 20 wires and read out via one electronics channel.

### Cathode Strip Chambers

In the first layer of the forward region  $2.0 < |\eta| < 2.7$  CSC's are used instead of MDT's for the precision coordinates to cope with the extreme particle rates in this region. The CSC's are similar to the TGC's multi-wire proportional chambers, but with the cathodes itself segmented into strips. On one cathode layer the strips are aligned perpendicular to the wires, while on the other side they are aligned along the wires. For the CSC's

only the cathode strips are read-out. The strips along the wires are finer segmented and hence a better resolution of  $60 \mu\text{m}$  in the bending direction can be achieved. The resolution in the non-bending direction is, due to the wider strips only 5 mm.

### 3.2.4 Trigger system

With a separation of only 25 ns between two subsequent bunch crossings the amount of data produced with the ATLAS detector is not recordable on disk. The ATLAS detector is therefore equipped with a two-level trigger system. A fast hardware-based Level-1 trigger [69] which has to make a decision within  $2 \mu\text{s}$ , and an entirely software-based High-Level Trigger (HLT) [70].

The Level-1 trigger uses information from the trigger chambers of the MS (RPC's and TGC's) and from the calorimeters but not with the full granularity. Both, calorimeters and MS, run fast algorithms to estimate numbers and passed thresholds for muons or calorimeter objects. The information is sent to the Central Trigger Processor, which decides if a event is accepted and further processed. The objects that can be selected by the triggers are high- $p_T$  muons, high-energy EM calorimeter objects (electrons and photons), or hadronic calorimeter objects (hadronic taus and jets). Also some eventwise properties like  $E_T$  can be determined. During the beginning of Run-2 the Level-1 Topological Trigger was installed and commissioned which now also allows to select on topological or kinematic information like e.g. angular separation between the objects. The event rate is reduced by the first trigger level to 75 kHz.

The objects selected by the Level-1 trigger are used to define so called regions of interest, which are used in the first part of the HLT, the Level-2. In Level-2 the objects get reconstructed in the regions of interest with full detector information, including also the ID. With this refined reconstruction the trigger event rate is further reduced to about 3.5 kHz. The last selection step on trigger level is the Event Filter. At this level the events are fully reconstructed with the full event information and algorithms similar to the ones used in the offline analysis. The Event Filter reduces the event rate to about 200 Hz, which then can be written on disk and used in the offline analysis.

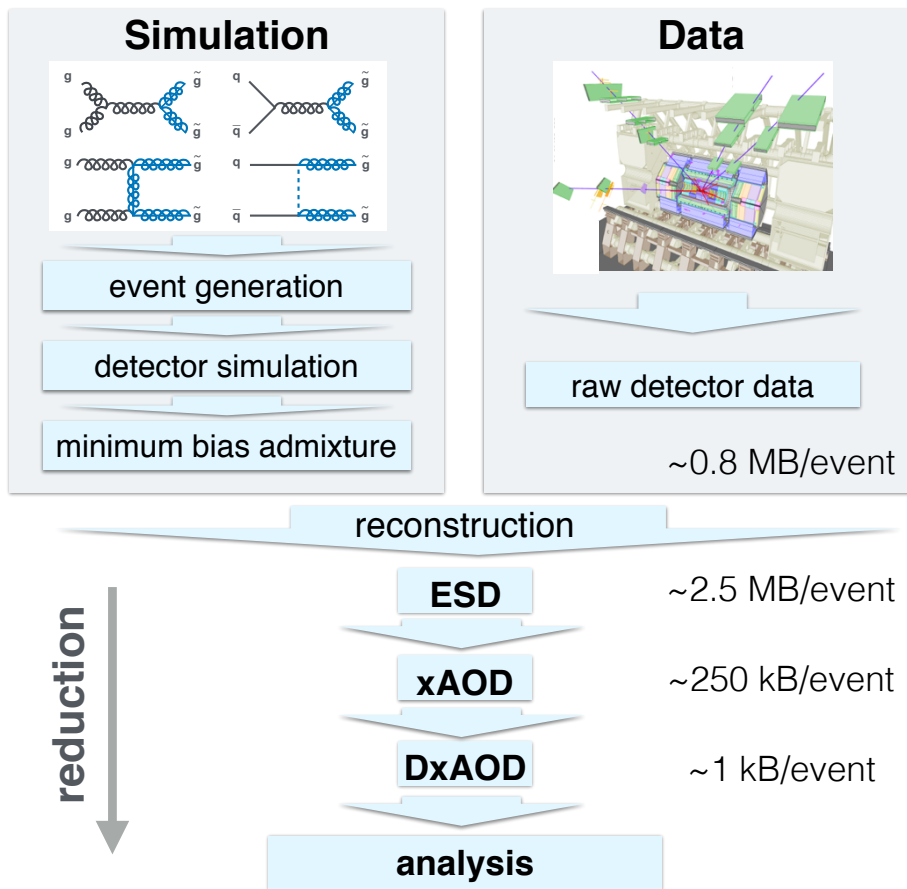


Figure 3.15: Illustration of the ATLAS offline data preparation chain. The event size for the different reduction formats are taken from Reference [71]

### 3.3 Data preparation

The data selected by the ATLAS trigger system are per se not yet in a format that can be used for the analysis. The information from the detector has to be combined to identify objects and it has to be on a level that is analysable in a reasonable time scale. Furthermore the known background processes as well as the expected signal have to be simulated to understand the signatures and backgrounds and optimise the searches. The ATLAS data preparation is conducted in a multi-step procedure, aiming for an optimal usage of the available computing resources and will be discussed in the following. The procedure is illustrated in Figure 3.15.

The first step in the simulation chain is the event generation. A large variety of Monte Carlo event generators [72], having one or the other benefit, is available and can be used to simulate different processes. Different approaches are chosen in the different generators e.g. how initial and final state radiation are treated, how many partons are included in the matrix

elements, or how hadronisation and parton shower are treated. Comparing different generators can be used to access the systematic uncertainty related to the generation of those processes. The next step is the simulation of the detector interaction and the readout. A full ATLAS model is incorporated in GEANT 4 [73], which allows for both the simulation of interactions and detector responses. This is followed by an admixture of minimum bias events to emulate the additional collisions from pile-up [74]. All different sources of pile-up are simulated separately. The difficulty in this approach is in particular in the simulation of soft QCD, which is the dominant pile-up contribution. It can not be treated perturbatively, but only with phenomenological models with large uncertainties. A variety of parameters have to be tuned in this phenomenological approaches to match data.

At this stage real events (data) and simulated events (simulation) are basically identical as the information consists of the real/simulated raw detector responses. The only difference is that for simulation the generated particles are kept as truth information. The next step is the reconstruction of the physics objects, such as electrons or jets from the detector data. The reconstruction is applied in the same way to data and simulation to avoid any bias. The output format after the reconstruction is called Event Summary Data (ESD) and is with an average event size of 2.5 MB per event too large to be easily analysed. Though the information has to be reduced. The ESD is reduced to Analysis Object Data (xAOD) [75], where only physics objects with a subset of observables are left. In Run 2 the sample size is further reduced from xAOD to Derived Analysis Object Data (DxAOD) [76], which has only information left relevant for a given analysis (or group of analyses). This improves the processing time for the analyses and saves local disk space.

## Chapter 4

# Heavy Charged Long-Lived Particles at Colliders

In this section the specifics of HCLLPs at colliders, in particular at a proton-proton collider like the Large Hadron Collider, will be discussed. First the production and the velocities with which they are produced will be discussed. This is followed by a section about the expected energy loss of HCLLPs. While colour-singlet states can be treated like "heavy muons", colour charged states can have several interesting phenomenological features due to hadronic interactions discussed in the following section. Finally the relevant lifetime regime for the search described in this thesis will be discussed.

### 4.1 Production

Typically BSM particles are assumed to be pair-produced as the new sectors are protected by some type of quantum-number/parity. If the long-lived particles are directly produced at tree-level, the production can be via s- or t-channel as e.g. shown for a stau and chargino from supersymmetric models in Figures 4.1 and 4.2. For a stau only the production via s-channel is possible, while for charginos both s- and t-channel are possible. The composition of the contributions for the production channels of the charginos largely rely on the masses of the internal particles. For the t-channel the internal particles are squarks, while for the s-channel Z-bosons or photons are the exchange particle. In the models considered in this analysis the squarks are at very high masses and hence the t-channel is suppressed. The main difference between staus and charginos in the considered cases comes from spin-couplings between the produced par-



Figure 4.1: Feynman-diagram for the production of sleptons via quark-quark-fusion (s-channel).

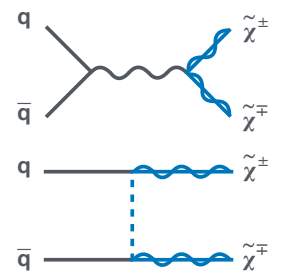


Figure 4.2: Feynman-diagram for production channels of charginos via quark-quark-fusion (s-channel, upper) and quark-quark-scattering (t-channel, lower).

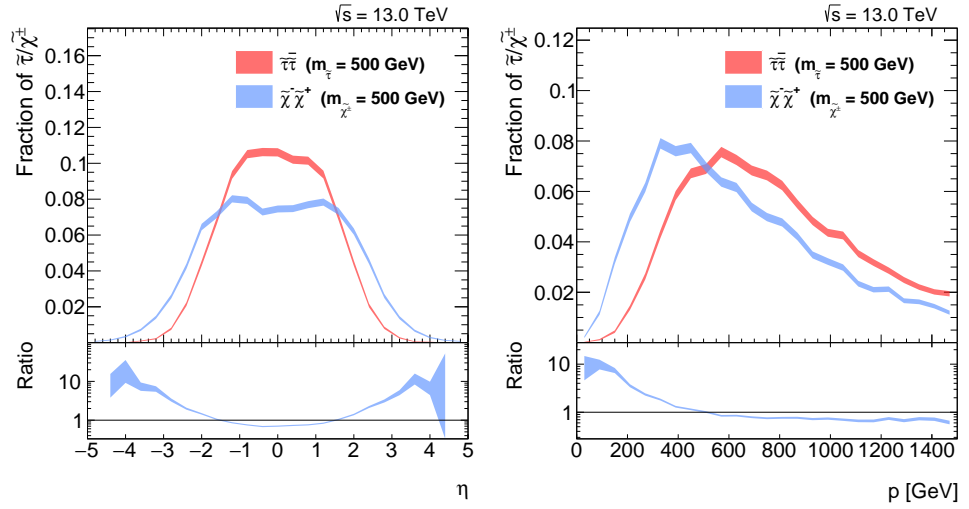


Figure 4.3: Left:  $\eta$ -distribution for direct-stau production red and direct-chargino ( $\tilde{\chi}^+ \tilde{\chi}^-$ ) production blue. Right: momentum-distribution for direct-stau production red and direct-chargino ( $\tilde{\chi}^+ \tilde{\chi}^-$ ) production blue. For both signals the same mass is used ( $m_{\tilde{\tau}} = m_{\tilde{\chi}^\pm} = 500$  GeV).

ticles, as charginos are fermions, while staus are scalars. To balance the spin of the virtual Z-boson the scalars have to be produced with an angular momentum  $l = 1$  in a p-wave. The produced particles can only have an angular momentum if not produced in rest, the p-wave is hence largely suppressed at the kinematic threshold [?]. The stau production process is therefore tending to larger energy transfer, which leads to more central and harder particles in the final state, compared to fermions produced via s-channel. This can be seen in Figure 4.3, which shows the kinematic distributions for staus and charginos. The rather large differences in the kinematics for HCLLPs with the same mass, encourage, to rely as less as possible on geometric/kinematic observables to be model independent.

If the long-lived particles are produced as decay products of heavier particles, or even in decay cascades, the kinematic spectra will be different, in particular, as more energy is taken away by other particles, they might be less energetic. The additional particles produced in the decays can be visible in the detector, which could increase the trigger efficiency. For the cases where both direct production and decay from a heavier primary particle to the HCLLPs are allowed, two things have to be kept in mind: The heavier the primary particle, the lower the cross-section for this channel, while the closer the mass of the primary particle to the mass of the HCLLP, the less energetic the other decay products and hence the lower the impact on the kinematics of the long-lived particle. Those two effects result in decays of heavy primary particles having only little impact on the effective signature of HCLLPs in the detector. The picture can be quite different if the heavy decaying particles have significantly higher cross section, as it is e.g. for production via strong-interaction, while the

direct-production is via ew-interaction. The same as for the direct production holds: To be as model independent as possible only loose geometric/kinematic requirements should be applied.

Another interesting scenario for collider searches is, if the HCLLP is produced together with uncharged stable/long-lived particles <sup>1</sup>. This signature is typically featured in models where the HCLLP is (almost) mass degenerated with the lightest particle with a new conserved quantum-number, and both particles have similar couplings. The detector signature for such scenarios are that the HCLLP is produced in association with an undetectable particle, giving rise to larger missing transverse energy in the event.

<sup>1</sup>mostly the dark matter candidate of the respective BSM model

In principle also the single production of HCLLPs is possible. But for those cases the production cross-section is proportional to the decay width due to crossing symmetry, where the constant of proportionality does not rely on specific details of the model. Hence particles would be either short-lived or have an negligible cross-section [23].

## 4.2 Hadronisation

Coloured HCLLPs have to obey the confinement and hence hadronise. As additional BSM particles are too heavy to be produced during hadronisation, they hadronise with SM particles forming so called  $R$ -hadrons. The  $R$  is borrowed from supersymmetry and used for all BSM theories in common. Similar to the hadrons in the SM, also for the  $R$ -hadrons,  $R$ -mesons,  $R$ -baryons and  $R$ -glueballs are possible states, formed from one BSM colour triplet (e.g. sbottom) or colour octet (e.g. gluino) and SM particles. Examples would be  $R_{b\bar{u}}^-$  for an  $R$ -meson and  $R_{g u u d}^+$  for an  $R$ -baryon, where the lower indices are giving the (s)particle content and the upper the electric charge.

One model used for the description of the hadronisation is the Lund string fragmentation model [77]. In this model the coloured particles are the endpoints of a colour string with constant tension of 1 GeV/fm. Through the movement a part of the initial coloured particles, energy gets transferred to the string. At some point the energy in the string reaches a critical value, where it is energetically favourable to produce a quark-anti-quark pair and hence the string breaks. This repeats until at some point not enough energy is present anymore to produce additional quark-anti-quark pairs. All those particles are produced in the colour field spanned

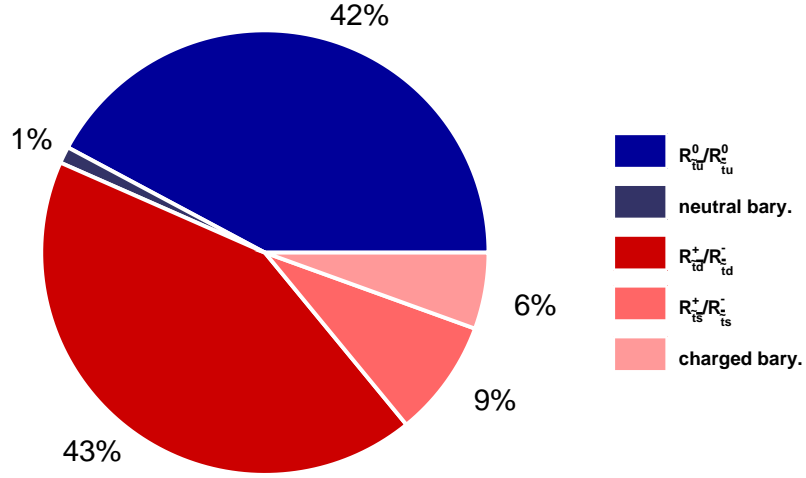


Figure 4.4: Composition of  $R$ -hadron types with a stop as BSM particle estimated with PYTHIA6 [78].

behind the initial coloured particles. This means that the velocity of end-points of the colour field, hence the velocity of the HCLLPs, serves as an upper bound for the velocity of the produced hadrons formed from the quarks from the string break ups. As will be discussed in the next section HCLLPs move significantly slower than the speed of light, due to their high masses. This means that the typical energy of the light hadrons surrounding the massive  $R$ -hadrons is very low. In Reference [23] the typical energy carried by the normal hadrons is given as

$$E_{hads} \approx 1 \text{ GeV} \cdot \gamma_{C_3}, \quad (4.1)$$

with  $\gamma_{C_3}$  being the boost of a colour triplet (e.g. a squark). For a colour octet like the gluino the fraction carried by the normal hadrons would be roughly twice as big as for a colour triplet, and hence still almost negligible.

The flavour composition of the quarks produced during the string breaking is assumed to be universal and measured to be roughly ( $u : d : s \approx 1 : 1 : 0.3$ ) [79]. The heavy SM quarks can be neglected as they are suppressed due to the relatively high masses. Producing di-quarks is further suppressed. Hence, during hadronisation mostly  $R$ -mesons are produced. Important for detector searches is the fraction of charged  $R$ -hadrons as only those are detectable in the tracking system. Assuming roughly 10 % baryons and using the light-quark composition as men-

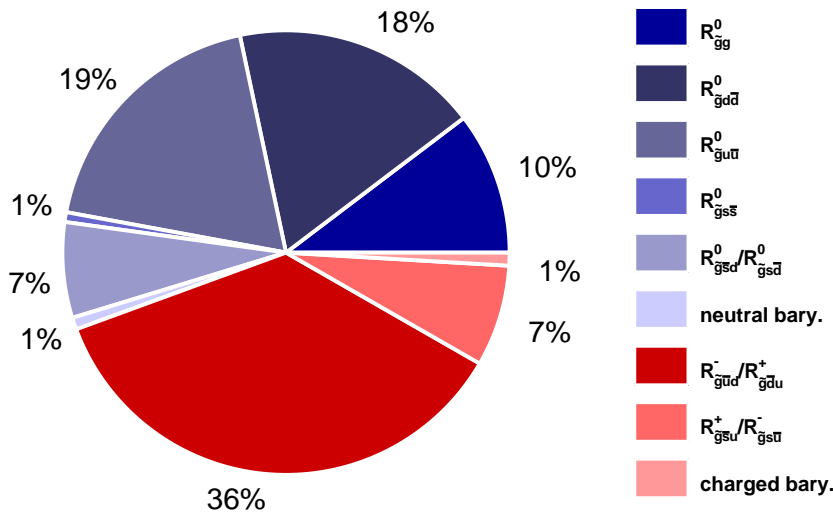


Figure 4.5: Composition of  $R$ -hadron types with a gluino as BSM particle estimated with PYTHIA6.

tioned above, for BSM quarks roughly 40% are  $R_{\bar{q}\bar{d}}$  another 40% are  $R_{\bar{q}\bar{u}}$  and 10% are  $R_{\bar{q}\bar{s}}$ , while the remaining states are baryonic. This matches well the predictions from PYTHIA6 [78] shown in Figure 4.4. An important difference is between up- and down-type BSM quarks, as for an up-type quark the  $R$ -meson with the strange quark would be charged, while neutral for a down-type. Hence a significantly higher fraction of charged  $R$ -hadrons is expected for stops ( $\sim 60\%$ ) than for sbottom quarks ( $\sim 40\%$ ). For gluinos (or any similar BSM colour octet) it has to be taken into account that two SM quarks have to be produced to form  $R$ -mesons. The respective composition of gluino  $R$ -hadrons is shown in Figure 4.5. For gluino  $R$ -mesons only the mix states ( $u\bar{d}$  or  $\bar{u}d$  and  $u\bar{s}$  or  $\bar{u}s$ ) are charged and hence slightly less charged  $R$ -hadrons are expected ( $\sim 45\%$ ). The fraction of  $R$ -glueballs can not be predicted by the current hadronisation models, as also SM glueballs have not been observed so far. It is therefore a free parameter for the hadronisation, and typically chosen to be 10% due to combinatorial arguments [80].

### 4.3 Velocity

To understand the velocities at which HCLLPs are expected to be produced at the LHC, first the available kinetic energy has to be understood. The kinetic energy is what is left after the production of the particles with the respective masses and hence is reflected in the probabilities of the

Figure 4.8: The kinetic energy distribution for different gluino masses simulated with PYTHIA6 using the CTEQ6L1 PDFs.

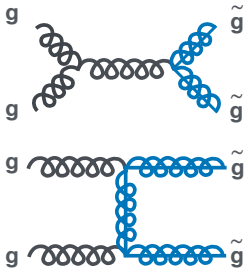
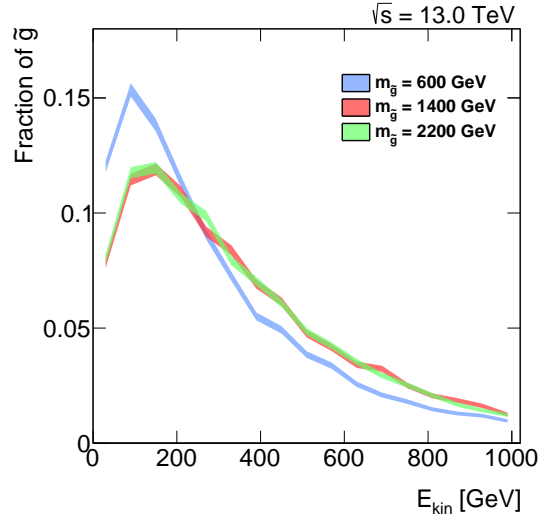


Figure 4.6: Leading production channels for gluinos over gluonic initial state. The u-channel would be also possible (particles crossed in t-channel), but not shown here.

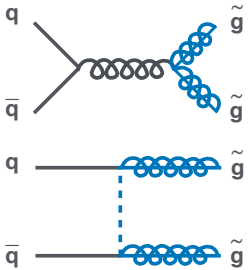


Figure 4.7: Leading production channels for gluinos over quark initial state. The u-channel would be also possible (particles crossed in t-channel), but not shown here.

colliding partons for having more than the minimum  $x$  needed to produce the respective particles. For gluinos both t- and s-channel production is possible via quarks and gluons on tree-level [81]. The corresponding Feynman-diagrams are shown in Figures 4.6 and 4.7. The kinetic energy for gluinos simulated with PYTHIA6 using the CTEQ6L1 PDF set [82] are shown in Figure 4.8. It can be seen that for all masses the peak of the kinetic energy distribution is between 100 GeV and 200 GeV. While the distribution for gluino masses of 1400 GeV and 2200 GeV are almost the same, a slightly softer spectrum is expected for 600 GeV gluinos. The reason for this difference is the change in the leading production mechanism, as above  $m > 0.2 \times 6.5 \text{ TeV} = 1.3 \text{ TeV}$  it is more likely that the valence quarks carry the needed momentum fraction of the proton, which can be seen in Figure 3.3. The difference in kinematics between production via gluons or quarks comes from the difference in the contribution of s- and t-channel. For the production via quarks in the t-channel the internal line has to be a squark, which is in the underlying split-supersymmetry models at very high masses, and hence largely suppressed due to its virtuality. In contrast for the production through gluons, the internal particle in the t-channel is also a gluino and hence not suppressed. For purely s-channel production harder objects are expected as for the production via gluons where both s- and t-channel have significant contributions. Knowing the kinetic energy of the particles the momentum ( $p$ ) can be estimated with

$$p = E_{kin} \sqrt{1 + 2 \frac{m_0}{E_{kin}}}. \quad (4.2)$$

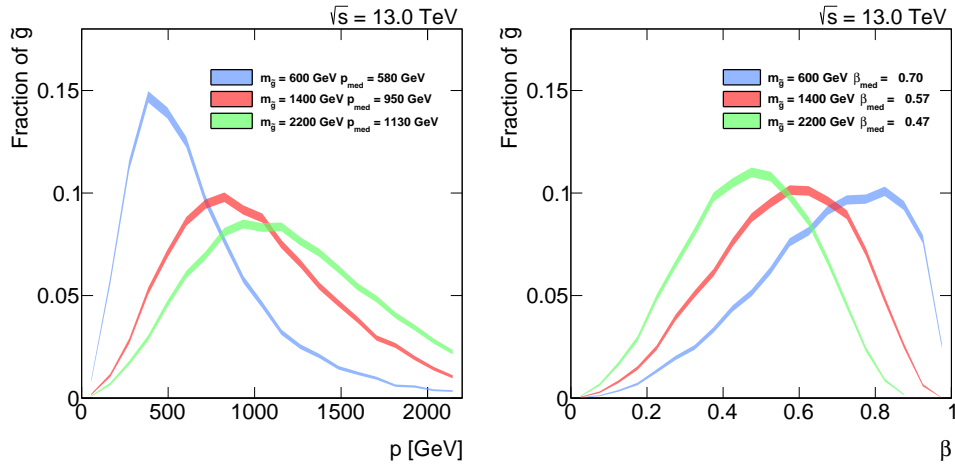


Figure 4.9: The momentum distribution (left) and the  $\beta$  distribution (right) for different gluino masses simulated with PYTHIA using the CTEQ6L1 PDFs.

Using the maxima of the kinetic energy distributions (100 GeV/150 GeV) the expected momenta are  $\sim 400$  GeV ( $m_{\tilde{g}} = 600$  GeV),  $\sim 650$  GeV ( $m_{\tilde{g}} = 1400$  GeV), and  $\sim 850$  GeV ( $m_{\tilde{g}} = 2200$  GeV), which nicely matches the maxima of the momentum distributions shown in Figure 4.9 (left). The HCLLPs have hence high momenta, mostly due to the high masses. Knowing the momentum as well as the mass one can also calculate the velocities of the particles using

$$\beta = \frac{p/m}{\sqrt{1 + (p/m)^2}}, \text{ with } \beta = \frac{v}{c}. \quad (4.3)$$

But as the translation from momentum into  $\beta$  changes the form of the distribution quite a bit it makes sense to use the median instead of the maximum. Using Equation 4.3 and the medians from the momentum distributions in Figure 4.9 (left) one obtains: 0.70 (600 GeV), 0.57 (1400 GeV) and 0.47 (2200 GeV). This matches exactly the medians of simulated  $\beta$  distribution drawn in Figure 4.9 (right). It can be seen that HCLLPs are produced with velocities significantly lower than the speed-of-light. This is in contrast to all SM particles, which, at the LHC, are produced with almost the speed-of-light or with energies too low to be detectable. Hence measuring the velocity of the particles is one of the main observables to identify HCLLPs.

## 4.4 Energy Loss

As the lifetimes considered for HCLLPs are sufficient to allow for a direct interaction with the detector, it is important to understand the different types of interactions with the detector material and hence the en-

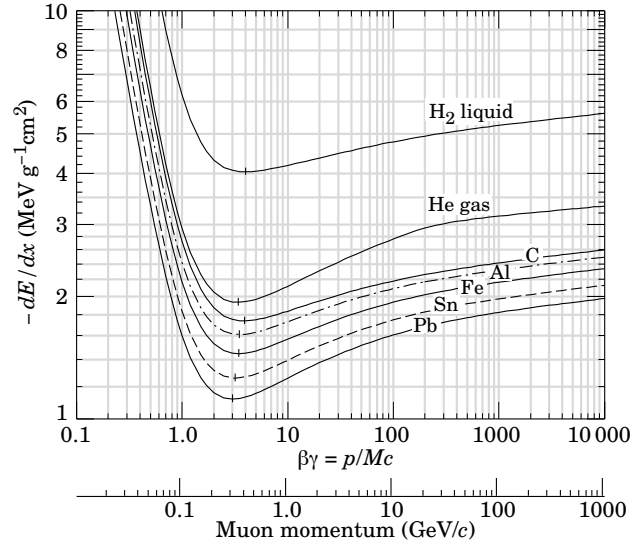


Figure 4.10: The mean energy loss of particles in several different materials. The minima of the distributions are roughly at a velocity  $\beta\gamma$  of 3–4 for the different material. The figure is taken from [7].

ergy loss. For heavy electrically charged particles the main source of energy loss is due to the ionisation of the atoms in the material. Heavy in this context already refers to the heavier SM particles such as the muon and hence the models describing the interaction are well established [7]. For moderate relativistic particles the mean ionisation energy loss is described by the Bethe–Bloch formula

$$\left\langle \frac{dE}{dx} \right\rangle = \frac{4\pi e^4 z^2}{m_e c^2 \beta^2} n \left( \frac{1}{2} \ln \left( \frac{2m_e c^2 \beta^2 \gamma^2 T_{max}}{I_e^2} \right) - \beta^2 - \frac{\delta}{2} \right) [7], \quad (4.4)$$

with  $m_e$  the mass and  $e$  the charge of the electron,  $z$  the charge of the projectile in multiples of  $e$ ,  $n$  the volume density of electrons in the material, the  $\beta\gamma$  of the particle with the Lorentz factor  $\gamma$  defined as  $1/\sqrt{1-\beta^2}$ ,  $I_e$  the mean ionisation potential, the  $\delta$  term, which accounts for density effects and  $T_{max}$  the maximum energy transfer to an electron in a single collision, for heavy particles given by

$$T_{max} = 2m_e c^2 \beta^2 \gamma^2. \quad (4.5)$$

It can be seen from Equations 4.4 and 4.5 that the ionisation energy loss is solely dependent on the velocity of the particles, besides some material quantities and the charge of the particle. Hence it can serve as a measure for the velocity. The form of the mean energy loss as a function of the particle velocity  $\beta\gamma$  are shown in Figure 4.10. For low velocities the mean energy loss is falling until it reaches a minimum at roughly  $\beta\gamma = 3 - 4$ .

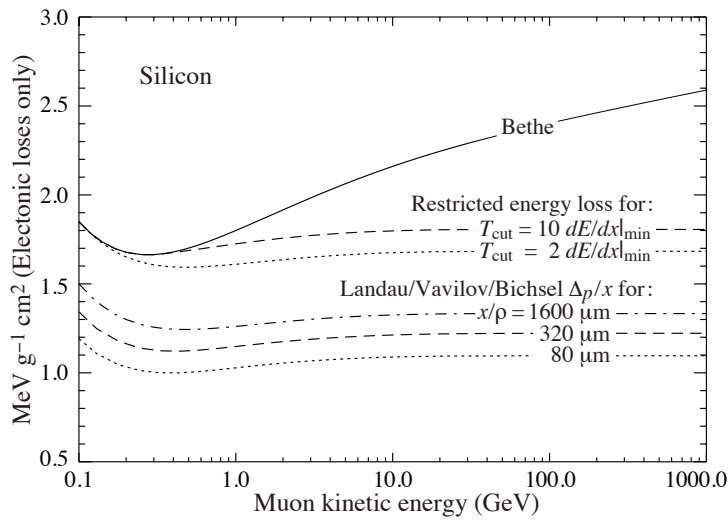


Figure 4.11: The mean energy loss as given by the Bethe-Bloch formula (Bethe), the restricted energy loss and the MPV of the energy loss (Landau/Vavilov/Bichsel) as a function of the kinetic energy of a muon. For the restricted energy loss a maximal energy transfer  $T_{cut}$  is introduced. The figure is taken from [7].

The particles at these velocities are accordingly called minimum ionising particles. For higher boosts the mean energy loss starts increasing again but with a lower gradient. The reason for the falling slope is that the particle transverse the electric field of the electrons in the material for a shorter time. This effect stops as the particle velocity approaches its upper bound, the speed-of-light. The boost of the particles leads to an increase of transversal component of the electric field, while the parallel component is decreasing. For the interaction of the particles only the transversal component is relevant as the parallel component gets integrated out. Hence for boosts higher than roughly  $\beta\gamma = 3 - 4$  the mean energy loss is increasing again. The mean energy loss of a muon with a momentum of roughly 100 GeV would correspond to a HCLLP with a typical velocity  $\beta = 0.65$  ( $\beta\gamma = 0.85$ ), which can be seen from Figure 4.10. Hence due to the ambiguity of the  $\beta\gamma - dE/dx_{mean}$ -relation the mean energy loss can not be used to identify HCLLPs. In the relativistic rise the increase of the mean energy loss is mostly driven by single highly energetic interactions. For thin absorbers like e.g. silicon detectors the probability for measuring a certain energy loss follows a Landau distribution. Instead of measuring the mean energy loss the Most Probable Value (MPV) is what can and should be measured. The MPV as a function of kinetic energy of a muon in contrast to the mean energy loss from Bethe-Bloch is shown in Figure 4.11. It can be seen that the MPV is almost flat as a function of the kinetic energy of the muon and hence by measuring the MPV instead of the mean energy loss the ambiguity between relativistic rise and low energetic tail can be minimised. Hence, measuring the MPV of the energy

loss can be a powerful tool to identify HCLLPs.

## 4.5 Hadronic Interaction

For colour charged HCLLPs, also hadronic interaction with the detector material are important to understand their signature in the detector. As no comparable SM particles exist, only little is known about the hadronic interactions of  $R$ -hadrons. For the simulation of the hadronic interactions two different phenomenological approaches are considered here. The triple Regge model [83, 84] and a more pragmatic approach, with the Generic model [85].

To understand the interactions of  $R$ -hadrons in the detector, it is crucial to estimate their expected mass spectra. If some states are significantly lighter than others, those would be dominant in the detector, as after hadronisation the heavier states would immediately decay to the light ones. If the lightest state is either electrically neutral or charged (or even doubly charged) a completely different signature would be expected. A variety of approaches were used to calculate the mass spectra e.g. using the bag model [86] or lattice QCD [87]. Common to all of them is that the HCLLP is, due to the high mass, spin decoupled and forming an almost static colour field [88]. For colour triplet states (e.g. squarks) the SM hadrons containing heavy quarks such as charm and bottom can serve as a guideline for the mass spectra, while for colour octets (e.g. gluinos) the mass spectra fully rely on the phenomenological calculations. The details of the lowest lying states in the mass hierarchy used in the triple Regge and Generic model differ, but some important general features do not. For both mass spectra the light  $R$ -mesons are almost mass degenerated (in particular the mass splitting is smaller than the pion mass) and hence they do not decay. Furthermore for both models the mass splitting between the mesonic and baryonic states is smaller than the proton mass. This leads, together with the absence of mesons in the material, to baryonic states not being able to convert into mesonic states by hadronic interactions. This does not hold for the anti-baryonic-states as those can have annihilation interactions with the nucleons. An important difference between the assumed mass spectra is in the  $R$ -baryon sector. For the  $R$ -hadrons formed from the colour triplet state ( $C_3$ ) the lightest state is the ( $C_3ud$ ) with zero spin of the di-quark system ( $s_{qq} = 0$ ). While for the Regge model only this state is taken into account, the generic model also includes the heavier  $s_{qq} = 1$  states ( $C_3uu$ ), ( $C_3ud$ ) and ( $C_3dd$ ). The main dif-

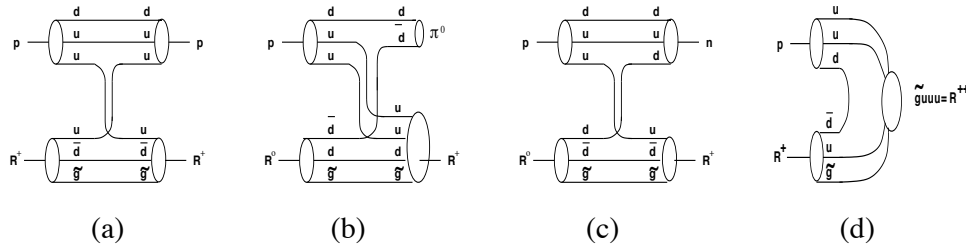


Figure 4.12: Examples for hadronic interactions of a  $R$ -hadron with a proton: a) elastic scattering b) baryon exchange c) charge exchange d) resonance formation. The figure is taken from [23].

ference between the Generic and Regge mass spectra is the mass splitting for the  $C_8$  baryonic states. In the Regge model the lightest baryonic state is the electrically neutral ( $C_8 uds$ ) while all others are neglected as they are expected to decay almost immediately to the lightest baryonic state. In contrast, the Generic model assumes all baryonic states formed from the light quark ( $u$  and  $d$ ) to be mass degenerated. Overall the Generic model includes more different  $R$ -hadron states in its modelling. More details on the mass spectra can be found in References [84, 85].

One basic idea common to all hadronic interaction models of  $R$ -hadrons is, that the heavy exotic particle has, due to its high mass, a very localised wave-function and hence does not participate in the interaction. The probability for the heavy exotic particle to interact with quarks in the nuclei is suppressed by the inverse mass squared [85]. Hence the exotic particle will act as a spectator and energy reservoir, while the hadronic interaction is carried out by the light quarks forming the  $R$ -hadron. To understand the energy regime at which those interactions take place one can do the following gedankenexperiment: The Lorentz factor for a 600 GeV gluino  $R$ -hadron at the peak in beta (0.8, see Figure 4.9 right) is roughly 1.7. Furthermore the mass of the light-quark system can be approximated by the mass of the  $R$ -hadron minus the mass of the exotic particle. For the mesonic states this results in a typical mass of the di-quark system of  $m_{q\bar{q}} = (0.6 - 0.7)$  GeV with the light quarks being up and/or down. Using those the kinetic energy of the quark system can be calculated with

$$E_{kin} = (\gamma - 1) \times m_{q\bar{q}} \approx 0.5 \text{ GeV.} \quad (4.6)$$

The hadronic interactions of the  $R$ -hadrons are therefore expected to be treatable like low-energy hadron-hadron scattering of the light SM quark system, with the exotic particle serving as an energy reservoir.

The scattering processes of  $R$ -hadrons on protons are shown in Figure 4.12. Process a) is expected to result only in a small energy loss as the heavy

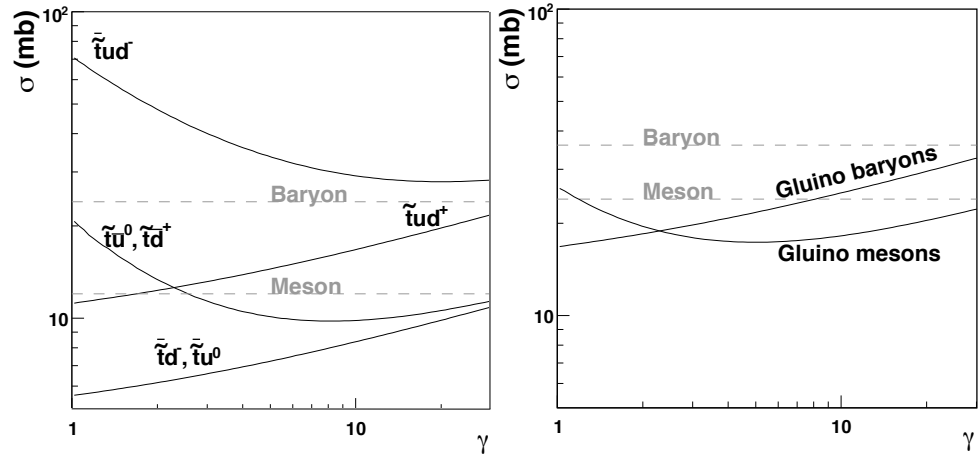


Figure 4.13: The interaction cross section with a nucleus containing equal numbers of protons and neutrons as a function of the Lorentz boost for stop  $R$ -hadrons (left) and gluino  $R$ -hadrons (right). The solid lines are showing the cross section for different types of  $R$ -hadrons estimated with the triple Regge model while the dashed lines are indicating the constant cross sections estimated with the Generic model. The figure is taken from [85].

$R$ -hadron is scattering with a low-mass target, comparable to the classic picture of an elastic scattering. Also process d) is argued to play a minor role, but is so far not implemented in any interaction model, and hence could be an important limitation of the interaction models [23, 85]. The most important processes in the modelling of the hadronic interactions of  $R$ -hadrons are therefore inelastic scattering processes like shown in b) and c) of Figure 4.12. An important feature of those inelastic scattering processes is that the  $R$ -hadrons can change their electric charge. A summary of possible processes implemented in the triple Regge interaction model can be found in Reference [80], which includes both  $2 \rightarrow 2$  and  $2 \rightarrow 3$  processes. The main difference between the two interaction models is the estimation of cross sections for the different processes as this is non-trivial. Even for SM hadron low-energy hadron scattering is poorly understood, and hence can only be treated phenomenological. The Generic model uses a pragmatic approach with a black disk approximation, which uses a constant cross section for each involved light quark (up and down) of 12 mb, while for s-quarks 6 mb are used. These values are inspired by the asymptotic values of pion and kaon scattering with protons. In contrast to that the triple Regge model is using the Regge formalism [89] for low-energy hadron scattering. Therefore the light-quark system is decoupled from the heavy quark before scattering and after the interaction recombined. The relevant parameters for the Regge formalism are estimated from low-energy hadron-hadron scattering data. The triple Regge model is giving a more dynamic picture with the cross section being dependent on the boost of the system, which can be seen in

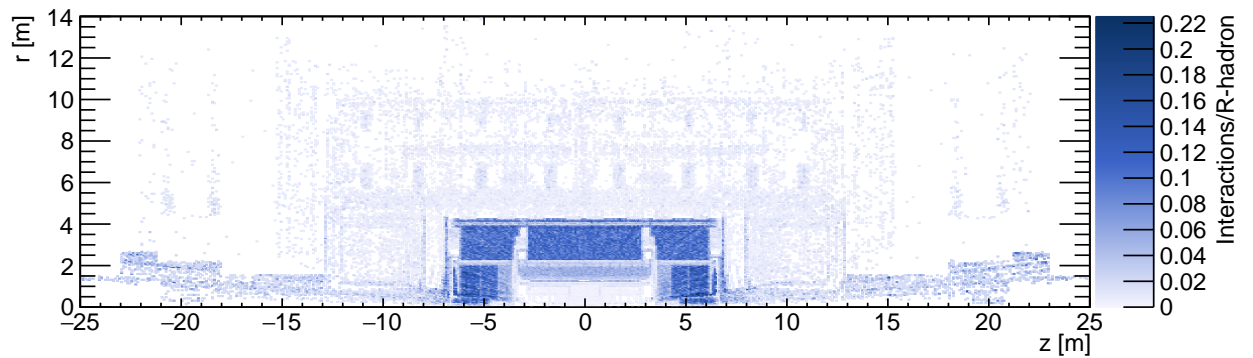


Figure 4.14: The radial- ( $r$ ) vs.  $z$  position (along the beamline) of hadronic interactions of  $R$ -hadrons with the ATLAS detector simulated with GEANT4. The Figure is number of interaction is divided by the number of particles traversing the the respective bin.

Figure 4.13.

The higher cross section for  $R$ -hadrons with light anti-quarks is due to the additional Reggeon interaction channel where the anti-quark annihilates with the respective quark from the nuclei to a gluon which decays to a quark-anti-quark pair.

In the following the results of the simulation of the hadronic interactions of stop and gluino  $R$ -hadrons using the Generic or triple Regge model with the ATLAS detector are discussed. Both interaction models are implemented in GEANT4 [73], which is used in the following for the modelling of the interactions of  $R$ -hadrons with the detector. The hadronic interactions of  $R$ -hadrons are mainly in the dense regions of the detector which can be seen from Figure 4.14 and Figure 4.15. It can be seen that most of the interactions take place in the calorimeters, which matches expectations as those are the most dense regions of the detector. The high number of hadronic interactions closer to the origin of the coordinate system in Figure 4.15 is not due to super dense detector parts but due to the fact that all particles are produced roughly at the origin (modulo beam spread) and hence the particle density transversing the region spanned by each bin is significantly higher.

Particles are only detectable in the tracker systems if charged, hence the composition of  $R$ -hadron flavours and in particular the ratio between charged and uncharge states is essential to understand the efficiency to reconstruct  $R$ -hadrons in the detector. Figures 4.16 and 4.17 are showing the flavour composition of  $R$ -hadrons for stop  $R$ -hadrons ( $m_{\tilde{t}} = 800$  GeV). One important difference is that in the Generic model strange quarks are included while this is not the case for the triple Regge model. Throughout the full inner tracking system no significant changes in the flavour composition is visible, which matches the lower rate of hadronic interactions

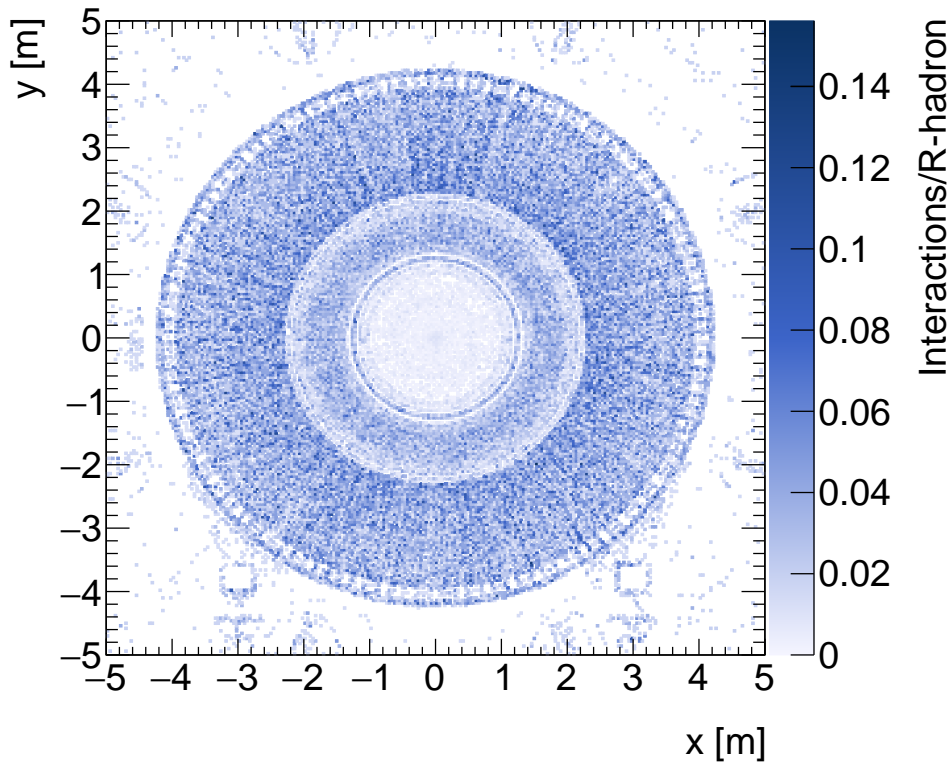


Figure 4.15: The x- vs. y-positon of hadronic interactions of  $R$ -hadrons with the ATLAS detector simulated with GEANT4.

visible in this region in Figures 4.14 and 4.15. The flavour fraction at small  $r$  for the Generic model is matching the one estimated earlier in this chapter for after hadronisation, as the light mesonic states are degenerated in mass and hence do not decay. For the triple Regge model, due to the absence of strange quarks, this is not the case, but the additional charged  $R$ -hadrons seem to be absorbed in the states with down quarks. Hence, for both models the same fraction of charged  $R$ -hadrons is expected in the inner detector.

For both models the flavour composition starts to change significantly when traversing the dense calorimeters. For  $R$ -hadrons formed from stop quarks with both models the baryonic states get dominant after traversing the calorimeters. The reason for this is the lack of allowed reactions transforming baryonic to mesonic states. On the one hand the mass difference between the mesonic and baryonic states is smaller than the proton mass, hence decays are kinematically forbidden. On the other hand, due to the lack of SM mesons or anti-matter in the detector material, no hadronic interactions from baryonic to mesonic states are allowed (baryon number conservation). For the Generic model only baryonic states are present after the calorimeters, while the triple Regge model

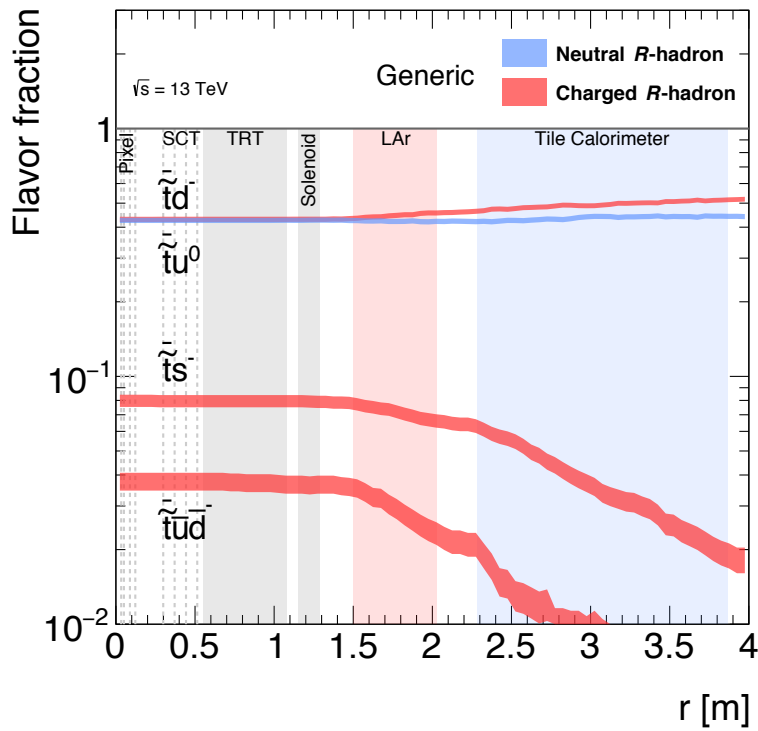
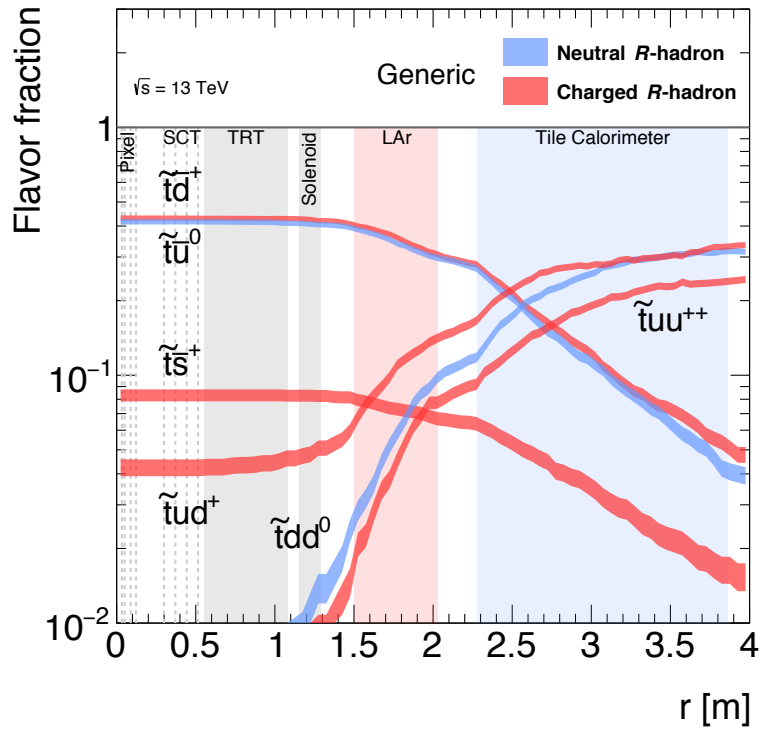


Figure 4.16: The flavour composition of stop (top) and anti-stop (bottom)  $R$ -hadrons simulated with the Generic model as a function of  $r$  in the ATLAS detector. The  $R$ -hadrons are restricted to a region where they transverse the ATLAS Tile Calorimeter ( $\eta < 1.65$ ). The different detectors are indicated by dashed lines for the different layers of silicon detectors and solid regions for the other detectors. A detailed description of the different components can be found in Section 3.2. In blue the neutral  $R$ -hadron states are drawn, while the charged states are shown as red bands. The width of the bands gives the statistic uncertainty due to the limited number of simulated  $R$ -hadrons. [5]

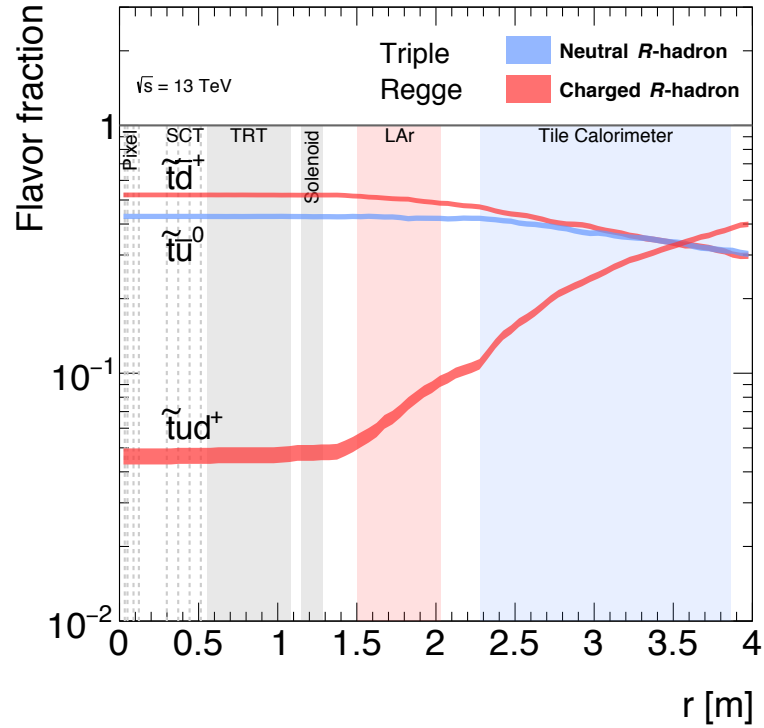
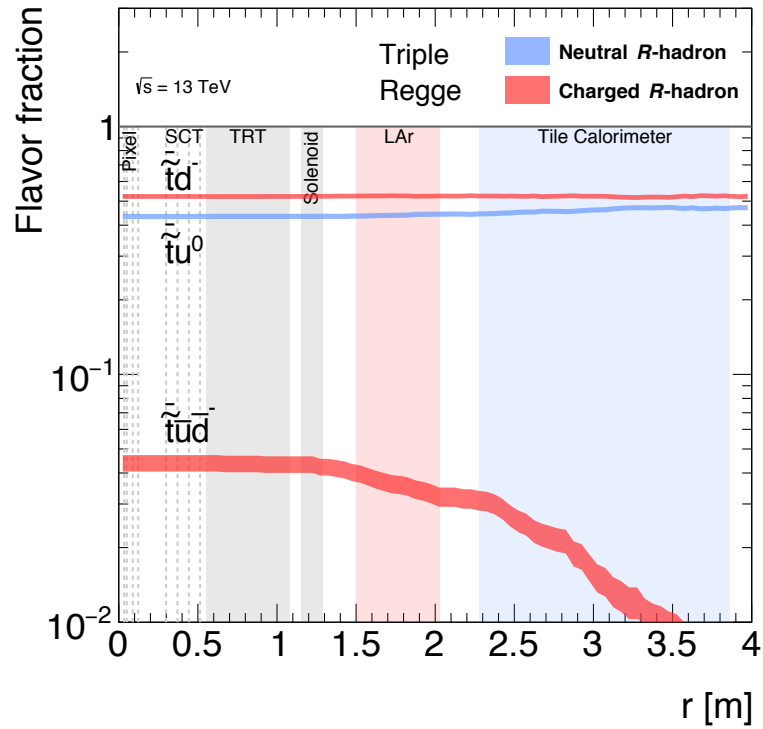


Figure 4.17: The flavour composition of stop (upper) and anti-stop (lower)  $R$ -hadrons simulated with the triple Regge model as a function of  $r$  in the ATLAS detector. The  $R$ -hadrons are restricted to a region where they transverse the ATLAS Tile Calorimeter ( $\eta < 1.65$ ). The different detectors are indicated by dashed lines for the different layers of silicon detectors and solid regions for the other detectors. A detailed description of the different components can be found in Section 3.2. In blue the neutral  $R$ -hadron states are drawn, while the charged states are shown as red bands. The width of the bands gives the statistic uncertainty due to the limited number of simulated  $R$ -hadrons. [5]



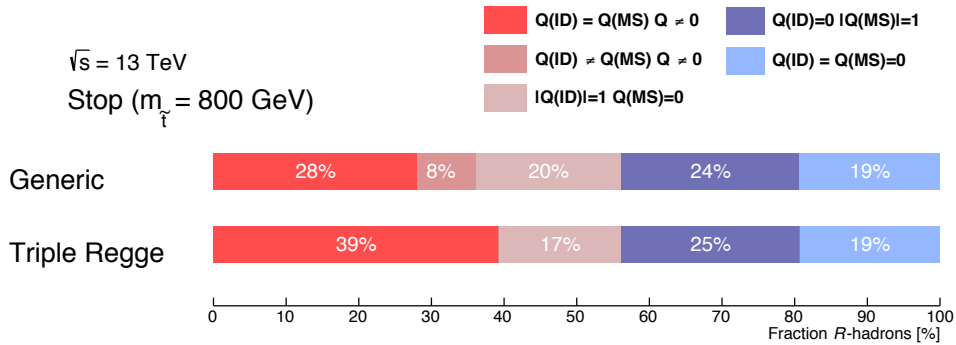


Figure 4.18: The composition *R*-hadron charge states. The first value in the legend is referring to the charge of the *R*-hadron in the inner detector and the second one to the charge of the particle in the muon system. The composition is shown for stop *R*-hadrons with  $m_{\tilde{t}} = 800 \text{ GeV}$ . [5]

is predicting a slower transition rate to baryonic states. A major difference is that the triple Regge model includes only the lightest baryonic state, while the generic model has a broader spectrum of baryonic states included. For stop quarks the difference is not as significant as for sbottom quarks as there the lightest baryonic state is uncharged. Sbottom *R*-hadrons have a behaviour similar to stop *R*-hadrons regarding the interaction, though they are charged differently, lowered by one with respect to the corresponding stop states. For the generic model a large fraction of the sbottom *R*-hadrons is charged after the calorimeters, while the fraction of charged rhads is suppressed with the triple Regge model. This predicts only for stop *R*-hadrons a large fraction of charged states after the calorimeters, while for sbottom *R*-hadrons the majority is uncharged. The triple Regge model is therefore sometimes referred to as charge suppressed interaction model.

In contrast to stop *R*-hadrons, the flavour composition in different parts of the detector is rather similar for anti-stop *R*-hadrons in the Generic and the triple Regge model. The reason is that the baryonic states, which are a major difference between the two models, play a minor role as for those annihilation processes with the protons and neutrons in the detector material are allowed, they are hence fading away in the dense calorimeters. One potential model-dependent feature that could change the above described predictions on the flavour composition of *R*-hadrons is if oscillations between squark–anti-quark and anti-squark–quark states are allowed.

The composition of charges of stop *R*-hadrons in the inner detector and the muon system, and hence visibility in the two different tracking systems is shown in Figure 4.18. While the fraction of charged states in the inner detector (red to blue) is almost the same for both models, large differences can be seen in the composition of charge states in the muon system. The generic model is e.g. predicting 8% *R*-hadrons having a dif-

ferent charge in the inner detector than in the muon system, whereas the triple Regge model is not predicting such charge changes. The reason are the  $\tilde{t}uu$  states, which are not present in the triple Regge model.

An interesting signature for  $R$ -hadrons arises, when they get stopped in the detector (mostly in the dense calorimeters) due to hadronic interactions and ionisation energy losses. If not stable those particles will decay later and hence can be searched for with out-of-time signals, depending on the SM decay products. This signature will not be targeted in this thesis, but searches were performed e.g. in References [90, 91].

The important features of the different interaction models for  $R$ -hadrons can be summarised as follows: Both interaction models predict similar fractions of charged  $R$ -hadrons in the inner detector while the fraction of charged states in the MS are quite different for the two interaction models. Both interaction models show some limitations for different cases. While the triple Regge model incorporates a simplified spectrum of  $R$ -hadron states, this is slightly extended for the Generic model. For the case of the cross sections of the different  $R$ -hadron states the Generic model is rather pragmatic, while the more dynamic modelling of cross sections from the triple Regge model, maybe more realistic.

## 4.6 Lifetime

As discussed in Section 2.1.3, lifetimes in quantum field theory have an intrinsic random element and hence the lifetime of particles has to be described with the exponential decay law and correspondingly with a mean lifetime. The fraction of particles surviving to a certain distance can be calculated, including the time dilation due to the boost of the particles, with

$$N(x)/N_0 = \exp\left(-\frac{x}{\beta\gamma c\tau}\right). \quad (4.7)$$

This can be used to estimate the fraction of particles that decay in a certain detector volume. Figure 4.19 shows a sketch of the number of remaining particles as a function of the radial distance in the detector as well as the decay probabilities in the different subdetectors. It can be seen that the fraction of particles that are expected to decay in a certain subdetector is not shifted but rather smoothed out the longer the mean lifetime. This means that even for a large mean lifetime of 50 ns, which corresponds to a  $c\tau$  of 150 m, a significant fraction (13%) of particles has decayed before the tile calorimeter, which is the minimum life-

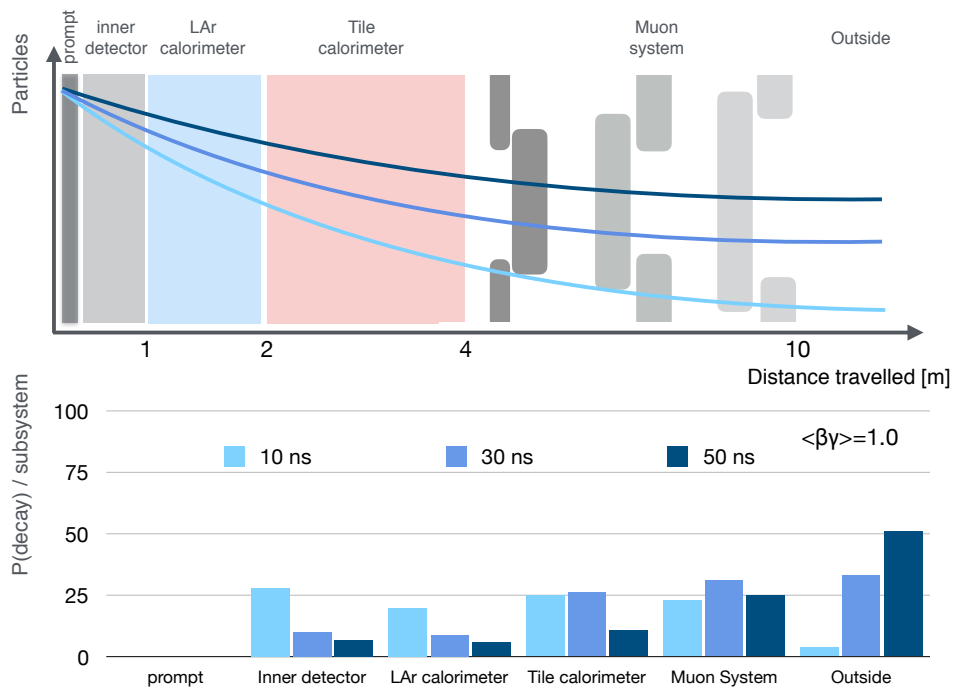


Figure 4.19: The number of particles illustrated as function of the distance traveled in the detector (top). The decay probability in the different subsystems for mean lifetimes of 10 ns, 30 ns and 50 ns assuming  $\beta\gamma = 1$  (bottom).

time requirement for particles targeted with the search described in this thesis. Particles which are decaying earlier in the detector are targeted with dedicated search, which are not using or even vetoing corresponding signals in the outer parts of the detector [92, 93, 94]. For short mean lifetimes of 10 ns a significant fraction of particles would still be able to reach the tile calorimeter (50%) and some efficiency for this models is expected. All in all, for a search which targets particles that at least reach the Tile Calorimeter the efficiency significantly drops for mean lifetimes lower than 10 ns, while lifetimes larger than 50 ns are almost fully efficient.

## 4.7 Summary

Heavy charged long-lived particles are an interesting target for detector searches as they can have lifetimes sufficient to directly interact with the detector. Due to their mass, HCLLPs are expected to be produced with velocities significantly lower than the speed-of-light. This can be used to identify them, as all SM particles are expected to be produced at the LHC with almost speed-of-light. Furthermore, the low velocity leads to a high ionisation energy loss, which is another important observable to identify HCLLPs. The production mechanisms of such particles are rather model dependent and can have significant impact on the kinematics. For

a model independent approach, the searches have to rely as little as possible on the kinematic features of the different models. For colour-charged HCLLPs the hadronic interactions are hard to predict, as no comparable SM particles exist. An important feature of the hadronic interactions is that the  $R$ -hadrons can change their charge due to the exchange of SM particles. While the predictions of the fraction of charged  $R$ -hadrons in the inner detector agrees between the different interaction models, significant differences can be seen for the charge composition in the outer components of the detector. The mean particle lifetimes relevant for the search described in this thesis start at about 10 ns, while for mean lifetimes larger than 50 ns no significant fraction of particles is expected to decay before the Tile Calorimeter, the particles can hence be assumed stable.

## Chapter 5

# Search for Heavy Charged Long-lived Particles

In this chapter the main work of this thesis will be described, the search for HCLLPs with the ATLAS detector. First the analysis strategy will be explained. This is followed by a discussion of previous results in collider physics with the ATLAS experiment as well as with other experiments. In the next parts the detector objects which are used as HCLLP candidates are introduced as well as the main observables that are used to identify them. Also the custom calibration steps needed to achieve optimal separation power to SM particles with those variables will be given. The following parts discuss the event and candidate selection criteria applied. A purely data-driven background estimate is used that will be presented in the subsequent section, followed by a discussion of the systematic uncertainties. Last but not least the results of this search will be discussed.

### 5.1 Analysis Strategy

The basic idea of this analysis is to use both the high ionisation energy loss as well as the Time-of-Flight (ToF) to identify HCLLPs. There are no SM particles having a similar signature in the detector and therefore the main backgrounds are particles with mis-measured observables. The energy loss (pixel detector) and the ToF (Tile Calorimeter, MS) are measured with different sub-detectors. The measurements are hence independent and reduce, as fluctuations in both would be needed for SM particles to be identified as HCLLP, the background significantly. An illustration of the analysis strategy is given in Figure 5.1 and will be discussed in the following.

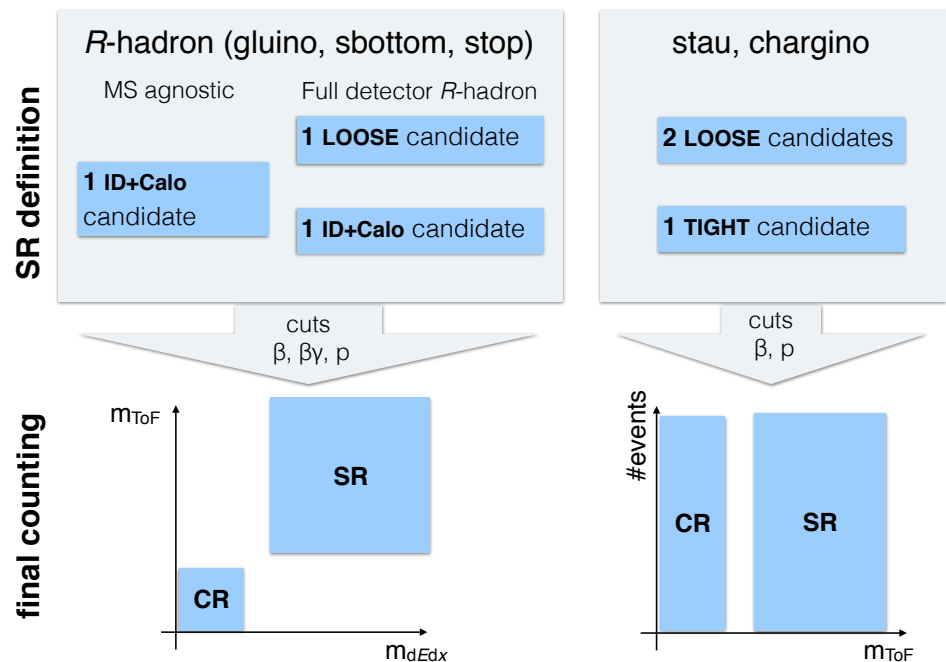


Figure 5.1: Illustration of the analysis strategy. The abbreviations SR and CR stand for signal region and control region, respectively.

The benchmark models that are targeted span the full range of charged supersymmetric particles. Stable charginos as well as staus are considered as electrically charged particles and for both the direct pair-production is chosen. As discussed in Section 4.1, those particles mainly differ in the kinematics and hence can be used to design the search as independent of the kinematics as possible. Selectrons and smuons would not differ from staus in the detector as well as in the production mechanisms at a hadron collider and are therefore without any loss of generality not considered. For colour charged supersymmetric particles models with stable stops, sbottoms and gluinos are used as benchmarks. In principle also sup and sdown would be interesting as they offer additional production channels like  $uu \rightarrow \tilde{u}\tilde{u}$ , but as those are highly model dependent, they are not considered here. With sbottom, stop and gluinos the different aspects due to hadronic interactions of up- and down-type colour triplets and colour octets, as discussed in Section 4.5, can be explored. To explore the sensitivity of this analysis strategy for shorter lifetimes, gluino  $R$ -hadrons with lifetimes of 10 ns, 30 ns and 50 ns are used as benchmark models. Two different triggers are used to select the relevant events,  $\cancel{E}_T$  and muon triggers. The muon triggers are of particular relevance for charginos and sleptons which are charged throughout the detector. A problem of the muon triggers can be the acceptance window as HCLLPs can be sufficiently slow to be associated to the wrong bunch

crossing. For  $R$ -hadrons in contrast  $\cancel{E}_T$  triggers are more important as significant fractions are uncharged in the MS as discussed before. Intrinsically the  $R$ -hadrons are not expected to produce large amount of  $\cancel{E}_T$ . The strategy therefore relies on QCD radiation recoiling against the gluino system. For  $R$ -hadrons predominantly radiation from the incoming partons, Initial State Radiation (ISR), is important as hard collinear radiations from the outgoing particles, Final State Radiation (FSR), are suppressed by the mass of the colour charged particle [95].

As HCLLPs directly interact with the detector, candidate objects based on their expected signatures have to be designed. This analysis is based on three different types of candidates, an Inner Detector track with associated Tile Calorimeter cells, from now on referred to as  $ID+CALO$ , as well as loose and tight full-detector candidates ( $LOOSE$  and  $TIGHT$ ), which have both an ID track and a MS track. The ionisation energy loss is measured in the pixel detector and ToF measurements are performed with the Tile Calorimeter, the MDT's and the RPC's.

With those candidates different event signature selections are designed targeting the different bench mark models. For charginos and staus which are pair-produced and charged through the hole detector, a signal region requiring two loose full-detector candidates ( $SR-2Cand-FullDet$ ) in the event is complemented by an orthogonal fall-back region requiring exactly one, but  $TIGHT$ , full-detector candidate ( $SR-1Cand-FullDet$ ). The one-candidate region restores efficiency if one of the candidates is not reconstructed or out of the acceptance window. Furthermore it also helps to have sensitivity for models where only one HCLLP is produced e.g. for chargino-neutralino production. For colour charged HCLLPs it has to be taken into account that the particles can be produced neutral or undergo a charge-flip via hadronic interactions. Two different approaches are used: A signal region requiring at least one  $LOOSE$  candidate with an orthogonal fall-back signal region requiring at least one  $ID+CALO$  candidate ( $SR-Rhad-FullDet$ ). And a signal region which is only requiring at least one  $ID+CALO$  candidate. This signal region is designed to be blind to any information from the MS and is accordingly called MS-agnostic ( $SR-Rhad-MSagno$ ). The benefit of the MS-agnostic signal region is that it is less dependent on the  $R$ -hadron interaction model, due to the low number of hadronic interactions in the ID (Section 4.5) and the similar results from the different models for the charge composition of  $R$ -hadrons after hadronisation (Section 4.2). In contrast the  $SR-Rhad-FullDet$  region also uses the MS for triggering, reconstruction and ToF measurements and

therefore allows for a better background rejection with a slightly better acceptance, but with a strong dependence on the interaction model.

The final selection is conducted on the momentum,  $\beta_{\text{ToF}}$  estimate from the ToF measurements and  $\beta\gamma_{dE/dx}$  determined from the  $dE/dx$  measured with the pixel detector. For the MS-agnostic analysis only the ToF measured in the Tile Calorimeter is used, whereas for the other signal regions the combined beta from Tile Calorimeter, MDT's and RPC's is used. The stau and chargino signal regions do not apply selection requirements on  $\beta\gamma_{dE/dx}$ , as they are produced over weak interactions accordingly their mass limits are significantly weaker. At such low masses almost no separation power to SM particles is expected from  $\beta\gamma_{dE/dx}$ , hence it is not used there.

The event counting for the statistical interpretation of the results is done in a one-bin mass window. The mass is estimated from momentum,  $\beta_{\text{ToF}}$  or  $\beta\gamma_{dE/dx}$  with

$$m = \frac{p}{\beta\gamma}, \quad (5.1)$$

labeled as  $m_{\text{ToF}}$  or  $m_{dE/dx}$ , respectively. For the  $R$ -hadron signal regions the final counting mass window is defined in the two-dimensional  $m_{\text{ToF}}-m_{dE/dx}$ -plane, while for the stau and chargino signal regions the window is only defined in the  $m_{\text{ToF}}$ -plane.

The background is estimated in a purely data-driven manner by estimating the shape of the key variables from data and randomly sampling a mass distribution from combinations of momentum and  $\beta$  ( $\beta\gamma$ ). The background is normalised to the events seen in data in low mass control regions where signals have been excluded by previous searches.

## 5.2 Previous Searches

Heavy charged long-lived particles have been an active target of collider searches for the last decades. It was searched for with ATLAS but also with other experiments at the LHC and other colliders. Searches were performed that can be categorised into three types [23]: Generic searches where only mass, charge and spin of the HCLLP are assumed, an intermediate category with some assumptions on the type and on the quantum numbers of the HCLLPs and last but not least searches which use full-blown models as benchmarks. For the first category model independent upper limits on the production cross section can be placed, while for the latter two also lower mass limits can be obtained. Table 5.1 summarises

| Particle                    | Collisions | $\sqrt{s}$ [GeV] | Experiment | Lower mass limit [GeV] | Ref.   |
|-----------------------------|------------|------------------|------------|------------------------|--------|
| <b>slepton</b>              |            |                  |            |                        |        |
| $\tilde{\tau}, \tilde{\mu}$ | $e^+e^-$   | 130 – 208        | DELPHI     | 98                     | [96]   |
| $\tilde{\tau}$              | $pp$       | 13000            | CMS        | 240                    | [93]   |
| $\tilde{\tau}$              | $pp$       | 8000             | ATLAS      | 286                    | [97]   |
| <b>chargino</b>             |            |                  |            |                        |        |
| $\tilde{\chi}^\pm$          | $e^+e^-$   | 130 – 209        | OPAL       | 102                    | [98]   |
| $\tilde{\chi}^\pm$          | $p\bar{p}$ | 1960             | D0         | 278                    | [99]   |
| $\tilde{\chi}^\pm$          | $pp$       | 800              | ATLAS      | 620                    | [97]   |
| <b>squark</b>               |            |                  |            |                        |        |
| $\tilde{b}$                 | $e^+e^-$   | 183 – 209        | ALEPH      | 92                     | [100]  |
| $\tilde{b}$                 | $pp$       | 8000             | ATLAS      | 845                    | [97]   |
| $\tilde{t}$                 | $e^+e^-$   | 183 – 209        | ALEPH      | 95                     | [100]  |
| $\tilde{t}$                 | $p\bar{p}$ | 1960             | D0         | 285                    | [99]   |
| $\tilde{t}$                 | $pp$       | 13000            | CMS        | 1000                   | [93]   |
| <b>gluino</b>               |            |                  |            |                        |        |
| $\tilde{g}$                 | $e^+e^-$   | 183 – 209        | ALEPH      | 27                     | [100]  |
| $\tilde{g}$                 | $pp$       | 13000            | ATLAS      | 1570                   | [92]   |
| $\tilde{g}$                 | $pp$       | 13000            | ATLAS      | 1580                   | [101]* |
| $\tilde{g}$                 | $pp$       | 13000            | CMS        | 1580                   | [93]   |

Table 5.1: Summary of selected searches for detector stable HCLLPs. The table gives the lower mass limits from the best results of the respective experiments. Where possible the limits are given for the direct pair-production to be comparable between the different limits. A detailed summary of the results of HCLLP searches can be found in Reference [7].  
\*I also contribute to this analysis during my PhD.

previous results of searches for HCLLPs. The mass limits given are the strongest obtained by the respective experiment and to be comparable between the experiments, the direct production limits are given, where available.

As these searches are rather unconventional and in particular the signatures are different to SM particles, the detectors are primarily not designed for those searches. The searches hence have to be conducted in a way to perfectly exploit the capabilities of the detectors available. For example the search at the DELPHI experiment [96] uses an energy loss measurement in a Time Projection Chamber as well as Ring Imaging Cherenkov detectors, where HCLLPs are expected to produce no

Cherenkov light due to their low velocities. The ALEPH experiment in contrast was looking for  $R$ -hadrons by requiring either missing energy, for neutral  $R$ -hadrons or a particle track with large ionisation energy loss measured in a Time Projection Chamber [100]. The searches performed at the LHC experiments ATLAS and CMS are basically similar and require either only tracks with high ionisation energy loss measured in the inner silicon detectors or with both high ionisation energy loss and low velocities estimated from ToF measurements in the calorimeters and the muon systems.

Important results for the analysis described in this thesis are also the ATLAS results from Reference [102]. There instead of a data-driven method, the background was estimated from simulations. This together with the successive improvement of the cross section limits in References [103, 97, 101] ensures that no large low-mass signals are overseen. This is a key assumption for the validity of the background estimate, as large low-mass signals would contaminate the control regions, described in Section 5.1. These low-mass signals could hence be hidden in the corrupted background.

### 5.3 Data and Simulation

The data analysed in the searches described in this thesis are proton-proton collisions taken in 2015 and 2016 at a center-of-mass energy of 13 TeV and with a bunch spacing of 25 ns. The dataset collected in 2015 corresponds to an integrated luminosity of  $3.2 \text{ fb}^{-1}$  and is used in the analysis published in Reference [101]. The search presented in Reference [5], which will be the main focus of this thesis, analyses both the data collected in 2015 and 2016, which sum up to an integrated luminosity of  $36.1 \text{ fb}^{-1}$ .

Besides data samples also simulated samples are needed for testing and calibration as well as for the estimation of the signal behaviour. For the testing and calibration a  $Z \rightarrow \mu\mu$  sample is used. The hard process is simulated with Powheg [104] in next-to-leading order (NLO), while for parton shower and hadronisation PYTHIA8 [105] (version 8.186) and EvtGen [106] (version 1.2.0) are used. For the parton shower and multiple parton interaction parameters of PYTHIA8 the AZNLO [107] tune is used and as PDFs the CTEQ6L1 [48] set.

For the simulation of the  $R$ -hadron signal samples PYTHIA6 [108] with the AUET2B [109] tune and the CTEQ6L1 PDF set is used for both matrix el-

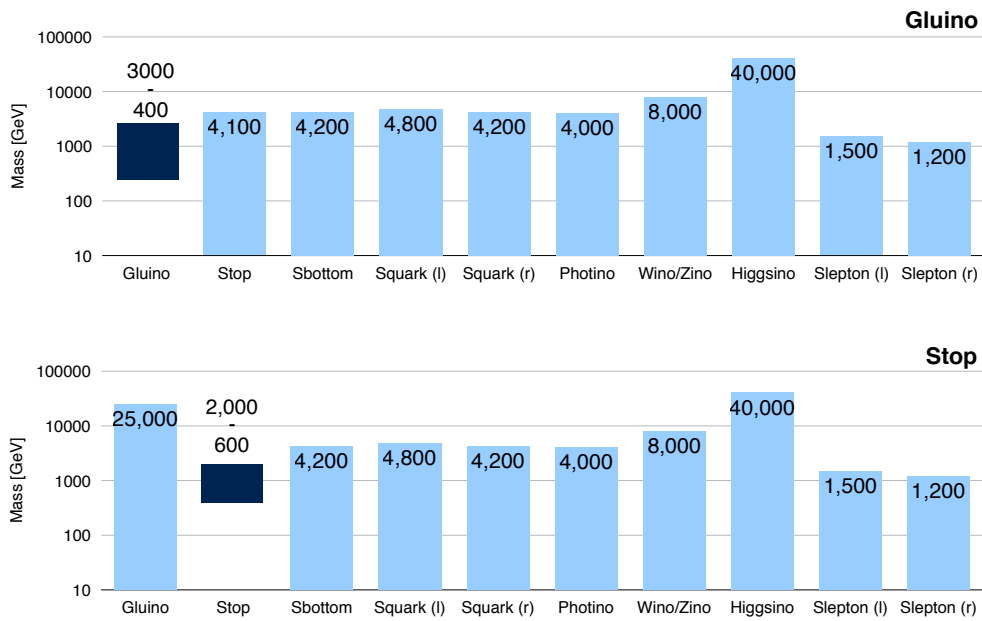


Figure 5.2: The mass spectrum of the SUSY particles used for the production of the gluino signal samples. The dark blue bar is indicating the range of simulated gluino masses.

Figure 5.3: The mass spectrum of the SUSY particles used for the production of the stop signal samples. The dark blue bar is indicating the range of simulated stop masses.

ement and showering. Dedicated hadronisation routines based on the Generic or the triple Regge model are incorporated in PYTHIA6 and used for the hadronisation of squarks and gluinos. For both cases a  $R$ -glueball fraction of 10% is assumed[80]. The Generic and triple Regge interaction models are implemented in GEANT4 to simulate the hadronic interactions of  $R$ -hadrons. For gluino  $R$ -hadrons the generic interaction model is applied, while for squarks the triple Regge model is used. A description of the different interaction models can be found in Section 4.5. The mass spectra used for the simulation of gluino and stop samples are shown in Figure 5.2 and Figure 5.3, respectively. For gluino as well as for squark samples a direct pair-production is assumed. Effects from other relevant SUSY particles (gauginos, higgsinos and squarks/gluinos) are negligible as they are set to high masses. For gluinos, signals with masses between 400 GeV and 3000 GeV are simulated in steps of 200 GeV, whereas for sbottom and stop only masses between 600 GeV and 2000 GeV are produced, due to the significantly lower expected cross sections. The squarks and gluinos are forced to be stable for those samples. Besides the stable samples also meta-stable signals are simulated for gluinos with mean lifetimes of 10 ns, 30 ns and 50 ns to explore the breakdown of the analysis strategy described in Section 5.1. Similar mass spectra as for the stable gluinos are used with the one main difference, the photino mass is set to 100 GeV, as shown in Figure 5.4. The lightest neutralino is purely photino and hence the decay of the gluino to two quarks and the lightest neutralino is possible. As discussed in Section 5.1 the selection of  $R$ -hadron

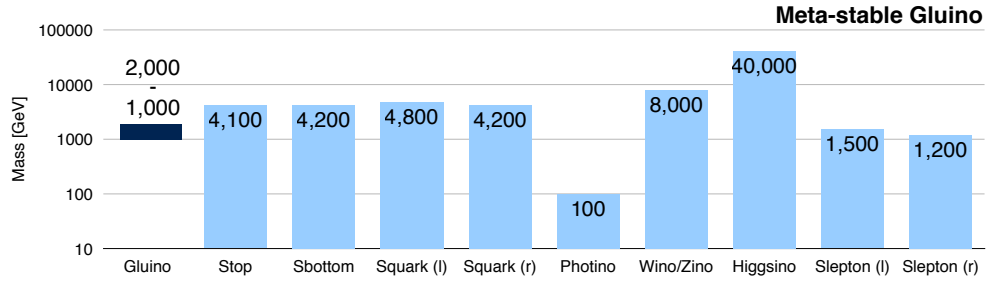


Figure 5.4: The mass spectrum of the SUSY particles used for the production of the meta-stable gluino signal samples. The dark blue bar is indicating the range of simulated gluino masses.

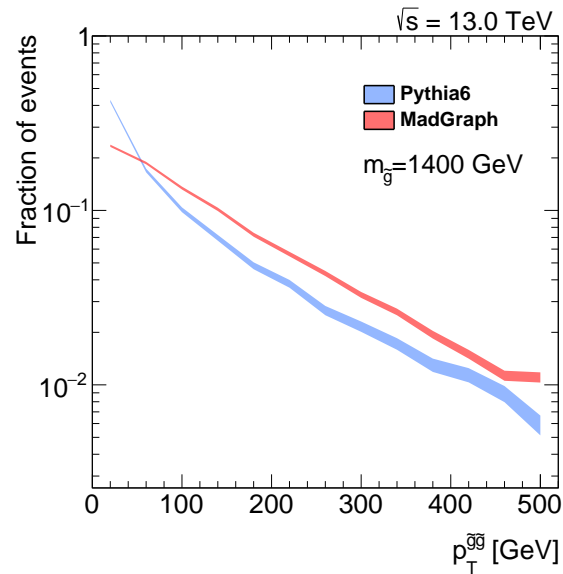


Figure 5.5: The  $p_T$  spectrum of the di-gluino system, which serves as a measure for the ISR for 1400 GeV gluinos. The spectrum is simulated with PYTHIA6, which relies solely on the parton shower for the simulation of QCD radiations, and MadGraph (MG5\_AMC@NLO), which includes an additional QCD radiation in the matrix element calculation.

events with the  $\cancel{E}_T$  trigger largely relies on ISR jets recoiling against the gluino system. While PYTHIA6 models QCD radiations only phenomenological with the parton shower, MG5\_AMC@NLO [110] (version 2.2.3) includes an additional QCD radiation in the calculation of the matrix element. The modelling of ISR in MG5\_AMC@NLO is hence more reliable and a re-weighting of the events from PYTHIA6 to MG5\_AMC@NLO along the  $p_T$ -spectrum of the gluino-system, as measure for the ISR, is introduced. The  $p_T$ -spectra of the gluino system from PYTHIA6 and MG5\_AMC@NLO for one example are shown in Figure 5.5. With MG5\_AMC@NLO a higher boost of the gluino-system is expected, which results in higher  $\cancel{E}_T$  and according to that a higher trigger efficiency. The cross sections are calculated taking into account NLO order QCD corrections. Further corrections due to soft gluon emission are also included as resummation of threshold corrections at next-to-leading logarithmic (NLL) accuracy, which leads to matched NLO+NLL predictions [81, 111, 112, 113, 114].

Pair produced staus are simulated with MG5\_AMC@NLO (version 2.3.3) for the matrix element in combination with PYTHIA8 (version 8.212) and

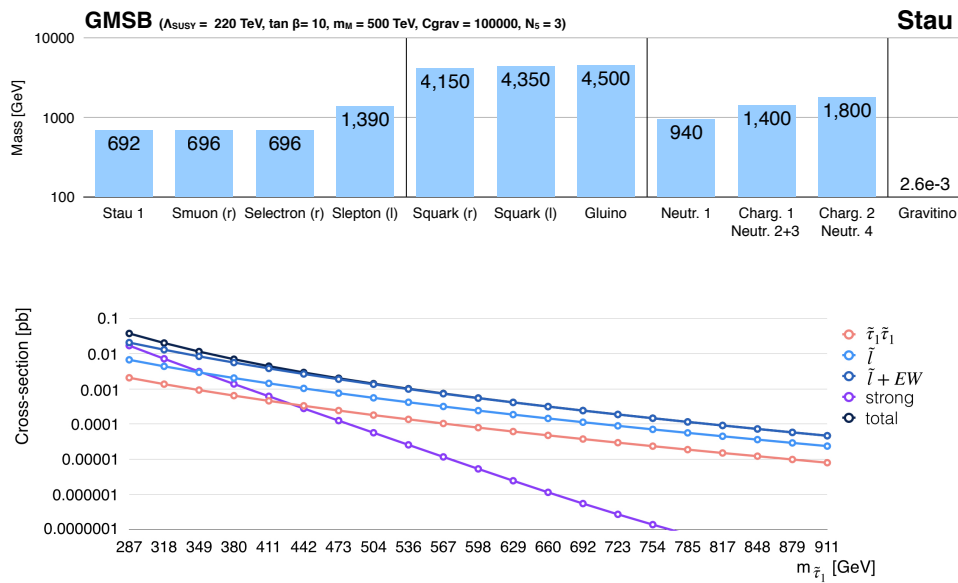
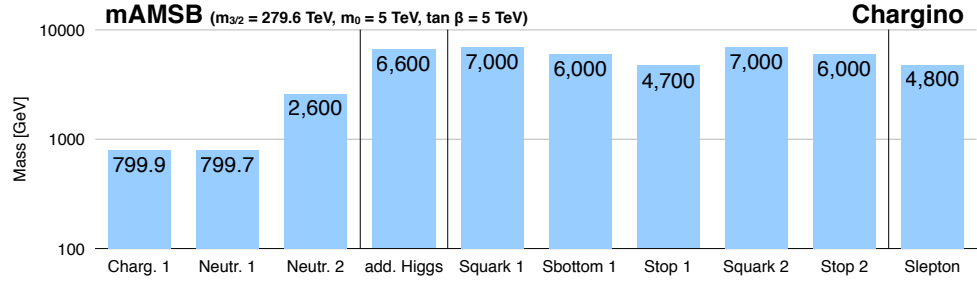


Figure 5.6: The mass spectrum for the production of long-lived staus ( $m_{\tilde{\tau}_1} = 692$  GeV) in a GMSB model. The lightest supersymmetric particle is the Gravitino, with a soft coupling to all other particles. The stau 1 as next-to-lightest particle is therefore long-lived.

Figure 5.7: The cross section as function of the  $\tilde{\tau}_1$  mass for different production mechanisms of  $\tilde{\tau}_1$  in the GMSB parameter space. As model parameters  $\tan \beta = 220$  GeV,  $m_M = 500$  TeV,  $C_{grav} = 100000$ ,  $N_5 = 3$  are chosen, while the slepton mass is changed by a scan along the susy breaking scale ( $\Lambda_{SUSY}$ ) between 90 TeV and 290 TeV.

EvtGen [106] (version 1.2.0) for parton-shower and hadronisation. For the hadonisation and underlying event parameters the A14 [115] set is used and as PDF set NNPDF23LO [116] is chosen. The underlying model is inspired by the GMSB, but only the direct pair-production of  $\tilde{\tau}_1 \tilde{\tau}_1$  is considered, where the  $\tilde{\tau}_1$  is a mixture of the right-handed and left-handed  $\tilde{\tau}$ , but in this model to 99% the right-handed  $\tilde{\tau}$ . The mass spectrum for one particular mass point ( $m_{\tilde{\tau}_1} = 692$  GeV) is shown in Figure 5.6. The model parameters are set to  $\tan \beta = 220$  GeV,  $m_M = 500$  TeV,  $C_{grav} = 100000$  and  $N_5 = 3$ , only the SUSY breaking scale ( $\Lambda_{SUSY}$ ) is varied between 90 TeV and 290 TeV to change the mass of the  $\tilde{\tau}_1$ . But, as only direct pair production of  $\tilde{\tau}_1 \tilde{\tau}_1$  is considered, no other SUSY particles are involved in the production. It is therefore independent from the underlying model and only depends on the mass of the  $\tilde{\tau}_1$ . The production cross section involving also other production mechanisms for the long-lived  $\tilde{\tau}_1$  are calculated with PROSPINO2 [117] to NLO in the strong coupling constant and are shown in Figure 5.7. The cross section would be significantly enlarged if besides the direct pair production also productions via other sleptons or Electroweak (EW) particles would be allowed. For the low mass region also production over sparticles interacting via the strong interaction significantly contribute. Using only the direct production is therefore a conservative approach and, as the search is designed to be robust against the kinematics of the HCLLPs, no significant loss in sensitivity is expected for other production mechanisms. The results can therefore be rather easily reinterpreted for the full-blown GMSB scenario as well as for other models.

Figure 5.8: The mass spectrum with a long-lived chargino ( $m_{\chi_{1\pm}} = 799.9$  GeV) from a mAMSB model. The lightest supersymmetric particle is the neutralino 1, which is almost mass degenerated with the next-to-lightest particle, the chargino 1. The chargino 1 is therefore long-lived.



Charginos are also assumed to be only directly pair-produced. They are simulated with the same setup as used for the direct production of staus, MG5\_AMC@NLO (version 2.3.3) in combination with PYTHIA8 (version 8.212) and EvtGen (version 1.2.0), with the A14 tune and the NNPDF23LO PDF set. The samples are produced using the mAMSB parameter space, fixing  $\tan\beta = 5$  TeV,  $m_M = 5$  TeV and  $\text{sign}(\mu) = 1$  and scanning along  $m_{3/2}$  between 68 TeV and 534 TeV. A typical mass spectrum for  $m_{3/2} = 279.6$  TeV, which corresponds to a chargino mass of roughly 800 GeV, is shown in Figure 5.8. In those models the chargino 1 is typically almost mass degenerated with the neutralino 1. The lifetimes of the charginos given from the models are typically too short for this search to be sensitive. The charginos are therefore artificially enforced to be stable. In contrast to the stau samples the charginos are not fully decoupled from the other SUSY particles as t-channel contributions with virtual squarks are possible at leading order, but are largely suppressed due to the high masses of the squarks. The cross sections calculated for the direct pair-production of charginos as well as for other production mechanisms are calculated in NLO with PROSPINO2 and are shown in Figure 5.9. A significant production channel can also be the associated production with a neutralino. The cross section for  $\chi_1^+\chi_1^0$  is higher than for  $\chi_1^-\chi_1^0$  as the proton consists of two positively charged up-quarks and only one negatively charged down quark. The  $\chi_1^\pm\chi_1^0$  channels can be targeted with dedicated signal regions that besides a HCLLP candidate also require large  $\cancel{E}_T$ . For technical reasons this was not included in this analysis round but nevertheless with SR-1Cand-FullDet as described in Section 5.1 some sensitivity should be achieved for such production channels.

All generated processes are overlaid by simulated minimum-bias collisions to model the in-time and out-of-time pile-up collisions. Those collisions are simulated with PYTHIA8 (version 8.186) and EvtGen (version 1.2.0) using the A2 [118] tune and the MSTW2008LO [119] PDF set. As the distribution of the number of collisions per bunch crossing is unknown

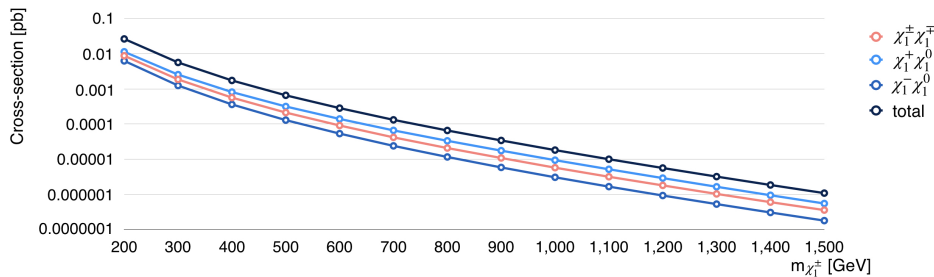


Figure 5.9: The cross section as function of the  $\tilde{\chi}_1^\pm$  mass for different production mechanisms of  $\tilde{\chi}_1^\pm$  in the mAMSB parameter space. As model parameters  $\tan\beta = 5$  TeV,  $m_M = 5$  TeV and  $\text{sign}(\mu) = 1$  are chosen, while the chargino mass is adjusted by a scan along  $(m_{3/2})$  between 68 TeV and 534 TeV.

prior to the data taking a re-weighting is introduced in the offline analysis to match the distribution observed in data.

## 5.4 Object reconstruction

The lifetime range of HCLLPs targeted with this analysis is sufficient for the particles to directly interact with the detector. Instead of looking for the decay products, this search can reconstruct the HCLLPs themselves. Two different objects are used: An ID track with associated Tile Calorimeter hits and a muon like object, called SlowMuon, reconstructed with a dedicate algorithm for slow particles in the MS, referred to as MuGirlStau algorithm[120]. In the following the reconstruction methods as well as their performance for HCLLPs will be discussed.

### 5.4.1 Inner Detector Track with Calorimeter Hits

The ID track reconstruction [121] is optimised to reconstruct charged particle trajectories in the dense environment of proton-proton collisions provided by the LHC. First clusters are formed from the individual silicon hits as charged particles are likely to deposit energy not only in a single pixel. Using these clusters three-dimensional space points are estimated. For the pixel detector a space point can be estimated for each sensor while in the SCT the information from both sides of a layer have to be combined to get a position information in the non-precision direction. These space points are used as input for the iterative combinatorial track finding, which forms track seeds from three space-points. A crude momentum as well as a rough estimate of the impact parameters, defined as the closest approaches in transversal plane or z direction to the IP, is already possible for those track seeds and can be used to reduce random combinations of space points. Using the seed tracks a full track is then build by adding additional space points using a Kalman filter [122]. As a

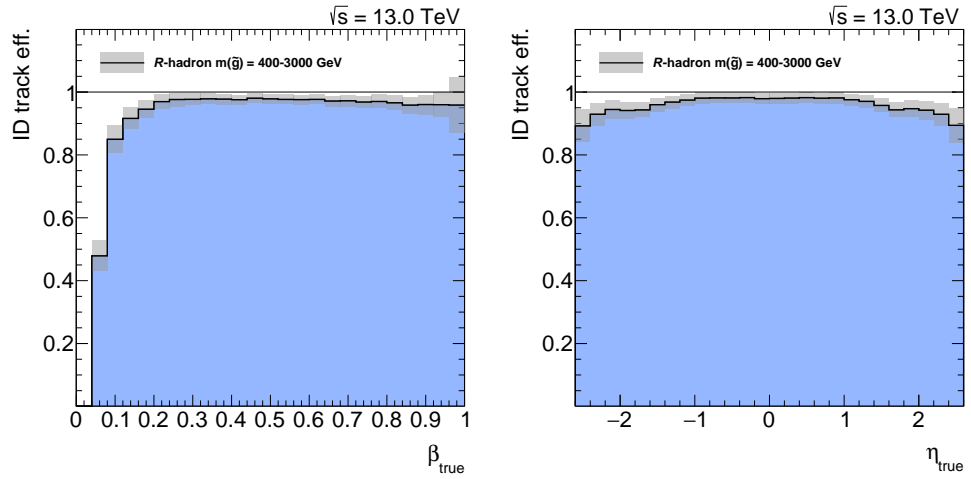


Figure 5.10: The reconstruction efficiency as function of  $\beta_{true}$  (left) and  $\eta_{true}$  (right) measured with a combined sample from all available gluino  $R$ -hadron samples. The simulated truth particles are matched to the reconstructed particles using  $\Delta R < 0.1$ , with  $\Delta R = \sqrt{\Delta\phi^2 + \delta\eta^2}$

next step a track score is assigned to the tracks taking into account the number of assigned clusters, detector holes and also the track momentum to promote highly energetic ones. The tracks are then fed into the ambiguity resolver, which is applying several requirements on the track quality to accept tracks that are worth for further consideration. Those quality criteria involve a requirement on the transverse momentum to be larger than 400 MeV as well as requirements on the numbers of associated clusters in the different subdetectors. After a track being accepted by the ambiguity solver its second task is to resolve clusters associated to multiple tracks. The last step is a high-resolution fit using all available information. If the estimated tracks still pass the ambiguity resolver they are added to the final track collection. If not they are either modified and refitted or rejected. The hits from the TRT are either used as an extension of the silicon tracks or as standalone TRT track segments, which is not used for this analysis.

The reconstruction efficiency measured with signal  $R$ -hadrons as a function of  $\beta_{true}$  and  $\eta_{true}$  is shown in Figures 5.10. True refers to the observables of the generated particles. The reconstruction efficiency for charged  $R$ -hadrons after hadronisation is larger than 95% for  $\beta > 0.2$ . Along  $\eta$  only in the forward regions a slight degradation is visible. The ID reconstruction efficiency breaks down for  $\beta < 0.1$ . The reason is that the SCT hits start to be associated to the wrong bunch crossing. Assuming  $\beta = 0.1$  and as distance the outermost SCT layer ( $r \approx 0.5$  m) the delay with respect to a particle traveling with the speed-of-light can be calculated as

$$\Delta t = \frac{r}{\beta * c} - \frac{r}{c} = 15 \text{ ns.} \quad (5.2)$$

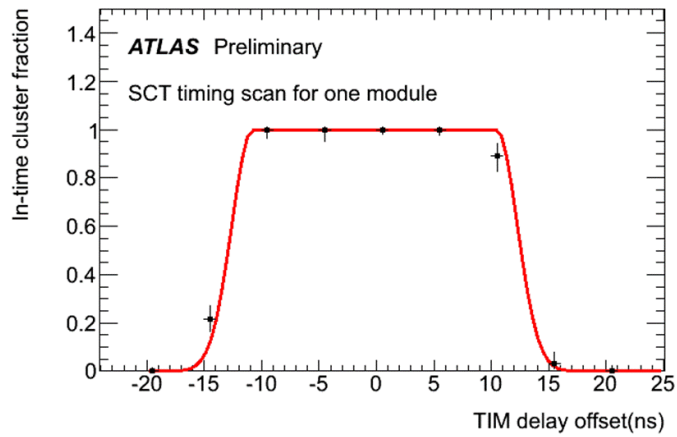


Figure 5.11: The SCT timing window for out of time signal. The particles are associated to the previous or following bunch crossing for timing differences larger than about 13 ns. [123]

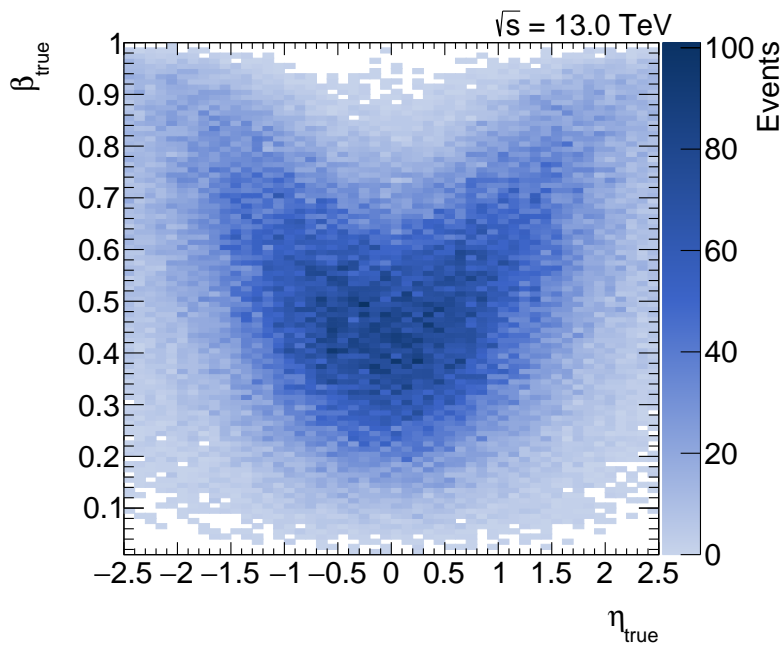


Figure 5.12: Correlation between  $\beta_{\text{true}}$  and  $\eta_{\text{true}}$  measured with a combined sample from all available gluino  $R$ -hadron samples.

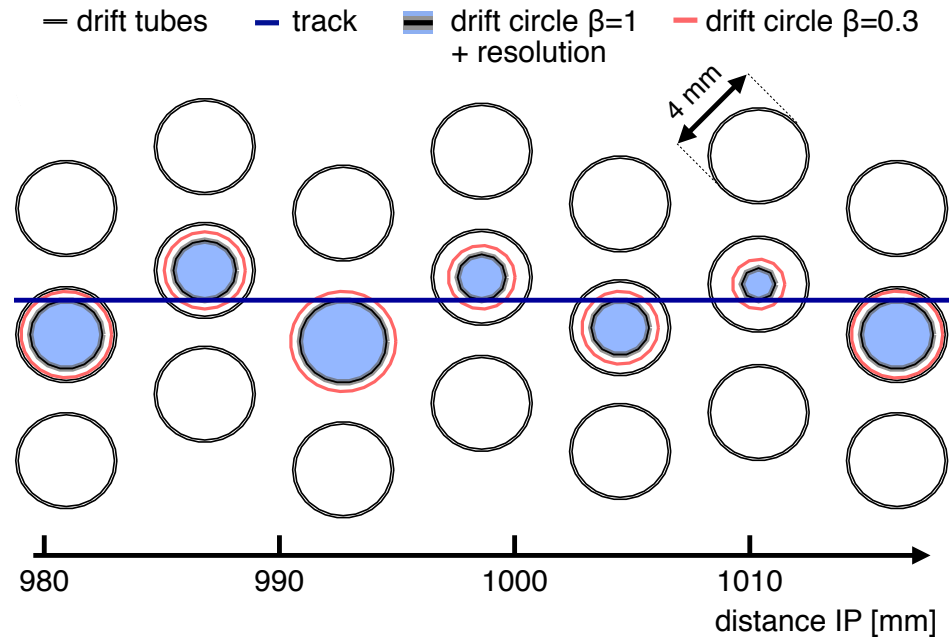


Figure 5.13: Drift circles for an exemplary TRT geometry roughly at 1 m distance to the IP for  $\beta = 0.1$  and  $\beta = 0.3$ . Also the resolution [124] is drawn for the  $\beta = 1$  drift circles as a grey band.

Comparing this to the timing window of the SCT shown in Figure 5.11 it can be seen that those hits would be associated to the wrong bunch crossing. The SCT hits start being wrongly associated from outside-in due to the larger distances and also first for forward tracks due to the additional path length. The tracks can at some point no longer be correctly reconstructed as the minimum requirement of SCT hits is no longer fulfilled.

A further feature that can be observed in Figure 5.10 is that the efficiency is slightly decreasing the higher the  $\beta$  of the particle. This can be understood as for  $R$ -hadrons  $\beta$  is correlated with  $\eta$ , due to the additional boost from asymmetries in the momenta of the colliding partons, as can be seen in Figure 5.12.  $R$ -hadrons with high  $\beta$  are therefore rather in the forward direction where the tracking resolution is slightly worse. This results in the observed degradation of the efficiency for high  $\beta$ .

Also the TRT has problems with out-of-time signal. The reason is illustrated in Figure 5.13. The estimation of the TRT drift circle needs a start point. As all relevant SM particles are produced at the speed-of-light the zero point is set to a particle produced at the IP travelling at the speed-of-light and traversing the anode-wire. The estimated drift circle is hence too large for a particle travelling significantly slower than the speed-of-light. The drift tubes are arranged in a way that the particles traverse tubes on different sides to get an unambiguous solution. In Figure 5.13 the particle is traversing tubes altering in the upper and lower half. The drift circles

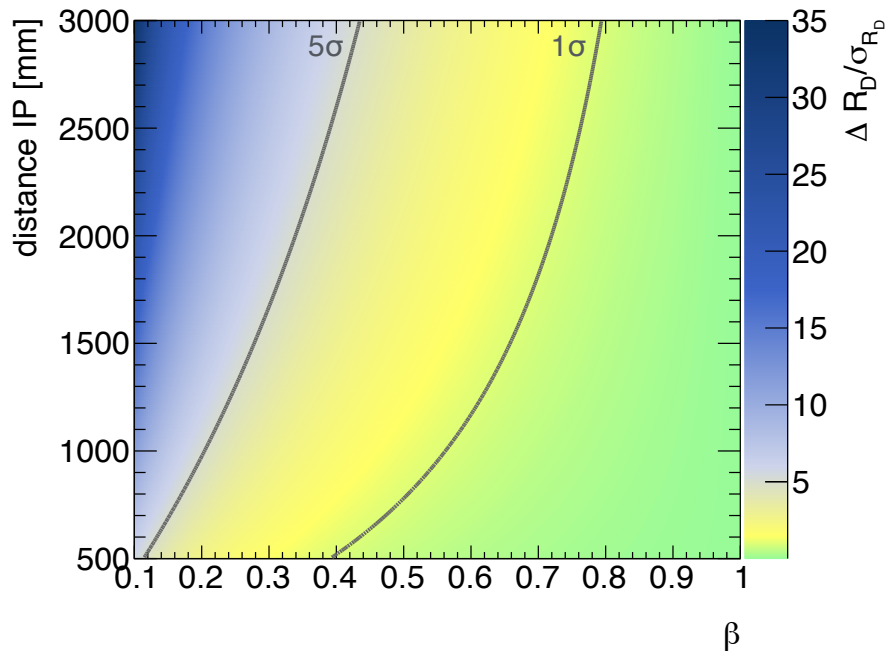


Figure 5.14: The difference in radius of the drift circles in multiples of the position accuracy of the TRT ( $\sigma_{R_D} \approx 130 \mu\text{m}$  [125]) as function of  $\beta$  and the distance to the IP. The  $1\sigma$  and  $5\sigma$  contours are superimposed. The differences in the timing are calculated using Equation 5.2 and translated to a difference in the drift circles using as drift velocity  $v_{drift} = 50000 \text{ km/s}$  [125].

from the lower tubes correspond to a track shifted upwards while it is opposite for the upper tubes. This results in an ambiguity of the fit solution and at some point the circles can no longer be matched to a single track. The difference of the drift circle as function of the particle  $\beta$  and the distance to the IP is shown in Figure 5.14. For a large  $\beta$  range and for most of the distances the effect is below one  $\sigma$  of the positioning accuracy of the TRT and hence negligible. But for  $\beta$  smaller than about 0.3 the drift circles are off by  $5\sigma$  and hence a significant impact is expected. For even lower velocities the drift circles are expected to be totally off ( $35\sigma$  for  $\beta = 0.1$  at a distance to the IP of 3000 mm). The fraction of tracks without TRT hits as a function of the particle  $\beta$  is shown in Figure 5.15. It can be seen that roughly at  $\beta = 0.3$  the fraction of tracks without TRT hits starts increasing, which matches nicely with the previously discussed expectations. While for high velocities ( $\beta > 0.4$ ) the fraction of tracks without TRT hits is about 5%, for  $\beta = 0.2$  almost half of the tracks are expected to have no TRT hits. For low-mass HCLLPs this will probably have no significant impact but if super heavy HCLLPs get accessible, problems with the TRT might get relevant. Also HCLLPs produced in a decay chain can be produced with very low velocities and therefore could be affected by those problems. These studies are so far solely based on simulation. Using e.g. satellite-satellite collisions as introduced in Section 3.1 one could potentially expand these studies to some discrete out-of-time windows to validate the effects seen in simulation.

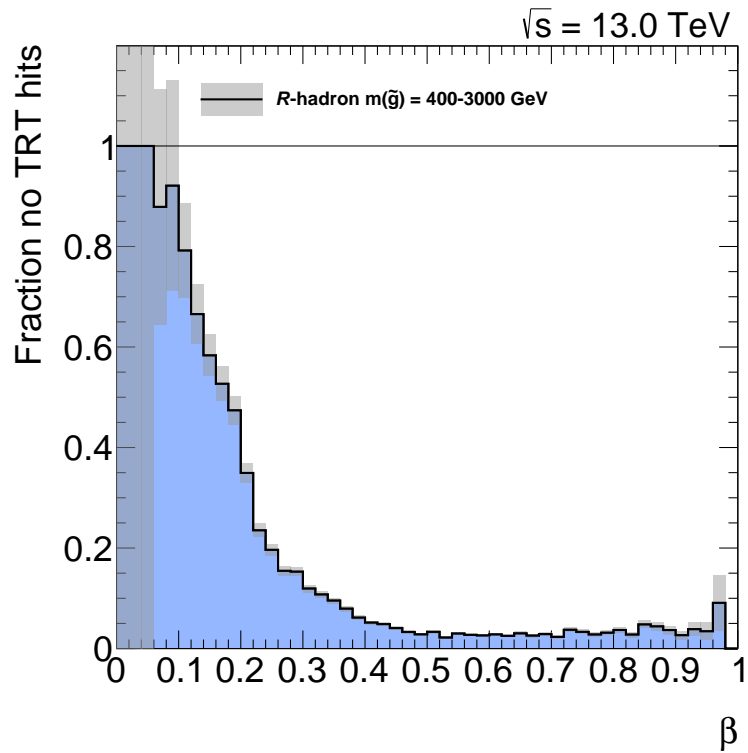


Figure 5.15: Fraction of ID tracks without TRT hits as function of the particle velocity  $\beta$ . The fraction is measured with a mix of all gluino  $R$ -hadron samples.

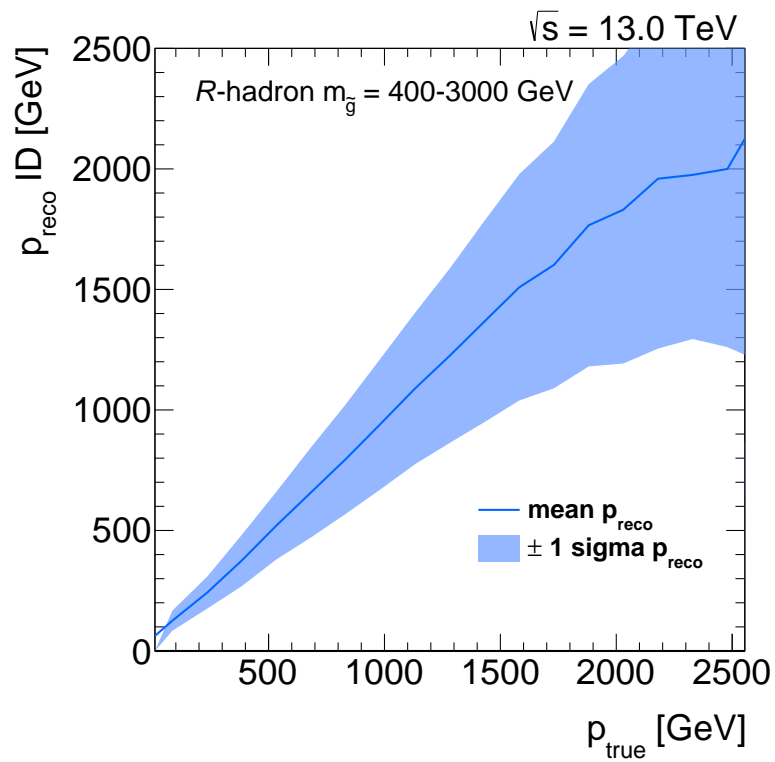


Figure 5.16: The momentum resolution and bias as function of the truth momentum for ID tracks. The resolution is measured with a mix of all gluino  $R$ -hadron samples.

The momentum resolution as well as the mean value as function of the truth momentum is shown in Figure 5.16. It can be seen that for a momentum of roughly 2 TeV the reconstructed momentum saturates. The reason for this is that for these momenta the curvature of the track is too small to be resolved. Also the resolution is getting very poor for momenta above 1 – 1.5 TeV for the same reasons. All those problems of the ID for reconstructing HCLLPs have to be kept in mind to avoid over-constraining the ID tracking requirements in this analysis.

### 5.4.2 SlowMuon

The reconstruction of HCLLPs with a combined ID and MS track is more problematic than the ID-only-tracks due to the additional distance to the MS. Therefore a dedicated reconstruction algorithm is used which does, in contrast to standard muon algorithms used in ATLAS [126], not assume the particles to travel with the speed-of-light but treats the velocity as a free parameter of the track fit.

The standard muon algorithms start by forming track segments in each of the three MS stations. For a slow particle a behaviour similar to that in the TRT is expected for the MDT, as illustrated in Figure 5.17. This means that the track segments are wrongly reconstructed and hence might be incompatible. Also hits can be associated to the next bunch crossing and hence no proper track segments are reconstructed. The track segments are in the next step combined to a muon-only tracks and in the last step extrapolated and matched to an ID track. The reconstruction efficiency as a function of  $\beta$  for the standard muon algorithm is shown in Figure 5.18. While the standard algorithms are almost fully efficient for  $\beta > 0.9$ , the efficiency drops at about  $\beta = 0.75$  and is only about 20% for  $\beta = 0.5$ . From Figure 4.9 one can see that for higher masses the bulk of the particles is produced with velocities of about  $\beta = 0.5$ , therefore a dedicated reconstruction algorithm is needed.

The reconstruction algorithm for slow particles is called MuGirlStau algorithm [120] and starts, in contrast to the standard algorithms, from a high  $p_T$  inner detector track. The  $p_T$ -threshold for running this algorithm was changed in the data-taking period used in this analysis from 70 GeV to 25 GeV. This inside-out approach allows to associate hits even if the pointing of the MS segments is imperfect. The MuGirlStau algorithm also uses the trigger hits from the following bunch crossing and estimates a rough particle velocity from the RPCs. This allows to subtract the time-of-flight from the drift times to estimate the correct drift circle. For the standard

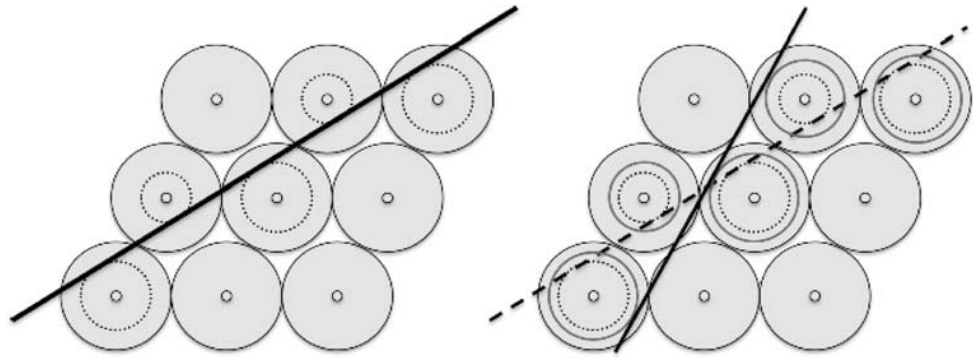


Figure 5.17: Left: Correctly reconstructed track for in-time particle. Right: Incorrectly reconstructed track (solid) for a slow particle traveling along the dashed line.[120]

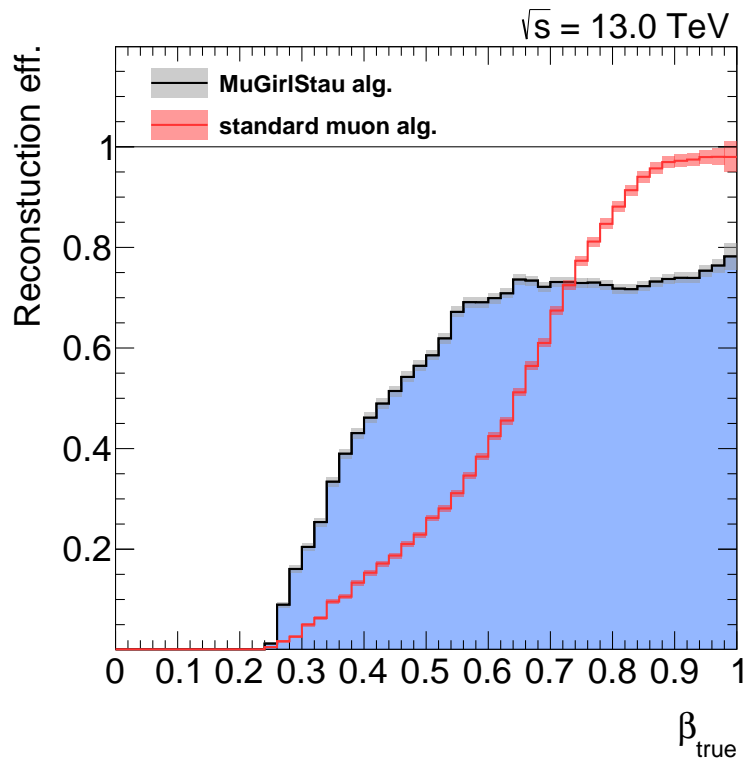


Figure 5.18: The reconstruction efficiency as function of the truth  $\beta$  with standard muon algorithms and with the MuGirlStau algorithm. The efficiency is measured with pair produced charginos in a combined sample with chargino masses between 200 GeV and 1500 GeV.

algorithms  $\beta = 1$  is assumed for the calculation of the time-of-flight. For each group of MDT hits associated to an ID track a fit is applied using  $\beta$  as a free parameter to get also from the MDT's an estimate on the particle velocity. The  $\beta$  from MDT's and RPC's are combined to improve the resolution and used to refit the MDT hits with the given  $\beta$  hypothesis. Objects reconstructed with the MuGirlStau algorithm are from now on referred to as SlowMuons.

The reconstruction efficiency of pair-produced charginos as function of  $\beta$  is also shown in Figure 5.18. It can be seen that the MuGirlStau algorithm is still more than 50% efficient for  $\beta = 0.5$  and breaks down for lower  $\beta$  than the standard algorithm. In contrast to the standard algorithms the

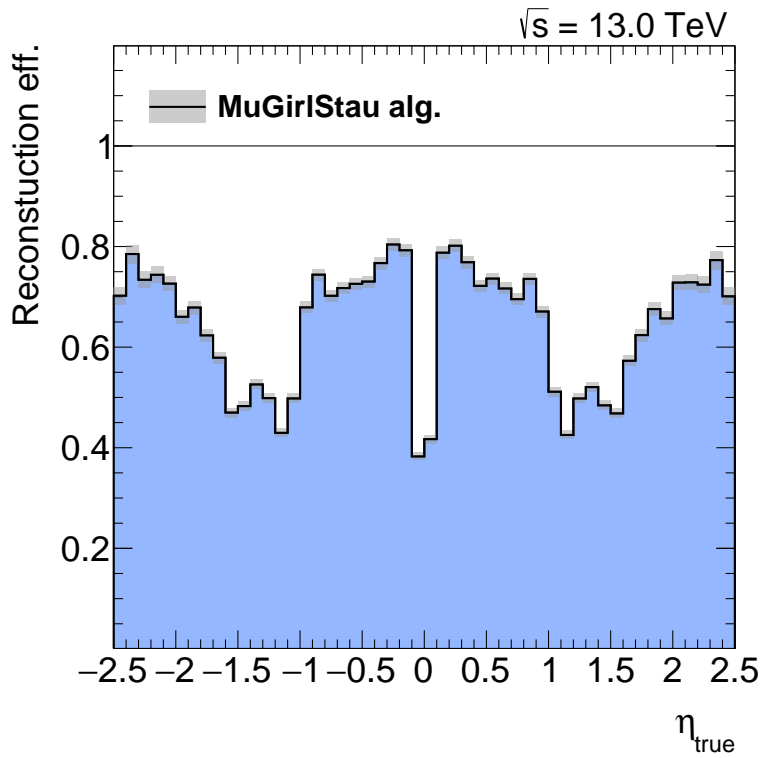


Figure 5.19: The reconstruction efficiency as function of the truth  $\eta$  with the MuGirlStau algorithm. The efficiency is measured with pair produced charginos in a combined sample with chargino masses between 200 GeV and 1500 GeV.

MuGirlStau algorithm is not fully efficient for high  $\beta$ , the reason is that the algorithm is imperfectly implemented. For the new ATLAS software release 21.0 this algorithm was rewritten from scratch and now achieves efficiencies comparable to the ones from the standard algorithms. The reconstruction efficiency as function of  $\eta$  is shown in Figure 5.19. The drop in efficiency at  $\eta = 0$  is due to the service cables which are placed in this region in the ATLAS detector and hence the missing MS chambers/hits. A further drop in efficiency can be observed between 1 and 1.5 in  $|\eta|$ . This region corresponds to the transition region between the MS barrel and the MS endcaps. The momentum resolution and bias of particles reconstructed with the MuGirlStau algorithm is shown in Figure 5.20. In contrast to HCLLPs reconstructed solely as ID tracks no bias for high momenta is visible due to the significantly longer flight distance in the toroidal magnetic field. Also the relative momentum resolution for SlowMuons is significantly better than the one observed for ID tracks. All in all the MuGirlStau algorithm is able to recover efficiency for particles with  $\beta$  between 0.3 and 0.7. It achieves a very good momentum resolution up to momenta of 2.5 TeV without introducing any bias. The SlowMuon objects are in particular important for the search for colour singlets which are charged throughout the whole detector.

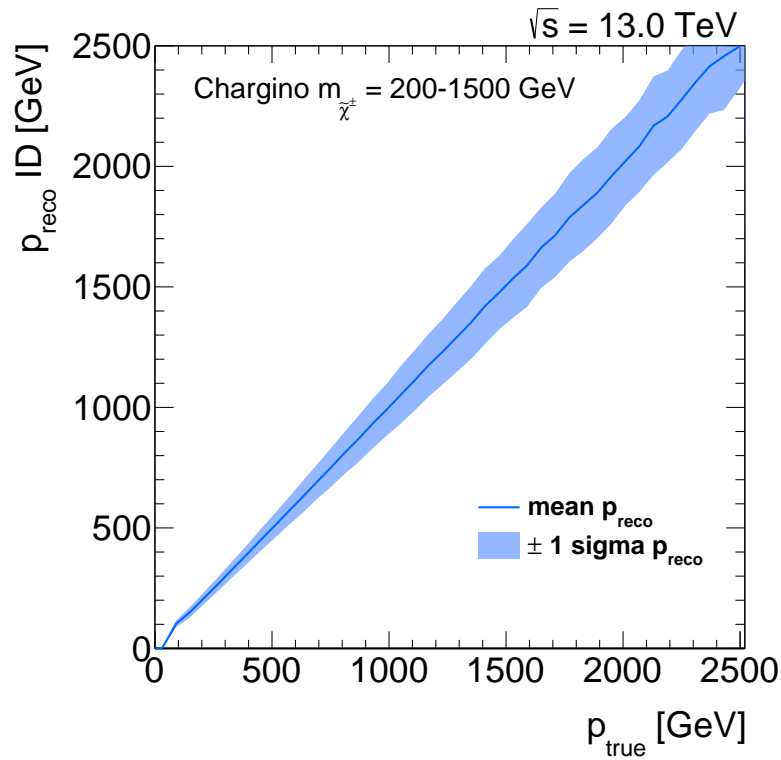


Figure 5.20: The momentum resolution and bias as function of the truth momentum for charginos reconstructed with the MuGirlStau algorithm. A combined sample with chargino masses between 200 GeV and 1500 GeV is used.

## 5.5 Identifying heavy charged long-lived particles

The main observables used to identify HCLLPs in this analysis are described in this section. To achieve an optimal performance those observables have to be calibrated and as those are no standard observables this has to be done on analysis level. First, a brief introduction of the measurement of  $dE/dx$  with the pixel detector will be given, where also the necessary calibrations steps will be explained. The calibration and mass estimation from the pixel  $dE/dx$  can be taken from another analysis which is only using ID tracks and  $dE/dx$  to identify HCLLPs [127]. In the second part, the time-of-flight measurement in the Tile Calorimeter with all the applied calibrations will be described in some detail as this was one of my major contributions to this analysis. In the last part the calibration of the time-of-flight measurement in the MDT's and RPC's will be discussed. A detailed description of the calibration of the MS time-of-flight measurements can be found in Reference [128].

### 5.5.1 Pixel $dE/dx$

As discussed in Section 4.4, a thin detector, such as a silicon detector has the benefit of measuring rather the Most Probable Value (MPV) than the

mean value and suffers less from the ambiguity between the relativistic rise and the low-momentum rise. The best choice for an ionisation-energy loss measurement for singly charged particles in the ATLAS experiment is therefore the pixel detector. Also other subsystems are capable of measuring the energy loss: the Calorimeters, the TRT and the MDT, but have a worse identification power than the pixel detector. Nevertheless the TRT and MDT  $dE/dx$  measurements are used, e.g. for the search for multi-charged particles [129]. For these particles the pixel detector is expected to be in saturation due to the huge energy losses.

In Section 5.4.1 it was discussed that the particles mostly release energy not only in one but rather in a group of pixels, which are then combined into pixel clusters. Also for the estimation of the pixel  $dE/dx$  the total cluster energy is used. Together with the extrapolated particle track in the pixel material a  $dE/dx$  per cluster is calculated. The combined pixel  $dE/dx$  is then estimated from the individual clusters using a truncated mean to get rid of Landau tail effects. The truncation removes the highest  $dE/dx$  value from the mean for two to four clusters and the highest two for the rare case of five clusters per track. Some high- $dE/dx$  hits from the Landau tail can shift the estimated value away from the MPV and as discussed before lower the separation power between slow and fast moving particles. To achieve an optimal performance of the pixel  $dE/dx$  to identify HCLLPs, a series of calibrations has to be performed. One crucial calibration is to ensure the stability over time or delivered luminosity to ensure that the data does not have to be split in time periods for the analysis. Two main influences can change the MPV of the  $dE/dx$  measurement over time: Changes of the operational parameters of the pixel detector and radiation damage caused by the enormous amount of integrated luminosity delivered by the LHC. Both influences can be treated with a run-wise calibration of the MPV. The MPV of the track  $dE/dx$  as function of the delivered integrated luminosity is shown on Figure 5.21. From those per-run MPV values scale factors are derived and applied to data to ensure the stability of the track  $dE/dx$  MPV over time. Furthermore it was found that the  $dE/dx$  depends on the incident angle and hence on the thickness of the material traversed. To account for this an  $\eta$  dependent calibration of the  $dE/dx$  MPV is applied performed in a similar way as the run-wise calibration. It was found that this effect depends on the momentum of the particles (only relevant for low momenta, stable for  $p > 1$  GeV) as well as on the number of used pixel clusters and the sign of the charge of the particles. Different calibrations are therefore applied depending on the

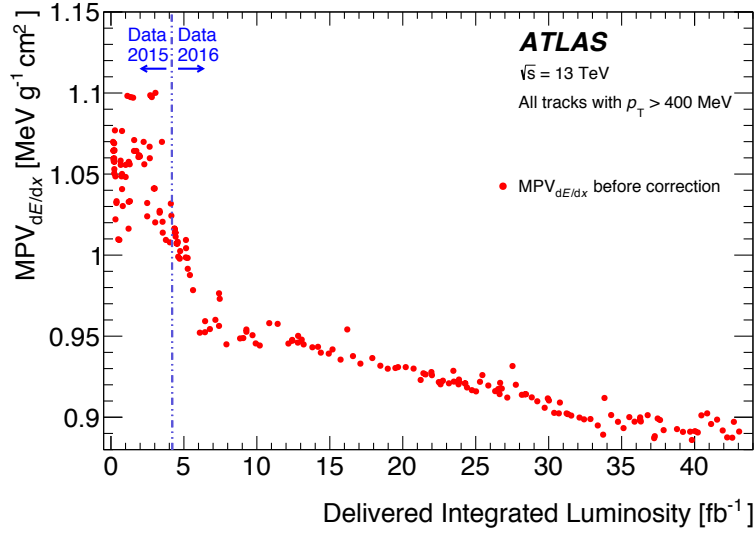


Figure 5.21: The MPV of the track  $dE/dx$  measured with all tracks with  $p_T > 400$  MeV as function of the delivered integrated luminosity to the ATLAS experiment. Each point correspond to a data-taking run. [127]

category the particle belongs to. Furthermore as the radiation damage and detector conditions are not simulated, the MPV from Monte Carlo Simulation (MC) has to be aligned to the one seen in data. This is done using the difference between MPV of  $dE/dx$  from minimum ionising particles in data and simulation as scale factors.

After all those calibrations the MPV is solely dependent on the velocity of the particle. Using low-momentum kaons, protons and pions a functional parametrisation can be estimated relating the MPV to the  $\beta\gamma_{dE/dx}$ . For the parametrisation a three parameter function as given in Equation 5.3 is used, which is inspired by the Bethe-Bloch distribution in the low- $\beta$  region.

$$\text{MPV}_{dE/dx}(\beta\gamma) = A/(\beta\gamma)^C + B \quad (5.3)$$

Six different sets of fit parameters  $A$ ,  $B$  and  $C$  are estimated depending on whether one, two or three clusters are used to calculate the MPV and separate sets for positively or negatively charged particles. The parameter sets are derived from minimum-bias data taken in 2016 by estimating the mean MPV as function of  $\beta\gamma$ , which is calculated from the known mass of pions, kaons and protons and the measured momentum, as shown in Figure 5.22. The particle type can be clearly identified in the low-momentum regime using the  $dE/dx$  momentum times charge plane as shown in Figure 5.23. This Figure is taken from the previous analysis [92], where separate fits were applied to the different particle types as drawn. In the current approach the momenta are translated to a  $\beta\gamma$  and then fitted with a

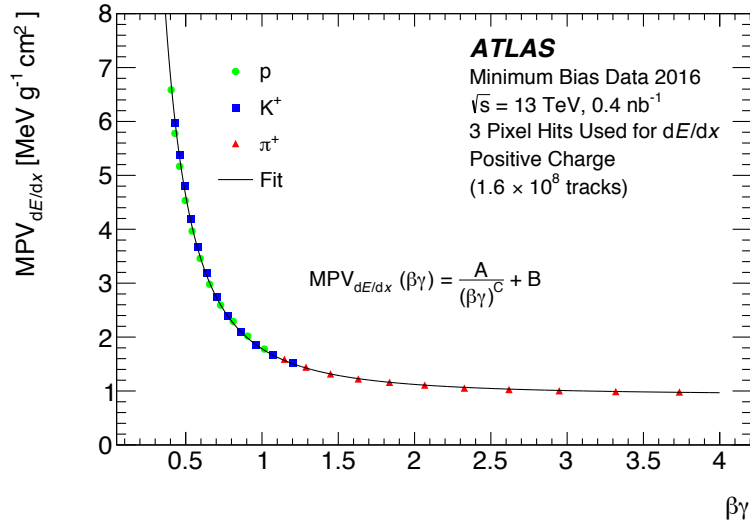


Figure 5.22: The MPV $_{dE/dx}$  as a function of  $\beta\gamma$  for protons, kaons and pions from a sample of minimum-bias data taken in 2016. For this case  $\beta\gamma$  is estimated from the particle momentum and the known particle mass. Fitting those data points the parameters of Equation 5.3 can be extracted. The data points shown correspond to positively charged tracks with three pixel hits used for the  $dE/dx$  estimation. [127]

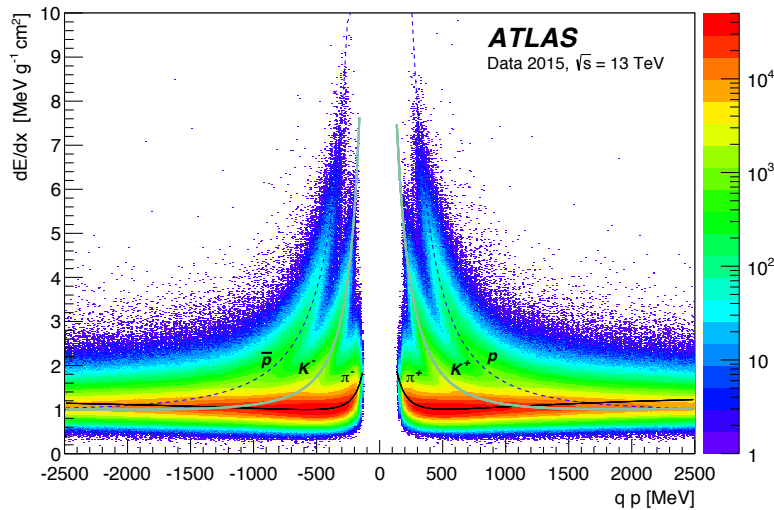


Figure 5.23: The MPV $_{dE/dx}$  for tracks from minimum-bias data taken in 2015 as function of momentum times charge. The tracks from protons, kaons, pions and their anti-particles can be clearly identified for low momenta. [92]

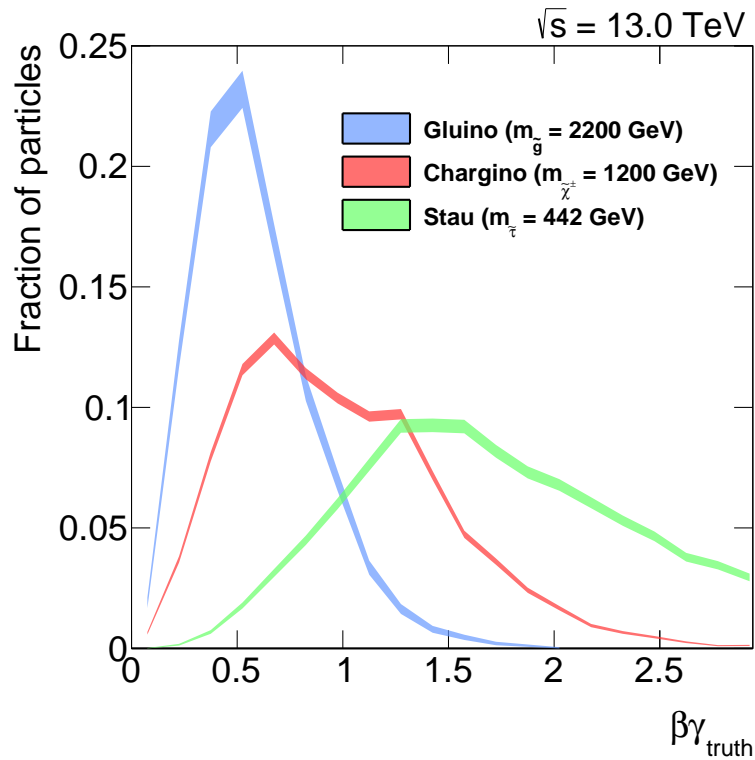


Figure 5.24:  $\beta\gamma$  distribution for HCLLPs (gluinos, charginos and staus). As particle masses the ones roughly at the expected mass limit are used.

single function as shown in Figure 5.22. Inverting Equation 5.3  $\beta\gamma_{dE/dx}$  for a particle can be calculated for the estimated MPV.

As discussed in Section 5.1  $\beta\gamma_{dE/dx}$  is only used for the  $R$ -hadron searches while for SR-1Cand-FullDet only a high  $dE/dx$  is required. For the SR-2Cand-FullDet no requirements on  $dE/dx$  or  $\beta\gamma_{dE/dx}$  are used. The reason for this is that for a  $\beta\gamma > 1$  almost no difference in the expected MPV is visible and hence no separation power is expected, as can be seen in Figure 5.22. The true  $\beta\gamma$  distributions for the different signal models for the mass points roughly at the expected lower mass exclusion limit are shown in Figure 5.24. For  $R$ -hadrons with 2200 GeV the vast majority of the particles is expected with a  $\beta\gamma$  below one, while for charginos (1200 GeV) and staus (442 GeV) a significant fraction of HCLLPs are likely to have a  $\beta\gamma$  value larger than one. The SR-1Cand-FullDet suffers from relatively large backgrounds and hence did not contribute to the sensitivity in the previous analyses. An additional cut on  $dE/dx$  was therefore placed to suppress the backgrounds even if a significant fraction of signal candidates is lost. This helped to gain sensitivity from SR-1Cand-FullDet, which has now a significant contribution for charginos at the expected mass limit.

### 5.5.2 Time-of-flight Tile Calorimeter

One subsystem capable of a ToF measurement to estimate the particle velocity is the Tile Calorimeter. The Tile Calorimeter has a timing resolution of roughly 300 ps in the limit of large energy deposits, which is one of the best timing resolutions of all subsystems in the ATLAS detector. Only the LAr calorimeter has a slightly better timing resolution of about 250 ps in the limit of high-energy deposits. The benefit of the Tile Calorimeter over the LAr calorimeter is that it is further out in the detector and hence the distance travelled is longer resulting in a larger time difference at the point of the measurement. The uncertainty of the velocity measurement  $\beta$  is given by

$$\sigma_{\beta} = \frac{c\sigma_t}{d}\beta, \quad (5.4)$$

with  $c$  being the speed-of-light,  $\sigma_t$  the timing uncertainty,  $d$  the distance of space-point of the measurement to the IP, and  $\beta$  the particle velocity. The  $\beta$  uncertainty is reciprocally proportional to the distance of the timing measurement. The additional flight-distance to the Tile Calorimeter with an average distance to the IP of roughly 4 – 6 m compared to the LAr with an average distance to the IP of about 2 – 3 m results in a better  $\beta$  resolution in the Tile Calorimeter, even taking into account the slightly better timing resolution in the LAr calorimeter. All subsystems closer to the IP, even if potentially capable of time-of-flight measurements, are hence not suitable to be used for the identification of HCLLPs. This is under the assumption of a similar timing resolution, but might be different if some precision timing layers are installed as considered for future upgrades of the ATLAS detector [130], which claim a timing resolution of 30 ps. For this analysis only the time-of-flight from the Tile Calorimeter is used. It was also considered to use the LAr, to have another independent  $\beta$  measurement. But in Reference [131] it was found that the LAr calorimeter does not give the expected timing for out-of-time signals. This was estimated using electrons from satellite–satellite collisions (Section 3.1) at  $\pm 5$  ns. Similar studies were conducted with muons, as shown in Appendix A.1, to check whether or not the same features are visible for minimum ionising particles. So far the achieved resolution for muons is not sufficient to resolve the muons from satellite–satellite collisions and hence no statement about the performance of the LAr for out-of-time signals can be made. As this cross-check is not possible and only a small gain in resolution is expected from the LAr calorimeter it was not used for this analysis.

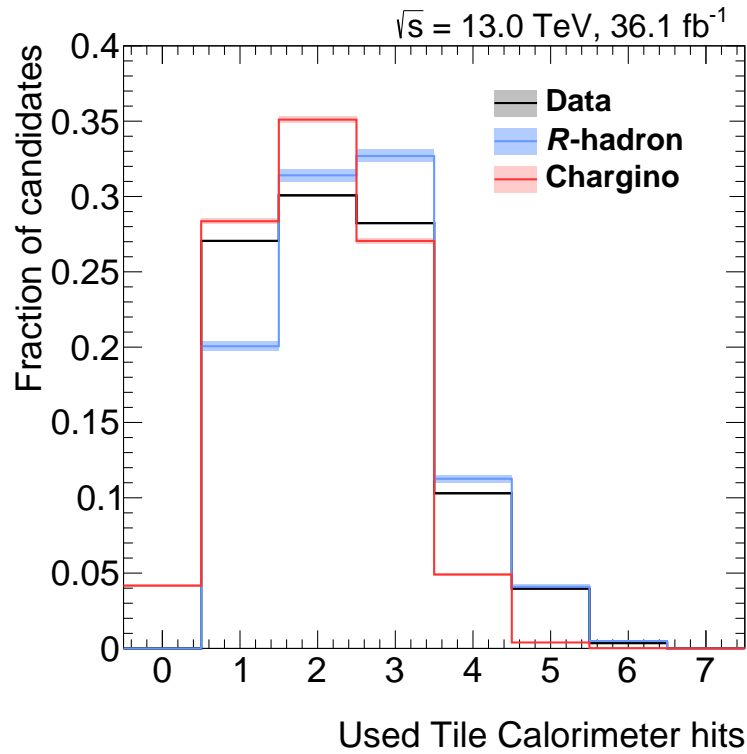


Figure 5.25: The number of used Tile Calorimeter hits for the  $\beta_{\text{TILE}}$  estimation for  $R$ -hadrons, charginos and muons from data. For  $R$ -hadrons the  $\text{ID}+\text{CALO}$  selection is applied while for charginos the  $\text{LOOSE}$  selection is used. In data a selection demanding muons with a minimum  $p_{\text{T}}$  of 25 GeV and satisfying basic quality requirements.

### The $\beta_{\text{TILE}}$ measurement

The  $\beta_{\text{TILE}}$  estimation starts with Tile Calorimeter cells associated to an ID track. Cells are associated if passed by an extrapolation of the ID track to the Tile Calorimeter. To reduce effects of detector noise, only cells with a minimum energy deposit of  $E_{\text{hit}} = 500$  MeV associated to a track are taken into account. The number of Tile Calorimeter hits used for simulated signals ( $R$ -hadrons and charginos) and muons from data is shown in Figure 5.25. For muons the mean number of Tile Calorimeter hits is two but also with a high fraction of tracks with one or three hits. As the Tile Calorimeter consist of three radial layers an average number of three hits would be expected but as muons are minimal ionising a significant fraction of hits is lost due to the minimum requirement on the  $E_{\text{hit}}$ . For charginos even fewer hits per track are expected. The reason is that the Tile Calorimeter is not a thin detector and hence the energy measured follows the mean energy loss of the Bethe-Bloch formula. Muons with a momentum larger than 25 GeV are already in the relativistic rise as can be seen from Figure 4.10. They are hence expected to have larger energy deposits than charginos, which are closer to the minimum of the ionisation energy loss. Muons therefore lose less hits due to  $E_{\text{hit}}$  requirement than charginos. For  $R$ -hadrons slightly more hits than for muons are expected,

which can be explained on the one hand by the larger ionisation energy loss due to the higher mass and hence lower  $\beta$  of the  $R$ -hadrons and on the other hand by the additional energy loss due to hadronic interactions. The observable for the timing measurement with the Tile Calorimeter is  $t_0$ , which is defined as the relative time difference to a particle produced at the ATLAS origin travelling with the speed-of-light and arriving at the centre of the cell. To reduce the background from particles originating from the following bunch crossing  $|t_0|$  is limited to be less than 25 ns. From  $t_0$  the velocity of the particle can be calculated using

$$\beta = \frac{d}{t_0 c + d}. \quad (5.5)$$

Muons can be used for calibration and to estimate the timing resolution, as they are expected to be produced with almost the speed-of-light at the LHC and hence there  $\langle t_0 \rangle = 0$  ns. The measurements in the individual Tile Calorimeter cells are combined to a weighted average using

$$\beta_{\text{TILE}}^{-1} = \frac{\sum_{i=1}^N \beta_i^{-1} / \sigma_{\beta_i}^2}{\sum_{i=1}^N 1 / \sigma_{\beta_i}^2}. \quad (5.6)$$

Also an uncertainty on the combined  $\beta_{\text{TILE}}$  can be calculated using

$$\sigma_{\beta^{-1}}^2 = \frac{1}{\sum_{i=1}^N 1 / \sigma_{\beta_i}^2} \quad \text{and} \quad \sigma_{\beta} = \beta^2 \sigma_{\beta^{-1}}. \quad (5.7)$$

The benefit of combining the measurements as  $\beta^{-1}$  is the direct proportionality to  $t_0$  which ensures that  $\beta^{-1}$  is also Gaussian distributed, an assumption on the uncertainty for combination.

### Calibration

The calibrations are estimated and validated with a data sample corresponding to  $36.1 \text{ fb}^{-1}$  and a sample of simulated  $Z \rightarrow \mu\mu$  events. Two different pre-selections are applied, a muon and a  $Z \rightarrow \mu\mu$  selection. Both use all events that are triggered by either a muon or a  $\cancel{E}_T$  trigger. Furthermore the events are required to be recorded in data-taking periods when the detector was fully operational and ready for physics data taking. For both selections all muons are used that satisfy the medium quality requirements as defined in Reference [126]. The muon  $p_T$  has to be larger than 25 GeV for both selection. But as for the first  $14 \text{ fb}^{-1}$  the cell as-

sociation was only applied for ID tracks with  $p_T > 50$  GeV this harder  $p_T$  requirement has to be used for this period. For the  $Z \rightarrow \mu\mu$  selection additionally exactly two muons with opposite charge have to be in the event and their invariant mass has to be in agreement with the Z-boson mass within 10 GeV. From the muons passing these selections the ID track with the associated Tile Calorimeter hits is used for the calibration and validation studies. The reason why both selections are needed is that the muon selection significantly increases the available statistic which is necessary for some calibrations. But if comparing data and simulation in particular integrated over a certain  $\eta$  range it is essential to use the  $Z \rightarrow \mu\mu$  selection, because not all muons in data originate from a Z-boson decay and hence a different  $\eta$  composition is expected. If distributions integrated over a certain  $\eta$  range are considered this different composition can also change the overall resolution as some good or bad regions are overrepresented. Using the  $Z \rightarrow \mu\mu$  selection ensures that the events seen in data also originate from a Z-boson decay and hence the same  $\eta$  distribution are expected for data and simulation. This guarantees that the overall distributions of  $t_0$  or  $\beta_{\text{TILE}}$  in data and simulation are comparable.

To gain optimal performance of the timing measurement with the Tile Calorimeter a sequence of calibration steps has to be applied. The different calibration steps are summarised in Figure 5.26. After masking Tile Calorimeter cells with unexpected  $t_0$  distributions the first actual correction is to remove a bias introduced by the readout algorithm of the Tile Calorimeter, the OFA algorithm. This bias correction is implemented in the common ATLAS reconstruction software since mid 2016. On analysis level this correction has to be applied therefore only to the first  $14 \text{ fb}^{-1}$ . Also the signal samples have this correction implemented on reconstruction level. The OFA correction is chosen as the first calibration step as  $t_0$  is closest to the  $t_0$  on reconstruction level. This is followed by a distance- and  $\eta$ -correction ensuring a flat response over the full  $\eta$ -range. The last common step is the energy correction which ensures stability of the response for different energy deposits. This first set of calibration steps correct for potential asymmetries in the  $t_0$  distributions, which could lead to a bias in the following cell- and run-wise corrections. Those calibration steps ensure the stability of the measurement over time (run-wise) and the fiducial volume (cell-wise) and are applied only on data. Simulation is smeared to match the resolution observed in data. The final calibration step is a pull correction, separate for data and simulation, that ensures a well described uncertainty of the  $\beta$  measurement. The different calibra-

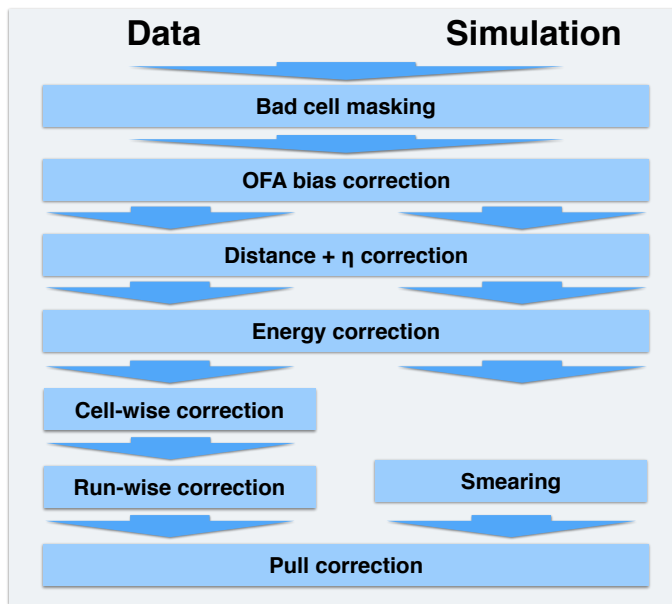


Figure 5.26: The ordering of the timing calibration steps for the Tile Calorimeter. The arrows indicated if separate or combined parameter sets are used for the calibration.

tion steps will be discussed in the following.

**Bad-cell masking** It was found that some of the 4672 Tile Calorimeter cells show strange  $t_0$  distributions, which are not expected and also not present in simulation. Three different types of features have been observed in a few specific cells, while the vast majority of the cells have a  $t_0$  distribution in agreement with a Gaussian like shape, as shown in Figure 5.27 (left). One unexpected feature found in exactly one Tile Calorimeter cell ( $-D6$ ,  $\phi = -2.6$ ) is shown in Figure 5.27 (right). This Tile Calorimeter cell shows a strong dependence of the measured  $t_0$  value on the  $E_{hit}$ . As this was only found for one specific cell this cell is masked and excluded from the timing measurements in data a simulation. Furthermore it was observed that 20 Tile Calorimeter cells have very low hit occupancy, as shown in Figure 5.28 (left), which is due to parts of the Tile Calorimeter not operating for some periods [20]. As this is not included in simulation also those cells are excluded from the  $\beta$  estimation. The third feature that was observed in the  $t_0$  distributions of the Tile Calorimeter cells are cells with a largely assymmetric  $t_0$  distribution, as shown in Figure 5.28 (right). The reason for this assymmetric distributions can be changes in the settings or Tile Calorimeter cells loosing their synchronisation with the ATLAS clock. This issue might be solvable via a correction over time for the specific cell but as only 22 Tile Calorimeter cells are affected and due to the limited statistics those are simply excluded from the  $\beta$  estimation as well. Overall

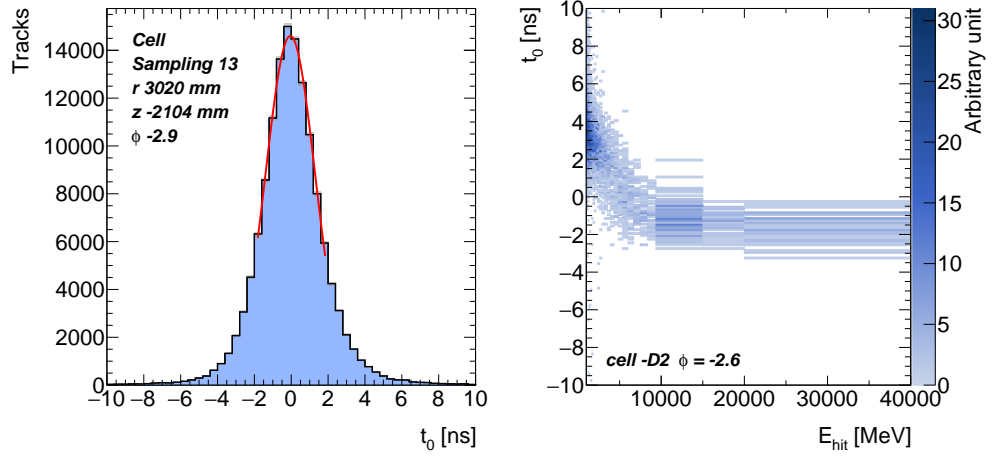


Figure 5.27: Left: The  $t_0$  distribution for a good Tile Calorimeter cell. Right: strong dependence of  $t_0$  on  $E_{hit}$  found in one specific Tile Calorimeter cell (-D6,  $\phi = -2.6$ ).

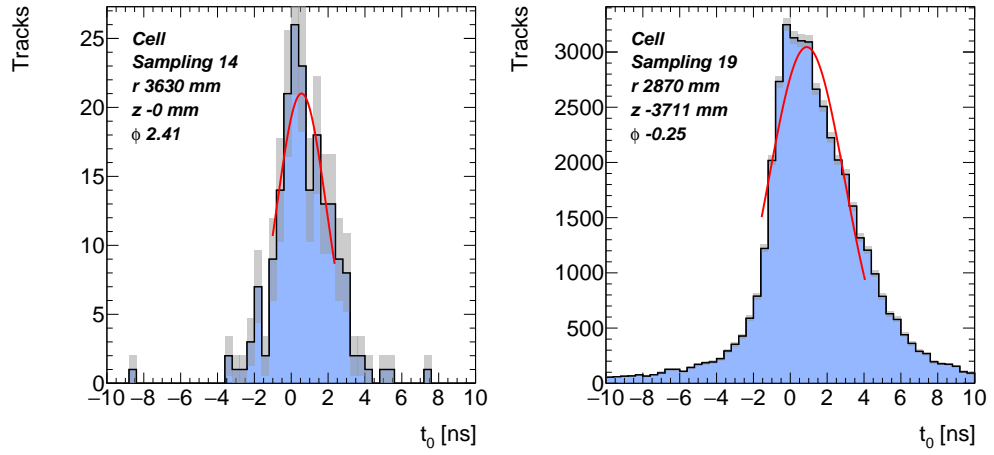


Figure 5.28: Left: Tile Calorimeter cell with only view hits. Right: Tile Calorimeter cell with an asymmetric  $t_0$  distribution.

about 1% of the Tile Calorimeter cells are masked and not used for the time-of-flight measurement, which corresponds to a loss of 0.5% of the hits. Only 0.5% of the hits are lost as a significant fraction of the masked cells are low occupancy cells.

**OFA correction** The OFA algorithm, introduced in Section 3.2.2, used for the readout of the Tile Calorimeter is a fast and robust way to calculate amplitude, pedestal and phase ( $t_0$ ) as a linear combination of the seven samplings described by following Equation

$$A = \sum_{i=1}^n a_i S_i, \quad At_0 = \sum_{i=1}^n b_i S_i \quad \text{and} \quad p = \sum_{i=1}^n c_i S_i, \quad (5.8)$$

with  $A$  being the amplitude,  $\tau$  the phase and  $p$  the pedestal. The coefficients  $a_i$ ,  $b_i$  and  $c_i$  are called optimal filtering coefficients and are obtained as the set with the minimum variance of the parameters against pile-up

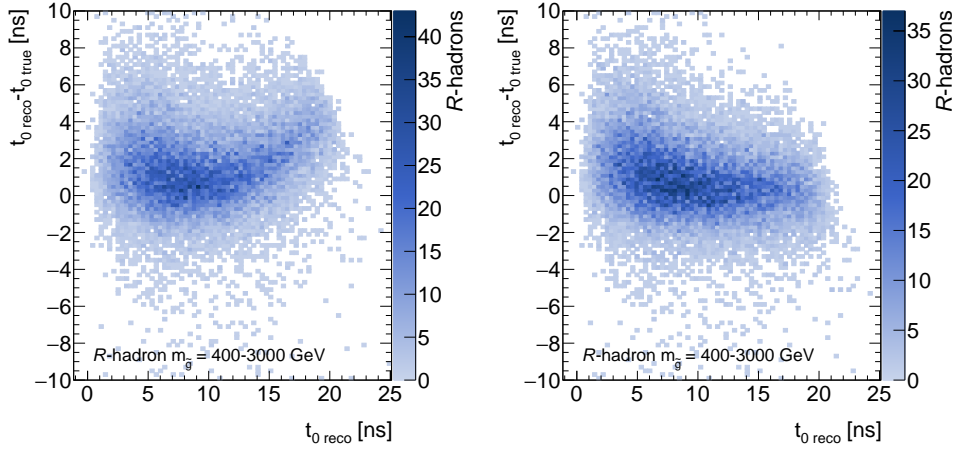


Figure 5.29: The difference between the true  $t_0^{true}$  and the reconstructed  $t_0^{reco}$  as function of the reconstructed time for a sample without online OFA correction. The true time is estimated from the velocity of the particles and the distance to the measurement. A combined sample of  $R$ -hadrons is used with masses between 400 GeV and 3000 GeV. Left: No OFA correction applied. Right: OFA correction applied offline.

and electronic noise under the assumption of the known pulse shape, which was measured in test-beam data. The procedure to estimate the optimal filtering coefficients is based on the assumption that  $t_0 = 0$ , which is not the case for out-of-time signal e.g. from HCLLPs. Two different approaches are possible to correct the expected bias. One is to use an iterative OFA [132], using the output of the phase as input for the next iteration with phase corrected OF coefficients. This procedure is rather computing intense due to the additional iterations. Another approach is to estimate the bias using ideal pulses. Injecting ideal pulses with a known phase into the OFA gives the response and hence the bias as function of the true phase. This bias can be parametrised and inverted to get a correction for the bias of the measured  $t_0$ . The correction function was provided by the ATLAS Tile Calorimeter group as two fourth-order polynomial as

$$F(t_0) = \begin{cases} p_1 + (p_2 - (p_3 + p_4 t_0) t_0) t_0 & \text{for } t_0 < 0 \\ (q_1 + (q_2 + (q_3 + q_4 t_0) t_0) t_0) t_0 & \text{for } t_0 \geq 0 \end{cases} \quad (5.9)$$

with

$$p_1 = -0.00695743, p_2 = 0.0020673, p_3 = 0.0002976, p_4 = 3.61305 \times 10^{-6} \quad (5.10)$$

and

$$q_1 = 0.0130013, q_2 = 0.00128769, q_3 = -0.000550218, q_4 = 7.55344 \times 10^{-6}. \quad (5.11)$$

This correction function is now implemented in the ATLAS reconstruction software and hence the non-iterative OFA can be used. As mentioned above the  $F$  correction was only applied for parts of the data on recon-

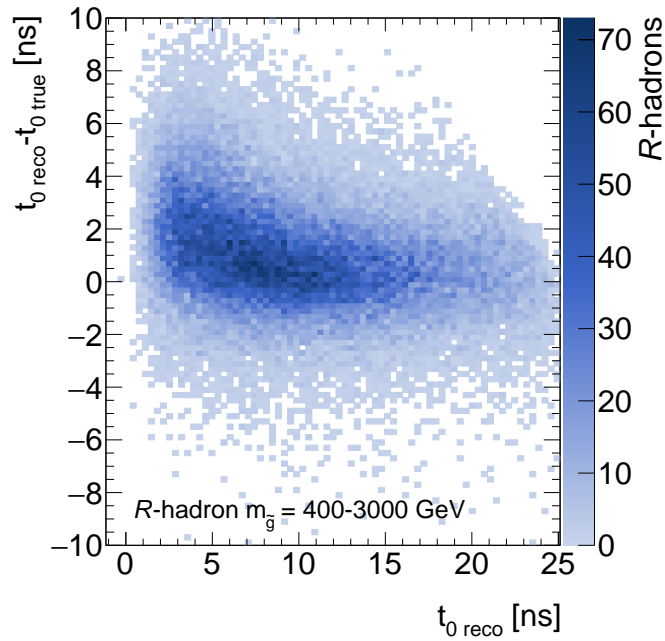


Figure 5.30: The difference between the true  $t_{0,true}$  and the reconstructed  $t_{0,reco}$  as function of the reconstructed time for a sample with online OFA correction. The true time is estimated from the velocity of the particles and the distance to the measurement. A combined sample of  $R$ -hadrons is used with masses between 400 GeV and 3000 GeV.

struction level (online) and therefore has to be applied for the rest of the data on analysis level (offline). The validity of the approach was tested by applying this correction offline on  $R$ -hadron signal samples without the online correction. The difference between the true  $t_{0,true}$  and the reconstructed  $t_{0,reco}$  as function of the reconstructed time is shown in Figure 5.29 with and without offline correction. It can be seen that the bias visible for  $t_{0,reco} > 10$  ns is gone after applying the offline correction. Comparing this with the results from a  $R$ -hadron signal sample with the online correction applied, as shown in Figure 5.30 it can be seen that both the online and offline correction give the same results. The overall  $t_0$  distribution with the OFA correction applied to the relevant data-runs together with the uncorrected distribution is shown in Figure 5.31. The effect on the  $t_0$  distribution measured with muons in data is almost negligible, as for small  $t_0$ , as expected for muons, the OFA correction is tiny and furthermore the correction is only applied to parts of the data. A larger effect is visible for the  $t_0$  resolution of HCLLPs as shown in Figure 5.32 for  $R$ -hadrons. The resolution is estimated as the difference between the expected  $t_{0,true}$  and the reconstructed  $t_{0,reco}$ . After correction the mean is significantly closer to 0 ns and the resolution is improved by roughly 20%.

**Distance and  $\eta$  correction** Without any correction it would be assumed that the spatial position of the  $t_0$  measurement in the Tile Calorimeter is always at the centre of the respective cell. This assumption breaks in par-

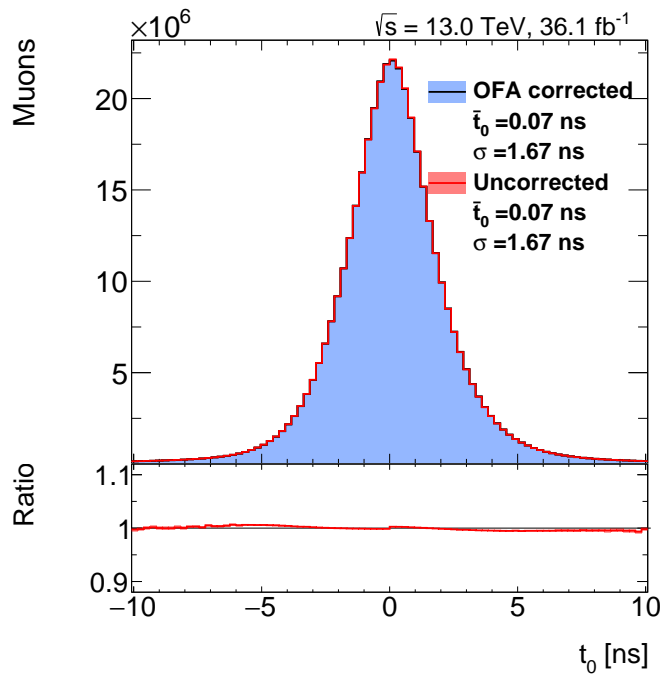


Figure 5.31: The  $t_0$  distribution without any correction and with the OFA correction applied offline for the data taking period where not already included online.

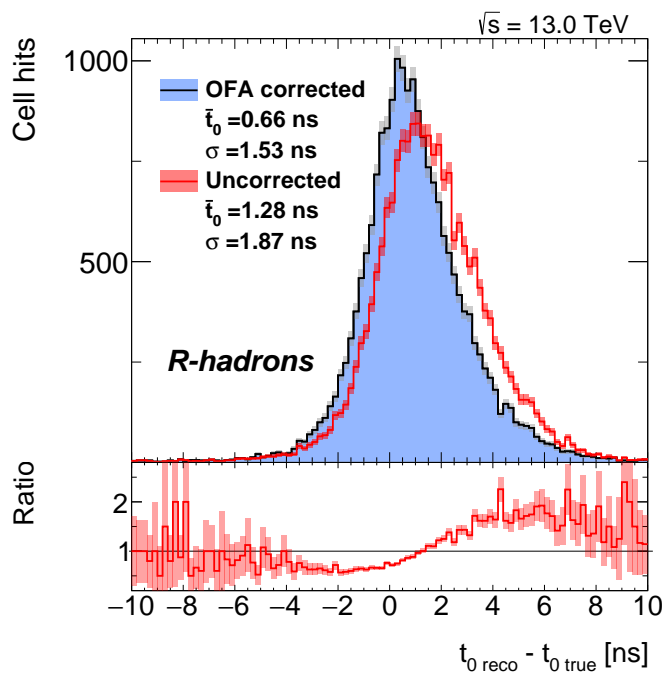


Figure 5.32: The  $t_0$  resolution without any correction and with the OFA correction applied for a combined sample of  $R$ -hadrons with masses between 400 GeV and 3000 GeV.

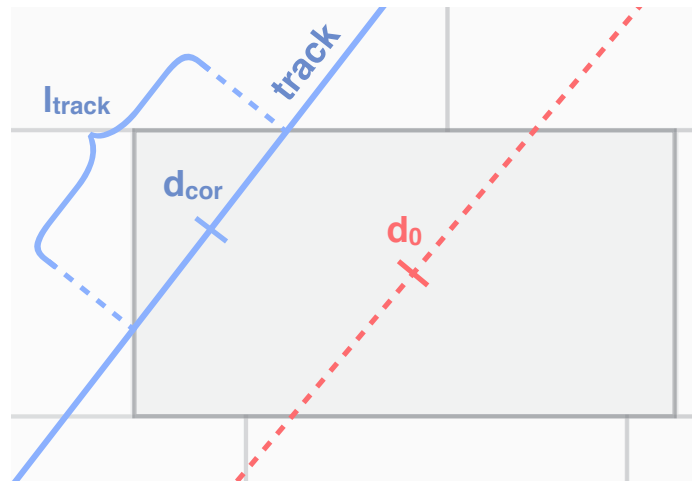


Figure 5.33: A schematic drawing of the idea of the distance correction. Shown are the distance to the centre of the cell ( $d_0$ ) the corrected distance ( $d_{cor}$ ) and the length of the track in the cell ( $l_{track}$ ). The blue line indicates the actual track and the red dashed line a track through the centre of the cell.

ticular for the large Tile Calorimeter cells in the extended barrel and a clear bias as function of  $\eta$  in the cell is visible, as shown in the first row of Figure 5.34. Those figures show a projection of all  $\phi$ -wedges, as the effect is only dependent on the  $r$ - $z$ -shape of the cell. This combination of all wedges of one cell type is from now on referred to as  $\phi$ -projected cells. A two step procedure was developed to correct for this  $\eta$  dependence. First the actual spatial position of the measurement is estimated from an extrapolation of the track to the Tile Calorimeter cell and used for a correction of the additional path length. Second a residual bias is corrected with an  $\eta$ -dependent correction. This residual bias in data is rather small and originates from the differences in the light path to the readout between the centre of the cell and the actual spatial position of the measurement. A larger bias was found in simulation, most likely due to mis-modelling of the light path as can be seen in the second row of Figure 5.34. The reason why this two-step procedure and not only an  $\eta$ -dependent correction is applied is that the particle is traveling the additional distance to the spatial position of the measurement with its specific velocity. As this analysis is looking for particles with velocities significantly lower than the speed-of-light an increasing bias in  $\eta$  the lower the particle  $\beta$  would be introduced [133].

The basic idea of the distance correction is illustrated in Figure 5.33. As the particle trajectory does not necessarily traverse the centre of the cell a corrected spatial position of the measurement has to be estimated. This is done by extrapolating the ID track to the respective Tile Calorimeter cell to obtain the entrance and exit points of the particle. The spatial position of the measurement is then estimated as the centre of the trajectory within the cell and accordingly the new distance of flight is given

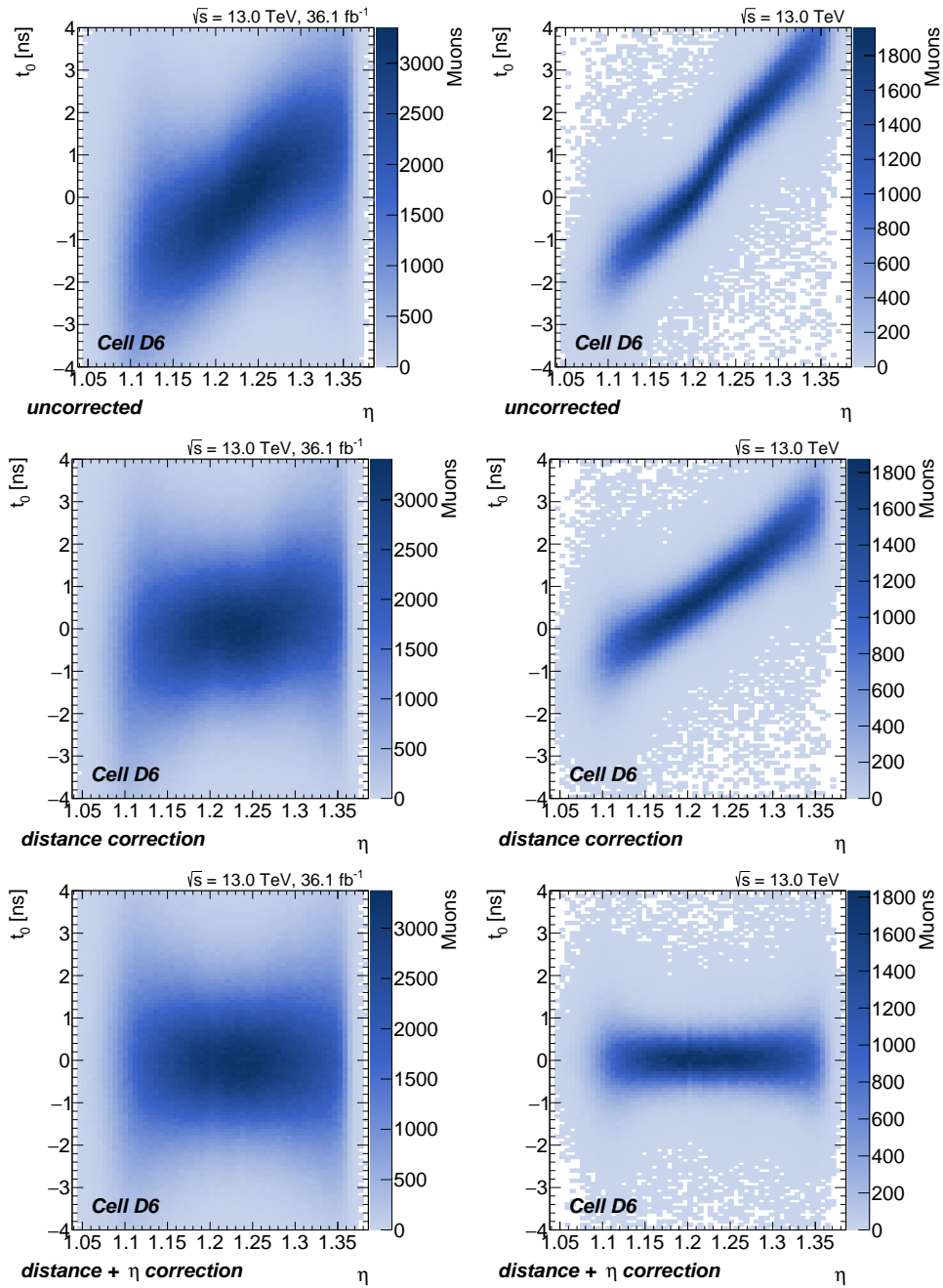


Figure 5.34: The  $t_0$  distribution as function of  $\eta$  for one  $\phi$ -projected Tile Calorimeter cell. Left: Muons in data. Right: Muons from a sample of simulated  $Z \rightarrow \mu\mu$  events. The first row shows the uncorrected distribution. The second row the  $t_0$  distribution after the distance correction and the third row after both the distance and the  $\eta$  correction

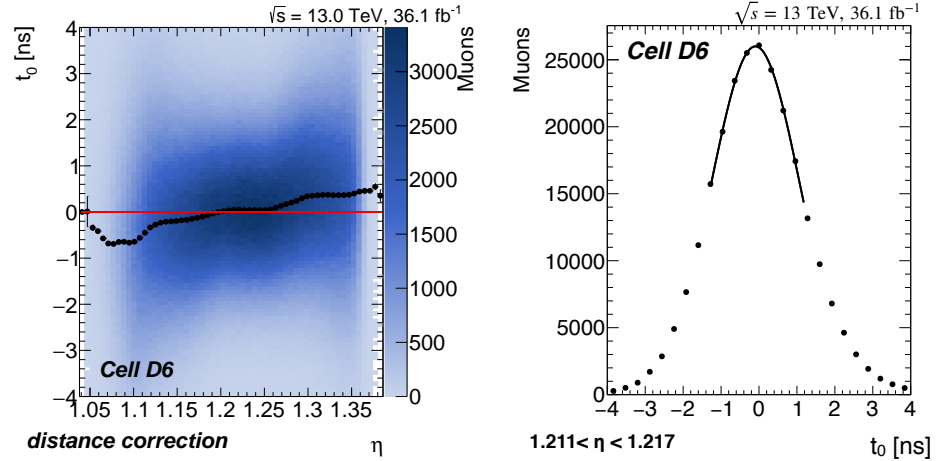


Figure 5.35: Left:  $t_0$  against  $\eta$  for cell D6 with the superimposed profile used for the  $\eta$  correction. Right: One  $\eta$  slice with a superimposed Gaussian. The mean of the Gaussian is used for the profile.

as  $d_{cor} = d_{in} + l_{track}/2$ . The correction is up to 30 cm for the outer regions of the largest cells D5 and D6. Furthermore also the position of the production vertex is taken into account as origin of the track. Detailed studies and also the treatment of the segmented cells in sampling 13 can be found in Reference [133]. For the  $t_0$  calibration the new distance is used to subtract the additional time-of-flight from the measurement under the assumption of particles travelling with the speed-of-light. The corrected time is accordingly given by

$$t_{0\ cor} = t_0 + \frac{d_0 - d_{cor}}{c}. \quad (5.12)$$

This corrected  $t_{0\ cor}$  is used for the calibrations but not for the  $\beta_{TILE}$  estimation as it assumes  $\beta = 1$ . For  $\beta_{TILE}$  instead the corrected distance is directly used in the calculation, as

$$\beta_{cor} = \frac{d_{cor}}{t_0 c + d_0}. \quad (5.13)$$

This ensures that the additional path length is also assumed to be travelled with the correct  $\beta$ . The effect of the correction can be seen in the second row of Figure 5.34. While in data almost no residual bias is left, a strong  $\eta$  dependence is still visible in simulation due to mis-modeling of  $\eta$ -dependence of the timing.

To account for the residual bias an additional  $\eta$  dependent correction is applied on top, separate for data and simulation. The  $t_0$  distribution is therefore split into bins of  $\eta$  as shown in Figure 5.35 (right). Each slice is fit first with a Gaussian in the range mean minus RMS to mean plus RMS and afterwards refit with a Gaussian using the mean of the first Gaussian

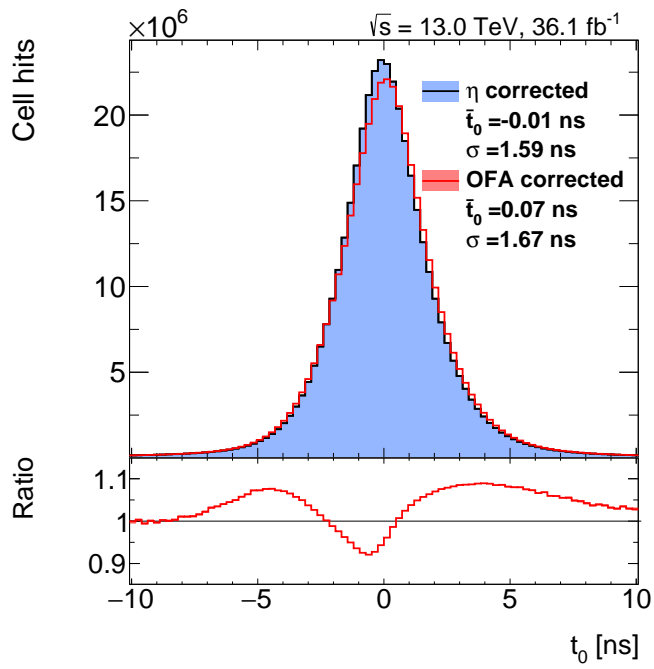


Figure 5.36: The  $t_0$  distribution with and without the additional  $\eta$  corrections for muons in data.

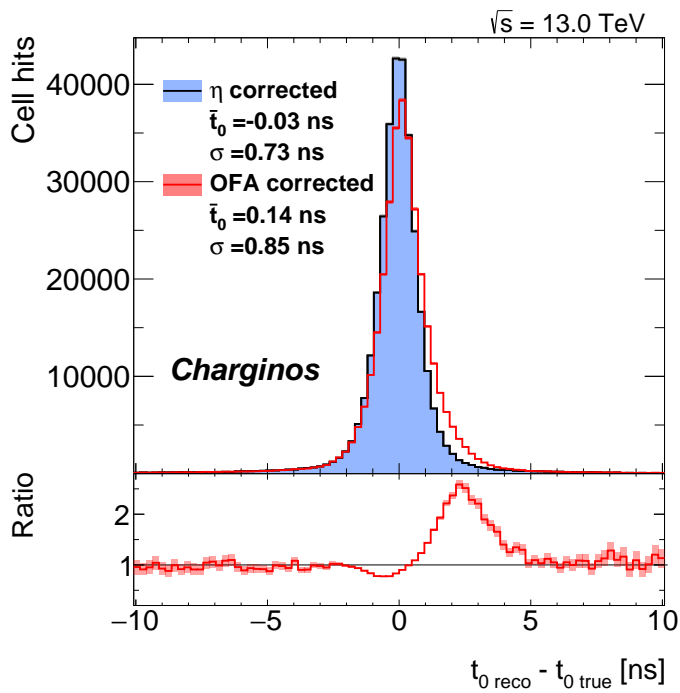


Figure 5.37: The  $t_0$  resolution ( $t_{0\text{reco}} - t_{0\text{true}}$ ) with and without the additional  $\eta$  corrections for a combined sample of pair-produced charginos with masses between 200 GeV and 1500 GeV.

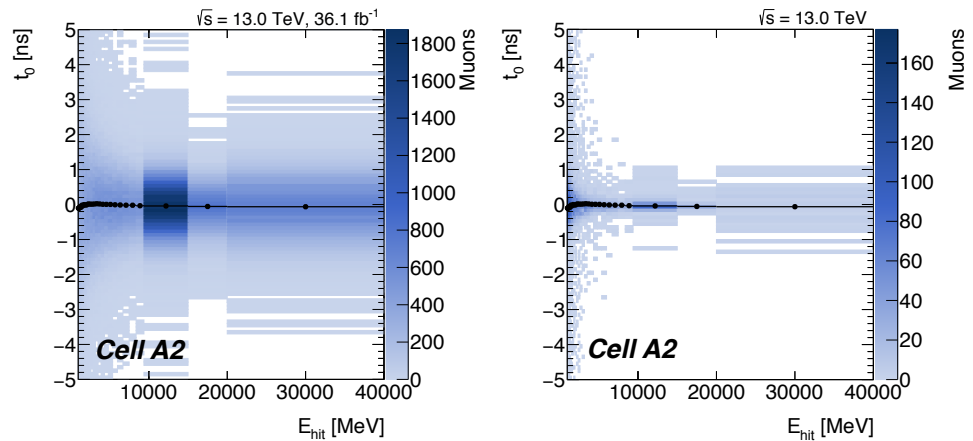


Figure 5.38: The  $t_0$  distribution as function of the energy deposit  $E_{hit}$  per cell with the profile superimposed for data (left) and simulation (right).

plus/minus the sigma of the first Gaussian as range. The mean of the final Gaussian is directly used as calibration constant and superimposed as profile in Figure 5.35. The results after applying both the distance and the  $\eta$  correction on data and simulation are shown in the last row of Figure 5.34. As expected for both data and simulation no residual  $t_0$  bias as function of  $\eta$  is visible.

The overall  $t_0$  distribution with and without the  $\eta$  corrections applied for muons in data is shown in Figure 5.36. With the  $\eta$  corrections the resolution of the timing measurement can be improved by roughly 5% and also the mean of the  $t_0$  distribution is closer to 0 ns after the correction. Also for the  $t_0$  resolution measured with charginos similar effects are visible as shown in Figure 5.37. As expected the effect on the resolution is larger (14%) as the  $\eta$  bin-wise correction is larger due to the mis-modelling of the  $\eta$  dependence. Also in simulation the mean of the  $t_0$  resolution is closer to the expected 0 ns.

**Energy correction** It was found that the timing distribution depends on the energy deposited in each cell. To correct for this dependence a similar approach as in the  $\eta$ -correction is made. The  $t_0$  is drawn against  $E_{hit}$  as shown in Figure 5.38. The binning is chosen to have reasonable statistics in each  $\eta$  slice for data as well as for simulation. Each slice is fitted as described for the  $\eta$  correction and the mean of the Gaussian is used as correction. This correction is done separate for each  $\phi$ -projected cell and separate for data and simulation. The effect on the final  $t_0$  distribution is shown in Figure 5.39. While the mean of the distribution stays the same a slightly better resolution can be observed.

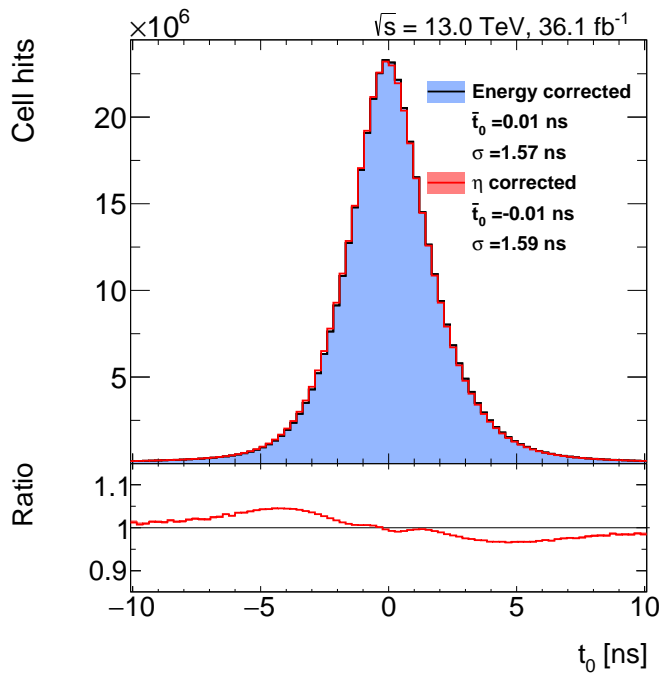


Figure 5.39: The  $t_0$  distribution with and without the additional energy correction for muons in data.

**Cell-wise correction (data)** To account for desynchronisation of single Tile Calorimeter cells calibration constants are estimated for each individual cell. This correction is only applied in data as such effects are not included in simulation. The calibration constants are obtained as the mean of a Gaussian fit to the  $t_0$  distribution in the region mean of the histogram plus/minus the RMS as shown in Figure 5.27 (left). The observed mean is then subtracted from the measurements in the respective cell to correct for these possible desynchronisations. The observed means of the  $t_0$  distributions are shown in Figures 5.40. Overall most of the Tile Calorimeter cells are within 200 ps around 0 ns as can be seen also from Figure 5.41. Nevertheless some regions show a constant shift, e.g. the wedge  $\phi = -0.15$  which has a constant bias of about 0.5 ns for all three layers in the extended barrel. Also some larger bias for individual cells of up to 2 ns can be observed. The impact of this calibration on the  $t_0$  distribution can be seen in Figure 5.42. The impact on the overall distribution is rather small but this is nevertheless an important calibration as it ensures that no desynchronised cells corrupt the time-of-flight measurements in the Tile Calorimeter and fake out-of-time particles.

**Run-wise correction (data)** It has been observed that the  $t_0$ -distributions of all Tile Calorimeter hits feature a run-dependent mean deviation from zero, which is attributed to a desynchronisation between the LHC clock,

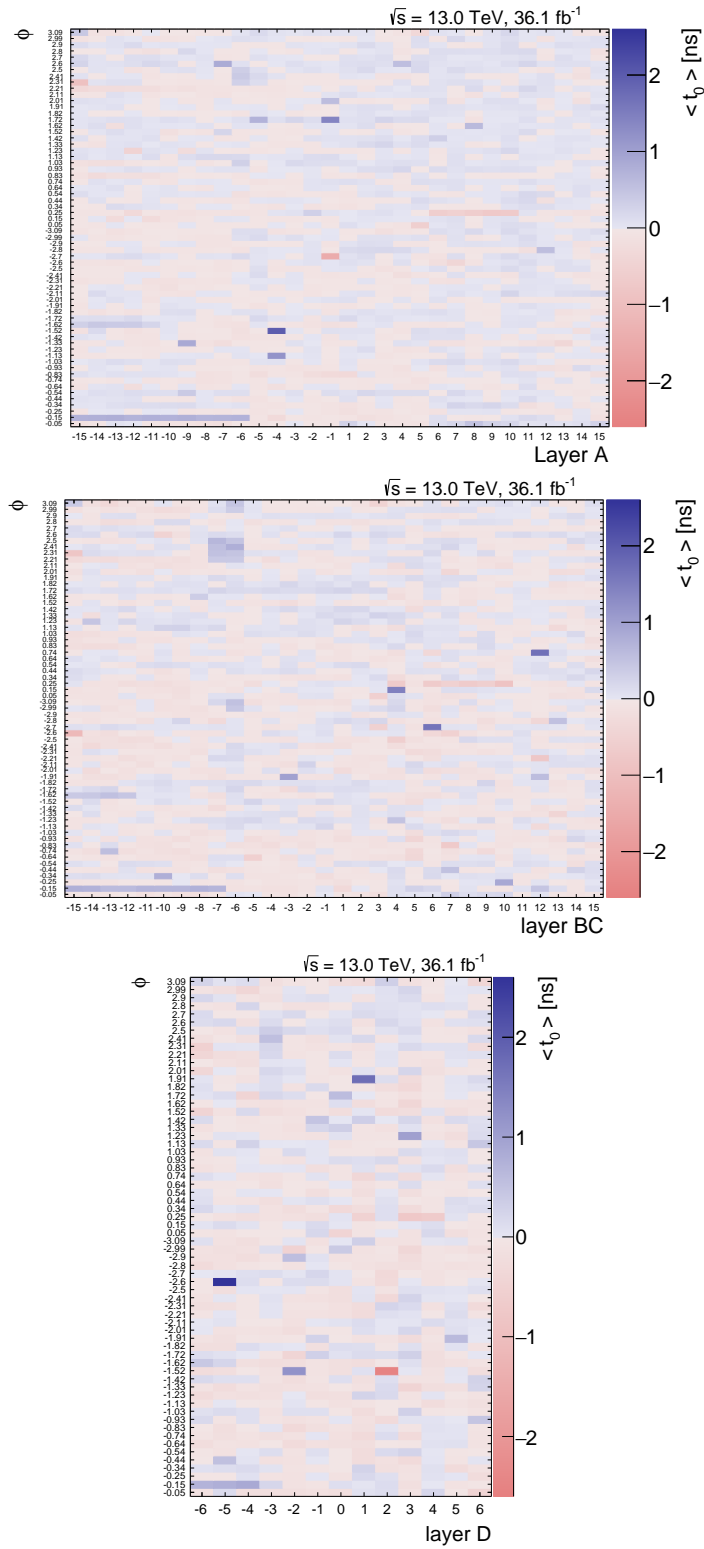


Figure 5.40: The mean of the  $t_0$  distributions per Tile Calorimeter cell. The three figures are the different Tile Calorimeter layers. The x-axis indicates the cell type in the respective layer and the y-axis the  $\phi$  wedge. Overall for each of the 4672 Tile Calorimeter cells one bin is drawn in these figures.

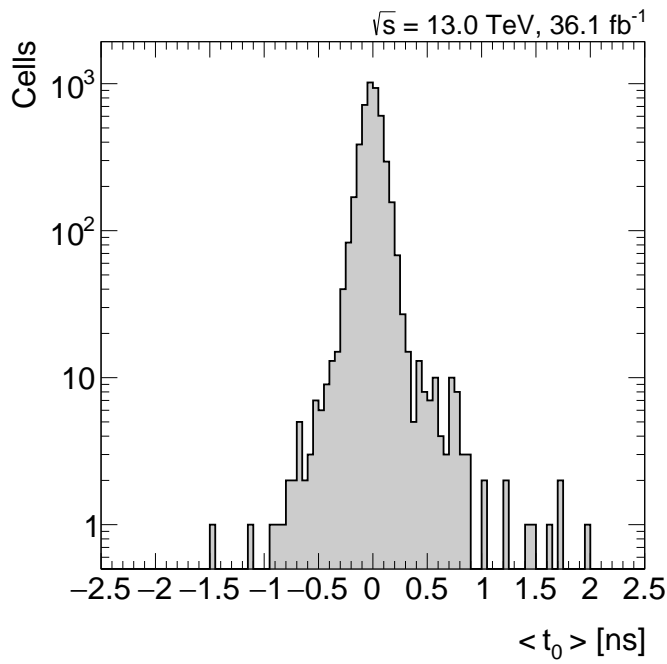


Figure 5.41: The distribution of the mean  $\langle t_0 \rangle$  values observed in the individual Tile Calorimeter cells.

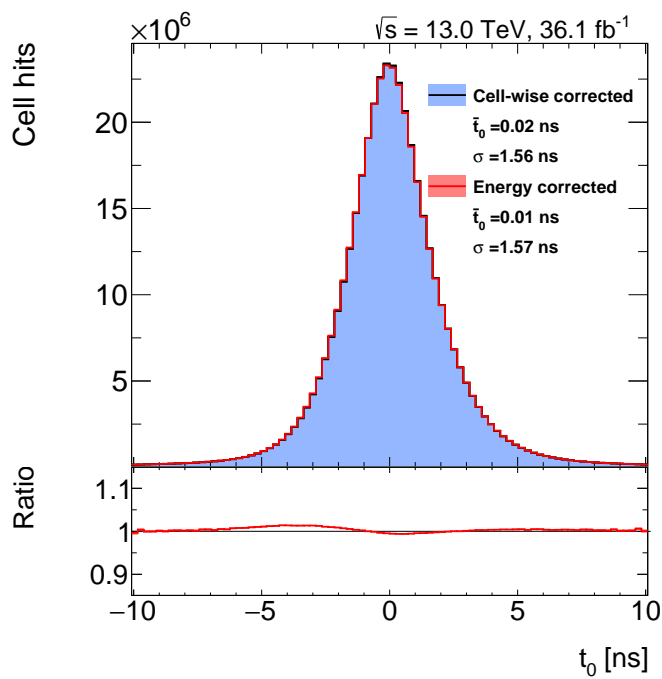


Figure 5.42: The  $t_0$  distribution with and without the additional cell-wise correction for muons in data.

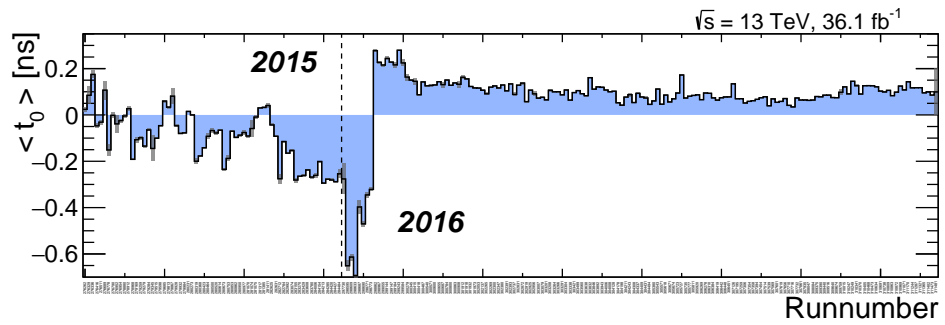


Figure 5.43: The mean of the  $t_0$  distributions per ATLAS run. The dashed line separates the runs from 2015 and 2016.

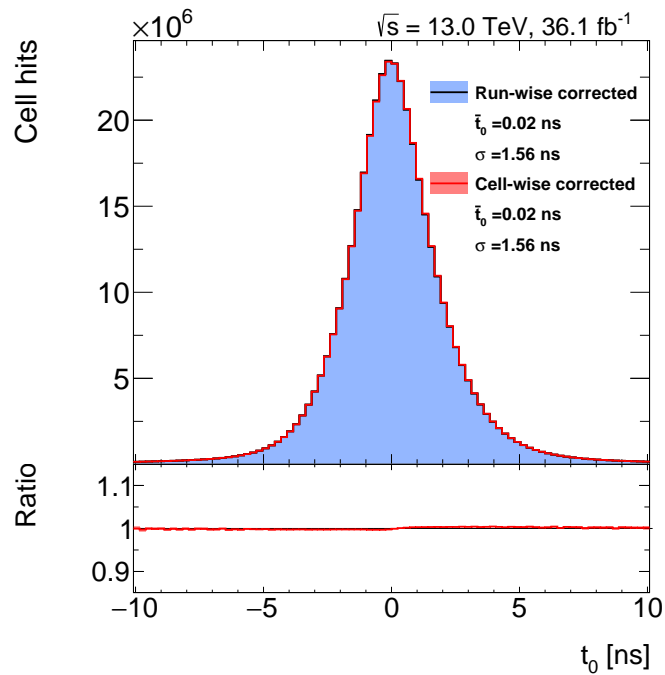


Figure 5.44: The  $t_0$  distribution with and without the additional run-wise correction for muons in data.

derived from the RF cavities at LHC Point 4, and the actual time of the collision within ATLAS, caused by the influence of weather on the fibre that transmits the signal to ATLAS. For the Tile Calorimeter a per run correction is applied based on the mean of all calorimeter time measurements. The mean is obtained similar as for the cell-wise correction from a Gaussian fit of the  $t_0$  distribution of all measurements in a given run. These calibration constants, as a function of the ATLAS run, are shown in Figure 5.43. In 2015 the fluctuations are slightly larger with about 400 ps, while in 2016 except for the first runs a very stable timing was observed with fluctuations of less than 200 ps due to an improved online monitoring of the timing. The effect of this correction on the overall timing measurement is shown in Figure 5.44. Also for the run-wise correction almost no difference in the overall distribution is observed, which is expected as the majority of the data are taken in 2016 where the timing was

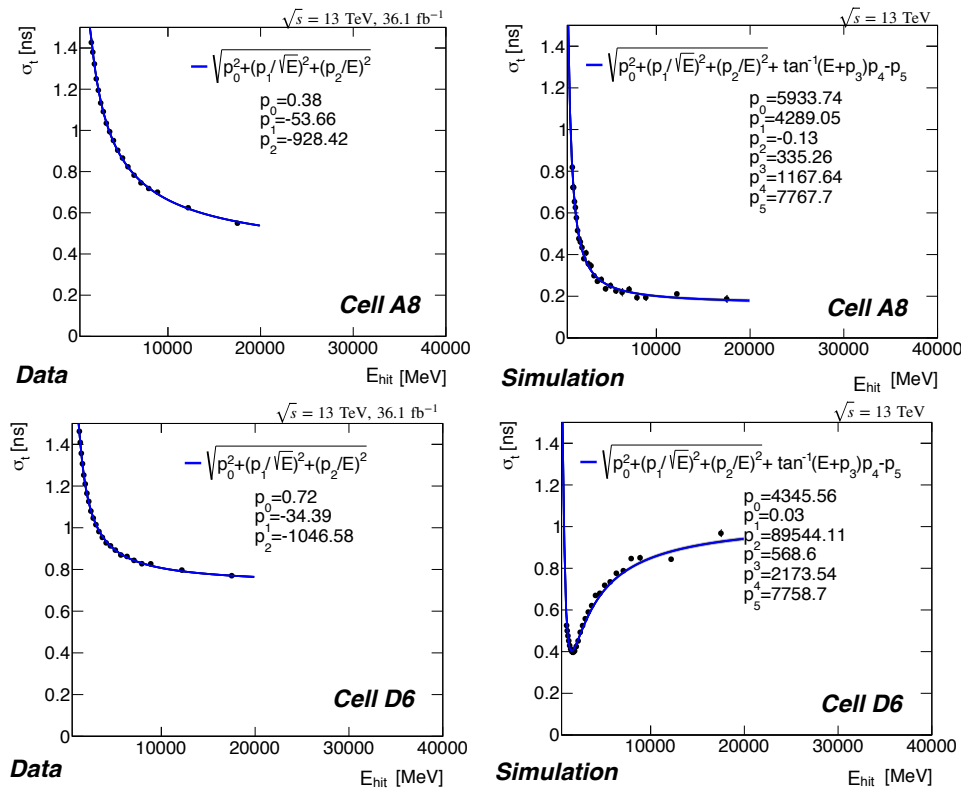


Figure 5.45: The timing resolution as function of the energy deposit  $E_{hit}$  for high-gain signals from two different  $\phi$ -projected Tile Calorimeter cells. The two sides of the detector are also combined to increase the statistics, so e.g. cell -A8 is combined with A8. The a parametrisation (blues) is superimposed on the measured values and also the fit parameters are given. The figures on the left show the resolution for muons in data, while the ones on the right the resolution for muons from simulated  $Z \rightarrow \mu\mu$  events.

very stable. Still this correction is necessary as it ensures a stable timing over the whole data taking period.

**Smearing (simulation)** It was observed that the resolutions of  $t_0$  in simulation ( $Z \rightarrow \mu\mu$ ) and data have a discrepancy in their behaviour as a function of the energy deposit as well in the resolution per cell, which can be seen from Figure 5.45. Those figures are produced similar to Figure 5.36 for the energy correction, but instead of the mean the width of the Gaussian fit per  $E_{hit}$  bin is drawn. The resolution is estimated separate for the high- and low-gain signals (high-gain  $< 20$  GeV  $<$  low-gain), but for the low-gain signals only a single energy bin (20 GeV – 40 GeV) is used due to the limited statistics. The differences between the cells are mostly due to the geometric shape. It is hence possible to increase the statistics for those figures by, besides using the  $\phi$ -projected cells, also combining both sides of the detector, so e.g. cell -A8 and A8, as they have the identical shapes. For most of the cells a similar shape of the resolution as function of  $E_{hit}$  for both data and simulation was observed but with the resolution being underestimated in simulation (Figure 5.45 upper). But in some cases an unphysical rise, as e.g. shown in Figures 5.45 (lower), was observed. This behaviour was investigated and checked for any dependencies that

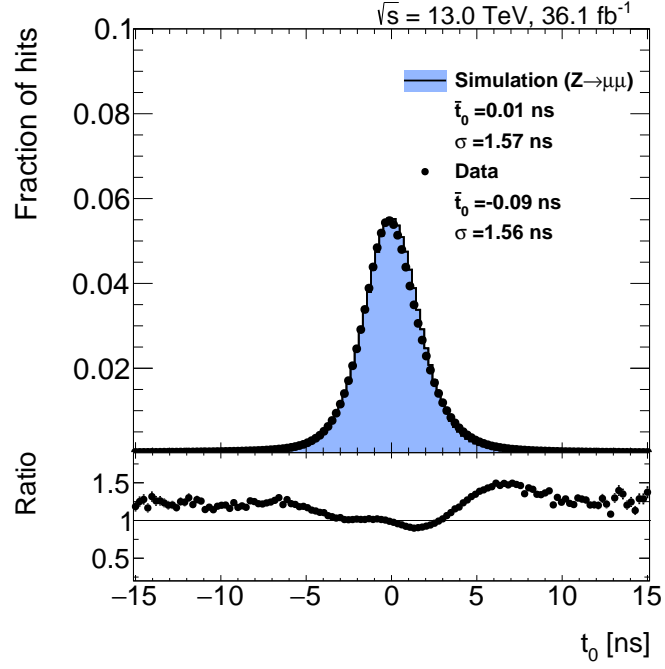


Figure 5.46: The final  $t_0$  distribution for muons in data and simulated  $Z \rightarrow \mu\mu$  events after the smearing.

could cause unexpected correlations for the analysis (e.g.  $\eta$ ,  $\phi$ ,  $p$ ). As no correlations were observed, and in particular no correlations with the observables used in the candidate selection (e.g.  $p$  and  $t_0$ ), this rise is simply washed out by applying the correct smearing as function of  $E_{hit}$ . The uncertainty is parametrised for high-gain hits in data using Equation 5.14 [134], while for simulation an additional  $\tan^{-1}$  term is added to account for the unphysical rise for higher  $E_{dep}$  (see Equation 5.16).

$$\sigma_{t_0} = \sqrt{p_0^2 + (p_1^2/\sqrt{E})^2 + (p_2^2/E)^2} \quad (5.14)$$

$$\sigma_{t_0} = \sqrt{p_0^2 + (p_1^2/\sqrt{E})^2 + (p_2^2/E)^2 + \tan^{-1}(E + p_3)p_4 - p_5} \quad (5.15)$$

Equation 5.14 consists of a constant term, a statistical term  $\sqrt{E}$  and a noise term  $E$ . For low-gain signals only one bin is used and the resolution is hence only estimated from the value of this single bin. The smeared  $t_{0\ smear}$  in simulation is then estimated with

$$t_{0\ smear} = t_0 + \text{Random.Gaus} \left( 0, \sqrt{\sigma_{data}^2(E_{hit}) - \sigma_{sim}^2(E_{hit})} \right). \quad (5.16)$$

It was observed that for some very rare cases the resolution in simulation is slightly worse than in data. As this is rare and also the differences are small no correction is applied for those cases. The final  $t_0$  distribution

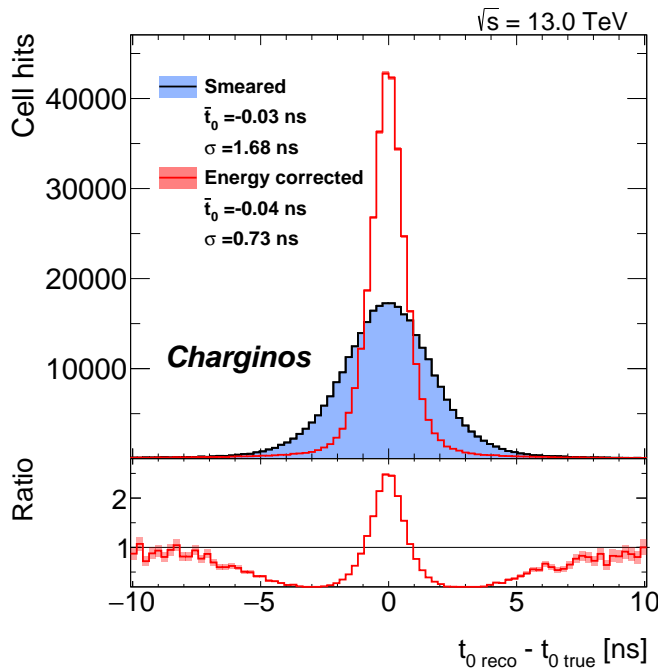


Figure 5.47: The final  $t_0$  distribution in simulated events of direct chargino production after the smearing. A combined sample of charginos with masses between 200 GeV and 1500 GeV is used.

after the smearing for simulation and data after the  $Z \rightarrow \mu\mu$  pre-selection is shown in Figure 5.48. A good agreement in the core of the distribution is observed while in the tails simulation underestimates the fraction of outliers by about 20%. As in this analysis simulation is only used for the signal samples and not for the background only a good agreement in the core of the distribution is relevant. The reason is that final signal distribution is the timing resolution folded with the truth spectrum. So to have any effect on the signal efficiency the HCLLP candidate has to be close to the  $\beta$  requirement for the signal region and in the tails of the resolution. The effect on the signal efficiency was studied by folding the data and the simulation resolution with the truth spectrum and evaluating the difference in the fraction of candidates surviving the  $\beta$  requirements used in the analysis. In any case the effect was found to be less than 1%. Compared to previous analyses [101, 103] the agreement between simulation and data is significantly improved as for the first time both energy- and cell-wise effects are simultaneously taken into account for the smearing. The final  $t_0$  resolution for charginos is shown in Figure 5.47. The resolution for charginos after the smearing is slightly worse than the resolution for muons. This is expected as the bulk of the charginos samples has rather low masses and as argued for the  $dE/dx$  measurement they are close to the minimum of the ionisation energy loss. As muons are already in the relativistic rise of the Bethe-Bloch formula they are expected to

have a slightly higher energy loss in the Tile Calorimeter and accordingly a better timing resolution.

**Uncertainty and pull correction** The uncertainty of the  $t_0$  measurement in data that was used to estimate the smearing is also used to calculate the uncertainty of the  $\beta$  measurement. For each Tile Calorimeter hit an uncertainty depending on the cell and the energy deposit can be evaluated. As the uncertainty on the distance of the measurement is almost negligible, the uncertainty on the inverse  $\beta$  measurement can be calculated with

$$\sigma_{\beta^{-1}} = \frac{c\sigma_{t_0}(\text{cell}, E_{hit})}{d}. \quad (5.17)$$

To validate and correct the estimated uncertainty of the single hits the pull distributions are considered separate for data and simulation. The pull is defined as

$$\text{pull} = \frac{1/\beta_{reco} - 1/\beta_{true}}{\sigma_{\beta^{-1}}}, \quad (5.18)$$

with  $\beta_{true} = 1$  for muons traveling basically with the speed-of-light, if taking into account the timing resolution achieved with the Tile Calorimeter. For a perfect  $\beta$  and  $\sigma_{\beta}$  measurement the pull distribution would match a Gaussian with a width of one and be centered around zero. The pull distributions for data and simulation are shown in Figure 5.48. For data the distribution is in almost perfect agreement with a unit Gaussian, the width is only off by 1.6%. As the 1.6% are statistically significant they are taken into account as constant scaling of the uncertainty. For simulation a slightly larger effect of about 5% is observed and also used as scaling on the uncertainty. Both pull corrections are significantly smaller than for previous analyses (11% [101]) and hence support that the estimation of the uncertainties is improved.

**Final distributions** The single hit  $t_0$  and  $\beta$  resolution for the Tile Calorimeter are shown in Figures 5.49. The resolution per cell is obtained as the width of a Gaussian fitted to the  $t_0$  or  $\beta$  distributions, respectively. The Figures also illustrate the shape and relative size of the cells. For the  $t_0$  the dominant factor is the size or more precise the path length of the tracks in the cell. The length of the track in the cell is roughly proportional to the energy deposit for minimum ionising particle. And as the  $t_0$  resolution is dependent on the energy deposit it is expected that the resolution is worse for smaller cells. The worst timing resolution is found for cells  $\pm A13$ , which are not the smallest cells. The reason for the resolution

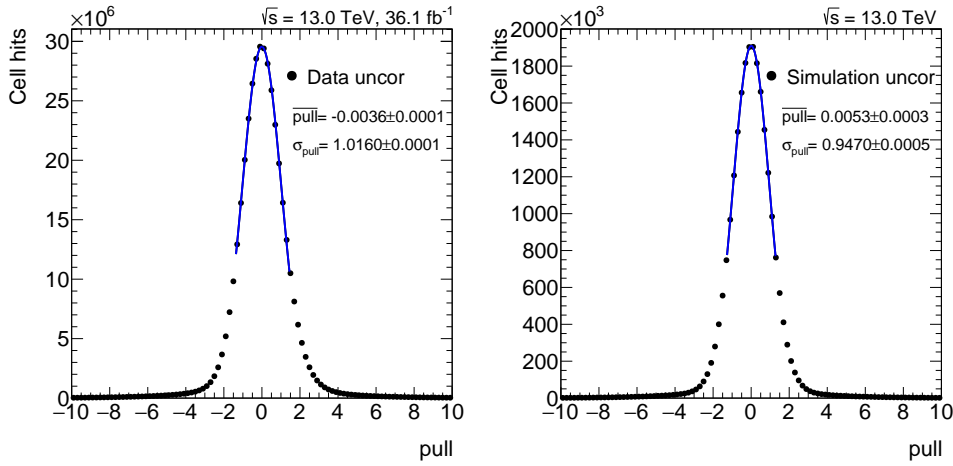


Figure 5.48: Pull distributions for the individual timing measurements with the Tile Calorimeter. The distributions are fitted with a Gaussian in the range mean plus minus one RMS. The left distribution shows data while the right simulated  $Z \rightarrow \mu\mu$  events.

being worse there is, that due to the angle to the IP, many particles are traversing the cell only with a small path length in the cell. The best timing resolution is indeed for the cells with the largest path lengths, which are the stacked cells in sampling 13 that are oriented along the expected particle paths and for the largest cells  $\pm D6$ . For the  $\beta$  resolution the dependence of the resolution on the distance of flight (Equation 5.7) can clearly be seen, as the resolution follows the distance circles. The best  $\beta$  resolution is hence achieved with the outermost cells in the extended barrel, cells  $\pm D6$ .

The final  $t_0$  distribution after all previously discussed corrections applied compared to the uncorrected distribution is shown in Figure 5.50. The main contribution to the improved resolution comes from the  $\eta$  dependent correction but nevertheless also the other corrections are needed and important to achieve a trustable timing measurement in the Tile Calorimeter.

The combined  $\beta_{\text{TILE}}$  is estimated using Equation 5.6 from the single  $\beta$  measurements as a weighted average, using the inverse of the uncertainties as weights. Two further important variables that can be estimated for the combined  $\beta_{\text{TILE}}$  are the combined uncertainty (Equation 5.7) and the consistency between the individual measurements. The consistency of  $N_{\text{hits}}$  measurements is defined as the probability of a  $\chi^2$  for  $\text{NdoF} = N_{\text{hits}} - 1$  degrees of freedom, with

$$\chi^2 = \sum_{i=1}^{N_{\text{hits}}} \frac{(\beta_{\text{comb}}^{-1} - \beta_i^{-1})^2}{\sigma_{\beta_i^{-1}}^2}. \quad (5.19)$$

Both the uncertainty of the combined  $\beta_{\text{TILE}}$  and the consistency between the measurements are important quantities to ensure a good quality of

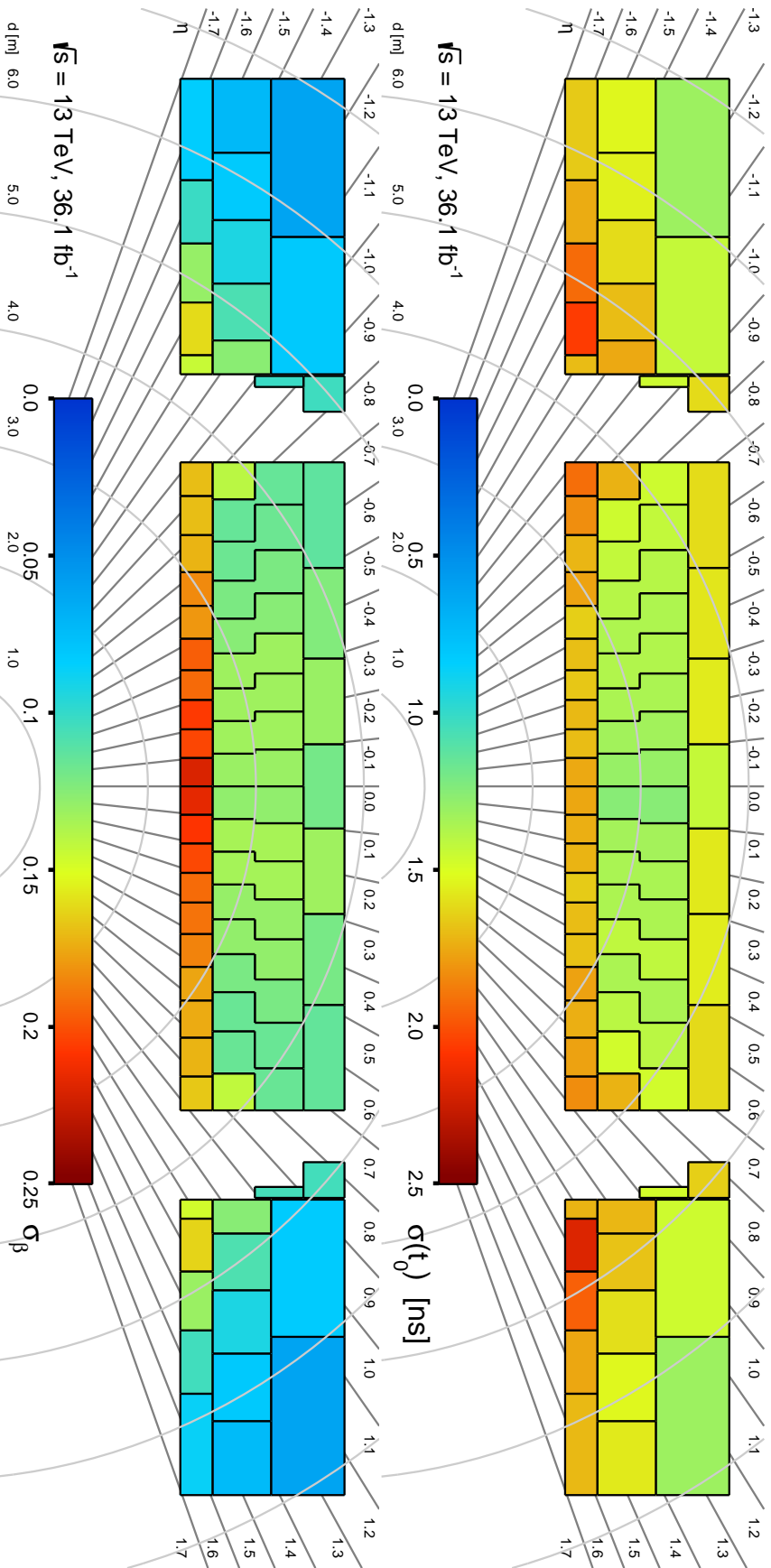


Figure 5.49: The timing (upper) and  $\beta$  (lower) resolution for each Tile Calorimeter cell. The form of the boxes illustrates the shape of the respective Tile Calorimeter cells and the grey lines indicate the different  $\eta$  directions. With the grey circles the distance to the IP is given. The  $t_0$  resolution mainly depends on the size of the cells and hence the path length in the cell, while the  $\beta$  resolution is largely dependent on the distance to the IP.

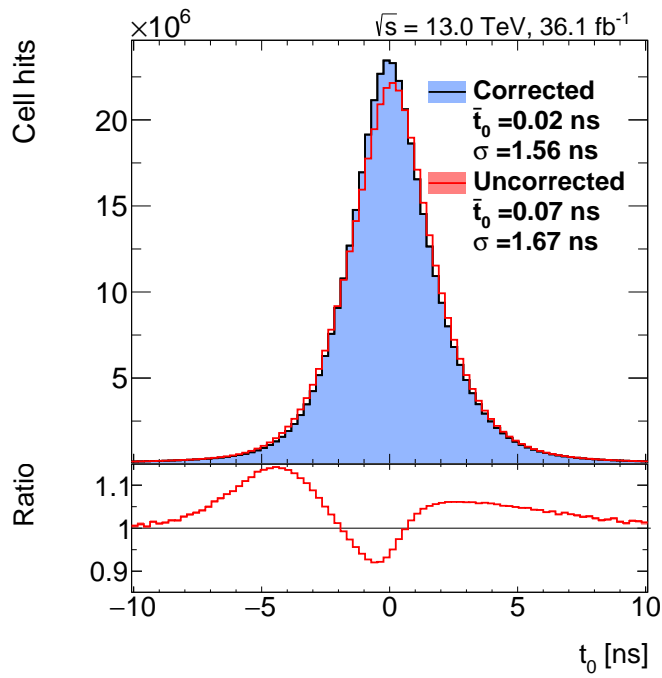


Figure 5.50: The final  $t_0$  distribution after all correction applied compared to the uncorrected  $t_0$  for muon in data.

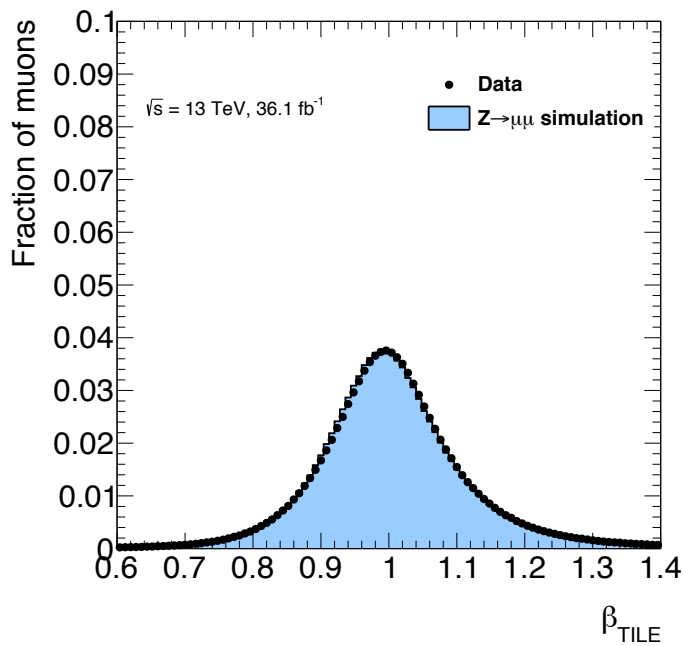


Figure 5.51: The combined  $\beta_{\text{TILE}}$  distribution measured with muons in a  $Z \rightarrow \mu\mu$  selection in data and simulated  $Z \rightarrow \mu\mu$  events. As the resolution has some  $\eta$  dependence due to the different traversed detector systems an  $\eta$  re-weighting is applied to this plot to ensure the same  $\eta$  composition in data and simulation. [5]

the measurement and can be used for the pre-selection of HCLLP candidates.

The final  $\beta_{\text{TILE}}$  distribution for data and simulation is shown in Figure 5.51. A good agreement between data and simulation is observed, which is due to the improved estimation of the uncertainties. The resolution achieved for the combined  $\beta_{\text{TILE}}$  is 0.068. This is a 14% improvement to the resolution achieved in the Run-1 analysis ( $\sigma_{\beta} = 0.079[97]$ ) and 6% better than the resolution achieved for the first Run-2 analysis ( $\sigma_{\beta} = 0.072$ ), which was also part of my work. This analysis hence achieved the best  $\beta_{\text{TILE}}$  resolution for muons in ATLAS so far.

### Timing validation with muons from satellite–satellite collisions

The LHC uses a 400 MHz RF system which means that buckets exist separated by 2.5 ns. In 2015 and 2016 the main bunches are separated by 25 ns but due to imperfections in the injection process also side buckets get filled, from now on referred to as satellite bunches. As the SPS is driven by a 200 MHz RF system [135] only satellites separated by multiples of 5 ns get filled with significant populations, where the  $\pm 5$  ns satellites are the most dominant ones. For the latter the population is suppressed by roughly  $\mathcal{O}(10^{-3})$ , which means that the collision rate of ( $\pm 5$  ns) satellite–satellite bunches is suppressed by  $\mathcal{O}(10^{-6})$ . The suppression of the population of the satellites can be seen in Figure 5.52. This figure shows measurements of the bunch populations in early LHC runs (2011) using a longitudinal density monitoring. Those measurements were performed with the LHC running at a 50 ns bunch spacing. But as migrations of the following bunch crossing to the 5 ns satellites are rather unlikely they can nevertheless be used to give at least a rough estimate of the expected suppression of satellite–satellite collisions with respect to central collisions.

The particles produced in those satellite–satellite collisions can be used, if identified, to validate the performance of the detectors for real out-of-time signals. It was shown that the LAr calorimeter is capable of identifying electrons from satellite–satellite collisions [136]. For the validation of the timing measurements for minimum ionising particles with the Tile Calorimeter muons have to be identified to originate from satellite–satellite collisions, which has two major difficulties. Muons, as they are minimum ionising, release significantly less energy in the Tile Calorimeter cells than electrons in the LAr calorimeter. As the timing resolution is strongly energy dependent, as can be seen from Figures 5.45, a worse

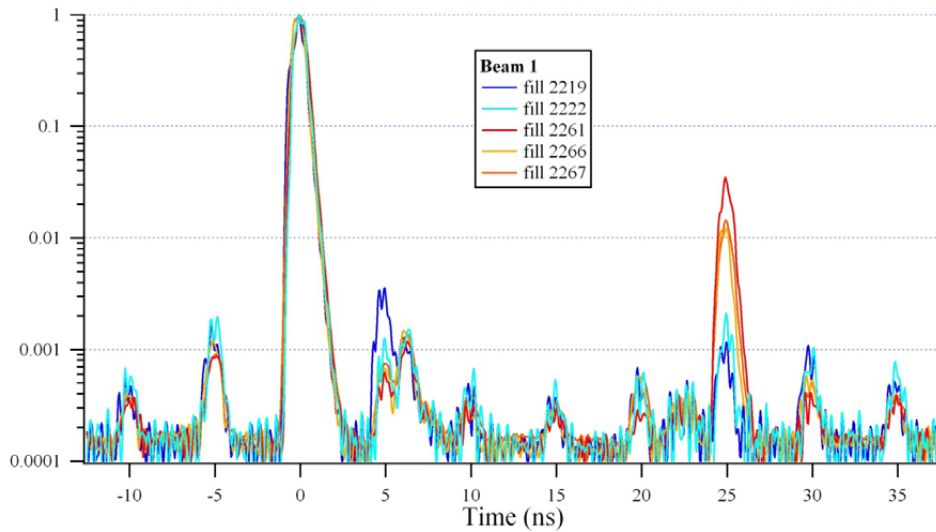


Figure 5.52: Measurements of the bunch populations for some LHC  $pp$  fills using a longitudinal density monitoring. This scans were performed on beam 1 in 2011. Fills 2219 and 2222 used the normal bunch scheme and had only spontaneously occurring satellites, while fills 2261, 2266 and 2267 used a modified scheme with enhanced satellites at 25 ns. [137]

timing resolution is expected. The particles originating from satellite-satellite collisions are, similar as the particles from the central collisions, expected to be produced with almost the speed-of-light. This means that there is no gain in resolution by being further away from the production vertex as for the velocity measurements of slow moving particles. So the slightly worse timing resolution in the Tile Calorimeter compared to the LAr calorimeter is a further complication. The overall timing resolution for the single hits is shown in Figure 5.53. The tails at  $\pm 5$  ns are only suppressed by  $\mathcal{O}(10^{-2})$  which completely hides all potential signals from muons produced in satellite-satellite collisions which are expected to be suppressed compared to the central collisions by  $\mathcal{O}(10^{-6})$ . This means that the intrinsic timing resolution of single ATLAS Tile Calorimeter measurements is not sufficient to resolve satellite-satellite collisions even after all previously mentioned calibrations.

To identify muons from satellite-satellite collisions a new method, combining the individual timing measurements to a combined timing per muon and afterwards rejecting candidates with bad resolution or timing measurements that are not consistent with each other, was developed. The combined  $t_0$  is calculated as

$$t_{0, \text{comb}} = \frac{\sum_{i=1}^N t_{0,i} / \sigma_{t_{0,i}}^2}{\sum_{i=1}^N 1 / \sigma_{t_{0,i}}^2} \quad (5.20)$$

from the single measurements and the estimated resolution per hit. For this combination it is assumed that the muons are produced late and travel almost with the speed-of-light, which is the case for muons with

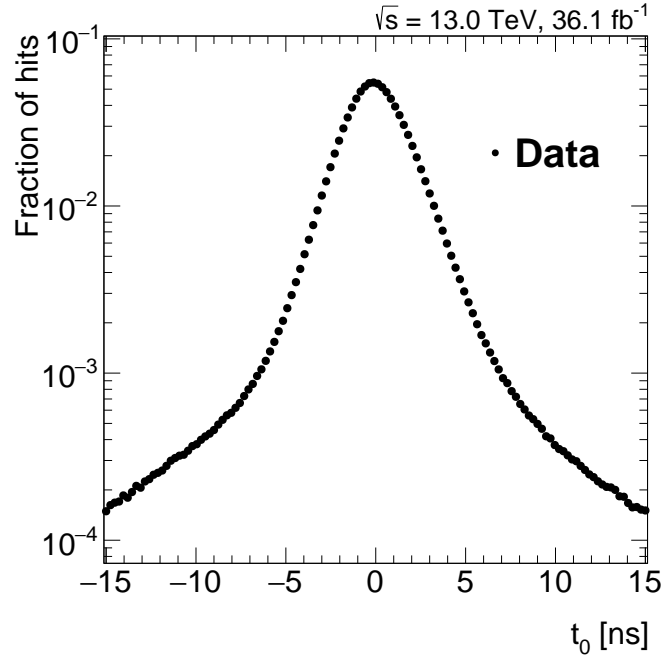


Figure 5.53: The timing resolution for muons in data measured with the ATLAS Tile Calorimeter. The tails at  $\pm 5$  ns are only suppressed by  $\mathcal{O}(10^{-2})$  which completely hides all potential signals from muons produced in satellite-satellite collisions which are expected to be suppressed compared to the central collisions by  $\mathcal{O}(10^{-6})$ .

a minimum  $p_T$  of 25 GeV. The combined uncertainty and the  $\chi^2$  between the measurements is obtained using

$$\sigma_{t_0, \text{comb}}^2 = \frac{1}{\sum_{i=1}^N 1/\sigma_{t_0, i}^2} \quad \text{and} \quad \chi^2 = \sum_{i=1}^N \frac{(t_{0, \text{comb}} - t_{0, i})^2}{\sigma_{t_0, i}^2}, \quad (5.21)$$

respectively. The 2D-plane of  $\sigma_{t_0, \text{comb}}$  and the probability  $P(\chi^2, N_{\text{hits}} - 1)$  is scanned to find the optimal combination of requirements to suppress the tails of the resolution sufficiently to resolve the signals from satellite-satellite collisions. As optimal combination  $\sigma_{t_0, \text{comb}} < 0.55$  ns and  $P(\chi^2, N_{\text{hits}} - 1) > 0.70$  was found. The corresponding  $t_0$  distribution is shown in Figure 5.54. Besides the central peak to side peaks at  $t_0 = -4.91 \pm 0.09$  ns and  $t_0 = 5.13 \pm 0.07$  ns are visible. To validate if those side peaks really originate from muons produced in satellite-satellite collisions potential correlations in particular with specific detector regions were checked. As no unexpected correlations were found those side peaks are assigned to satellite-satellite collisions. The mean position of the side peaks is in good agreement with the expectation ( $\pm 5$  ns) taken into account the uncertainties on the mean. This measurement represents the first validation of the behaviour of the ATLAS Tile Calorimeter for out-of-time signals in real collision data. This cross-check is in particular important, as for the LAr calorimeter some disagreements between the timing at the satellite-

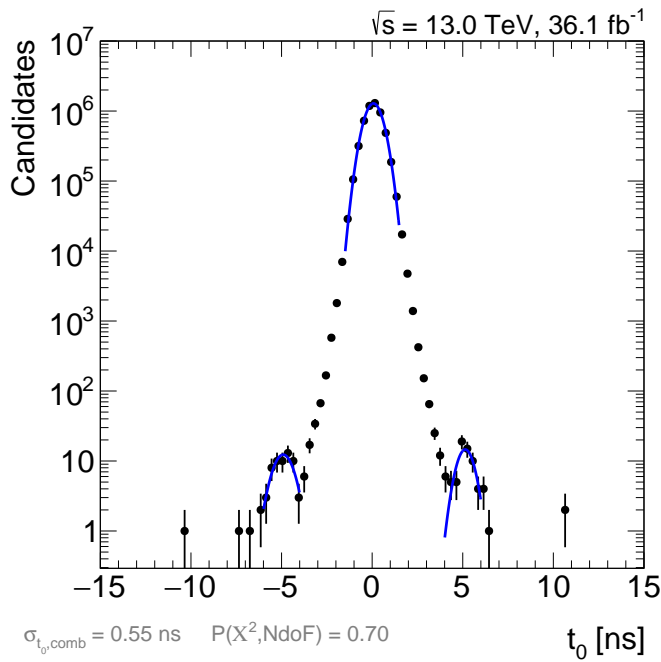


Figure 5.54: The  $t_0$  distribution for muons requiring  $\sigma_{t_0,comb} < 0.55$  ns and  $P(\chi^2, N_{dof}) > 0.70$ . Besides the central peak ( $t_{0,mean} = 0.07 \pm 0.01$  ns,  $\sigma_{t_0} = 0.49 \pm 0.01$  ns) to side peaks with ( $t_{0,mean} = -4.91 \pm 0.09$  ns,  $\sigma_{t_0} = 0.57 \pm 0.08$  ns) and ( $t_{0,mean} = 5.13 \pm 0.07$  ns,  $\sigma_{t_0} = 0.47 \pm 0.12$  ns) were observed.

satellite peaks and the expectation were observed [136]. Besides the mean value also other observables of the side peaks can be compared to the expectations. So far no dependence of the timing resolution on the timing itself was considered or observed. To validate this the width for the side peaks can be compared to the width of the central peak. Also the resolution agrees within the uncertainties, between the side-peaks and the central peak, and hence is in support of an equal timing resolution for out-of-time signals. Furthermore the size of the side peaks can be compared to the central peak to get a rough estimate on the population of the satellite bunches. For the observed side peaks a suppression of  $(1.2 \pm 0.1) \times 10^{-5}$  for both the left and the right peak are observed which is slightly above what was expected from the longitudinal density monitoring measurement from 2011 [137]. But as in particular those scans were done with a bunch spacing of 50 ns, while the data in this analysis were taken with a bunch spacing of 25 ns a slightly higher bunch population for the satellite is expected, as the subsequent central bunches are closer. The suppression is in good agreement with the suppression  $\mathcal{O}(10^{-5})$  obtained for electrons from satellite-satellite collisions with the LAr calorimeter [136].

Overall this study represents the first observation of particles from satellite-satellite collisions with the ATLAS Tile Calorimeter. This is in particular important to validate the trustability of the timing measurements with the Tile Calorimeter for out-of-time signals. With more data it might be

possible to also resolve the satellite peaks at  $\pm 10$  ns to validate the timing even for longer delays. Furthermore it should be possible to tag the muons identified as originating from satellite–satellite collisions to test the out-of-time behaviour in other sub-detectors. This might be in particular interesting to test the out-of-time behaviour of muons with the LAr calorimeter to check whether it is possible to include it in the  $\beta$  measurements for HCLLPs.

### 5.5.3 Time-of-flight Muon Spectrometer

Besides the Tile Calorimeter also the MDT's and RPC's are used for time-of-flight measurements to identify HCLLPs. This section gives a short summary of the calibration of those systems but with a focus on an additional correction that has to be applied on the RPC timing in simulation on top of the corrections described in Reference [128]. Similar as for the Tile Calorimeter the measured observable of the timing measurements is  $t_0$ . The timing resolution for muons with the RPC's (1.8 ns) and MDT's (3.0 ns) are worse than the resolution achieved with the Tile Calorimeter (1.56 ns), whereas the  $\beta$  resolution is significantly better with the MS systems due to the additional path length and the larger number of measurements. For the RPC's twelve hits and for the MDT's about 22 hits in the barrel and 15 hits in the endcaps per muon are expected. Similar pre-selections as for the Tile Calorimeter calibration are applied on the data used for calibration, though starting with SlowMuon objects that are matched to muons reconstructed with a standard algorithm. For the calibrations the muon selection is used while for the final comparison between data and simulation the  $Z \rightarrow \mu\mu$  selection is used. Separate calibrations are performed for the MDT's and the RPC's, while for the RPC's also different corrections are estimated for  $\eta$ - and  $\phi$ -strips as they are read out by individual electronics and optical links.

The first calibration step for the MDT's is a drift-tube calibration. The mean of the  $t_0$  distribution for each of the 323 799 drift tubes is estimated and used as calibration constant. This ensures a stable timing measurement for the MDT's over the full detector range. The second calibration step, similar as for the Tile Calorimeter, is run-wise correction which ensures the stability of the timing measurement over time. The mean of the  $t_0$  for all MDT hits in a given ATLAS run is obtained from Gaussian fits and used as calibration constant. The mean of the  $t_0$  distribution as function of the ATLAS-run is shown in Figure 5.55. Compared to the run-wise correction in the Tile Calorimeter (Figure 5.43) a larger variation over time

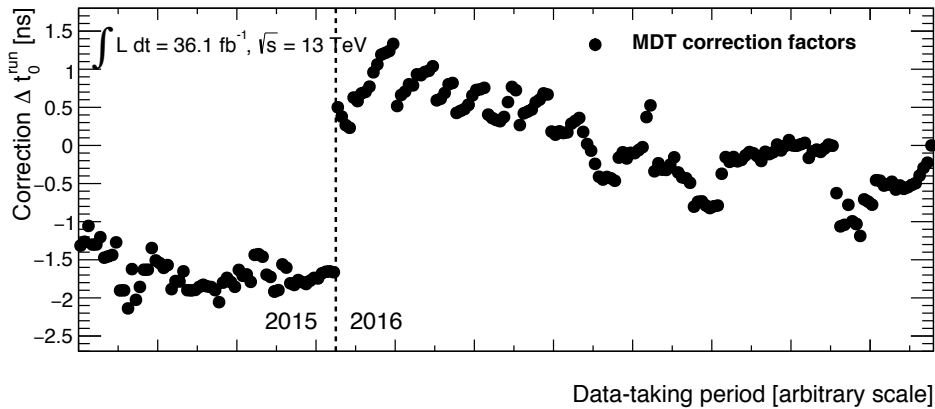


Figure 5.55: The mean of the  $t_0$  distributions measured with the MDT's per ATLAS run. The dashed line separates the runs from 2015 and 2016. [128]

is observed and in particular a the step between 2015 and 2016 is significantly larger. The uncertainties of the timing measurements with the MDT's are obtained as the width of the  $t_0$  distribution per tube. The final calibration step on data is a pull correction on the resolution of the single  $\beta$  measurements. For the MDT's a pull width of 0.92 is obtained and used as scaling on the uncertainty of the single measurements. To adjust the timing resolution in simulation to the resolution observed in data the resolution per chamber is estimated and used for the smearing due to the limited statistics in simulation. Unfortunately for a large fraction of chambers the resolution in simulation is larger than in data. For those cases no smearing is applicable to adjust the resolution. To treat this first a sharpening with a constant scaling of the resolution is applied and in a second step a random smearing on the sharpened distribution is used to match the distribution observed in data. The final distribution of the combined  $\beta$  measured in the MDT's for muons passing a  $Z \rightarrow \mu\mu$  selection in data and simulation is shown in Figure 5.56. A good agreement between data and simulation is achieved.

For RPC's first a coarse calibration over time is applied that estimates mean timing offset for periods with a constant global timing setting for the RPC's. The mean offset is hence estimated for six data taking periods and used as calibration constant. The next calibration is a detector-element-wise calibration, which is ensuring a stable timing measurement over the full  $\eta$  range. For the RPC's separate calibration constants are estimated for each of the 113 478  $\eta$ -strips and 248 784  $\phi$ -strips. This is followed by a fine time-dependent calibration, which is obtaining calibration constants per ATLAS run similar to MDT's and Tile Calorimeter but separate for  $\eta$ - and  $\phi$ -strips. The run-wise offset of the timing for the

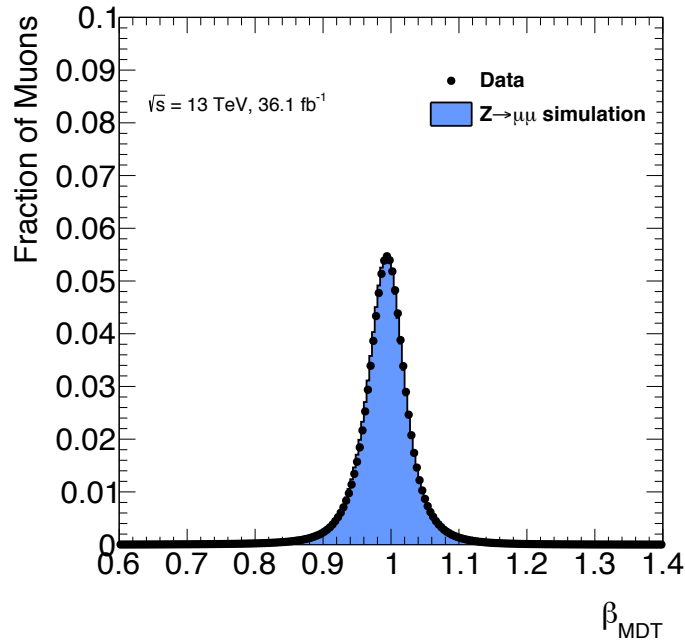


Figure 5.56: The combined  $\beta$  distribution for MDT's in data and simulation for muons passing a  $Z \rightarrow \mu\mu$  selection.

RPC's is shown in Figure 5.57. The distribution of the mean offsets of the timing resolution is similar to what is observed for the Tile Calorimeter (Figure 5.43) and hence shows the overall timing mis-alignment between the ATLAS and LHC clocks, while for the MDT's (Figure 5.55) the desynchronisation of the MDT's itself exceed the overall timing mis-alignment. For the RPC's the timing uncertainty is estimated from the width of the timing distribution obtained for the individual strips. As last calibration step in data also for the RPC's a pull correction on the individual hit  $\sigma_\beta$  is applied to adjust the timing resolution. For  $\eta$ -strips 0.988 and for  $\phi$ -strips 0.978 as width of the pull distribution are obtained and used as scaling

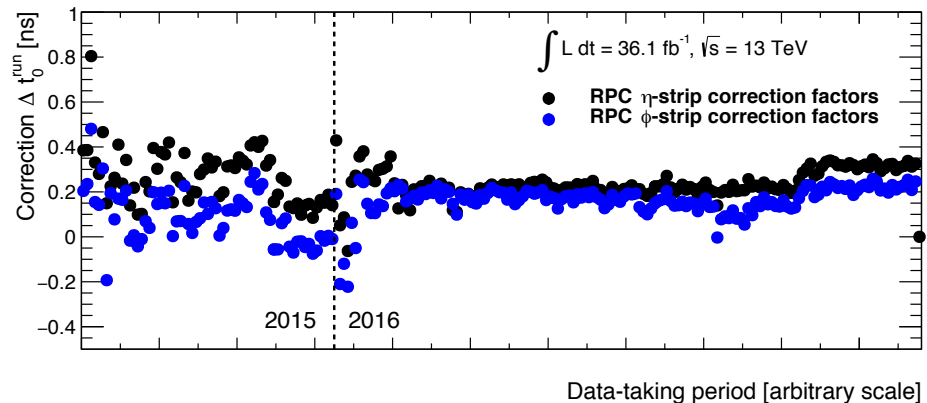


Figure 5.57: The mean of the  $t_0$  distributions measured with the RPC's per ATLAS run. The calibration constants are estimated separate for  $\eta$  (black) and  $\phi$ -strips (blue). The dashed line separates the runs from 2015 and 2016. [128]

on the estimated uncertainties. In simulation unexpected features for the RPC timing are found as separate peaks of the estimated timing resolution per strip, which are not observed in data. The following procedure is applied: For strips with a resolution smaller than 1.9 ns no correction is applied, for strips with a resolution  $1.9 \text{ ns} < \sigma_{sim} \leq 2.7 \text{ ns}$  the timing resolution is sharpened, and strips with an even worse resolution are masked and not used for the  $\beta$  measurement.

Finally it was observed that the combined RPC resolution as function of  $\eta$  does not match between data and simulation. To account for this an additional correction is applied on top of the previously mentioned adjustments for simulation. Also for this case both resolutions that are larger in data than in simulation and vice versa are observed. A new method based on a smearing/unfolding approach was developed as part of this work, to be able to treat both cases similarly. First the response matrix is estimated using the sharper of the distributions of data or simulation and smearing it to the broader. As smearing of the underlying histograms would be on the one hand time consuming due to the high number of samplings and on the other hand largely dominated by statistical fluctuations, instead ideal Gaussian functions are used to calculate the responses with the resolutions estimated from the histograms. Each bin is filled accordingly to

$$p(\beta_s, \beta_l) = \text{Gaus}(\beta_s, \text{mean}_s, \sigma_s) \times \text{Gaus}(\beta_l, \beta_s, \sqrt{\sigma_l^2 - \sigma_s^2}), \quad (5.22)$$

where the sub indices label the values of the smaller (s) or larger (l) Gaussian. The response matrix, shown in Figure 5.58 (left), gives the migration probabilities between bins due the smearing from the small to the larger Gaussian. The projection to the  $y$ -axis gives an ideal Gaussian with the larger width and the projection to the  $x$ -axis the ideal Gaussian with the smaller width. Using the ideal Gaussian and the response matrix the ROOUnfold package [138] can be used to estimate the unfolding matrix. The method applied is based on the Bayesian unfolding [139], which is a matrix inversion based on the repeated application of Bayes' theorem. The inverted matrix is shown in Figure 5.58 (right) using the response matrix (left) and the larger ideal Gaussian as input. Those matrices can be used to smear or unfold a distribution and are applicable on single measurements. For a given  $\beta$  value, e.g. of a candidate in simulation, the  $x$ -slice corresponding to the given  $\beta$  value is projected on the  $y$ -axis. From this projection the corrected  $\beta$  is sampled. The procedure is the same for smearing or unfolding which is one major benefit of this method, only

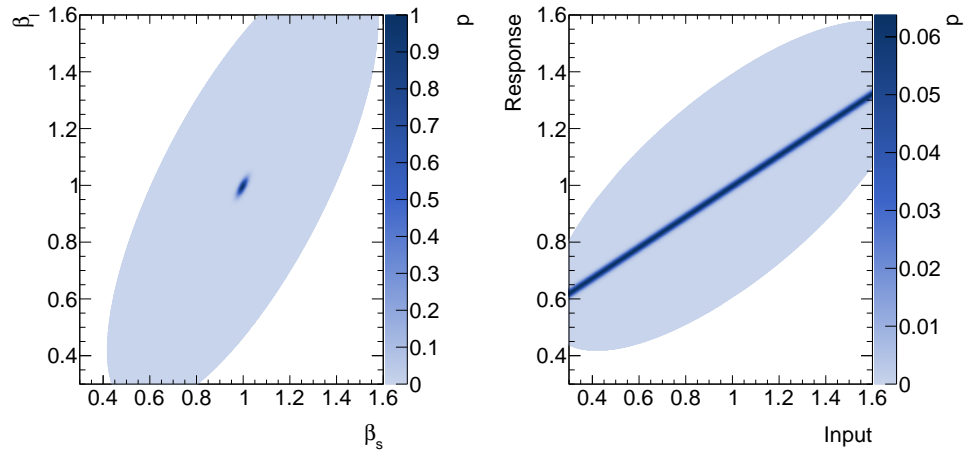


Figure 5.58: The response matrix for a smearing from a small to a larger Gaussian (left). The inverted matrix that can be used for an unfolding (right). For the smaller Gaussian a width of 0.015 is used while for the larger 0.0204.

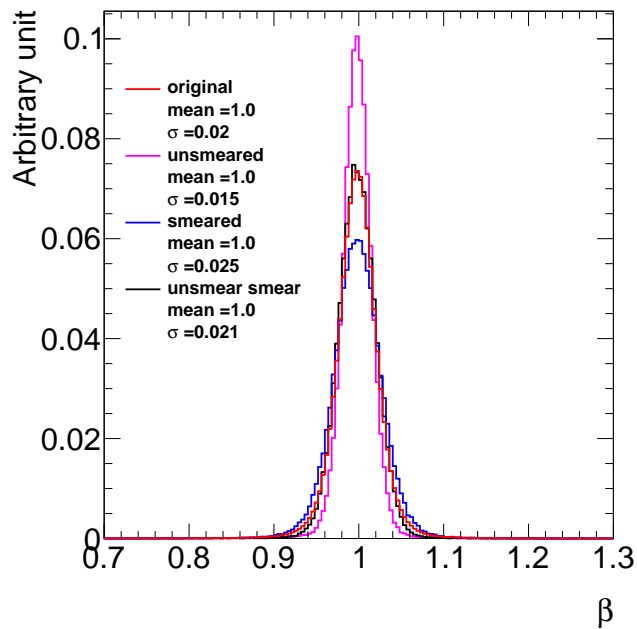


Figure 5.59: The results of the smearing/unfolding using the matrix method described in the text on a realistic  $\beta$  distribution. Also the closure with first unfolding and afterwards smearing applied is shown. The used smearing and unfolding matrices are shown in Figure 5.58.

the correct matrix has to be stored and used. The effect of a smearing and unfolding and also the closure for applying both after each other on a realistic  $\beta$  distribution are shown in Figure 5.59. It can be seen that the smeared and unfolded distributions have a width that is in agreement with the input we chose (0.015 for the smaller Gaussian). And also the closure seems to be in reasonable agreement with the input distribution, but with some deficits in the tails. This is mainly due to the choice of ideal Gaussians as input for this method. But as mentioned before, the agreement between data and simulation is mostly important in the core region of the distributions, so no significant problems due to a disagreement in the tails are expected.

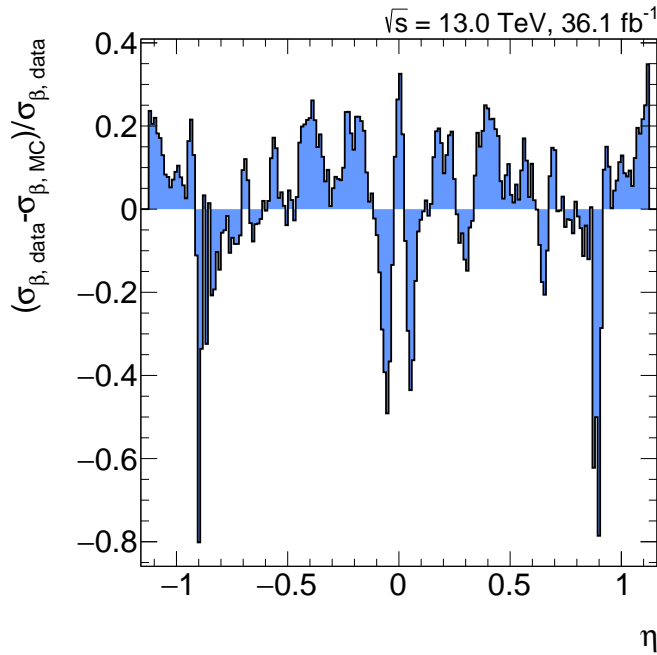


Figure 5.60: The relative difference between the  $\beta$  resolution observed in data and simulation along  $\eta$ .

The disagreement of the  $\beta$ -resolution along  $\eta$  between data and simulation observed for the RPC's is shown in Figure 5.60. For each  $\eta$  slice the resolutions observed in data and simulation are used as input for the above described method to obtain a correction matrix. Those correction matrices are then stored and depending on the  $\eta$  of the candidate applied to correct its  $\beta$ .

The combined  $\beta$  distribution measured for the RPC's measured with muons passing a  $Z \rightarrow \mu\mu$  selection in data and simulation is shown in Figure 5.61. A reasonable agreement between data and simulation is observed and all residual effects are covered by systematic uncertainties.

#### 5.5.4 Combination of time-of-flight measurements

The  $\beta$  measurements in the different subsystems are then combined to the  $\beta_{\text{TOF}}$  similar to the combinations in the subsystems. Also for the combined  $\beta_{\text{TOF}}$  an uncertainty as well as the consistency between the measurements in the different subsystems, are estimated.

The uncertainties which are used as inverse weights for the combination are shown in Figure 5.62. The combined uncertainty is to a large extent driven by the resolution of the RPC's. Furthermore it can be seen that both the MDT and Tile Calorimeter uncertainty distributions have separate peaks in the distributions. For the MDT's this can be explained by a

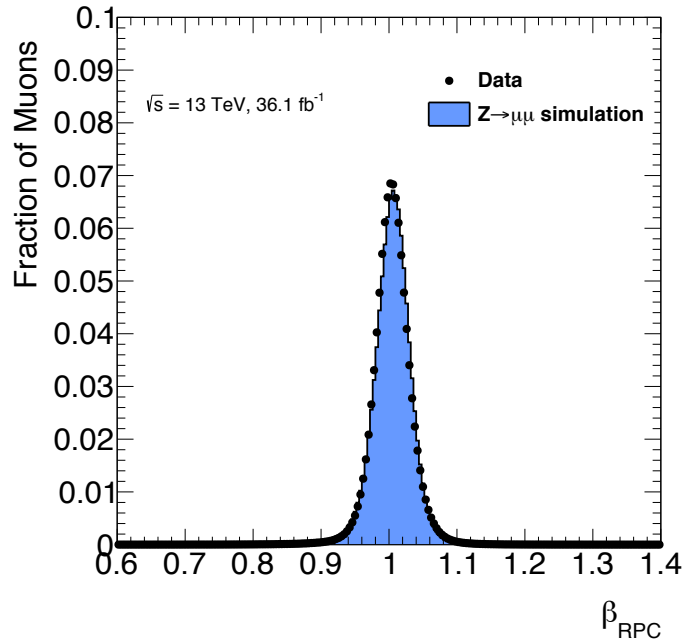


Figure 5.61: The combined  $\beta$  distribution for RPC's in data and simulation for muons passing a  $Z \rightarrow \mu\mu$  selection.

significant fraction of tubes with a worse timing resolution that are predominantly located in the end-caps. Furthermore the lower number of expected hits in the end-caps (15 end-caps, 22 barrel) contribute to the separation into separate peaks. For the Tile Calorimeter, due to the low number of expected hits, the separate peaks originate from the number of hits that are used for the combination. The combined  $\beta_{\text{TOF}}$  in data as well as the distributions for the different subsystems measured with muons passing a  $Z \rightarrow \mu\mu$  selection is shown in Figure 5.63. The  $\beta_{\text{TOF}}$  distribution is mostly dominated by the RPC's which is expected as they have the best resolution. But the combined resolution is marginally better than the pure RPC resolution. The reason is that the RPC's extend only up to  $|\eta| = 1.15$ . For the forward region between  $1.15 < |\eta| < 1.65$  MDT's and Tile Calorimeter can be used for time-of-flight measurements, while for  $|\eta| > 1.65$  only the MDT's are left.

The final combined  $\beta_{\text{TOF}}$  distribution for muons in a  $Z \rightarrow \mu\mu$  selection in data and simulation is shown in Figure 5.64. A good agreement between data and simulation is observed. All residual differences that are visible are covered by systematic uncertainties. Before the final RPC simulation correction was applied a significant difference between data and simulation was observed. This was used to study the impact of a bad modelling on the signal efficiency. The truth distribution was therefore smeared with either the resolution from data or the resolution from simulation.

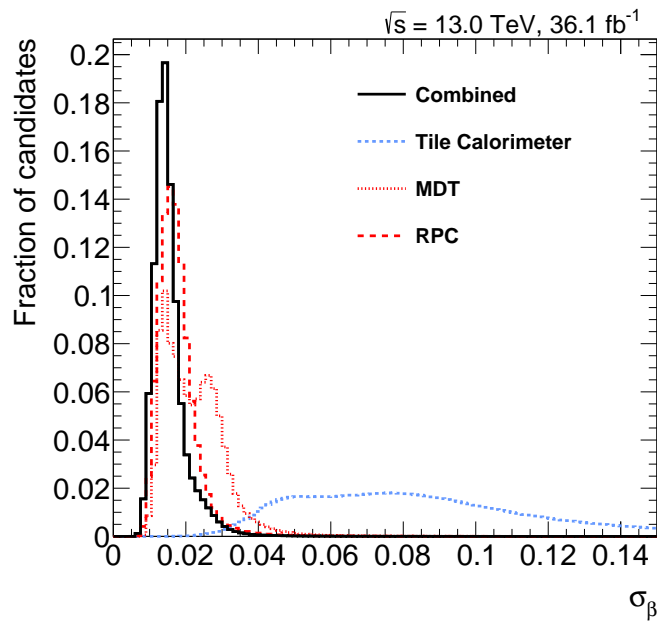


Figure 5.62: The timing uncertainties for the  $\beta$  measurements in the different subsystems as well as for the combined  $\beta_{\text{TOF}}$ . For the MDT's as well as for the Tile Calorimeter separate bulks of the distributions are visible. For the MDT's those are originating from tubes with worse resolution that are mainly in the end-caps [128] also the fewer expected hits there contribute. For the Tile Calorimeter this structure is mostly dominated by the number of hits that are used for the combination.

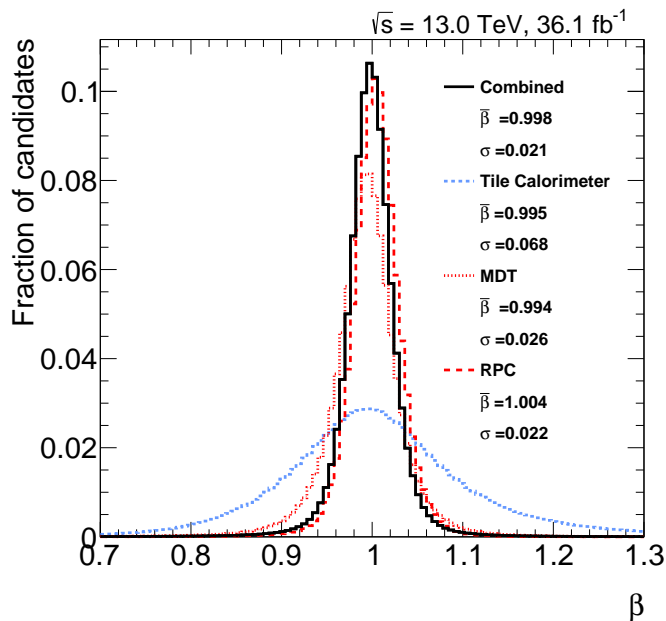


Figure 5.63: The combined  $\beta_{\text{TOF}}$  distribution together with the distributions for the different subsystems. The combined  $\beta_{\text{TOF}}$  is mostly dominated by the  $\beta_{\text{RPC}}$  and is in particular not significantly better than the pure  $\beta_{\text{RPC}}$ . The reason is that the RPC's only cover the  $|\eta|$  range up to 1.15 and hence for the remaining fiducial volume only the  $\beta_{\text{TILE}}$  and  $\beta_{\text{MDT}}$  are available.

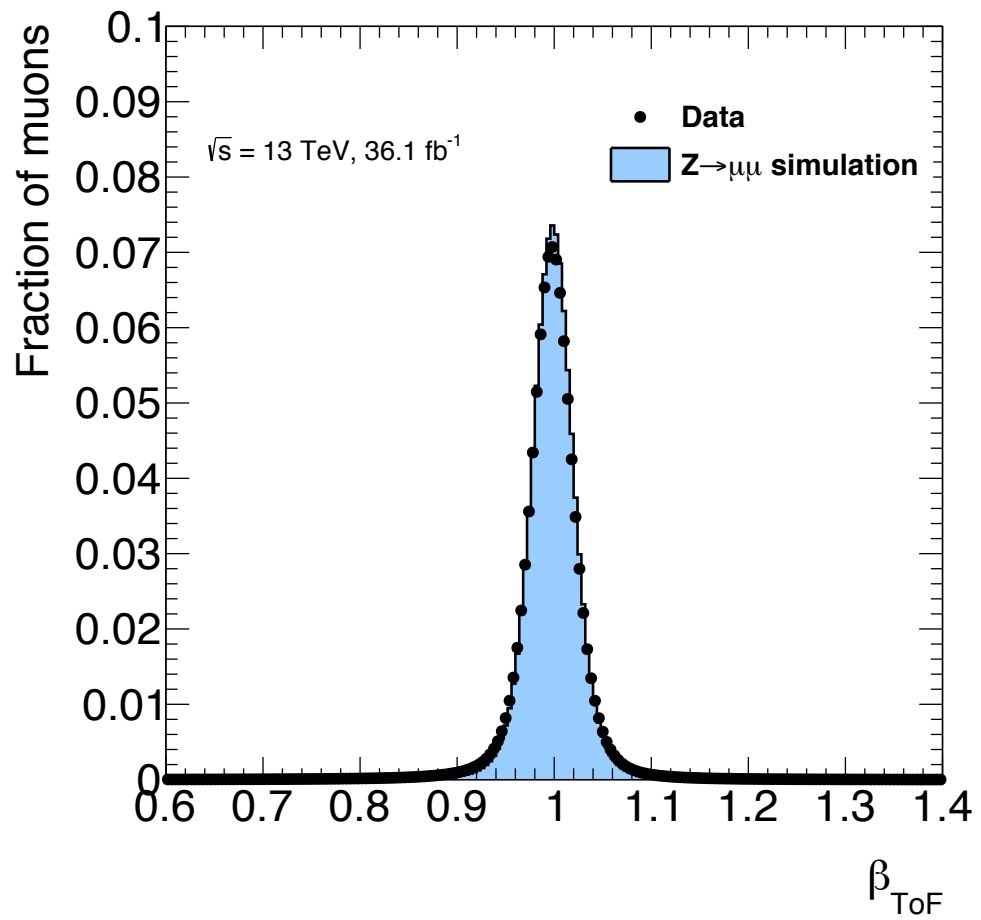


Figure 5.64: The combined  $\beta_{\text{ToF}}$  distribution for muons passing a  $Z \rightarrow \mu\mu$  selection in data and simulation. [5]

On the obtained distributions the final selection cuts on  $\beta$  are applied and the differences in the fraction of rejected candidates are compared. It was found that the impact was below 1.5% in any case. The impact is so low because the reconstructed  $\beta$  distribution is completely dominated by the truth spectrum. This means that as long as simulation is only used for the signals and not for the background the analysis is stable against mis-modelling as far as no strong correlations to important variables like momentum are involved.

## 5.6 Event Selection

In this section the event selection applied in the search for HCLLPs will be introduced. First the two types of triggers used,  $\cancel{E}_T$  and muon triggers will be discussed together with the expected efficiency to select events containing HCLLPs. The final part describes the event cleaning that has to be applied to ensure that the detector was fully operational while recording the event. This is of particular importance as malfunctions of the detector could potentially fake some HCLLPs in particular if they are related to some desynchronisation between the detector systems and the LHC clock.

### 5.6.1 Missing-transverse-energy trigger

One trigger type used for the searches for HCLLPs are  $\cancel{E}_T$  triggers. The  $\cancel{E}_T$  triggers are used for all different signal region in contrast to the single-muon triggers, which are not applied in the MS-agnostic selection. In principle events with HCLLPs feature no direct source of  $\cancel{E}_T$  except for associated productions with neutral LLP's, as e.g.  $\chi_1^\pm \chi_1^0$ . And also those cases give no rise to large  $\cancel{E}_T$  on Level-1 as there the  $\cancel{E}_T$  is solely estimated from the calorimeters, where HCLLPs are expected to release only moderate energy deposits. The reason why events with HCLLPs still can be selected by  $\cancel{E}_T$  triggers are QCD radiations from the initial or final states. Those jets can be seen in the calorimeters and, as the rest of hard interaction is invisible, lead to a significant imbalance in the event and hence give rise to  $\cancel{E}_T$ . For charginos and staus no QCD FSR is expected as they are colour-singlets, but also for  $R$ -hadrons hard FSR jets are suppressed as discussed in Section 4.2. Hence, mainly ISR jets contribute to the  $\cancel{E}_T$  seen on Level-1, and allow to trigger the events.

To deal with the increasing instantaneous luminosity the thresholds on

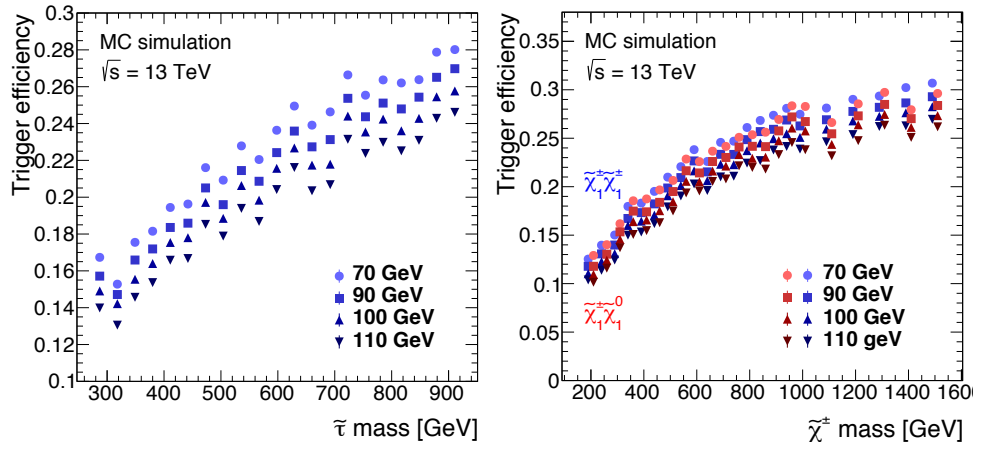
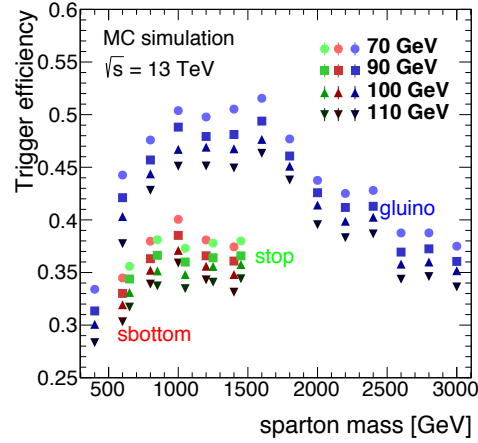


Figure 5.65: The trigger efficiencies for the different thresholds of the lowest unrescaled  $\cancel{E}_T$  triggers for  $R$ -hadrons (sbottom, stop, gluino), staus and charginos with different mass hypotheses. For charginos besides the direct pair production  $\tilde{\chi}_1^\pm \tilde{\chi}_1^\pm$  channel, also the associated production  $\tilde{\chi}_1^\pm \tilde{\chi}_1^0$  is shown. [128]

the HLT for the lowest unrescaled triggers had to be adjusted several times during the data-taking periods that are considered in this analysis. The different thresholds together with the ATLAS runs for the respective periods are summarised in Table 5.2. On Level-1 the same threshold of 50 GeV was used for the whole data-taking period considered in this analysis.

Table 5.2: The HLT  $\cancel{E}_T$  thresholds for the lowest unrescaled triggers in the corresponding data taking periods. Also the integrated luminosity recorded by the ATLAS detector in the given periods is stated.

| Run numbers     | Luminosity [ $\text{fb}^{-1}$ ] | HLT $\cancel{E}_T$ threshold [GeV] |
|-----------------|---------------------------------|------------------------------------|
| 276262 – 284484 | 3.2                             | 70                                 |
| 297730 – 302827 | 6.1                             | 90                                 |
| 302919 – 303892 | 6.5                             | 100                                |
| 303943 – 311481 | 20.3                            | 110                                |

The trigger efficiencies for the different thresholds of the lowest unrescaled  $\cancel{E}_T$  triggers for  $R$ -hadrons (sbottom, stop, gluino), staus and charginos with different mass hypotheses are shown in Figure 5.65. For

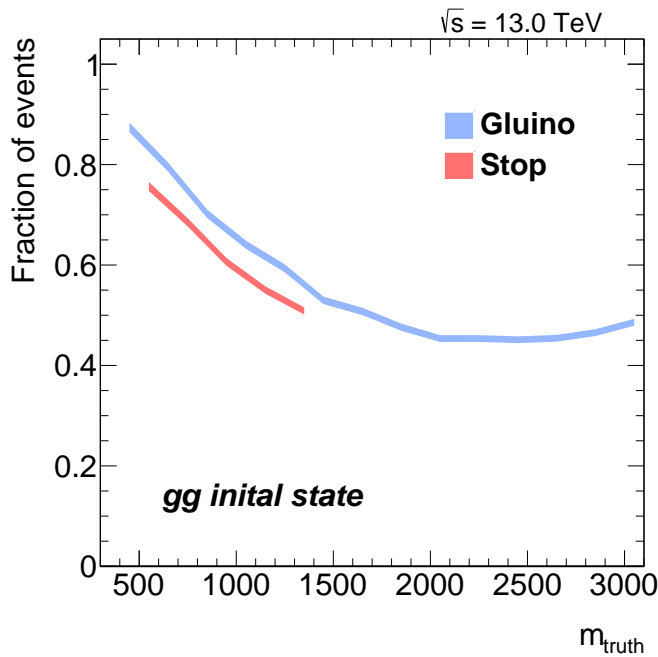


Figure 5.66: The fraction of events produced from a  $gg$ -initial state for different mass hypotheses of directly pair-produced stop-quarks and gluinos. The fraction of events produced from  $qq$  initial state is one minus the fraction of  $gg$ -initial states.

the  $R$ -hadron signals in the lower mass range the efficiency is increasing with mass reaching a plateau at a sparton mass of roughly 1 TeV. For gluino masses higher than about 1.5 TeV the trigger efficiency is degrading. The increase in efficiency is due to the increased momentum of the colliding partons that is needed to produce the heavier sparticles. The increased momentum results in an increase of the phase space for gluon radiation with larger momenta. Hence harder ISR jets and larger  $\cancel{E}_T$  are expected for higher momentum transfers in the hard collision. For a particle mass of about 1300 GeV it is more likely that the valence quarks carry the required momentum fraction of the protons to produce the spartons. This is obtained from a back-of-the-envelope calculation taking the crossing of the PDFs for gluons and quarks ( $x \approx 0.2$ ) from Figure 3.3 and multiplying it with the momentum of the proton (6.5 TeV). This gives, as two spartons have to be produced, a rough estimate for which mass the quark-quark initial states will take over. This assumption breaks if the production channels via  $gg$  or  $qq$  initial states are largely suppressed. The initial state is important for the expected ISR as gluons are doubly colour charged and hence have an increased probability for ISR radiations due to the larger colour factors. This is in agreement with what can be seen for the trigger efficiencies as for masses of about 1.3 TeV the plateau is reached. This argument can be further validated by estimating the fraction of events that are produced from a  $gg$  initial state which is shown in Figure 5.66.

Table 5.3: The HLT single-muon thresholds and muon isolation requirements for the lowest unrescaled triggers in the corresponding data taking periods. Also the integrated luminosity recorded by the ATLAS detector in the given periods is stated. The isolation requirements used are loose (l), medium (m) or varmedium (vm).

| Run numbers     | Luminosity [ $\text{fb}^{-1}$ ] | Muon threshold [GeV] | Isolation |
|-----------------|---------------------------------|----------------------|-----------|
| 276262 – 284484 | 3.2                             | 20                   | l         |
| 297730 – 300279 | 0.5                             | 24                   | l         |
| 300345 – 302872 | 11.0                            | 24                   | m/vm      |
| 302919 – 304494 | 3.4                             | 26                   | m/vm      |
| 305380 – 311481 | 18.0                            | 26                   | vm        |

It can be seen that roughly at 1.3 TeV about 50% of the events are produced from a qq initial state, while for the low masses about 90% of the events have a gg initial state. It can further be seen that the fraction of events produced from a gg initial state is smaller for stop quarks than for gluinos. This is the reason why the trigger efficiency is generally lower for squarks than for gluinos.

For staus and charginos the same increase in trigger efficiency with the mass of the sparticle is observed. Which can also be explained by the enhanced phase space for ISR radiations. But in general the  $\cancel{E}_T$  trigger efficiency is lower than for colour-charged sparticles. This can be explained as direct stau and chargino productions are at tree-level only possible from qq initial states. This is, as discussed before, lowering the probability of an ISR radiation.

For meta-stable particles the  $\cancel{E}_T$  efficiency can be significantly increased when the decay occurs before or within the calorimeters and the decay products contribute to an imbalance in the event. This is model specific as it depends on the type of the decay products as well as on the available phase space for the decay products. For the meta-stable gluinos considered in this analysis, the decay to a neutralino ( $m_{\chi_1^0} = 100$  GeV) and two quarks is assumed. The large mass difference between gluino and neutralino gives rise to hard jets and hence significantly increases the trigger efficiency if the particle decays before or in the calorimeters.

### 5.6.2 Single-muon trigger

Single-muon triggers are in contrast to the  $\cancel{E}_T$  triggers not used for the MS-agnostic selection as the efficiency depends on the fraction of  $R$ -hadrons charged in the MS and hence on the modelling of the hadronic interactions from which this signal channel is aiming to be independent. For all other signal channels both the lowest unrescaled  $\cancel{E}_T$  and muon triggers are used. The muon triggers directly detect HCLLPs if they reach the MS

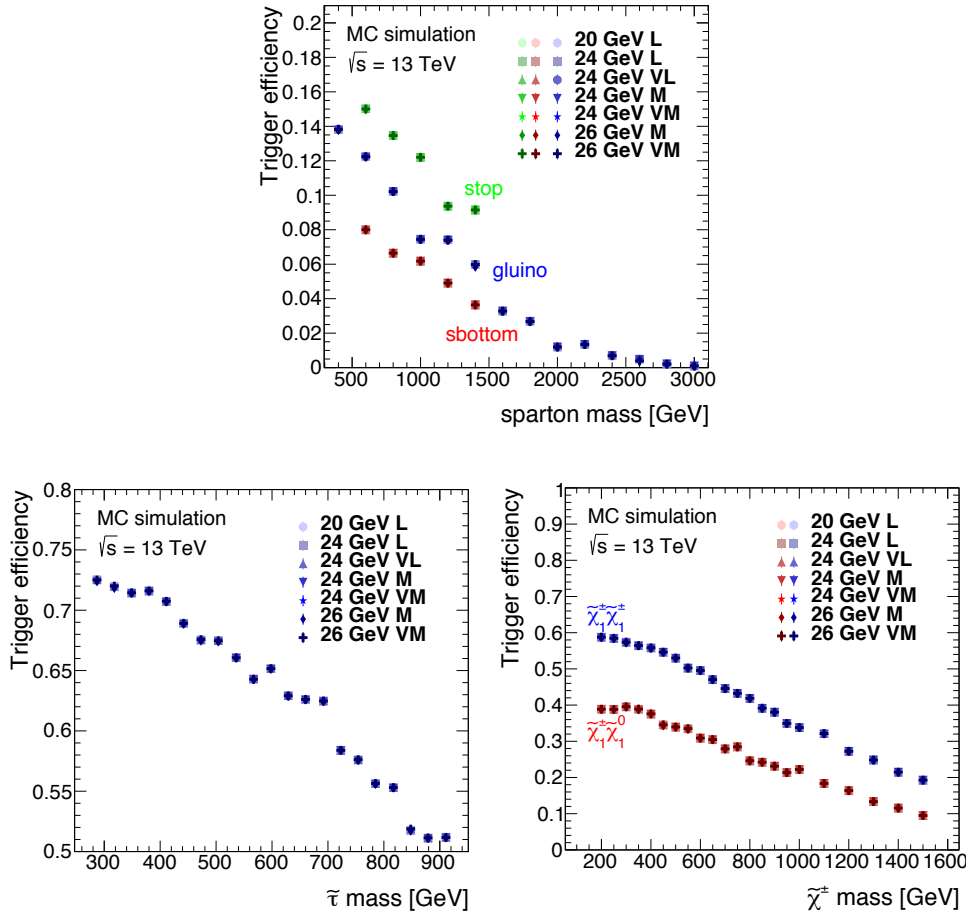


Figure 5.67: The trigger efficiencies for the different lowest unprescaled single-muon triggers for  $R$ -hadrons (sbottom, stop, gluino), staus and charginos with different mass hypotheses. For charginos besides the direct pair production  $\tilde{\chi}_1^\pm \tilde{\chi}_1^\pm$  channel, also the associated production  $\tilde{\chi}_1^\pm \tilde{\chi}_1^0$  is shown. [128]

in time. For the muon triggers it is in particular problematic if the HCLLPs are too slow as they might be associated to the wrong bunch crossing. A new trigger that is now implemented in the ATLAS trigger menu, but was not at the time of the data taking for this analysis, is designed to achieve a better trigger efficiency for slow HCLLPs. This late-muon trigger [120] combines an  $\cancel{E}_T$  trigger accept in the central bunch crossing with a muon accept in the following bunch crossing by the topological trigger processor. This allows to lower the  $\cancel{E}_T$  threshold on Level 1, which is crucial for HCLLPs as discussed in the previous section, and hence increases the efficiency for slow HCLLPs.

Also for the single-muon triggers the threshold and isolation requirements on the muons on HLT have been adjusted to account for the increased instantaneous luminosities and the associated increased occupancy of the detector, as can be seen from Table 5.3. The Level-1 threshold is 15 GeV for all periods used in this analysis.

The trigger efficiencies for the different lowest unprescaled single-muon

triggers for  $R$ -hadrons (sbottom, stop, gluino), staus and charginos as function of the truth sparticle mass are shown in Figures 5.67. All different signal models show a decrease in efficiency for higher sparticle masses. As HCLLPs are slower the higher their mass, it becomes more and more likely that the muon trigger accept is associated to the wrong bunch crossing. On HLT no corresponding ID extension can be found as those hits are associated to the central bunch crossing, the event gets rejected. In general a significantly lower muon trigger efficiency is observed for  $R$ -hadrons as they can be produced neutral or undergo charge-flips. As discussed in Section 4.5 stops are more likely to be charged in the MS than sbottoms, if the simulation of hadronic interactions is based on the Triple Regge approach. This effect is clearly visible in the increased single-muon trigger efficiency for stop quarks. The trigger efficiency for pair-produced charginos ( $\chi_1^\pm \chi_1^\pm$ ) is higher compared to the associated production ( $\chi_1^\pm \chi_1^0$ ), as two HCLLPs are present and able to trigger the event. The higher trigger efficiency for pair-produced staus compared to pair-produced charginos can be explained from their kinematic distributions shown in Figure 4.3. Charginos are produced more in the forward direction and softer compared to staus. The distance to the MS trigger chambers is longer in the forward direction and as charginos are also softer they are more likely to be associated to the wrong bunch crossing. Also effects that they are out of the trigger fiducial volume can have a small impact.

### 5.6.3 Event cleaning

All events that are selected by one of the triggers described in the previous sections has to pass quality requirements that ensure a fully operational detector and no corruptions from possible non-collision backgrounds. Some of the detector subsystems can have defects that could effect the recorded data. The ATLAS Data Quality team is therefore producing Good Runs Lists (GRL) which flag  $\mathcal{O}(1\text{ min})$  time intervals, so called lumi-blocks, as trustworthy data if no defects are reported. Furthermore it is required that none of the Tile Calorimeter, Liquid Argon calorimeter and SCT have flagged the event as bad. This is done on the single event basis and ensures no corruption of the data from the respective detectors in this event. Events can be incomplete after a restart of the ATLAS Timing and Trigger System (TTC), also those events are rejected. Jets originating from non-collision backgrounds can be present in the events and corrupt the  $\cancel{E}_T$  estimation. Those jets are selected as described in Reference [140],

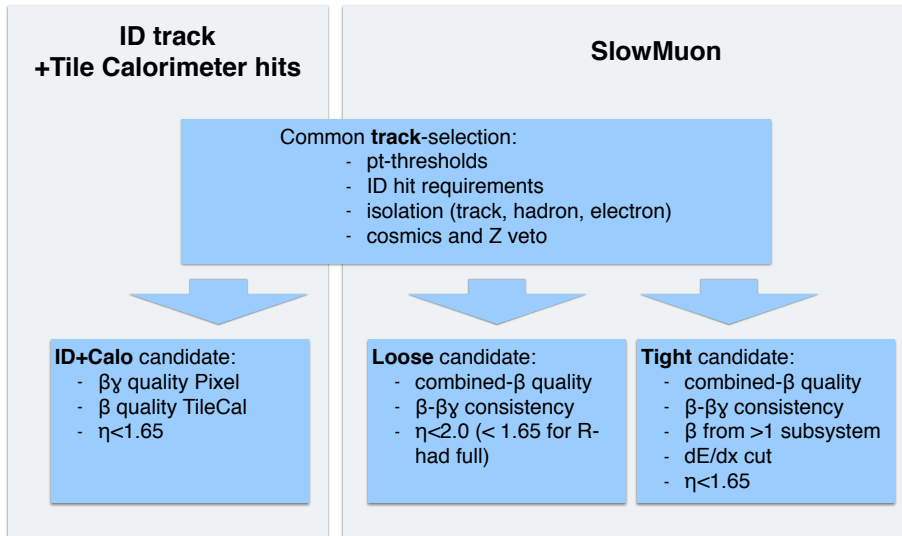


Figure 5.68: Illustration of the strategy for the HCLLP candidate pre-selection. To different types of objects are considered, an ID track with associated Tile Calorimeter hits and a SlowMuon object as described in Section 5.4. A common selection is applied on the ID tracks for both objects. This selection is also harmonised with the analysis using only the ionisation energy loss in the pixel detector to identify HCLLPs [127], to allow for a better comparison of the results. The selections applied separately on the different candidate types are mainly quality requirements on the main observables used to identify the HCLLPs.

and if present in an event the whole event is rejected. Selections aiming to reject particles from the beam halo<sup>1</sup> are excluded from the jet cleaning as they are likely to select jets from the decay of meta-stable HCLLPs. Those selections require that almost all the energy of the jet is released in the hadronic calorimeters. In particular events with neutrally produced  $R$ -hadrons which decay in the hadronic calorimeter could be rejected. Finally the events are required to have a Primary Vertex (PV)<sup>2</sup> with at least two associated tracks.

<sup>1</sup>Particles from the beam halo are particle that are flying along the beam line, but with some distance the beam pipe. They originate from main beams but are deflected due to imperfections of the magnets.

<sup>2</sup>The primary vertex is defined as the vertex with the highest sum of squared transverse momenta of associated tracks.

## 5.7 Candidate Selection

Three different types of candidates are considered in this analysis. Events are rejected if no candidate passing one of those selections is in the event. The three different candidate types are `ID+CALO` candidates as well as `LOOSE` and `TIGHT` full-detector candidates, which are reconstructed with the MuGirlStau algorithm. The candidate pre-selection strategy is illustrated in Figure 5.68. First a common pre-selection is applied on the ID tracks for both `ID+CALO` and full-detector candidates. This common track pre-selection is harmonised also with the analysis using only the ionisation energy loss in the pixel detector to identify HCLLPs [127], to allow a better comparison between the results. Requirements applied in this selection are track quality requirements, requirements on the isolation from other detector objects and cuts aiming to suppress dedicated backgrounds like cosmic-ray muons and muons from  $Z$ -boson decays. The

dedicated pre-selection parts for the different candidate types are mainly quality requirements on the observables used for the identification of HCLLPs. Stronger requirements are placed for the `TIGHT` compared to `LOOSE`. The different selections will be discussed in detail in the following sections.

### 5.7.1 Common track selection

The different selection criteria on ID tracks applied in common to all different candidate types are summarised in Table 5.4 and will be discussed in detail in the following.

| Description                          | Value  |
|--------------------------------------|--|
| Minimum transverse momentum          | $p_T^{track} > 50.0 \text{ GeV}$                                 |
| Sensible momentum                    | $0.0 \text{ TeV} < p^{track} < 6.5 \text{ TeV}$                  |
| Track matched to PV                  | $ z_0 \sin \theta  < 3 \text{ mm},  d_0  < 2 \text{ mm}$         |
| At least seven silicon hits          | $N_{Silicon}^{hits} > 6$   |
| No shared or split pixel clusters    | $N_{pix}^{shared} + N_{pix}^{split} = 0$                         |
| At least three possible SCT clusters | $N_{SCT}^{hits+dead} > 2$  |
| Isolation from tracks                | $p_T^{iso} < 5 \text{ GeV}$                                      |
| Hadron&electron veto                 | if $E_{EMcalo}/E_{calo} > 0.95$ or $E_{calo}/p_{trk} > 1$        |
| Hit in innermost pixel layer         | $N_{pix,innermost}^{hits} > 0$                                   |
| Cosmic veto                          | if $Q(cand) \cdot Q(trk) < 0$ &<br>$ \Delta R_{cosmics}  < 0.04$ |
| Z veto                               | if $ m_{inv}(cand, \mu) - m_Z  < 10 \text{ GeV}$                 |

Table 5.4: The requirements on the ID tracks used in common for all different candidate types.

**Minimum transverse momentum** A minimum transverse momentum of 50 GeV is required. This is in particular important for the `ID+CALO` selection as during the data-taking periods used in this analysis the  $p_T$  threshold for the association of Tile Calorimeter cells to ID tracks was lowered. To ensure a uniform data set the higher  $p_T$  threshold is applied to all data.

**Sensible momentum** The absolute momentum for pair-produced particles is limited to 6.5 TeV for proton-proton collisions at a centre-of-mass energy of 13 TeV. This is used as upper physical boarder for the momentum of the candidates.

**Track matched to primary vertex** The track is required to be matched to the PV using the longitudinal ( $|z_0 \sin \theta| < 3$  mm) and transverse ( $|d_0| < 2$  mm) impact parameter. As HCLLPs are expected to have large momenta they should originate from the PV. Requiring the match to the PV is mainly used to suppress particles from pile-up collisions. Furthermore particles produced in displaced decays could be problematic as they are delayed due to the additional path length.

**ID hit requirements** To ensure a well reconstructed ID track certain requirements on the number of hits in the different ID subsystems are used. Tracks are rejected if the sum of the hits in the pixel detector and in the SCT is less than seven. Furthermore the track is not allowed to have clusters shared with other tracks and the number of possible SCT clusters should be larger than two. The number of possible SCT hits is the sum of SCT hits and dead sensors on the track.

**Isolation from tracks** The sum of the  $p_T$  of tracks within a cone of  $\Delta R = 0.2$  around the candidate track is required to be less than 5 GeV. This is mainly important to ensure that no other particles corrupt the timing measurements in the Tile Calorimeter cells as they could potentially hit the same cell.

**Hadron and electron veto** This veto rejects candidate tracks that could be matched to an electron or hadron. The candidate is rejected, if the nearest calorimeter object within a cone of  $\Delta R = 0.05$  and with a  $p_T > 20$  GeV is identified as electron or hadron. The object is identified as electron if 95% of its energy deposit is in the EM calorimeters, whereas the object is classified as hadron, if the energy in the calorimeters ( $E_{calo}$ ) is larger than the momentum of the candidate. Hadrons are produced in jets, for which a significant energy fraction is carried by neutral hadrons that contribute to the energy deposit in the calorimeters but are not visible in the tracker.

**Hit in innermost pixel layer** A hit in the innermost pixel layer is required to ensure a good tracking quality. If no cluster is expected in the IBL the second pixel layer is required to have a cluster.

**Cosmic veto** One potential source of background for this analysis are cosmic-ray muons. They are not originating from the collisions and hence

can be present at any time and may be recorded as out-of-time signals. In particular in the lower half of the detector they could be registered as out-of-time particles. They are not slow but out-of-time so the consistency between the  $\beta$  measurements should be very bad. Furthermore they are expected to be minimal ionising and hence should not have a large  $dE/dx$  in the pixel detector. To further guarantee that the candidate tracks do not originate from cosmic-ray muons, candidates are rejected if an ID track of a muon with opposite charge is found on the other side of the detector (back-to-back). The tracks are labeled back-to-back if  $\Delta R_{cosmic} < 0.04$ , which is defined as  $\Delta R_{cosmic} = \sqrt{(\Delta\eta)^2 + (\Delta\phi - \pi)^2}$ , with  $\Delta\eta$  the difference in  $\eta$  and  $\Delta\phi$  the difference in  $\phi$  between the candidate and the track.

**Z veto** One of the main sources for isolated high- $p_T$  muons are decays of  $Z$ -bosons. As the main background for this search are muons with mis-measured  $\beta$  and  $dE/dx$ , a dedicated requirement is placed to suppress muons originating from  $Z$ -decays. The candidates are rejected if the invariant mass obtained with the highest- $p_T$  muon in the event agrees with the  $Z$ -boson mass within a window of 10 GeV. It was also tested to use all muons in the event, but a significant fraction of signal candidates was lost due to random combinations with soft muons giving the right mass.

### 5.7.2 ID+Calo candidates

ID track candidates that have passed the common track pre-selection and have at least one timing measurement in the Tile Calorimeter are further required to fulfill the selections described in Table 5.5 to be labeled as ID+CALO candidate.

| Description                            | Value                                    |
|--|--|
| Tile Calorimeter coverage              | $ \eta  < 1.65$                          |
| At least two clusters used for $dE/dx$ | $N_{good}^{hits} > 1$                    |
| Sensible $dE/dx$                       | $0 < dE/dx < 20$ [MeVg $^{-1}$ cm $^2$ ] |
| Sensible $\beta\gamma$                 | $0.2 < \beta\gamma_{dE/dx} < 10$         |
| Sensible $\beta_{TILE}$                | $0.2 < \beta_{TILE} < 2$                 |
| Quality $\beta_{TILE}$                 | $\sigma_{\beta_{TILE}} < 0.06$           |
| Consistency $\beta_{TILE}$             | $p(\chi^2, NdoF) > 0.01$                 |

Table 5.5: The requirements on ID tracks passing the common track pre-selection to be labeled as ID+CALO candidate.

**Tile Calorimeter coverage** Candidates are restricted to  $\eta$  smaller 1.65. The Tile Calorimeter would in principle last until  $\eta \approx 1.7$ . But, as only one cell would be passed with a short path length, the range is restricted to 1.65.

**At least two clusters used for  $dE/dx$**  To reduce the effects of single high  $dE/dx$  hits from the Landau tail at least two clusters are required for the  $dE/dx$  measurement in the pixel detector. This requirement also ensures that no single pixel with defects could fake high  $dE/dx$  tracks.

**Sensible  $dE/dx$**  The measured  $dE/dx$  is restricted to be less than  $20 \text{ MeVg}^{-1} \text{ cm}^2$  as for higher energy losses the pixel detector is expected to be in saturation and hence no trustable  $dE/dx$  measurement is possible.

**Sensible  $\beta\gamma$**  For particles with a  $\beta\gamma = 0.2$  which corresponds to a  $\beta \approx 0.2$  particles are expected to exceed the timing window of the ToF measurement with the Tile Calorimeter. Furthermore for lower velocities the efficiency of the ID tracking is expected to drop, as can be seen in Figure 5.10. To get rid of potential mis-modelling effects in the turn on of the reconstruction efficiency a minimum requirement of 0.2 on  $\beta\gamma$  is used.

**Sensible  $\beta_{\text{TILE}}$**  The  $\beta_{\text{TILE}}$  has to be restricted to be less than 0.2, for the same arguments as used for the sensible  $\beta\gamma$  requirement.

**Quality  $\beta_{\text{TILE}}$**  Candidates with a combined uncertainty larger than 0.06 are refused to reject candidates with untrustworthy  $\beta_{\text{TILE}}$  measurements. The cut value was optimised by applying all requirements but this and scanning along  $\sigma_\beta$  to data and the signal samples. To be conservative a cut value is chosen that rejects no significant fractions of the signal events but as much background as possible. This is in particular important as  $\sigma_\beta$  relies on the modelling of correlations with the timing in simulation, which, as was discussed in the previous section, is not very trustworthy. The corresponding optimisation study is given in the Appendix A.2.

**Consistency  $\beta_{\text{TILE}}$**  Finally a consistency between the individual Tile Calorimeter  $\beta$  measurements  $p(\chi^2, NdoF) > 0.01$  is required. Besides the quality aspect rejecting miss-measured muons, this criterion is also able

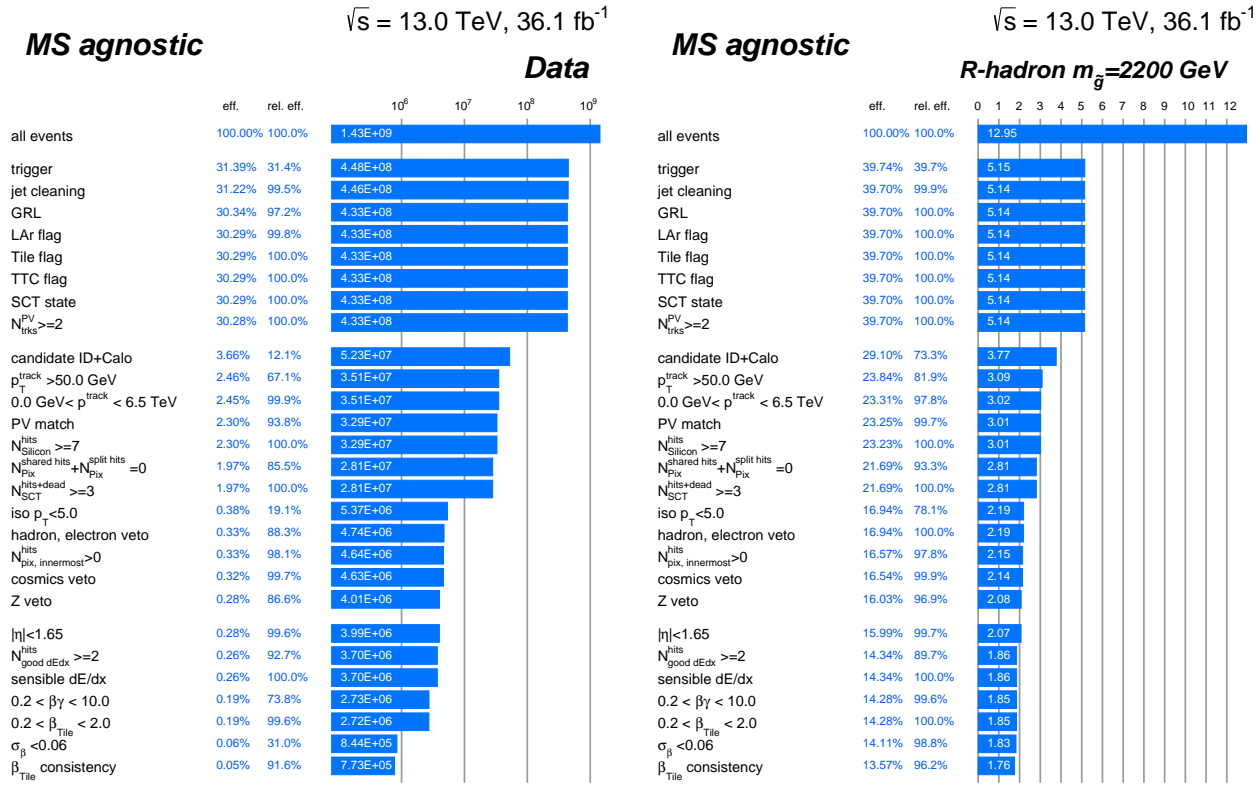


Figure 5.69: The MS-agnostic selection applied in data (left) and on a signal sample of  $R$ -hadrons with a gluino mass of 2200 GeV (right). A gluino mass hypothesis close to the expected mass limit is chosen. The  $ID+CALO$  is also used in as a fall-back in the full-detector  $R$ -hadron approach as introduced in Section 5.1. The only difference to the MS-agnostic selection is the usage of the single-muon triggers. The selection requirements are grouped into blocks. The first block are the event selection requirements, the second the common track pre-selection and the third the  $ID+CALO$  requirements. Beside the (expected) event yields also the efficiency and the relative efficiency are stated.

to reject out-of-time particles such as cosmic-ray muons. A slow moving particle is expected to have a larger delay, compared to a particle moving at the speed-of-light, the longer the distance of travel, while out-of-time particles moving with the speed-of-light would have the same delay at each distance. This would lead to an inconsistency between the  $\beta$  measurements at different distanced and hence to a rejection of out-of-time particles. This cut was optimised in a similar way as the  $\beta_{TILE}$  quality requirement. The optimisation is summarised in Appendix A.2.

The event yields for the MS-agnostic selection applied to data and a signal sample of  $R$ -hadrons with a gluino mass of 2200 GeV are shown in Figures 5.69. The requirements with the largest drop in efficiency are the requirement of one  $ID+CALO$  object in the event, the isolation from tracks and the requirement on the uncertainty of the  $\beta_{TILE}$  measurement. The  $ID+CALO$  object requirement has a significant impact for both data and signal as it has an implicit requirement on the  $p_T$  of the object through the Tile Calorimeter cell association requirements. The reason why the fol-

lowing  $p_T > 50$  GeV requirement still rejects events is that the association cut was lowered to 25 GeV during the data taking. The MS-agnostic search uses only  $\cancel{E}_T$  triggers and hence a lot calorimeter activity has to be present in the event, which is predominantly caused by jets, as the LHC is a p-p collider. The isolation from tracks with significant  $p_T$  is effective to reject candidate tracks that belong to a jet and hence suppresses the according background significantly.  $R$ -hadrons are expected to have larger energy deposits in the calorimeters than minimum ionising particles due to the additional hadronic interactions. As this results in a better timing resolution a relatively hard cut on  $\sigma_\beta$  can be applied which is actively reducing the background from muons, which are the main source of background that is left at that point of the cutflow.

For  $R$ -hadrons the selection requirements resulting in a significant drop of the signal efficiency are the `ID+CALO` candidate requirement and the isolation-from-track requirement. The `ID+CALO` candidate criterion is implicitly reducing the fiducial volume to the area covered by the Tile Calorimeter and hence rejecting a significant fraction of  $R$ -hadrons. The isolation requirement for  $R$ -hadrons can be problematic as the additional hadronic activity around the particle is low but not negligible, as discussed in Section 4.2.

### 5.7.3 Full-detector candidates

SlowMuon objects, for which their ID track has passed the common track selection are considered further for the full-detector candidate selections. Two different selections are used, the `LOOSE` and the `TIGHT` selection. The `TIGHT` selection has the same requirements as the `LOOSE`, but with some cuts being tightened and an additional cut on the  $dE/dx$  from the pixel detector. The `LOOSE` selection will be discussed first and is summarised in Table 5.6. Afterwards the additional requirements for the `TIGHT` selection will be described, which are summarised in Table 5.7.

**Minimum transverse momentum** The threshold for the MuGirlStau algorithm to be used for the reconstruction of a HCLLP candidate was lowered from  $p_T^{online} > 60.0$  GeV to 30 GeV, at the same time as the cell association cut was changed for the ID tracks. To ensure that no turn-on effects have to be considered and to have a uniform dataset without time dependencies a  $p_T > 70$  GeV of the SlowMuon is required.

| Description   | Value  |
|---|--|
| Minimum transverse momentum                             | $p_T^{comb} > 70.0 \text{ GeV}$                |
| $\eta$ requirement                                      | $ \eta  < 2.0$                                 |
| At least two two MS stations                            | $N_{station}^{MS} > 1$                         |
| $\beta_{\text{ToF}}$ consistency                        | $p(\chi^2, N_{\text{dof}}) > 0.0023 (4\sigma)$ |
| $\beta_{\text{ToF}} - \beta_{\text{dE/dx}}$ consistency | $p(\chi^2, N_{\text{dof}}) > 0.0023 (4\sigma)$ |
| Quality $\beta_{\text{ToF}}$                            | $\sigma_{\beta_{\text{ToF}}} < 0.0025$         |
| $\beta$ from at least one subsystem                     | $N_{\text{subsystem}}^{\text{ToF}} > 0$        |
| Sensible $\beta_{\text{ToF}}$                           | $0.2 < \beta_{\text{ToF}} < 2$                 |

Table 5.6: The requirements on SlowMuon objects for which their ID track has passed the common track selection to be labeled as `LOOSE` candidate.

**$\eta$  requirement** The  $\eta$  range for `LOOSE` candidates is restricted to  $\eta < 2.0$ , as the region up to  $\eta = 2.5$ , for which an ToF measurement from the MDT's is available, suffers from large backgrounds and is also problematic for the background estimate.

**At least two MS stations** To ensure a good quality of the MS track, hits in at least two stations are required.

**$\beta_{\text{ToF}}$  consistency** The  $\beta$  measurements in the different ToF subsystems have to be consistent on the  $4\sigma$  level. This is an effective way to suppress backgrounds due to mis-measurements or outliers in the  $\beta$  distributions in different subsystems as they are likely to be inconsistent when originating from independent measurements. Furthermore as discussed for the consistency between the individual Tile Calorimeter  $\beta$  measurements this states an effective requirement to reject out-of-time signals. The rejection of potential out-of-time signals is larger for the  $\beta_{\text{ToF}}$  consistency due to the increased distance between the measurements compared to the Tile Calorimeter only consistency. This cut is optimised in a similar way as the  $\beta$  quality and consistency requirements in the `ID+CALO` selection. The optimisation is summarised in Appendix A.2.

**$\beta_{\text{ToF}} - \beta_{\text{dE/dx}}$  consistency** If a  $\beta_{\text{dE/dx}}$  measurement exists for a given candidate it is required to be consistent with the  $\beta$  measured by the ToF measurements on the  $4\sigma$  level. An uncertainty of 14% is used for  $\beta_{\text{dE/dx}}$ , motivated by simulation and by low- $p_T$  proton-mass measurements in minimum-bias data. This is nevertheless not a very accurate estimation of the uncertainty and should be investigated in more detail for future analyses. As the same approach is used for data and simulation this

is not problematic for the analysis. A similar conservative optimisation approach as used for the quality cuts discussed before is used and also shown in Appendix A.2.

**Quality  $\beta_{\text{TOF}}$**  An uncertainty on the combined  $\beta_{\text{TOF}}$  smaller than 0.0025 is required, which ensures a trustworthy measurement. Also this quality cut is optimised with the approach discussed before and summarised in Appendix A.2.

**$\beta$  from at least one subsystem** At least one subsystem has to yield a reliable  $\beta$  measurement. This is rejecting candidates where timing measurements exist but do not full-fill the requirements mentioned in Section 5.5 to give a proper  $\beta$  measurement.

**Sensible  $\beta_{\text{TOF}}$**  A  $\beta$  value in a sensible range between 0.2 and 2.0 is required. In principle the MuGirlStau algorithm is not efficient anymore for  $\beta < 0.25$ . Hence a  $\beta$  smaller than 0.2 is not trustable and the candidates are rejected.

The event yields for the `LOOSE` selection applied to data and a signal sample of charginos with a mass of 1200 GeV are shown in Figures 5.70. The main reduction in data is achieved by the SlowMuon object requirement, which has an implicit  $p_T$  requirement, and an explicit  $p_T$  cut. The objects that are reconstructed as SlowMuons are almost entirely muons as they are required to have an MS track. The main sources of high- $p_T$  muons at the LHC are  $Z$  or  $W$  decays and top-quark decays. In particular the decays of  $Z$  and  $W$  bosons are expected to give muons with a  $p_T$  lower than 70 GeV as their restmass is basically at the same scale. The muons from those decays are hence significantly suppressed.

The most interesting drop in signal efficiency for charginos is for the  $\beta_{\text{TOF}}$  consistency requirement. The reason why this is rather large for signal is, that a bug in the estimation of the RPC measurements was found, that was rejecting significant fractions of the measurements there. This was found after unblinding of the analysis and hence no re-optimisation of this cut was possible. Comparing the efficiency of the  $\beta_{\text{TOF}}$  consistency between data and simulation suggests that it is rejecting more signal than background. But this is not entirely true as no cuts on a low  $\beta$  are applied so far and for muons no mis-measurements or outliers in the  $\beta$

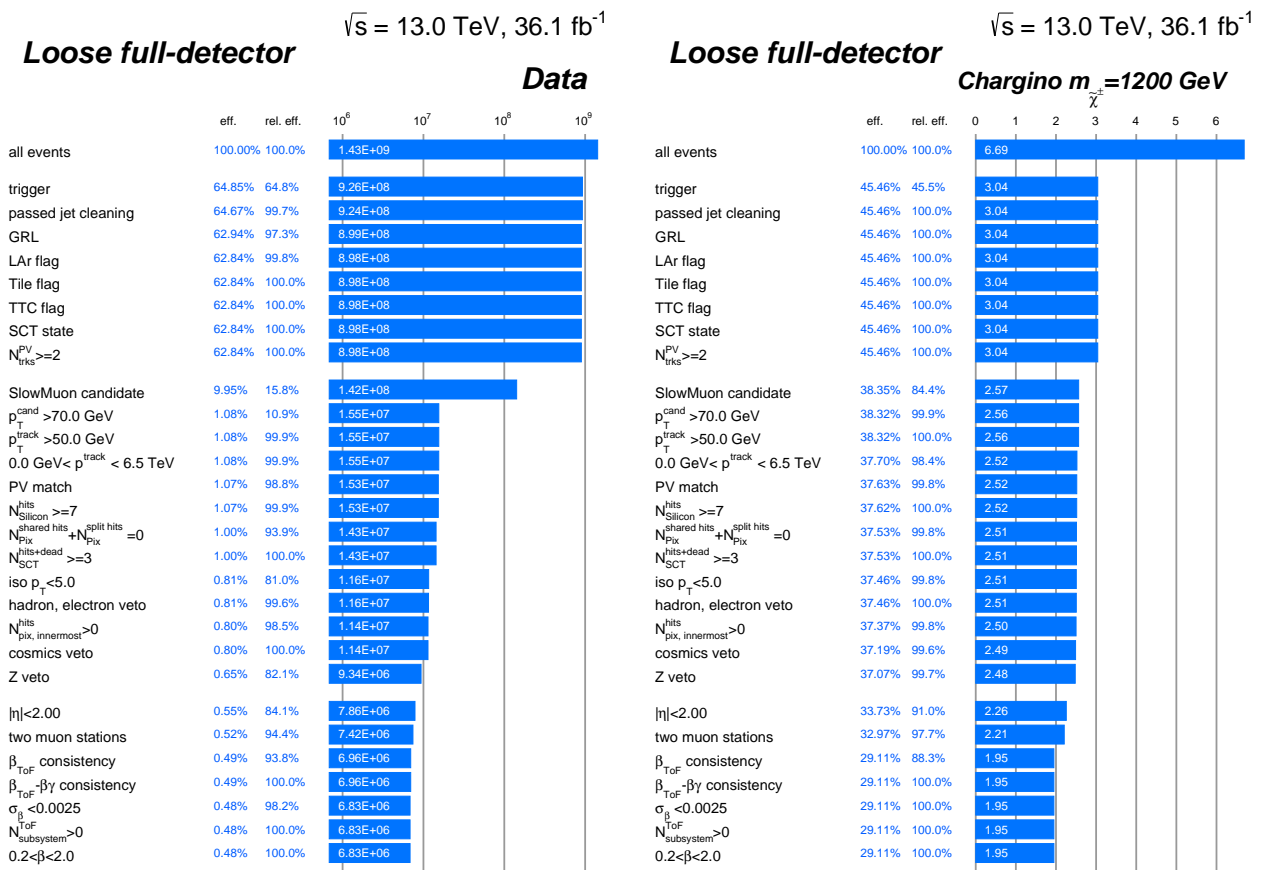


Figure 5.70: The `Loose` selection applied in data (left) and on a signal sample of charginos with a mass of 1200 GeV (right). A chargino mass hypothesis close to the expected mass limit is chosen. The selection requirements are grouped into blocks. The first block are the event selection requirements, the second the common track pre-selection and the third the `Loose` requirements. Besides the (expected) event yields also the efficiency and the relative efficiency are stated.

distribution are needed. If cuts on  $\beta$  are placed, as can be seen in Appendix A.2 the consistency requirement becomes an effective criterion as no real particles with low  $\beta$  are expected and hence the measurement is dominated by mostly inconsistent  $\beta$  outliers.

| Description                          | Value  |
|--------------------------------------|--|
| $\eta$ requirement                   | $ \eta  < 1.65$  |
| Large $dE/dx$                        | $1 < dE/dx < 20$ [MeVg <sup>-1</sup> cm <sup>2</sup> ] |
| $\beta$ from at least two subsystems | $N_{subsystem}^{ToF} > 1$                              |

Table 5.7: The additional requirements on a `LOOSE` candidate to be promoted to a `TIGHT` candidate.

The additional requirements on a `LOOSE` candidate to be promoted to a `TIGHT` candidate are summarised in Table 5.7 and will be discussed in the following.

**$\eta$  requirement** The  $\eta$  requirement is tightened to 1.65. This is also implicitly required by the later described criterion to have  $\beta$  measurements in at least two subsystems, as the Tile Calorimeter ends at  $|\eta| \approx 1.65$  and the RPC's even more central at  $|\eta| \approx 1.15$ .

**Large  $dE/dx$**  The tight selection is only used for `SR-1Cand-FullDet`, which is suffering from rather large backgrounds. To increase the sensitivity in this signal region, which had low sensitivity in previous analyses, an additional requirement on  $dE/dx$  is placed. This reduces the signal efficiency for the low-mass chargino and stau models, as discussed in Section 5.5.1, but to a larger extent the backgrounds, and hence helps to increase the sensitivity in `SR-1Cand-FullDet`.

**$\beta$  from at least two subsystems** Finally  $\beta$  measurements from at least two subsystems are required to ensure a better and more reliable measurement and hence reduce the backgrounds from mis-measurements significantly.

The event yields for the `TIGHT` selection applied to data and directly pair-produced charginos with a mass of 1200 GeV and directly pair-produced staus with a mass of 442 GeV are shown in Figures 5.71. Compared to the `LOOSE` the main difference is the additional cut on  $dE/dx$ . It can be seen that the requirement effectively reduces the events in data by 40%, while for charginos with a mass of 1200 GeV almost no events are lost. For staus with a mass of 442 GeV about 10% of the events are lost due to this

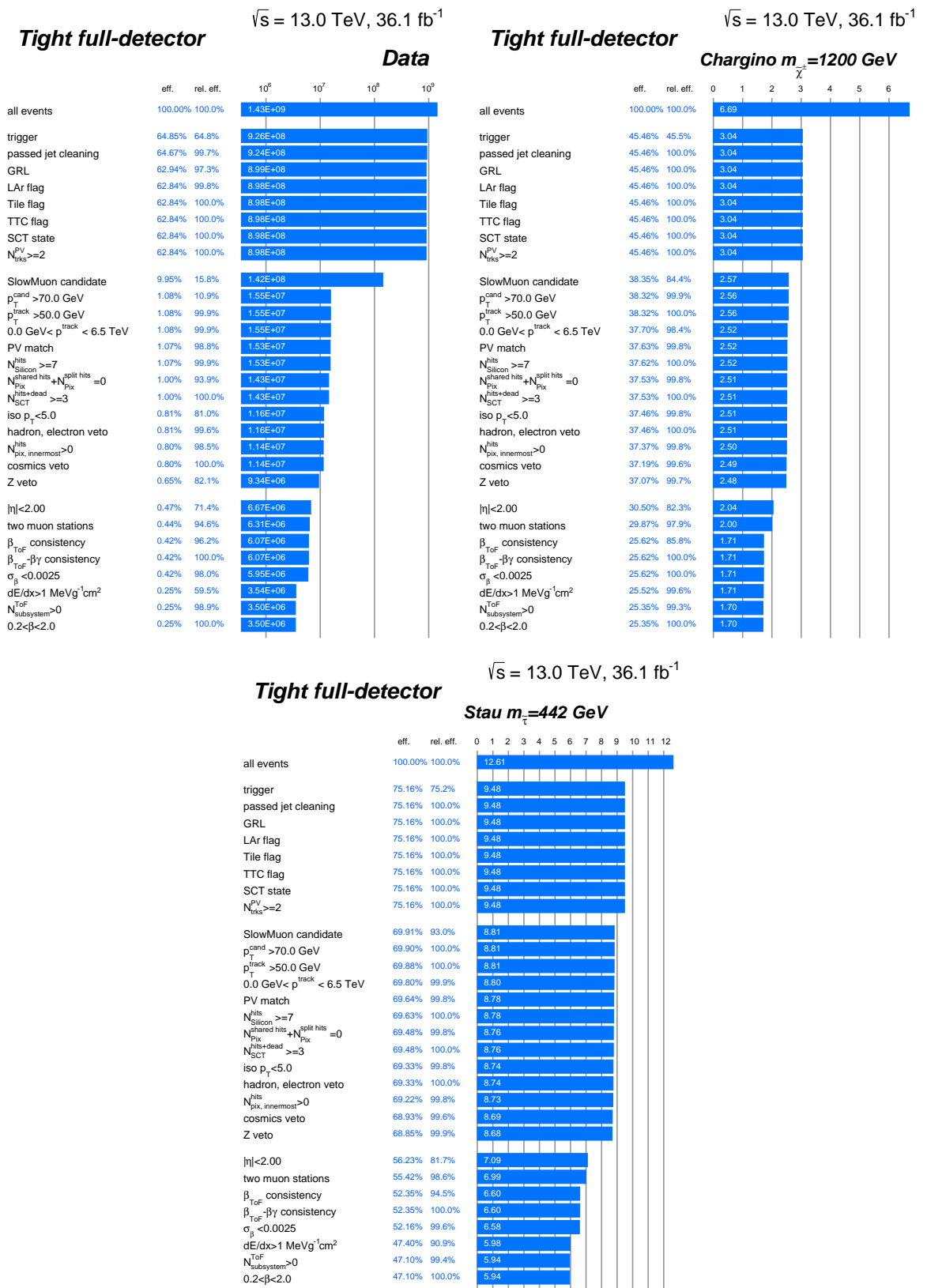


Figure 5.71: The TIGHT selection applied in data and on a signal sample of charginos with a mass of 1200 GeV and a sample of staus with a mass of 442 GeV. Mass hypothesis for charginos and staus are selected close to the expected mass limits. The selection requirements are grouped into blocks. The first block are the event selection requirements, the second the common track pre-selection and the third the TIGHT requirements. Besides the (expected) event yields also the efficiency and the relative efficiency are stated.

| signal region    | trigger            | candidate selection | candidates per event | final cuts  |            |                      |                       |            |
|------------------|--------------------|---------------------|----------------------|-------------|------------|----------------------|-----------------------|------------|
|                  |                    |                     |                      | $ \eta $    | $p$ [GeV]  | $\beta_{\text{ToF}}$ | $\beta\gamma_{dE/dx}$ | mass       |
| SR-Rhad-MSagno   | $\cancel{E}_T$     | ID+CALO             | $\geq 1$             | $\leq 1.65$ | $\geq 200$ | $\leq 0.75$          | $\leq 1.0$            | ToF& dE/dx |
| SR-Rhad-FullDet  | $\cancel{E}_T/\mu$ | LOOSE               | $\geq 1$             | $\leq 1.65$ | $\geq 200$ | $\leq 0.75$          | $\leq 1.3$            | ToF& dE/dx |
| SR-Rhad-FullDet  | $\cancel{E}_T/\mu$ | ID+CALO             | $\geq 1$             | $\leq 1.65$ | $\geq 200$ | $\leq 0.75$          | $\leq 1.0$            | ToF& dE/dx |
| SR-1Cand-FullDet | $\cancel{E}_T/\mu$ | TIGHT               | = 1                  | $\leq 1.65$ | $\geq 100$ | $\leq 0.95$          | -                     | ToF        |
| SR-2Cand-FullDet | $\cancel{E}_T/\mu$ | LOOSE               | = 2                  | $\leq 2.00$ | $\geq 200$ | $\leq 0.80$          | -                     | ToF        |

Table 5.8: A summary of the signal regions used for the search for HCLLPs. The triggers used and the required number of candidates per event fulfilling the stated selections are given. Furthermore the final selection cuts and whether a one or two-dimensional plane is used for the final counting is presented. The vertical lines indicate the signal regions that are combined in the statistical interpretation of the results.

additional requirement. As can be seen this cut is effectively suppressing the backgrounds with a moderate loss of signal efficiency and hence is able to achieve an improved sensitivity in SR-1Cand-FullDet.

## 5.8 Signal selection and optimisation

### 5.8.1 Signal regions

In total five different signal regions are used to target the different benchmark scenarios considered. This five signal regions are SR-Rhad-MSagno, SR-Rhad-FullDet LOOSE that is combined with SR-Rhad-FullDet ID+CALO and SR-2Cand-FullDet that is combined with the SR-1Cand-FullDet, which gives in total three different scenarios that are targeted. They are defined using the candidates passing the respective pre-selections described in the previous section. Those different scenarios and the definition of the signal regions will be discussed in the following. A summary of the different signal regions is given in Table 5.8.

#### MS-agnostic approach

The MS-agnostic signal region (SR-Rhad-MSagno) is targeting  $R$ -hadrons. This approach is aiming to be as independent of the hadronic-interaction model as possible as the phenomenology is not yet fully understood, which was discussed in detail in Section 4.5. Most of the hadronic interactions are expected in the dense calorimeters and hence, due to charge-flips, the fraction of charged  $R$ -hadrons after the calorimeters is largely model dependent. Only little difference between the interaction models is found in the fraction of charged  $R$ -hadrons after hadronisation. This and the model dependence of the fraction of  $R$ -hadrons charged in the MS can be seen in Figure 4.18. Information from the MS is therefore not used for the MS-agnostic approach. As trigger only  $\cancel{E}_T$  is used and at least one

ID+CALO candidate is required in the event. For the rare case of more than one candidate per event the candidate with the highest  $p_T$  is used for the final selections. The final selections are based on the momentum of the ID track ( $p_{ID} \geq 200$  GeV),  $\beta$  measured in the Tile Calorimeter ( $\beta_{\text{ToF}} \leq 0.75$ ) and  $\beta\gamma$  estimated from the pixel  $dE/dx$  ( $\beta\gamma_{dE/dx} \leq 1.0$ ). The optimisation of the final cuts on  $\beta_{\text{ToF}}$  and  $\beta\gamma_{dE/dx}$  will be discussed in Section 5.8.2. Finally a one-bin counting experiment is conducted in the two-dimensional plane spanned by  $m_{dE/dx}$  and  $m_{\text{ToF}}$ . Lower mass cuts are placed on  $m_{dE/dx}$  and  $m_{\text{ToF}}$  to define the final mass windows. Those lower mass cuts are defined for each signal particle mass hypothesis as the mean minus two times the reconstructed mass resolution of  $m_{dE/dx}$  and  $m_{\text{ToF}}$ , respectively. A harmonisation procedure applied between the lower mass cuts is described in Section 5.8.2.

### **R-hadron full-detector approach**

The *R*-hadron full-detector approach accepts the additional model dependence by using the information from the MS to improve the background suppression due to the better  $\beta$  resolution in the MS. Furthermore also the signal efficiency is slightly enhanced as besides the  $\cancel{E}_T$  triggers also single-muon triggers are used. The gain by using also single-muon triggers for *R*-hadrons is rather low as discussed in Section 5.6. The *R*-hadron full-detector approach consist of two orthogonal signal regions, a signal region requiring at least one LOOSE candidate in the event (SR-Rhad-FullDet LOOSE) and a fall-back, if no LOOSE candidate is found, at least one ID+CALO candidate is required (SR-Rhad-FullDet ID+CALO). The fall-back SR-Rhad-FullDet ID+CALO recovers sensitivity where the *R*-hadrons undergo a charge-flip from charged to uncharged in the calorimeters. The two signal regions are combined in the statistical interpretation of the results.

The final selection cuts for the SR-Rhad-FullDet LOOSE signal region are requiring a momentum of the ID track  $p_{ID} \geq 200$  GeV a combined  $\beta_{\text{ToF}} \leq 0.75$  and a  $\beta\gamma_{dE/dx} \leq 1.3$ . The momentum from the ID track is used as a significant fraction of *R*-hadrons can have, due to charge flips, a charge in the MS that does not match the charge in the ID. This can be seen from Figure 4.18. For those cases the combination of the momenta from ID and MS could fail or give unreliable results. The optimisation of the final selection cuts for the SR-Rhad-FullDet LOOSE will be also discussed in Section 5.8.2. The final counting is done similarity as in the SR-Rhad-MSagno in a two-dimensional plane of  $m_{dE/dx}$  and  $m_{\text{ToF}}$ . AS before the momentum

of the ID track is used for the mass estimates. The lower mass cuts are estimated in the same way as in SR-Rhad-MSagno.

The SR-Rhad-FullDet ID+CALO fall-back is requiring at least one ID+CALO candidate per event but no LOOSE candidates. The same final selection as well as lower mass cuts as in SR-Rhad-MSagno are also used for SR-Rhad-FullDet ID+CALO.

### Colour singlet approach

The colour singlet approach is targeting mainly pair-produced particles such as charginos or staus that are charged throughout the whole detector. They have hence a heavy-muon-like signature. As they are assumed to be pair-produced, two HCLLPs are expected to be reconstructed per event, if not too slow or out of the fiducial volume. Also for those benchmark scenarios two orthogonal signal regions are used. A signal region requiring exactly two LOOSE candidates in the event (SR-2Cand-FullDet) and a fall-back requiring exactly one TIGHT candidate per event (SR-1Cand-FullDet). The two candidate signal region is accounting for the two candidates that are expected per event for the benchmark scenarios, while the one candidate region is recovering sensitivity if one of the candidates is not reconstructed.

For the SR-2Cand-FullDet the candidate with the lower reconstructed mass is used for the final counting. For background events the probability of getting a candidate with higher mass is decreasing, while the mass of the signal candidate is expected to be reconstructed within the mass resolution around the simulated mass. Hence background candidates will just make it into the signal region, while signal events are expected to be rather central. Using the lower mass candidate is hence an effective way to reduce the background. For the SR-2Cand-FullDet candidate a minimum momentum of the SlowMuon of 100 GeV is required and for the combined  $\beta_{\text{ToF}}$  has to be below 0.95. The momentum cut is lowered as this signal region is almost background free also for low masses due to the requirement of two candidates. The  $\beta_{\text{ToF}}$  is chosen very loose, but tight enough to allow for the same estimate of the background systematic uncertainties as applied for the other signal regions, which will be discussed in detail in Section 5.10. The final counting is done in  $m_{\text{ToF}}$  and similar as for the R-hadron signal regions the lower mass cuts are estimated from the width and the mean of the reconstructed mass distributions for the different signals.

For the SR-1Cand-FullDet at least one candidate fulfilling the TIGHT se-

lection is required per event. The momentum of the SlowMuon object has to be larger than 200 GeV and  $\beta_{\text{TOF}}$  is required to be less or equal 0.95. Also for the SR-1Cand-FullDet the final counting is done in the one-dimensional  $m_{\text{TOF}}$ -plane.

## 5.8.2 Optimisation

This section describes the methods used to optimise the final selection for the different signal regions. First the optimisation of the final  $\beta$  and  $\beta\gamma$  cuts for the  $R$ -hadron signal regions are discussed. This is followed by a description of the smoothing applied to the lower mass limits for the final counting windows.

### Optimisation of final selection requirements

The final cuts for the  $R$ -hadron signal regions, where both  $\beta$  and  $\beta\gamma$  are used are optimised with a two-dimensional scan. For each of the potential cut combinations the full background estimate, discussed in detail in Section 5.9, is redone. This includes the estimation of the statistic uncertainties as well as of the dominant systematic uncertainty, which comes from the normalisation of the background in the low mass control region as defined in Section 5.1. For all other sources of systematic uncertainties on the background estimate 25% are assumed. The signal and background yields are then obtained for each cut combination and from those a Receiver Operating Characteristic (ROC)-curve is drawn, as shown in Figure 5.72. Each point corresponds to one cut combination and the signal (background) efficiencies are measured with respect to the largest signal (background) yield obtained for a single cut combination. For combinations yielding the same signal efficiency the best sensitivity is expected for the one with the largest background suppression, those are highlighted with red markers. This should be in particular true for the simple one-bin counting applied in this analysis. The computing-resource-intense calculations of p-values, which are used as final measure for the sensitivity, using histfitter [141] can hence be reduced as only the cut combination corresponding to the red points have to be considered further. It was observed that basically always the hardest cut combinations are preferred and therefore a requirement of at least five candidates in the control region was added. This is important as the validity of the background estimate is checked in this region. Furthermore a symmetric cut combination is preferred, which means that the significance  $sig = \frac{1-\beta}{\sigma_\beta}$  ( $\beta\gamma$  is translated

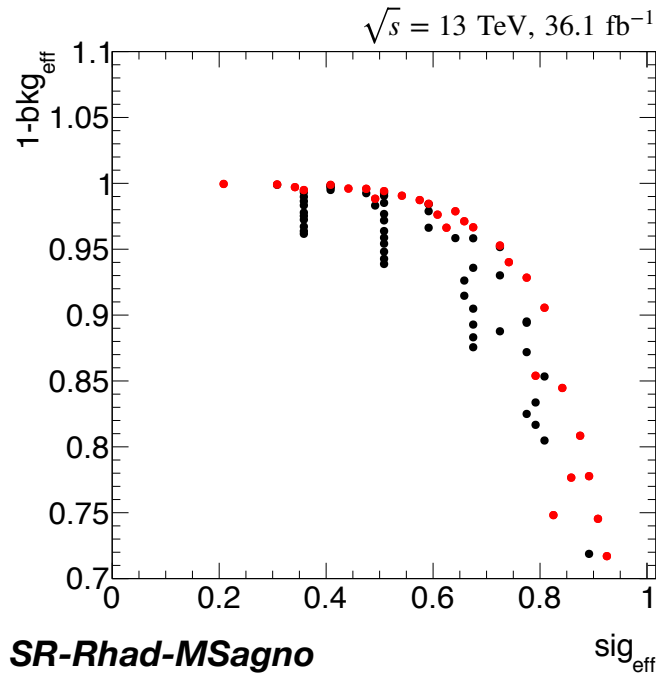


Figure 5.72: The ROC-curve produced from the signal and background yields from all scanned cut combinations of  $\beta$  and  $\beta\gamma$  for the SR-Rhad-MSagno. Each point corresponds to the yields for one cut combination, while the ones with the highest background suppression with the same signal efficiency are highlighted as red dots. The signal as well as the background efficiency are measured with respect to the largest background/signal yield of the cut combinations. The best sensitivity is expected for combinations with the same signal efficiency but higher background suppression. The clustering seen in the plot is due to the large scan range that was used. If a requirement is too loose it will not reject any signal and hence such clustering can occur.

to a  $\beta$ ) is similar. This helps to ensure large statistics in all templates used for the data-driven background estimation. The best combination including these criteria is  $\beta < 0.7$  and  $\beta\gamma < 0.9$ . The selection was later slightly relaxed to further increase the statistics in the control region and as final combination  $\beta < 0.75$  and  $\beta\gamma < 1.0$  are used. In a similar way the final selection criteria for the SR-Rhad-FullDet LOOSE are obtained as  $\beta < 0.7$  and  $\beta\gamma < 1.3$ .

### Lower mass limit smoothing

The lower mass limits for the final counting window are obtained from a fit of the simulated signal mass distribution with a Gaussian as shown in Figure 5.73. This procedure ensures that the full signal mass distribution is covered by the final counting window. In principle this could be done for each signal model and mass hypothesis separate. This has two caveats, the lower mass limits can have rather large fluctuations due to the statistics of the signal sample and a very large number of signal regions has to be dealt with. A smoothing is developed that is additionally aligning the lower mass cuts for different models with the same mass if appropriate. The different lower mass cuts estimated with the plane approach are drawn in Figures 5.74. All R-hadron searches use the same lower mass cuts for  $m_{\text{ToF}}$  and  $m_{dE/dx}$ , as the resolution is dominated by the large

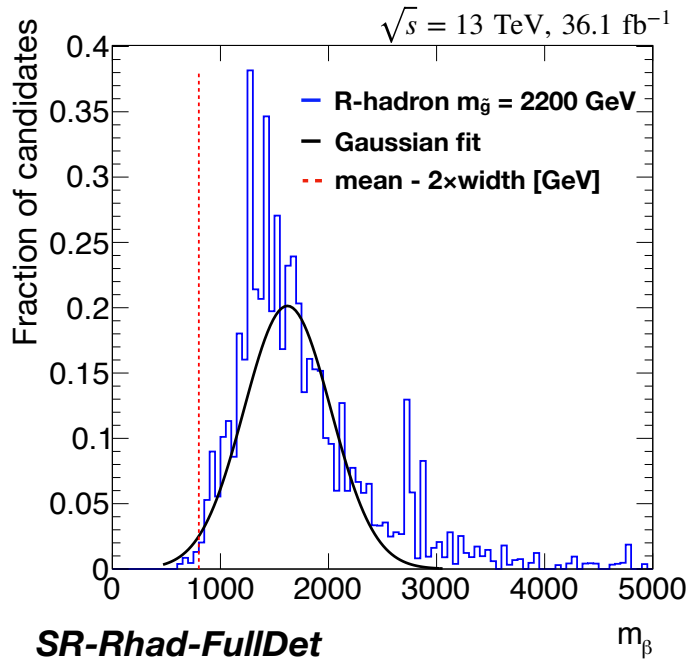


Figure 5.73: The lower mass limit obtained from a fit of the mass distribution for a signal sample with a Gaussian as  $\bar{m} - 2 \times \sigma_m$ . As signal a gluino  $R$ -hadron sample with  $m_{\tilde{g}} = 2200$  GeV is used. The mass distribution is shown for the SR-Rhad-FullDet LOOSE.

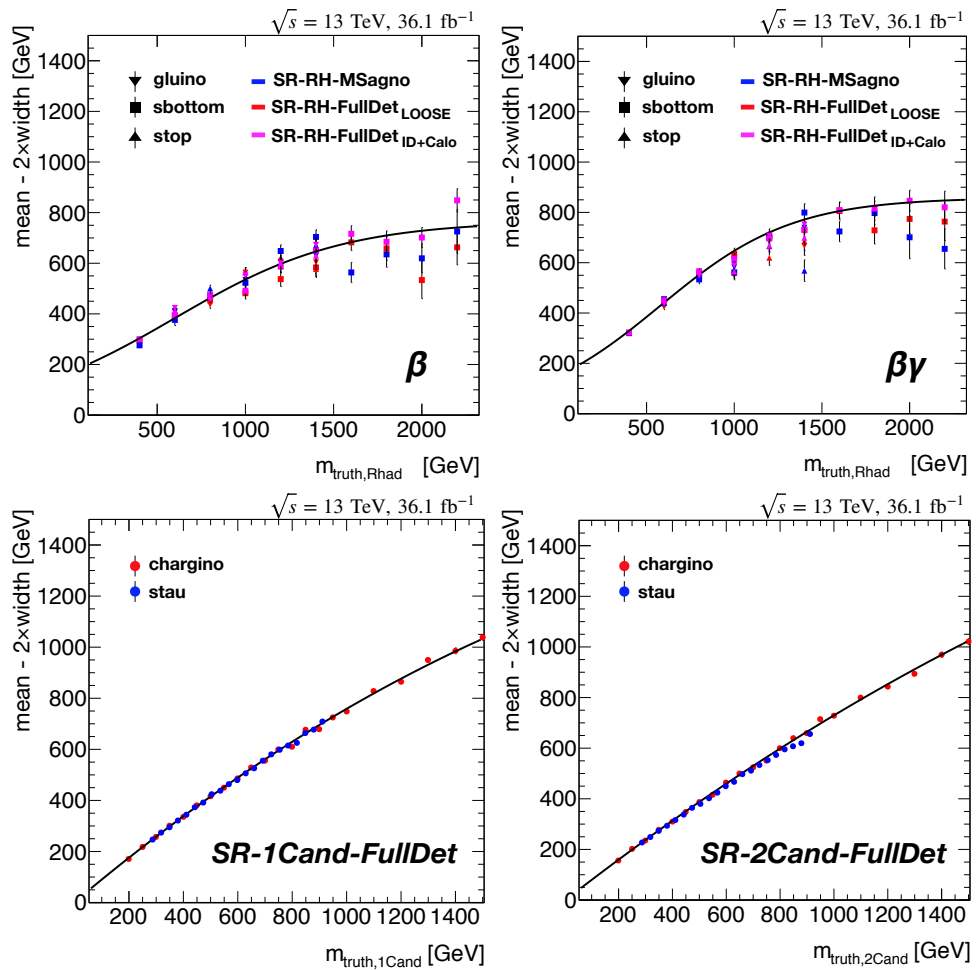


Figure 5.74: The lower mass limits estimated for each single model and mass hypothesis separate. They are overlaid by functional parameterisations that are used in common to estimate the smoothed lower mass cuts for the signal regions draw in the respective figures.

momentum uncertainties for high momentum ID tracks as discussed in Section 5.4.1. The plateau that is reached roughly for truth masses of 1500 GeV is due to a bias of the momentum and the larger momentum uncertainties, as can be seen in Figure 5.16. To find the best parametrisation for the functional form of the lower mass values for the  $R$ -hadron signal regions the software package *Eureqa* [142] is used. This package applies genetic algorithms to find the functional parametrisation of data points by mating, mutating and terminating functions that are made from user given mathematical blocks like  $+$ ,  $-$ ,  $\times$ ,  $/$ ,  $\exp$ . These algorithms optimise on the basis of fit quality and complexity. For the  $R$ -hadron signal regions the best result was obtained for

$$m_{low} = \frac{p_0}{p_1 + \exp(-m_{true} * p_2)}, \quad (5.23)$$

with

$$p_0 = 1.84 \cdot 10^2, \quad p_1 = 2.14 \cdot 10^{-1}, \quad \text{and} \quad p_2 = 2.66 \cdot 10^{-3} \quad (5.24)$$

for  $m_{TOF}$  and

$$p_0 = 2.17 \cdot 10^2, \quad p_1 = 2.82 \cdot 10^{-1}, \quad \text{and} \quad p_2 = 2.10 \cdot 10^{-3} \quad (5.25)$$

for  $m_{dE/dx}$ . Also the lower mass cuts for charginos and staus are estimated from the same parametrisation, but separate for the one candidate and two-candidate signal regions. A slightly lower mass cut is expected for the two-candidate regions as the lower mass candidate is used for the final counting. For the estimation of the lower mass cuts in the one and two-candidate signal regions a second order polynomial

$$m_{low} = p_0 + p_1 m_{true} + p_2 m_{true}^2 \quad (5.26)$$

is used and the parameters obtained are

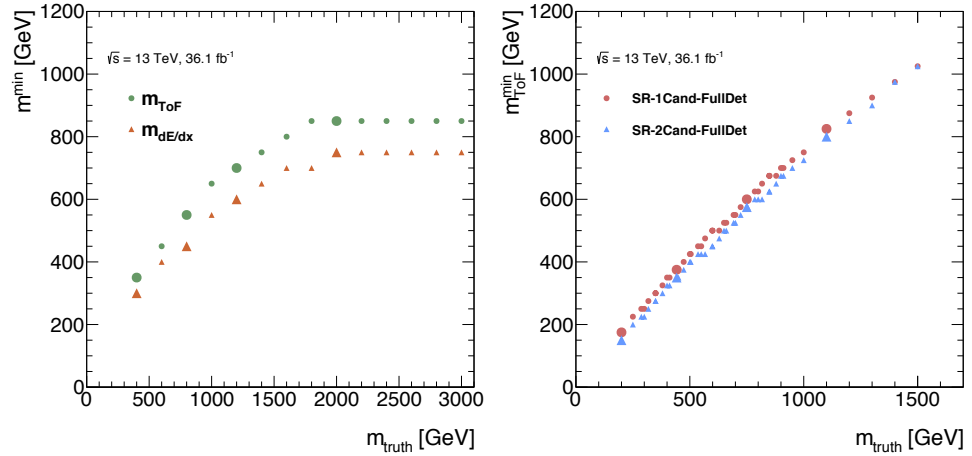
$$p_0 = 2.09, \quad p_1 = 0.90, \quad \text{and} \quad p_2 = -1.39 \cdot 10^{-4} \quad (5.27)$$

for the SR-1Cand-FullDet signal regions and

$$p_0 = -2.09, \quad p_1 = 0.83 \cdot 10^{-1}, \quad \text{and} \quad p_2 = -9.53 \cdot 10^{-5} \quad (5.28)$$

for the SR-2Cand-FullDet signal regions. From those parametrisations the lower mass cuts are calculated and rounded to the next bin border. The fi-

Figure 5.75: The lower mass requirements depending on the truth mass of the signal particles on  $m_{\text{ToF}}$  and  $m_{dE/dx}$  for the  $R$ -hadron signal regions and in  $m_{\text{ToF}}$  for the SR-1Cand-FullDet and SR-2Cand-FullDet. The visible steps in particular for SR-1Cand-FullDet and SR-2Cand-FullDet lower mass requirements originate from the rounding to the bin borders. The larger markers indicate the lower mass cuts used for the discovery regions. [5]



nal results for the lower mass requirements are shown in Figure 5.75. The difference between  $m_{\text{ToF}}$  and  $m_{dE/dx}$  originates mainly from the slightly different requirements on  $\beta$  and  $\beta\gamma$  in the final selections. In particular for the SR-1Cand-FullDet and SR-2Cand-FullDet steps in the lower mass requirements are visible. Those are originating from the rounding to the bin borders. Those final signal regions are used for the limit setting, but if some excess might be seen a subset of discovery regions, for which the p-values are calculated, was defined, to reduce the look-elsewhere effect [143]. The lower mass requirements for those discovery regions are indicated with the larger markers.

## 5.9 Background Estimation

The background in this analysis is estimated in a fully data-driven manner. First the shape of the key variables is estimated from sidebands where possible and stored in templates. The main background are high- $p_{\text{T}}$  muons with mis-measured  $\beta$  or  $\beta\gamma$ . Therefore no correlation between momentum and  $\beta/\beta\gamma$  is expected. The background can hence be estimated by sampling random combinations of  $\beta$ - $p$  ( $\beta\gamma$ - $p$ ) from the respective templates and calculating  $m = p/\beta\gamma$ . The normalisation of the background is obtained from low-mass control regions. The validity of the background estimate relies on two assumptions: Low signal contributions in the templates/control region and no significant correlation between  $\beta$  ( $\beta\gamma$ ) and momentum. Those assumptions are carefully checked as will be discussed in the following. The search is conducted as a blinded analysis and hence for the optimisation and tuning of the background estimate the mass region above 400 GeV was masked.

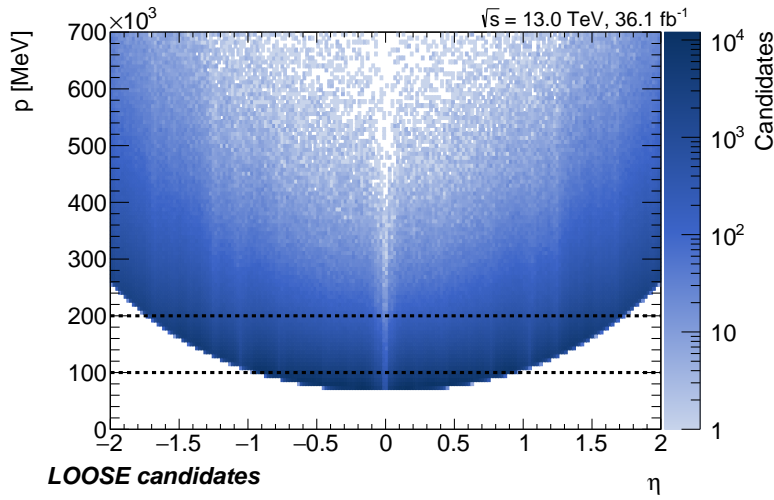


Figure 5.76: The momentum for all candidates passing the `LOOSE` pre-selection against  $\eta$ . Superimposed are the different momentum cuts (100 GeV and 200 GeV) used in the different final selections. It can be seen that the  $p_T$  cut from the preselection translates into a lower momentum requirement of roughly 250 GeV for  $|\eta| = 2.0$ .

**Sideband definitions** The templates are estimated from all candidates passing the respective pre-selection and fulfilling the final selection requirement for the respective observable. To ensure a low signal contamination in the templates the final selection cuts on the other observables are inverted. A study using a generic background and testing the influence of potential signal contribution in the templates is summarised in Appendix A.4. It was found that, if no sidebands are used, a significant change in the slope can be introduced from signal contaminations. The effect is larger for higher signal masses. This can be understood as the momentum as well as the velocities are further out in the tails of the respective templates for higher signal masses. There the statistics are low and therefore the relative signal contributions becomes significant.

The definition of the sidebands used for the templates of the  $R$ -hadron

| Template                     | $p$ [GeV]                  | $\beta_{\text{ToF}}$                            | $\beta\gamma_{\text{dE/dx}}$                                  |
|------------------------------|----------------------------|---|---|
| $p$                          | $> 200$                    | $1.0 > \beta_{\text{ToF}} > \beta_{\text{cut}}$ | $2.5 > \beta\gamma_{\text{dE/dx}} > \beta\gamma_{\text{cut}}$ |
| $\beta_{\text{ToF}}$         | $p_{\text{min}} < p < 200$ | $< \beta_{\text{cut}}$                          | -   |
| $\beta\gamma_{\text{dE/dx}}$ | $p_{\text{min}} < p < 200$ | -   | $< \beta\gamma_{\text{cut}}$                                  |

Table 5.9: The sideband definitions of the templates for the  $R$ -hadron signal regions.

signal regions are summarised in Table 5.9. All  $R$ -hadron signal regions are restricted to  $|\eta| < 1.65$ . For the ones using `ID+CALO` this is also indirectly required as  $|\eta| = 1.65$  corresponds to the outer edge of the Tile Calorimeter. For the full detector approach it is limited to  $\eta < 1.65$  as the mass limits

for  $R$ -hadrons are higher and hence the particles are expected more central. In the forward regions also large backgrounds from high-momentum muons are expected due to boosts from asymmetries in the momenta of the initial partons. Furthermore from Figure 5.76 it can be seen that the lower cut in  $p_T$  translates into a momentum cut larger than 200 GeV from  $\eta \approx 1.75$  on. This has two important consequences: On the one hand it introduces a correlation between  $\eta$  and momentum and on the other hand, due to the missing low momentum tracks, this region is underrepresented in the templates. For simplicity and as no huge gain is expected from increasing the  $\eta$  region, also `SR-Rhad-FullDet LOOSE` is restricted to  $|\eta| < 1.65$ . The template for momentum is obtained by applying the final momentum requirement but inverting the  $\beta_{\text{ToF}}$  and  $\beta\gamma_{dE/dx}$  requirements for the respective signal regions summarised in Table 5.8. For both  $\beta_{\text{ToF}}$  and  $\beta\gamma_{dE/dx}$  upper requirements are used. For  $\beta_{\text{ToF}}$  the upper requirement is needed as no mass can be calculated if  $\beta > 1$ . For the templates of  $\beta_{\text{ToF}}$  and  $\beta\gamma_{dE/dx}$  the momentum requirement is inverted. The definition of the sidebands used for the templates of the

| Template             | p [GeV]        | $\beta_{\text{ToF}}$              |
|----------------------|----------------|-----------------------------------|
| p                    | $> 200$        | $1.0 > \beta_{\text{ToF}} > 0.80$ |
| $\beta_{\text{ToF}}$ | $70 < p < 200$ | $< 0.80$                          |

Table 5.10: The sideband definitions of the templates for `SR-1Cand-FullDet`.

`SR-1Cand-FullDet` signal regions are summarised in Table 5.10. For the sidebands for the momentum template only the  $\beta_{\text{ToF}}$  requirement is inverted as for `SR-1Cand-FullDet` no  $\beta\gamma_{dE/dx}$  is used in the final selection. For the  $\beta_{\text{ToF}}$  template, similar as for the  $R$ -hadron signal regions, the final requirement on the momentum is inverted.

The `SR-2Cand-FullDet` has the strongest background suppression due to

| Template             | p [GeV] | $\beta_{\text{ToF}}$              |
|----------------------|---------|-----------------------------------|
| p                    | $> 100$ | $1.0 > \beta_{\text{ToF}} > 0.80$ |
| $\beta_{\text{ToF}}$ | -       | $< 0.80$                          |

Table 5.11: The sideband definitions of the templates for `SR-1Cand-FullDet`.

the requirement of two candidates in the event. This is critical for the background estimate as almost no events are left in the low-mass control region. To enlarge the statistics there all final requirements are chosen as loose as possible. The `SR-2Cand-FullDet` is therefore the only signal

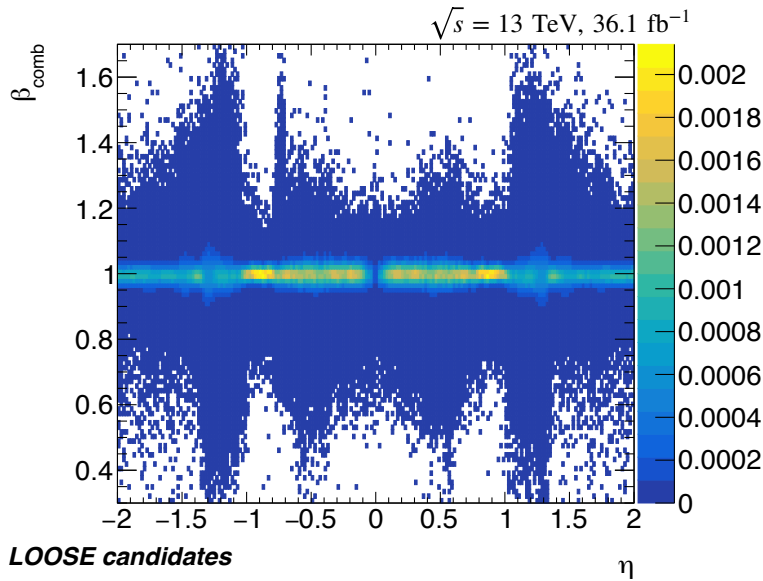


Figure 5.77: The combined  $\beta_{\text{TOF}}$  as function of  $\eta$  for all candidates passing the `LOOSE` selection. A slight asymmetry between  $\beta_{\text{TOF}}$  being larger and smaller one is visible which originates from the pre-selection requirement on  $\sigma_\beta$  and its dependence on  $\beta$  itself (Equation 5.7). Larger tails are visible for  $\eta = 0.5$  and  $\eta = 1.2$ . The  $\eta = 0.5$  originates from the MDT's as at this angle tracks can pass the tubes all on one side and hence purely from the drift circles no unambiguous track reconstruction is possible. The  $\eta = 1.2$  tails comes from the MS crack region where partially only view hits are expected.

region using candidates with  $|\eta|$  up to 2.0. Also the final momentum requirement is relaxed to 100 GeV for this signal region. Considering Figure 5.76 it can be seen that for  $|\eta| > 1$  no candidates with momentum smaller 100 GeV are left. If similar as for the  $R$ -hadron and one-candidate signal regions the momentum requirements would be inverted to estimate the  $\beta_{\text{TOF}}$  template no candidates from  $|\eta| > 1.0$  would be present and hence the  $\beta_{\text{TOF}}$  resolution from there would be not included. For the  $\beta_{\text{TOF}}$  template no sideband in momentum is used, while for the momentum template still the cuts on  $\beta_{\text{TOF}}$  are inverted. A possible influence by signal contamination using no sidebands was tested by injecting signal and found to be negligible as can be seen in Appendix A.5. For the `SR-2Cand-FullDet` templates no requirement on two `LOOSE` candidates per event is used as this would result in very low statistics in the templates. The shapes for templates with a two `LOOSE` candidate requirement were compared with the shapes using all `LOOSE` candidates and found to agree well within the statistic uncertainties.

**$\eta$ -binning of templates** As the background is basically high-momentum muons with mis-measured  $\beta$  or  $\beta\gamma$  no direct correlations are expected as muons with a high momentum are travelling with the speed-of-light at least on the  $\beta$ -resolution level achieved. Nevertheless correlation can occur indirectly mostly over  $\eta$ . For the combined  $\beta_{\text{TOF}}$  all three detectors are used and depending on whether they are present, different resolutions are expected, and hence also a correlation with  $\eta$ . Whereas the shape of the

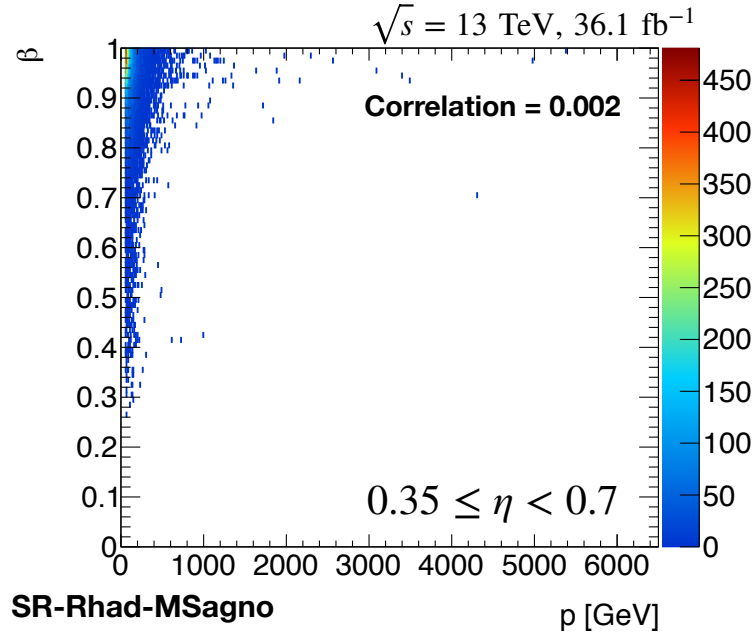


Figure 5.78: The correlation between  $\beta_{\text{ToF}}$  and the momentum for one  $\eta$ -bin for all candidates passing the MS-agnostic pre-selection. Before unblinding all candidates passing the final mass requirements were excluded from this plot.

| N | $ \eta $ lower | $ \eta $ upper |
|---|----------------|----------------|
| 1 | 0.0            | 0.35           |
| 2 | 0.35           | 0.7            |
| 3 | 0.7            | 1.1            |
| 4 | 1.1            | 1.25           |
| 5 | 1.25           | 1.65           |
| 6 | 1.65           | 2.0            |

Table 5.12: The lower and upper edges of the  $\eta$  bins used for the templates.

high momentum tail for ID tacks as well as SlowMuons is rather stable as function of  $\eta$ , which can be seen from Figure 5.76 or from the templates shown in Figures 5.79 and 5.80. Critical again is the SR-2Cand-FullDet as, due to the missing low momentum tracks for high  $\eta$ , an dependency of the momentum on  $\eta$  is introduced. An  $\eta$  binning of the templates is therefore introduced where at least the  $\beta_{\text{ToF}}$  resolution is roughly constant within a given  $\eta$  interval. The  $\eta$  bins where chosen by considering Figure 5.77, which shows the  $\beta_{\text{ToF}}$  of all candidates passing the LOOSE pre-selection. The  $\eta$  bins used are summarised in Table 5.12. The bins ending at 1.1 and 1.65 correspond approximately to the outer edges of the RPC's and Tile Calorimeter, respectively. All other bins are chosen due to the features found in the  $\beta_{\text{ToF}}$  distribution as function of  $|\eta|$ . The same  $\eta$  binning as used for SR-2Cand-FullDet is also applied to the other signal regions to reduce any possible residual correlations between  $\beta_{\text{ToF}}/\beta_{\text{dE/dx}}$  and the momentum. For each  $\eta$  bin and signal region the correlations between  $\beta/\beta_{\gamma}$  and momentum are estimated as shown in Figure 5.78. With the chosen  $\eta$  binning no significant correlations have been seen. Furthermore a systematic uncertainty is estimated by varying the  $\eta$ -binning, which will be described in more detail in Section 5.10.

The resulting templates for SR-Rhad-MSagno and SR-2Cand-FullDet are shown in Figures 5.79 and 5.80. The other templates are shown for completeness in Appendix A.3. For SR-Rhad-MSagno it can be seen that the distributions of  $\beta_{\text{dE/dx}}$  and momentum have a similar shape for the dif-

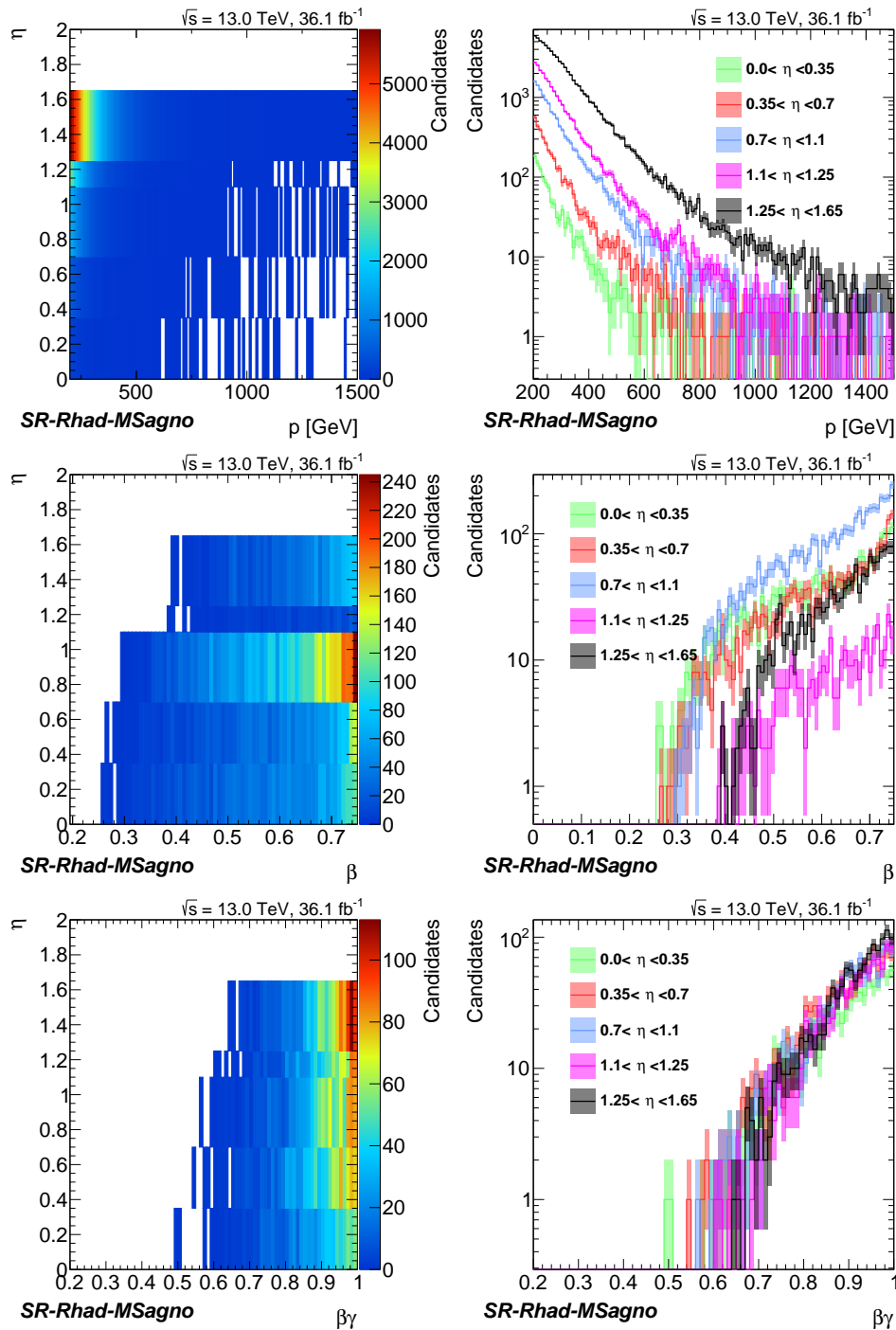


Figure 5.79: The templates used for the SR-Rhad-MSagno for the momentum (upper),  $\beta_{\text{ToF}}$  (middle) and  $\beta_{\gamma dE/dx}$  (lower). On the left the 2-dimensional distribution in  $\eta$  and the respective variable are shown, while the right plot shows the projection of each  $\eta$ -slice on the variable axis. While the distributions of  $\beta_{\gamma dE/dx}$  and momentum have a similar shape for the different  $\eta$ -bins, larger discrepancy can be found for  $\beta_{\text{ToF}}$ .

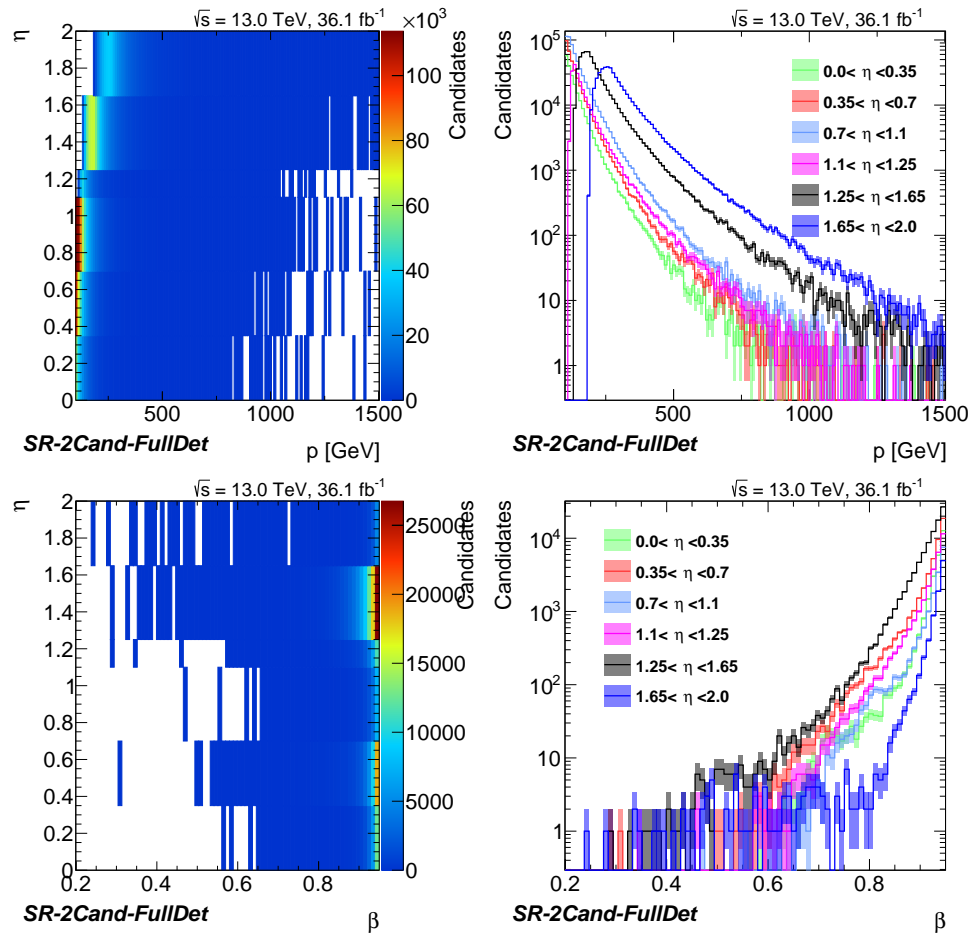


Figure 5.80: The templates used for the SR-2Cand-FullDet for the momentum (upper) and  $\beta_{\text{ToF}}$  (lower). On the left the 2-dimensional distribution in  $\eta$  and the respective variable are shown, while the right plot shows the projection of each  $\eta$ -slice on the variable axis. Clearly visible are the cut-offs at low-momenta due to the  $p_{\text{T}}$  requirement. For the  $\beta_{\text{ToF}}$  mainly the highest  $\eta$  bin shows a different shape. This  $\eta$  region has a rather good resolution in the core but many outliers as can be seen from Figure 5.77.

ferent  $\eta$ -bins, while larger discrepancies are found for  $\beta_{\text{ToF}}$ . Those discrepancies are due to inhomogeneous  $\beta$  resolution in the Tile Calorimeter originating mainly from the different shapes of the Tile Calorimeter cells. Clearly visible for the SR-2Cand-FullDet templates are the cut-offs at low-momenta due to the  $p_T$  requirement. For the  $\beta_{\text{ToF}}$  mainly the highest  $\eta$  bin shows a different shape. This  $\eta$  region has a rather good resolution in the core but many outliers as can be seen from Figure 5.77. The MS part in this region are the end-caps, where the path length to the measurement is long, which is the reason for the good core resolution of the distribution. But in this region only the MDT's are utilisable for ToF measurements, which on top have a lower number of expected hits, compared to the barrel, there. Due to the low statistics of single  $\beta$  measurements more outliers are expected, as can be seen in the respective template.

**Sampling and normalisation** In this section the estimation of the background from the templates will be discussed, which includes the propagation of the statistical uncertainties of the templates to the background estimate. First 50 variations of the templates are determined, where each content of a bin is sampled from a Poisson distribution using the content of the respective nominal bin as mean. For each candidate ending up in the control region 10000 combinations of  $\beta$  ( $\beta\gamma$ ) and momentum are sampled per Poisson-varied template in the  $\eta$  slices corresponding to the  $\eta$  of the candidate. From those combinations the mass distributions per Poisson-varied template are filled. The value ( $x$ ) and statistical uncertainty ( $\sigma_x$ ) of each mass bin are then calculated from the values ( $p_i$ ) of the mass distributions per poisson varied template with

$$x = \frac{\sum_i p_i}{50} \quad (5.29)$$

and

$$\sigma_x = \sqrt{\frac{\sum_i p_i^2}{50} - x^2}. \quad (5.30)$$

Finally the background is normalised to data using the low mass control regions. Potential issues for this approach can occur if significant signal contaminations arise in the control region. First a potential signal contamination in the control region would change the  $\eta$  distribution in the control region, mostly to be more central as HCLLPs are heavy. This could enhance  $\eta$  slices with long (short) tails and hence over (under) estimate the real background distribution. Second a potential signal contamination

would contribute to the normalisation of the background. This should be an even larger effect than the first, as the relative fraction between signal and background yield in the control region gives the overestimation of the normalisation and hence the overestimation of the background yield in the final counting window. An alternative approach (Appendix A.6) for the sampling of the background was developed, building also templates for the  $\eta$  distribution of the candidates, and successfully tested for the SR-Rhad-MSagno. This approach has the benefit of being more robust against contaminations of low-mass signals. The difficulty was in the fall-back signal regions as their  $\eta$  distribution is not independent from the prioritised signal region. This strategy is in the end not applied for the SR-Rhad-MSagno, to have a common approach for all signal regions, but might be interesting for future iterations of this analysis. For the approach using the  $\eta$  of the candidates, the control region requirements have to be carefully tuned to get rid of any potential signal contamination there. The expected signal yields in the control region are estimated using roughly the current cross section limits for the respective model. For charginos and staus the limits from Run-1 [97] are extrapolated to 13 TeV (stau 2.5 fb and chargino 5 fb), while for  $R$ -hadrons roughly the limits from the first  $\sqrt{s} = 13$  TeV analysis [101] are used ( $R$ -hadron 20 fb). Less than 2% signal contamination for all cases was achieved by using 300 GeV for  $m_{\text{ToF}}$  and  $m_{dE/dx}$  as upper mass limit for the  $R$ -hadron control regions and 200 GeV (150 GeV) as upper mass limits on  $m_{\text{ToF}}$  for SR-1Cand-FullDet (SR-2Cand-FullDet).

**Results of background estimate** The background estimate for SR-Rhad-MSagno overlaid by the data points and the expected distribution for a gluino  $R$ -hadron model with  $m_g = 2200$  GeV is shown in Figures 5.81. In the low mass region a good agreement between data and estimate background can be observed. A small excess can be seen in the signal region. Note that the background in the signal region is lower than what can be seen in the projections of the 2D-histograms. The two events in the signal region are rather diagonal and not suspiciously uncorrelated, which could be an hint for an outlier of the respective measurements. The estimated background for SR-Rhad-FullDet LOOSE overlaid by the data points and the expected distribution for a gluino  $R$ -hadron model with  $m_g = 2200$  GeV is shown in Figures 5.82. Also for this signal region a good agreement between the estimated background and the observed data in the low-mass region can be seen. Compared to SR-Rhad-MSagno

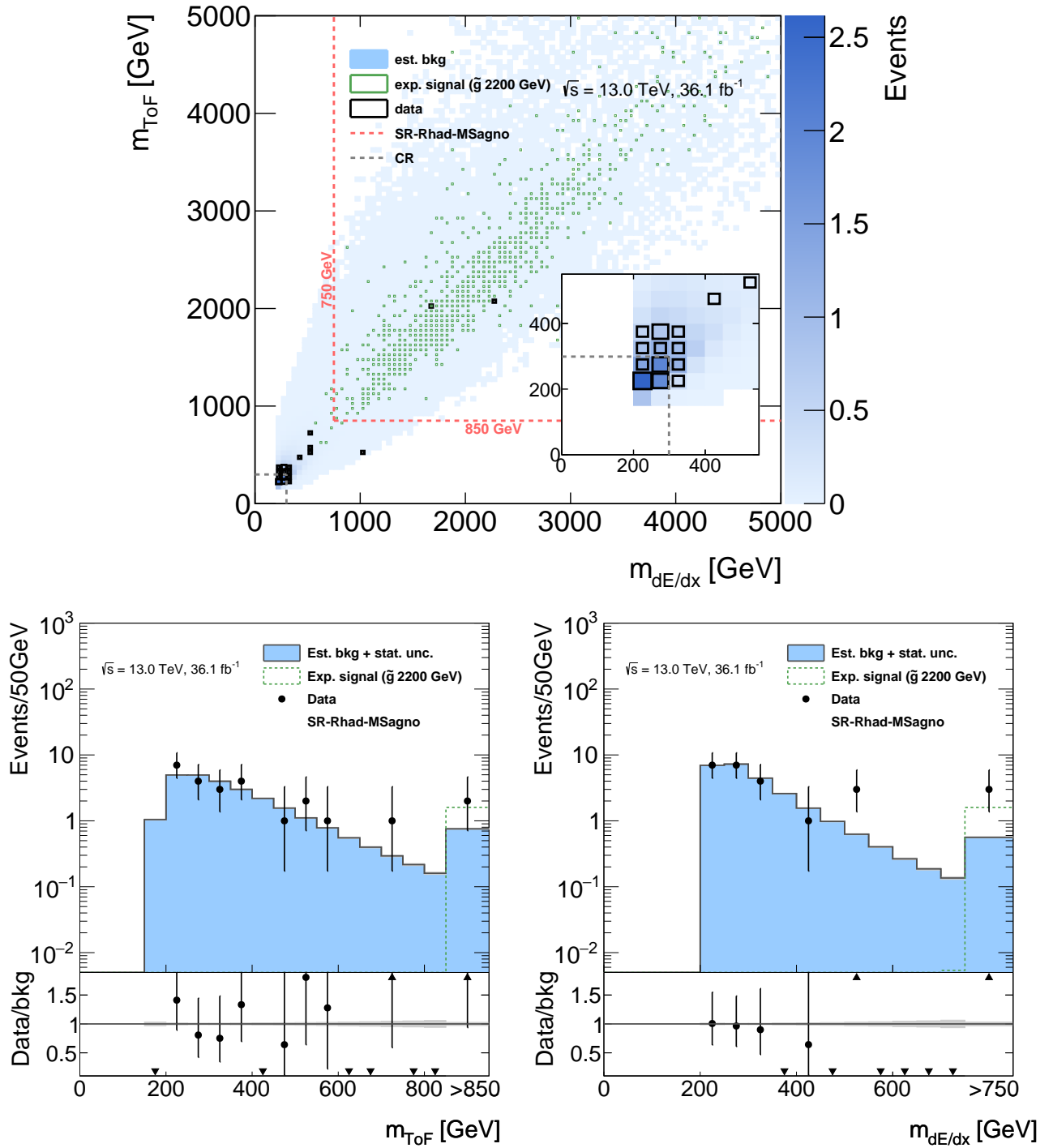


Figure 5.81: The estimated background for the SR-Rhad-MSagno signal region in the  $m_{\text{TOF}}-m_{\text{dE/dx}}$  plane (top), the  $m_{\text{TOF}}$ -projection (bottom-left) and the  $m_{\text{dE/dx}}$ -projection (bottom-right). The distribution is overlaid by the data points and the distribution for a gluino  $R$ -hadron model with  $m_g = 2200$  GeV. The overflow is included in the last bin of each distribution. The lower mass requirements of the signal region for one mass hypothesis of gluino  $R$ -hadrons is indicated by the dotted red lines in the upper figure, while the dotted grey lines are illustrating the upper bound for the control region, which is the same for all  $R$ -hadron signal regions. The inset in the two-dimensional distribution shows a zoomed version of the low-mass region. The statistical uncertainty on the background estimate is illustrated with the shaded grey area. The lower panels show the ratio of observed data over estimated background. [5]

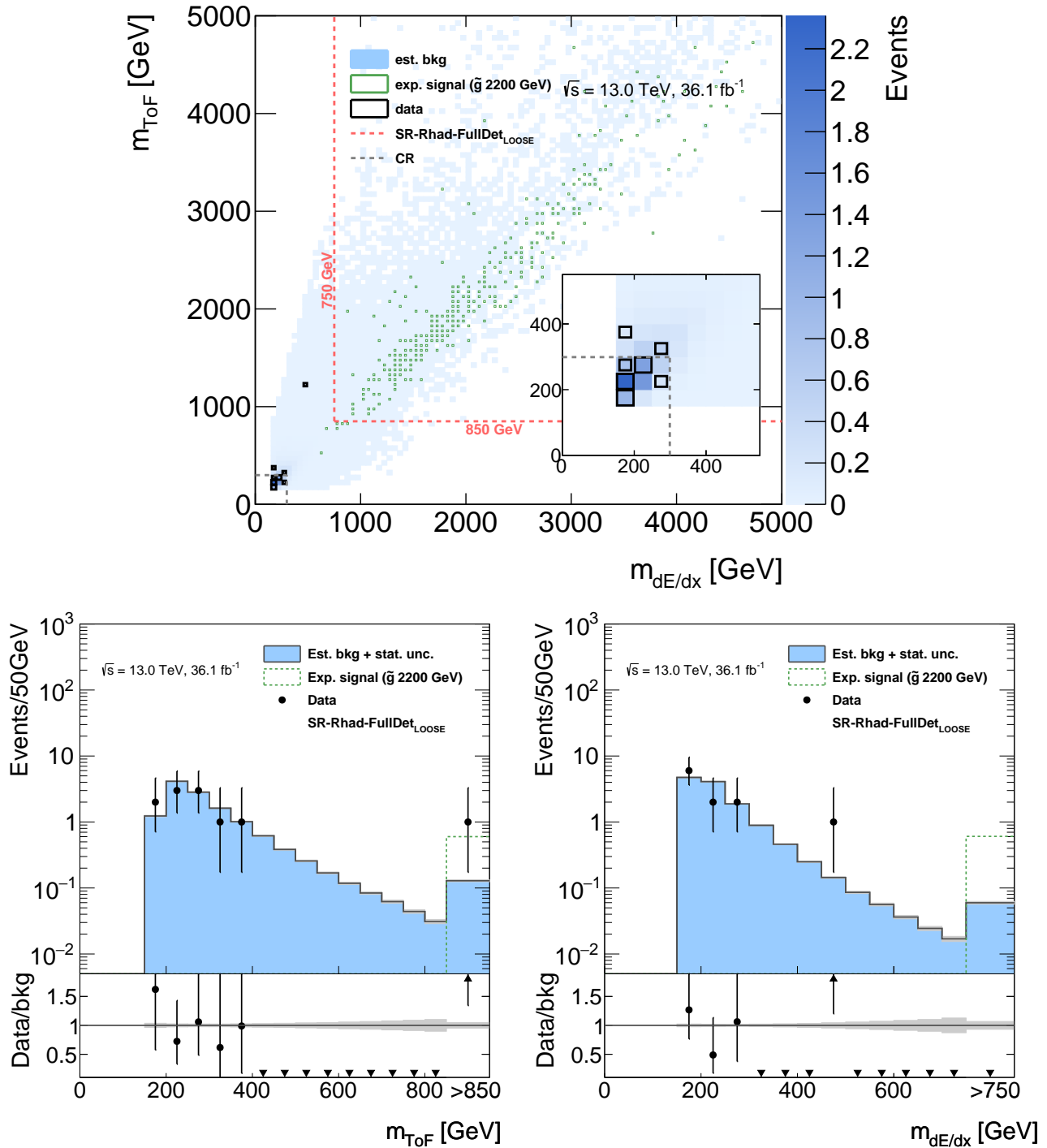


Figure 5.82: The estimated background for the SR-Rhad-FullDet<sub>LOOSE</sub> signal region in the  $m_{\text{ToF}}-m_{\text{dE/dx}}$  plane (top), the  $m_{\text{ToF}}$ -projection (bottom-left) and the  $m_{\text{dE/dx}}$ -projection (bottom-right). The distribution is overlaid by the data points and the distribution for a gluino  $R$ -hadron model with  $m_g = 2200$  GeV. The overflow is included in the last bin of each distribution. The lower mass requirements of the signal region for one mass hypothesis of gluino  $R$ -hadrons is indicated by the dotted red lines in the upper figure, while the dotted grey lines are illustrating the upper bound for the control region, which is the same for all  $R$ -hadron signal regions. The inset in the two-dimensional distribution shows a zoomed version of the low-mass region. The statistical uncertainty on the background estimate is illustrated with the shaded grey area. The lower panels show the ratio of observed data over estimated background. [5]

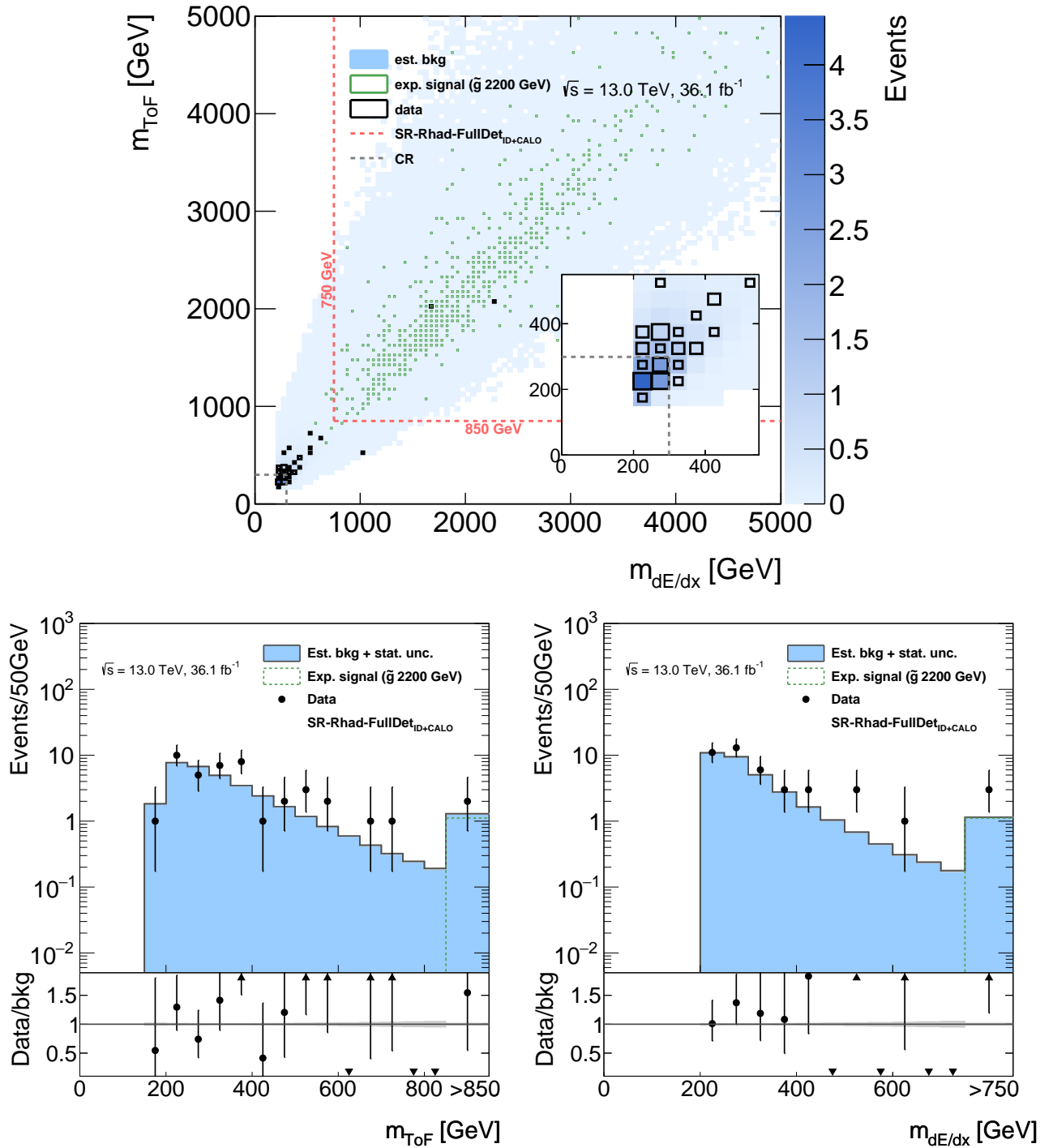


Figure 5.83: The estimated background for the SR-Rhad-FullDet<sub>ID+CALO</sub> signal region in the  $m_{\text{ToF}}-m_{\text{dE/dx}}$  plane (top), the  $m_{\text{ToF}}$ -projection (bottom-left) and the  $m_{\text{dE/dx}}$ -projection (bottom-right). The distribution is overlaid by the data points and the distribution for a gluino  $R$ -hadron model with  $m_g = 2200$  GeV. The overflow is included in the last bin of each distribution. The lower mass requirements of the signal region for the given mass hypothesis of gluino  $R$ -hadron is indicated by the dotted red lines in the upper figure, while the dotted grey lines are illustrating the upper bound for the control region, which is the same for all  $R$ -hadron signal regions. The inlay in the two-dimensional distribution shows a zoomed version of the low-mass region. The statistical uncertainty on the background estimate is illustrated with the shaded grey area. The lower panels show the ratio of observed data over estimated background. [5]

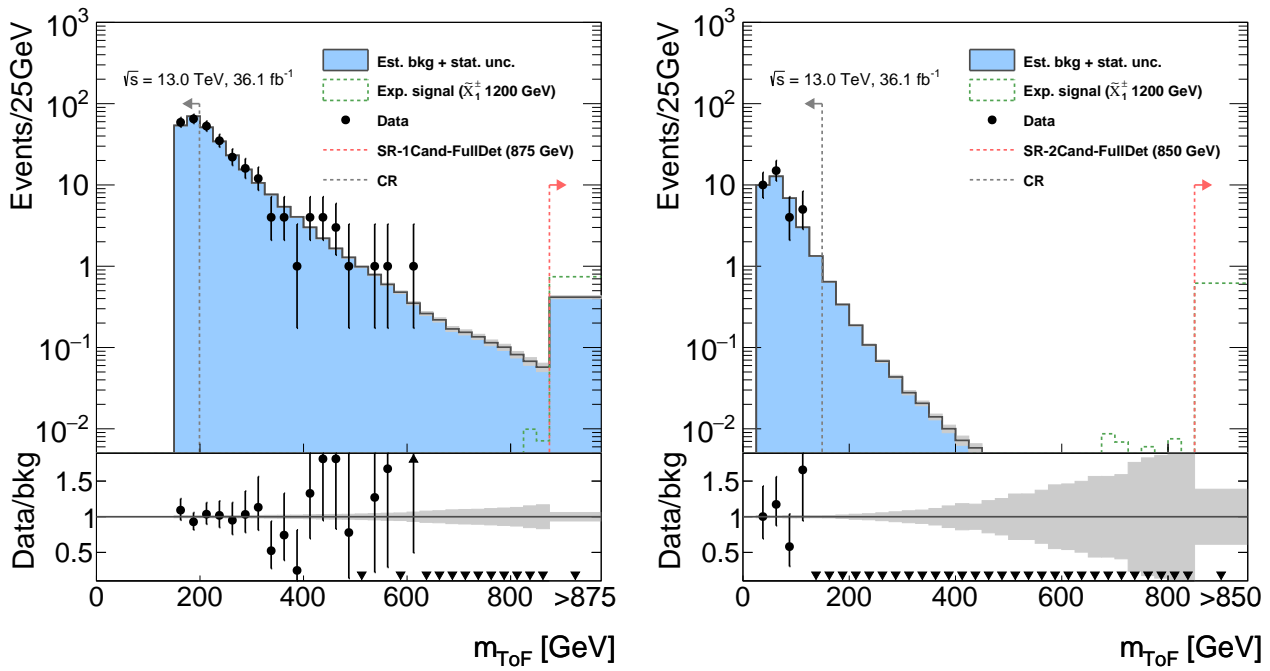


Figure 5.84: The estimated background for the one-TIGHT-candidate signal region (left) and the two-LOOSE-candidates signal region (right). The distributions are overlaid with the data points and the distribution for a pair-produced chargino model with  $m(\chi_{1\pm}^\pm) = 1200$  GeV. The last bin of each distribution includes the overflow. The dotted red line indicates the lower bound of the signal region for a representative signal choice, while the dotted grey line is illustrating the upper bound for the control region. The statistical uncertainty on the background estimate is illustrated with the shaded grey area. The lower panels show the ratio of observed data over estimated background. [5]

the background level is lower due to the better background suppression from the combined  $\beta_{\text{TOF}}$ . Only one high-mass outlier can be observed, which has largely different  $m_{\text{TOF}}$  and  $m_{dE/dx}$  and does not end up in the final signal region.

The estimated background for `SR-Rhad-FullDet ID+CALO` overlaid by the data points and a the expected distribution for a gluino  $R$ -hadron model with  $m_g = 2200$  GeV is shown in Figures 5.83. This signal region is largely similar to the `SR-Rhad-MSagno`, but the prioritised `SR-Rhad-FullDet LOOSE` does absorb less candidates than what is added by the additional single-muon triggers and hence higher statistics are seen. The same high-mass candidates as in the `SR-Rhad-MSagno` are observed, but are in better agreement with the background expectation.

The estimated background for `SR-1Cand-FullDet` and `SR-2Cand-FullDet` overlaid by the data points and the expected distribution for pair-produced charginos with  $m(\chi_1^\pm) = 1200$  GeV are shown in Figures 5.84. For both signal regions a good agreement between data and expected background is observed, in particular for the `SR-1Cand-FullDet`, where due to the large statistics a shape comparison over a broad range is possible.

## 5.10 Systematic uncertainties

A variety of potential sources of systematic uncertainties have to be considered. The resulting uncertainties for the search for HCLLPs are summarised in Table 5.13. They can be split into four different categories: The uncertainty on the theoretical cross section, the uncertainty on the signal efficiency, the uncertainty on the integrated luminosity recorded by the ATLAS detector and the uncertainty on the background estimate. The largest systematic uncertainties are found on the theoretical cross section and on the background estimate for  $R$ -hadron models with the highest considered sparton masses. All different sources of systematic uncertainties and their estimation will be discussed in the following.

### 5.10.1 Theoretical cross section

The  $R$ -hadron cross sections are calculated to NLO+NLL accuracy using NLL-fast [144]. For staus and charginos PROSPINO2 is used with a NLO accuracy, as mentioned in Section 5.3. Both the nominal value of the cross section as well as the uncertainty on the cross section are estimated from an envelope of calculations using different PDF sets and fac-

| Source                                 | MS-agnostic<br><i>R</i> -hadrons | Relative uncertainty [%]           |            |            |
|--|----------------------------------|------------------------------------|------------|------------|
|  |                                  | Full-detector<br><i>R</i> -hadrons | Staus      | Charginos  |
| Theoretical inclusive cross section    | 14 – 57                          | 14 – 57                            | 6 – 10     | 4 – 10     |
| Total uncertainty on signal efficiency | 17 – 19                          | 18 – 30                            | 7 – 15     | 9 – 18     |
| Trigger efficiency                     | 1.6                              | 1.9                                | 4.5        | 3.9        |
| $\cancel{E}_T$                         | 1.6                              | 1.6                                | 2.0        | 2.5        |
| Single-muon                            |                                  | 1.0                                | 4.0        | 3.0        |
| Theoretical uncertainty (ISR/FSR)      | 15                               | 15                                 | 4          | 7          |
| Pile-up                                | 0.2 – 3.8                        | 0.3 – 5.5                          | 0.1 – 3.1  | 0.2 – 4.4  |
| SlowMuon reconstruction                | -                                | 1.7 – 14.8                         | 0.2 – 12.8 | 0.8 – 13.0 |
| Track hit requirements                 | 2                                | 2                                  | 2          | 2          |
| Pixel $\beta\gamma$ measurement        | 6.0 – 11.6                       | 6.0 – 13.0                         | 0.5        | 0.5        |
| ToF $\beta$ measurement                | 0.5 – 3.6                        | 9.8 – 21.9                         | 1.0 – 3.6  | 2.0 – 12.0 |
| Calorimeter $\beta$ measurement        | 0.1 – 0.5                        | 0.1 – 1.1                          | 0.1 – 0.5  | 0.1 – 0.5  |
| Calorimeter OFA correction             | 0.4 – 3.6                        | 1.2 – 3.1                          | 0.1 – 0.4  | 0.1 – 1.3  |
| MS $\beta$ measurement                 | -                                | 9.7 – 21.7                         | 1.0 – 3.5  | 2.0 – 12.0 |
| Luminosity                             | 2.1                              | 2.1                                | 2.1        | 2.1        |
| Uncertainty on background estimate     | 33 – 34                          | 27 – 53                            | 9 – 31     | 9 – 34     |

Table 5.13: Summary of systematic uncertainties. The different blocks give the uncertainty on the cross section, the signal efficiency, the luminosity and on the background estimate. The given ranges indicate a dependence on the mass hypothesis.

torisation/renormalisation scales. The procedure is summarised in Reference [145]. For gluino *R*-hadron models an uncertainty on the theoretical cross section between 14% for the lowest mass (600 GeV) and 57% for the highest masses (3000 GeV) was obtained, while for squark *R*-hadrons the uncertainty varies between 14% (600 GeV) and 23% (1400 GeV). For the direct pair-production of charginos and staus smaller uncertainties are obtained as those are electroweak processes. They vary between 6% (290 GeV) and 10% (910 GeV) for staus and between 4% (200 GeV) and 10% (1500 GeV) for charginos.

### 5.10.2 Signal efficiency

The largest systematic uncertainty on the signal efficiency originates from the modelling of the ISR as the triggering of the events in particular for the *R*-hadron models largely rely on ISR jets. A further important systematic uncertainty comes from the modelling of the reconstruction efficiency of the MuGirlStau algorithm and from the uncertainty on the  $\beta$  estimate with the MS.

**Trigger efficiency** The efficiency of the  $\cancel{E}_T$  trigger can be assessed using muons. The  $\cancel{E}_T$  on trigger level is solely reconstructed from energy de-

positively in the calorimeters and as muons are similar to HCLLPs minimum ionising only moderate contributions from them are expected. The turn-on behaviour of the  $\cancel{E}_T$  triggers can hence be measured by using events selected by muon triggers. For this study single-muon triggers are used and the events in data and simulated  $Z \rightarrow \mu\mu$  events have to fulfil the  $Z \rightarrow \mu\mu$  selection described in Section 5.5.2. The turn-ons in both data and simulation are fitted with an error function. Those turn-ons are then applied to the offline  $\cancel{E}_T$  spectrum in the signal samples. The offline  $\cancel{E}_T$  used for this study is not using information from the MS. Four individual contributions to the systematic uncertainty are considered: The difference between data and simulation, a scale variation of signal  $\cancel{E}_T$  and a variation of the fit parameters by  $\pm 1\sigma$  for data and simulation, respectively. For each contribution an uncertainty is estimated. The differences in signal yield estimated from the variations are used as systematic uncertainty. The individual contributions are added in quadrature to obtain the total uncertainty. The total systematic uncertainty on the  $\cancel{E}_T$  trigger for  $R$ -hadrons is found to be 1.6%, while for charginos 2.5% and for staus 2.0% were obtained.

The turn-on behaviour for the muon trigger as function of  $p_T$  is not problematic for this search due to the high momenta HCLLPs are expected to be produced with as well as due to the hard offline  $p_T$  requirements on the candidates. More problematic is the turn-on behaviour as a function of the velocity of the particles as they might be associated to the wrong bunch crossing, and hence no muon reconstruction on HLT is possible due to the missing ID tracks. The correct simulation of the timing is hence crucial. For TGC's this is expected to be reliable, while for the RPC's some differences between data and simulation have been observed. A method using ideal turn-ons is applied, as now slow SM particles produced in the collisions are able to reach the MS and hence could be used to study the turn-on behaviour. The ideal turn-ons use the mean and width of the timing distribution to give an efficiency as function of the particle  $\beta$  and  $\eta$ . The dependence of  $\eta$  arises from the change in distance to the trigger chambers as function of  $\eta$ . The difference between the ideal turn-ons for data and simulation is used as event weight. Half the difference between the signal efficiency with and without the event weights applied is used as systematic uncertainty. The estimated uncertainty for  $R$ -hadrons in the full-detector signal region is 1%, while for staus 4% and for charginos 3% are obtained.

A detailed description of the estimation of the systematic uncertainties

on the trigger efficiency can be found in Reference [128].

**Initial state radiation** The modelling of QCD radiation is crucial for this analysis, as the triggering of HCLLPs with  $E_T$  triggers largely relies on an ISR jet recoiling against the sparticle system.

For  $R$ -hadron signals that are simulated with PYTHIA6 a re-weighting is introduced to match the ISR distribution, measured as the  $p_T$  of the gluino system, from MG5\_AMC@NLO as described in Section 5.3. As systematic uncertainty half the differences between the signal efficiencies with and without the ISR re-weighting is used. An uncertainty of 15% is obtained, which is the dominant contribution to the total systematic uncertainty on the signal efficiency for  $R$ -hadrons.

For charginos and staus a slightly different approach is applied as those samples are generated with MG5\_AMC@NLO and hence no re-weighting is necessary. The systematic uncertainty for those samples is assessed by varying the generator parameters. Three different variations were used: The renormalisation/factorisation scales are varied by a factor two, the CKKW-L merging [146, 147] scale is also varied by a factor of two and variations of the PYTHIA8 tunes are used to assess the uncertainty of the parton-shower generator tuning. The uncertainties from the different variations are added in quadrature to obtain the total uncertainty. The estimated uncertainties are 4% for staus and 5% for charginos.

As the variations of the MG5\_AMC@NLO generators are more trustworthy also gluino samples with the varied generator parameter were produced. For each variation a separate re-weighting was applied and the impact on the signal efficiency was estimated in the same way as for staus and charginos. The resulting uncertainty was found to be 13%. To be consistent with other analyses [94, 127, 148] using the same dataset the 15% uncertainty from the re-weighting between the generators is used for the analysis. A detailed description of the estimation of the ISR/FSR systematic uncertainties can be found in Reference [128].

**Pile-up** A re-weighting is applied to simulated events to match the pile-up conditions as observed in data. To account for differences between the estimation methods of the pile-up either by dedicated luminosity detectors or by the number of primary vertices, the scale of the pile-up re-weighting is varied. Half the difference between the maximal and minimal signal efficiency, obtained from the variations of the pile-up scale for the reweighting, is used as systematic uncertainty. The uncertainty varies

between 0.1% and 5.5% depending on the mass hypothesis and the considered signal model.

**SlowMuon reconstruction** The SlowMuon reconstruction efficiency was measured with respect to muons fulfilling the medium quality requirements as defined in Reference [126] reconstructed by a standard algorithm. It was found that the efficiency in simulation is underestimating the efficiency estimated in data by less than 10%. To estimate the effect of a 10% variation of the reconstruction efficiency on the signal efficiency 10% of the candidates reconstructed as SlowMuons are randomly rejected. For the SR-2Cand-FullDet the estimated uncertainty is about 10%, but the fall-back SR-1Cand-FullDet can recover some of the lost signal events, hence there a significantly lower uncertainty of 1% – 6% is found.

**Track hit requirements** Studies were carried out for the analysis described in Reference [127] on the efficiency of selecting tracks with the ID hit requirements described in Section 5.7. The difference in the efficiency between  $Z \rightarrow \mu\mu$  events in data and simulation is used as systematic uncertainty and found to be 2%.

**Pixel  $\beta\gamma$  measurement** The procedure of estimating the uncertainties and partially also the uncertainties themselves are taken from Reference [127]. Four different contributions were considered and in the end added in quadrature.

The requirement of at least two pixel clusters used for the  $dE/dx$  estimation was estimated in the same way as the uncertainty on the track hits requirements as discussed in the previous section. The corresponding uncertainty was found to be 6%.

The MPV of the  $dE/dx$  distribution is aligned between data and simulation. But a run-by-run variation of the MPV of 2% was observed. To test the effect of a potential misalignment between data and simulation a 2% variation is applied on the MPV for the signal samples. Half the difference between the signal efficiency from the variations is used as systematic uncertainty.

Besides the MPV also shape differences can be problematic. The shape of the  $dE/dx$  distribution in data and simulation is slightly different as shown in Figure 5.85. Furthermore it was observed that the shape of the  $dE/dx$  distribution is different between an initial and a final run of the data

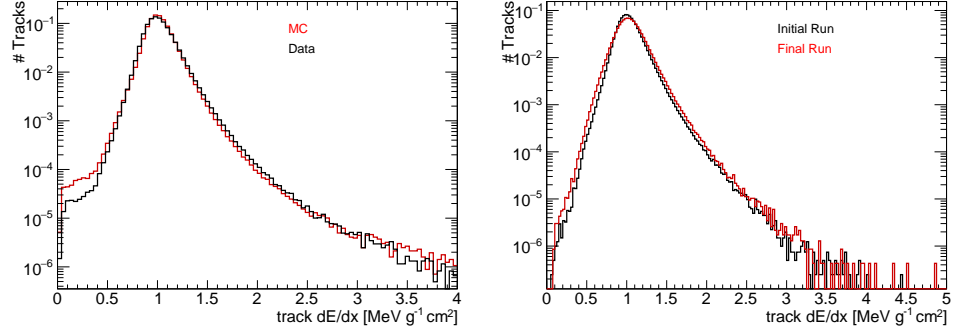


Figure 5.85: Left: Shape comparison between the  $dE/dx$  distribution from tracks in data and simulation using minimum bias data. Right: Shape comparison between the  $dE/dx$  distribution from tracks of an initial and a final run of the data taking period considered in this analysis. [149]

taking periods considered in this analysis. Due to radiation damage the  $dE/dx$  distribution is observed to be slightly broader for a final run. In the analysis using only the ionisation energy loss the final requirements are made on  $dE/dx$  itself and not  $\beta\gamma_{dE/dx}$ . To obtain a systematic uncertainty first the fraction of tracks above the final  $dE/dx$  requirement is estimated for the  $dE/dx$  distribution in data. This is used to get the  $dE/dx$  value for which the same fraction of tracks is above the requirement in simulation. This value is used as variation of the  $dE/dx$  cut in the final selection and the effect on the signal efficiency is used as systematic uncertainty. In a similar way the cut variations are also obtained for the  $dE/dx$  shape differences between an initial and a final run. This is not directly applicable for this analysis as the final requirements for the  $R$ -hadron signal regions are made on  $\beta\gamma_{dE/dx}$ . To get the variation in  $\beta\gamma_{dE/dx}$  first the six different  $dE/dx$  values from the different transformation functions<sup>3</sup> are calculated, each of the values is transformed like described above and translated back to a  $\beta\gamma_{dE/dx}$  value. The largest difference to the nominal  $\beta\gamma_{dE/dx}$  cut is used conservative variation for all cases. The cut variations used in this analysis are summarised in Table 5.14. The different cuts are then applied

<sup>3</sup>Three different functions depending on number of used pixel clusters times two charges, as described in Section 5.5.1

Table 5.14: Cut variations on  $\beta\gamma_{dE/dx}$  or  $dE/dx$  depending on the signal region. The difference for cut variations is small for the SR-1Cand-FullDet as the cut is almost exactly at the MPV. The largest difference between the cut variations is in the SR-Rhad-FullDet LOOSE.

|                      | SR-Rhad-MSagno<br>$\beta\gamma_{dE/dx}$ | SR-Rhad-FullDet LOOSE<br>$\beta\gamma_{dE/dx}$ | SR-1Cand-FullDet<br>$dE/dx$ [MeVg <sup>-1</sup> cm <sup>2</sup> ] |
|----------------------|---|--|---|
| nominal              | 1.0                                     | 1.3  | 1.0   |
| data/simulation      | 1.02                                    | 1.25   | 1.01  |
| intial run/final run | 0.97                                    | 1.37   | 1.01  |

and the difference in signal efficiency is used as systematic uncertainty. The overall systematic uncertainty due to the  $\beta\gamma_{dE/dx}$  measurement is found to be between 6% and 11.6% for SR-Rhad-MSagno, between 6% and 13% for SR-Rhad-FullDet LOOSE and below 0.5% for all chargino and stau

signal models. For the  $R$ -hadron signal regions the largest uncertainty are observed for the low masses while for high masses only the uncertainty from the two pixel cluster requirement is left. The reason is that for the high masses the  $\beta_{\gamma_{dE/dx}}$  cuts are in the tails of the distribution and hence the variations have very little impact.

**ToF  $\beta$  measurement** The systematic uncertainty due to potential mis-modelling of the  $\beta$  measurements in simulation have to be tested as it is one main variable to identify HCLLPs. The methods are slightly different between the measurements from the different subsystems and will be explained in the following.

For the MDT's a smearing/sharpening procedure is applied to adjust the timing resolution observed in simulation to the one observed in data, as described in Section 5.5.3. The  $\beta_{RPC}$  distributions estimated using 5% variations of the calibration constants are found to bracket the  $\beta_{RPC}$  observed in data. The effect of these variations on the signal efficiency is evaluated and half the difference between the up and downward variation are used as systematic uncertainty.

For the RPC's a more complicated correction for the timing in simulation, to match the timing resolutions observed in data, was necessary, as described in Section 5.5.3. To be conservative the difference between the signal efficiency with and without the RPC simulation corrections is used as systematic uncertainties. The RPC  $\beta_{ToF}$  uncertainty is up to 22% for  $R$ -hadron signal models while significantly lower for chargino and stau models. The reason for the large uncertainties for the  $R$ -hadron models is that due to a bug a significant fraction of  $\beta_{RPC}$  measurements in simulation was rejected. For  $R$ -hadrons a slightly asymmetric  $\beta$  resolution is observed due to the hadronic interactions. After solving the RPC issue the consistency between the measurements get problematic as RPC  $\beta$  measurements are added to a significant fraction of candidates. The RPC has the best  $\beta$  resolution and is likely to be in conflict with the Tile Calorimeter measurement due to the described asymmetry there. A re-optimisation of the consistency requirement could solve this problem but as the bug was found after unblinding this was not possible anymore and matching systematic uncertainty has to be assigned to the RPC measurement.

Two different sources of systematic uncertainties on the Tile Calorimeter  $\beta_{TILE}$  estimation are considered: A potential mis-modelling of the resolution and an under or over estimation of the OFA correction as described in Section 5.5.2. To assess the potential mis-modelling of the timing resolu-

tion the smearing that was applied in simulation to match the resolution seen in data is scaled up and down by 5%. The uncertainty due to a potential bias for large  $t_0$  potentially introduced by an under or over estimation of the OFA correction is address by scaling the correction by  $\pm 50\%$ . The effect of the resolution variations is very small and found to be below 1.1% for any case. Also the effect of the scaling of the OFA correction is rather small ( $< 3.6\%$ ), while the correction on the timing is rather large. This can be explained as the correction is significant for large  $t_0$  but negligible for small  $t_0$ . Large  $t_0$  values correspond to a low  $\beta$  and are hence far away from the final  $\beta$  requirements, which results in a moderate impact of this variation on the signal efficiency.

### 5.10.3 Luminosity

The uncertainty on the integrated luminosity used for this analysis was found to be 2.1%. The procedure of the uncertainty determination follows the one described in Reference [150] and uses beam-separation scans that were carried out in August 2015 and May 2016.

### 5.10.4 Background estimation

Three different contributions to the total uncertainty on the background estimate are considered. The  $\eta$ -binning for the templates, the composition in the templates, and the normalisation of the background.

To estimate an uncertainty due to the particular choice of the  $\eta$  binning used to uncorrelate  $\beta$  ( $\beta\gamma$ ) and momentum, the number of  $\eta$  bins is varied. The number of  $\eta$  bins is lowered to three and increased to seven from the nominal five for all signal regions using  $\eta < 1.65$ . For SR-2Cand-FullDet the only signal region which uses the  $|\eta|$  range up to 2, the variation is from nominal six to four and nine  $\eta$  bins, respectively. The  $\eta$  intervals used for the lowered and the increased number of bins are shown in Figure 5.17 and Figure 5.16, respectively. For the lowered number of bins  $\eta$  roughly similar  $\eta$  intervals are, while for the increased number of bins in particular for  $\eta > 1.65$  smaller slices are chosen, as there the effect of the missing low momentum tracks (Figure 5.76) gives the strongest  $\eta$ -momentum correlation.

To assess the systematic uncertainty due to a residual correlation in the  $\eta$  bins and on the definition of the sidebands, the composition of the templates is slightly changed by tightening the sideband requirements. In the  $R$ -hadron signal regions the  $\beta_{\text{ToF}}$  and  $\beta\gamma_{dE/dx}$  requirements are tightened

| N | $ \eta $ lower | $ \eta $ upper |
|---|----------------|----------------|
| 1 | 0.0            | 0.70           |
| 2 | 0.70           | 1.25           |
| 3 | 1.25           | 1.65           |
| 4 | 1.65           | 2.00           |

Table 5.15: The lower and upper edges for the lowered number of  $\eta$  bins in the templates.

| N | $ \eta $ lower | $ \eta $ upper |
|---|----------------|----------------|
| 1 | 0.0            | 0.35           |
| 2 | 0.35           | 0.55           |
| 3 | 0.55           | 0.90           |
| 4 | 0.90           | 1.10           |
| 5 | 1.1            | 1.25           |
| 6 | 1.25           | 1.65           |
| 7 | 1.65           | 1.75           |
| 8 | 1.75           | 1.85           |
| 9 | 1.85           | 2.00           |

Table 5.16: The lower and upper edges for the increased number of  $\eta$  bins in the templates.

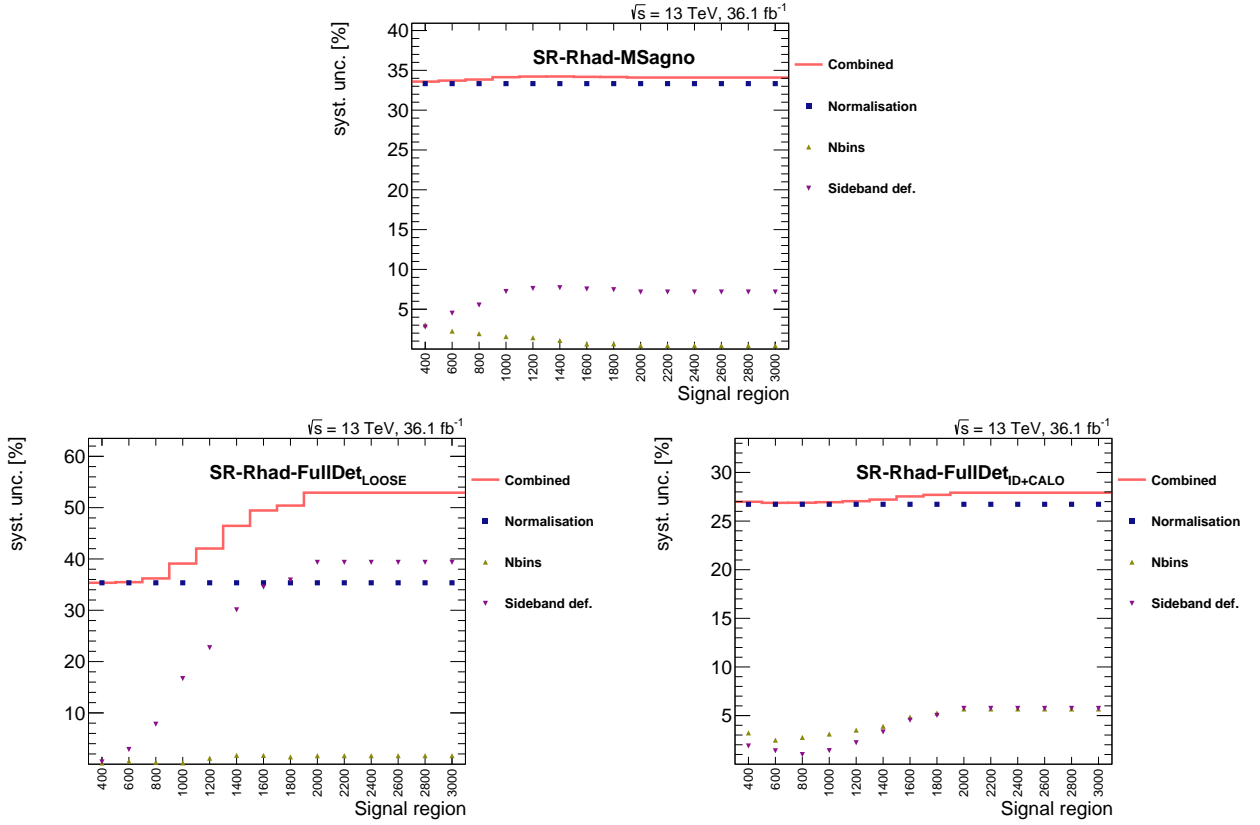


Figure 5.86: The systematic uncertainty on the background estimate as function of the signal region. The upper plot shows the SR-Rhad-MSagno signal region, while the lower the SR-Rhad-FullDet regions <sub>LOOSE</sub> (left) and <sub>ID+CALO</sub> (right). The different contributions are shown as markers, while the combined uncertainty is given as red line. For  $R$ -hadrons the same mass window is used for all mass hypotheses above 2000 GeV, and hence the identical background uncertainties are expected.

for the momentum template while the momentum requirement is tightened for the  $\beta_{\text{ToF}}/\beta_{\gamma_{\text{dE/dx}}}$  template. For the SR-1Cand-FullDet only the  $\beta_{\text{ToF}}$  requirement is changed for the momentum template as  $\beta_{\gamma_{\text{dE/dx}}}$  is not used in this signal region. In the SR-2Cand-FullDet no sidebands are used for the  $\beta_{\text{ToF}}$  template and hence there only the sideband definition for the momentum template can be changed. The different requirements for the tightened sideband definitions are summarised in Table 5.17.

The third contribution to the systematic uncertainty on the background estimate considered is the normalisation. The background is normalised using the low mass control regions. The relative statistical uncertainty from the number of events in the control region is used as relative uncertainty on the number of background events in the signal region. The different contributions are added in quadrature to obtain the total uncertainty on the background estimate.

The estimated systematic uncertainties as function of the final mass hypothesis for the  $R$ -hadron signal regions SR-Rhad-MSagno,

|                  | nom. | med. | tight |
|------------------|------|------|-------|
| $\beta$          | 1.0  | 0.98 | 0.96  |
| $\beta_{\gamma}$ | 2.5  | 2.45 | 2.4   |
| p                | 200  | 190  | 180   |

Table 5.17: The nominal medium and tight sideband requirements for the templates. The momentum is given in GeV.

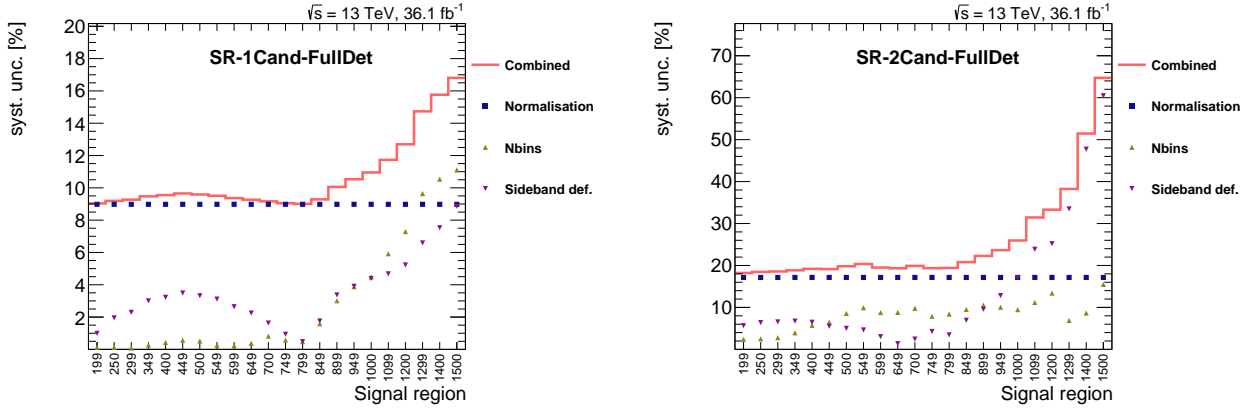


Figure 5.87: The systematic uncertainty on the background estimate as function of the signal region. The uncertainty for the SR-1Cand-FullDet is shown in the left figure while the one for the SR-2Cand-FullDet is given in the right figure. The different contributions are drawn as markers and the combined uncertainty is indicated by the red line.

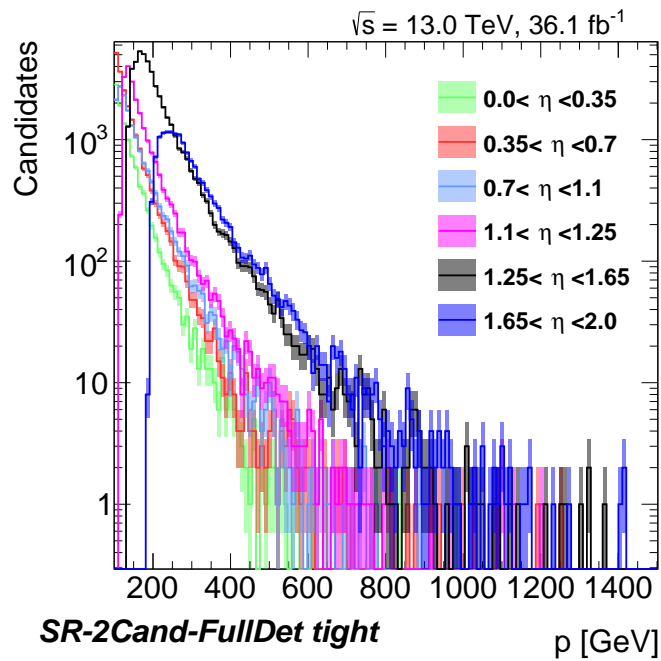


Figure 5.88: The template distributions for the momentum in the different  $\eta$  bins of the SR-2Cand-FullDet with the tight sideband definition. The nominal distributions are shown in Figure 5.80.

SR-Rhad-FullDet<sub>LOOSE</sub> and SR-Rhad-FullDet<sub>ID+CALO</sub> are shown in Figure 5.86 and for SR-1Cand-FullDet and SR-2Cand-FullDet in Figure 5.87. For most of the signal regions the uncertainty from the normalisation of the backgrounds is dominant. The statistics in the control regions are rather limited as the optimisation of the final requirements would prefer hard selection requirements. A general feature that is visible for all different signal region types is that for higher mass hypotheses the systematic uncertainty originating from the change of the sideband requirements increases. The reason is that for a tightened sideband the statistics in the template decreases and in particular the tails to high momenta or low  $\beta/\beta\gamma$  fade away. This can e.g. be seen by comparing the momentum templates produced with the tight selection as shown in Figure 5.88, with the nominal distribution shown in Figure 5.80 (upper right). A longer tail in e.g. the momentum template increases the whole background mass tail, as it is folded with the  $\beta/\beta\gamma$  template. This general trend can be seen, excluding the feature at 650 GeV, in Figure 5.89, which shows a comparison between the background estimated from the nominal and the tight templates. The feature at 650 GeV is the reason for the dip in the trend of the uncertainty from the change in the sideband definitions visible for SR-1Cand-FullDet and to a smaller extent also for SR-2Cand-FullDet but at lower masses, shown in Figure 5.87. The lower mass requirement for a mass hypothesis of about 800 GeV is roughly at 600 GeV. This peak at 650 GeV in the background estimate from the tight sideband definition can be explained by the momentum templates in the inner part of the detector fading away roughly at 800 GeV as can be seen in Figure 5.88. At the end of the distribution only single candidates are left and if those discrete values are folded with the  $\beta$  spectrum, that is highly peaked at the cut value (e.g. visible in Figure 5.80 bottom), also peak in the sampled mass distribution is expected. The final  $\beta$  requirement of 0.8 translates into a  $\beta\gamma = 1.33$  and using a momentum of 800 GeV a mass  $m = p/\beta\gamma = 600$  GeV is expected, which roughly corresponds to what we see in Figure 5.89. The effect of the change in the  $\eta$  binning is almost negligible in the signal regions using the ID+CALO candidates, while an uncertainty of 3%-15% is found for the high masses in the signal regions using full-detector candidates. The reason is that for those candidates the tails of the  $\beta$ /momentum templates are less prominent due to the better resolutions including the MS. Some single outliers that are combined or separated by the change of the  $\eta$  bins can hence have significant impact on the tails of the distribution.

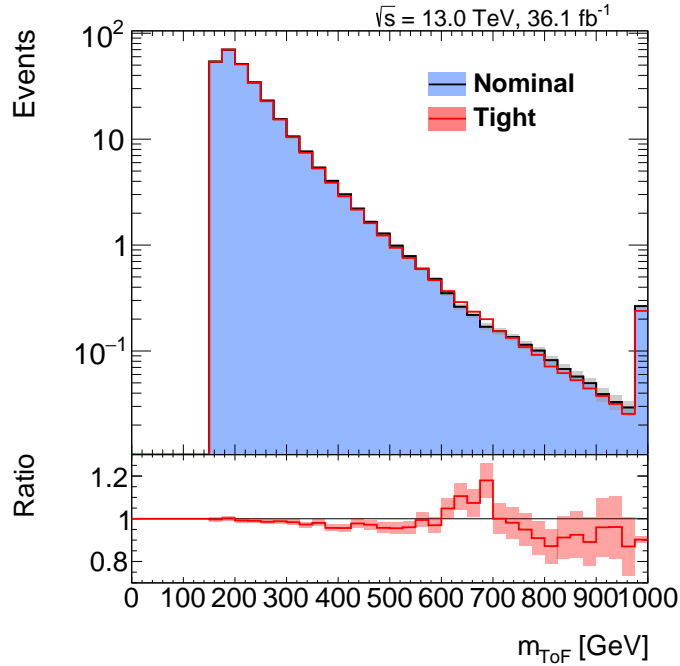


Figure 5.89: The nominal estimated background for the SR-2Cand-FullDet overlaid by the background estimate from the templates produced with the tight requirements. The lower pad shows the ratio between the tight and the nominal background. The statistical uncertainty from the templates is only propagated to the nominal background (shaded grey) and is also the only contribution to the uncertainty of the ratio.

The values obtained for the systematic uncertainties due to the background estimated are spanning a wide range. The lowest uncertainties are found for the SR-1Cand-FullDet at low masses, which can be explained by the high statistics in the control region. The largest uncertainties are obtained for the SR-Rhad-FullDet LOOSE and the SR-2Cand-FullDet for high masses, but there also the expected background yields are very small, 0.05 for SR-Rhad-FullDet LOOSE ( $m_{\tilde{g}} = 2000$  GeV) and 0.0007 for SR-2Cand-FullDet ( $m_{\tilde{\chi}_1^\pm} = 2000$  GeV).

## 5.11 Results

In this section the results for the search for HCLLPs with the ATLAS detector in 36.1 fb<sup>1</sup> data taken in 2015 and 2016 are summarised. Firstly the statistical model used for the interpretation of the results will be described. This is followed by a detailed discussion of the statistical interpretation of the results in the different signal regions with the previously defined benchmark models.

### 5.11.1 Statistical method

The  $p_0$ -values and upper limits that are obtained from the results of the analysis are estimated using the HistFitter package [141]. Two different

hypotheses are tested. First the compatibility of the background with the observed data is tested to check whether the data are in agreement with the background-only-hypothesis or if a new signal is likely. And second if signal is disfavoured, the signal-plus-background hypothesis can be excluded. For both  $p_0$ -values are determined as a measure for the compatibility, which are defined as the probability of measuring a certain or more extreme outcome of the experiment.

The determination of the  $p_0$ -values is based on a frequentist approach using the profile-log-likelihood ratio as test statistic. To do so first the likelihood  $L$  has to be constructed for this analysis. Depending on whether one (SR-Rhad-MSagno) or two signal regions are used (SR-Rhad-FullDet LOOSE + ID+CALO and SR-2Cand-FullDet + SR-1Cand-FullDet) one or two bins for the likelihood are used. For each bin a Poisson counting model is assumed for the observed number of events. The systematic uncertainties are taken into account as nuisance parameters  $\theta_i$  and are assumed to be gaussian distributed. For this analysis only the combined systematic uncertainties for background and signal, respectively, are used and set to be independent between the different bins. The likelihood ratio is defined as

$$\Lambda(\mu) = \frac{L(\mu, \hat{\theta}_i)}{L(\hat{\mu}, \hat{\theta}_i)}, \quad (5.31)$$

with the signal strength  $\mu$ , a scaling factor on the number of signal events,  $\hat{\theta}$  the value of  $\theta$  that maximises the likelihood for the given  $\mu$  and  $\hat{\mu}/\hat{\theta}$  the parameters that maximise the likelihood. The denominator is called conditional maximum-likelihood function for the given  $\mu$ , while the numerator is called the unconditional maximum-likelihood function. The test statistic used for the discovery  $p_0$ -value estimation is given by

$$q_0 = -2 \ln \Lambda(0), \quad (5.32)$$

where  $\mu = 0$  as the background only hypothesis is tested. The p-value for the background only hypothesis is then given by

$$p_0 = \int_{q_{obs}}^{\infty} f(q_0|0) dq, \quad (5.33)$$

where  $q_{obs}$  the value of the test statistic observed in the experiment and  $f$  the probability density function, which is determined sampling pseudo experiments. The  $p_0$ -values can be translated into the number of standard deviations from a Gaussian, called significance. In particle physics it is convenient that an evidence is claimed for  $3\sigma$ , while a discovery needs

$5\sigma$ .

For the limit setting and exclusion of signal models the test statistic is given by

$$q_\mu = -2 \ln \Lambda(\mu). \quad (5.34)$$

The confidence level  $CL_{s+b}$  for the compatibility with the signal plus background hypothesis is given by

$$CL_{s+b} = \int_{-\infty}^{q_{obs}} f(q_\mu|0) dq. \quad (5.35)$$

To be less effected by fluctuations of the background, instead of the pure  $CL_{s+b}$ , the  $CL_s$  [151, 152] is used, which is defined as

$$CL_s = \frac{CL_{s+b}}{CL_b}, \quad (5.36)$$

where  $CL_b$  is the confidence level under the background-only hypothesis, but in contrast to the discovery  $p$ -value the exclusion test statistic is used. In particle physics it is convenient that a model is excluded if  $CL_s < 0.05$ , which corresponds to a 95% Confidence Level (CL). To estimate an upper limit on the cross section the signal strength  $\mu$  can be scanned to obtain the value for which the  $CL_s$  falls below 0.05. The upper limit on the signal strength  $\mu_{limit}$  can be translated to an upper limit on the cross section, with

$$\sigma_{limit} = \mu_{limit} \times \sigma_{signal}, \quad (5.37)$$

using the signal cross section  $\sigma_{signal}$ . In principle an arbitrary value for  $\sigma_{signal}$  can be used as this is only setting the start value for the signal strength scan.

### 5.11.2 Results and interpretation

First the results in the 16 discovery regions that were defined before unblinding are discussed. As no significant excess is observed the results from all signal regions are used to set upper cross-section limits and, by using the theoretical cross section, lower mass limits on the respective models.

#### Discovery regions

A set of 16 discovery regions was defined before unblinding for which the  $p_0$ -values are estimated. The estimated and observed event yields

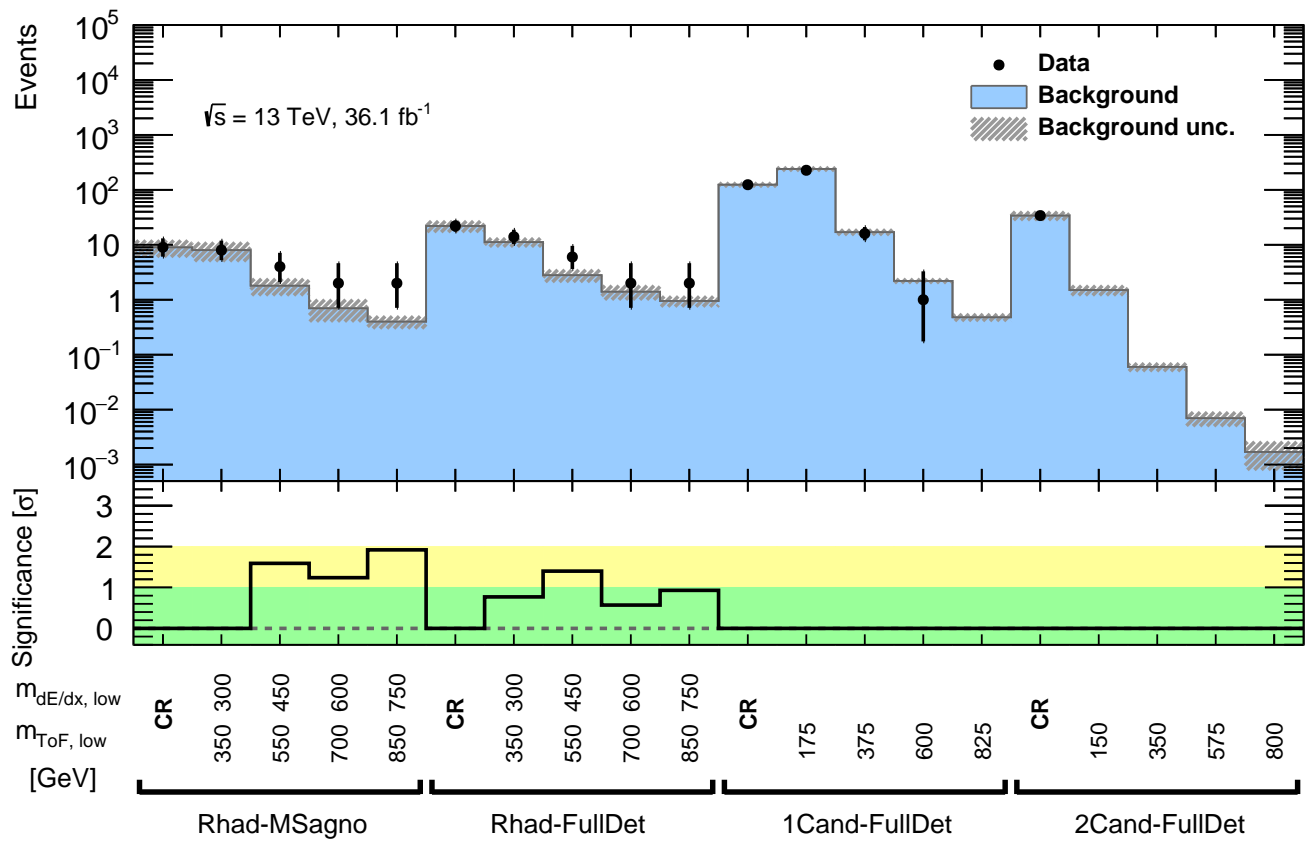


Figure 5.90: The observed and expected numbers of events for the 16 discovery regions as well as for the four control regions that are used for the normalisation, hence agreement there is by construction. The uncertainty shown on the background estimate as grey dashed area includes both statistic and systematic uncertainties. For data a poisson error is drawn. The lower pad is shown the significance of the regions with a surplus of observed data events above the expected background. For the Rhad-FullDet signal regions the event yields from the `LOOSE` and `ID-CALO` are added together to obtain a model independent  $p_0$ -value. [5]

| Selection        | Mass requirements                   |                                       | $N_{\text{est.}} \pm \sigma_{N_{\text{est.}}}$ | $N_{\text{obs.}}$ | $p_0$ | sign. $\sigma$ | 95% CL upper limit<br>$\sigma \times a \times \epsilon$ [fb] |
|------------------|-------------------------------------|---------------------------------------|--|-------------------|-------|----------------|--|
|                  | $m_{\text{ToF}}^{\text{min}}$ [GeV] | $m_{\text{dE/dx}}^{\text{min}}$ [GeV] |  |                   |       |                |  |
| SR-Rhad-MSagno   | 350                                 | 300                                   | $8.0 \pm 3.0$                                  | 8                 | 0.5   |                | 0.25   |
|                  | 550                                 | 450                                   | $1.8 \pm 0.6$                                  | 4                 | 0.056 | 1.59           | 0.20   |
|                  | 700                                 | 600                                   | $0.7 \pm 0.3$                                  | 2                 | 0.11  | 1.24           | 0.17   |
|                  | 850                                 | 750                                   | $0.4 \pm 0.1$                                  | 2                 | 0.028 | 1.92           | 0.17   |
| SR-Rhad-FullDet  | 350                                 | 300                                   | $11 \pm 2$                                     | 14                | 0.22  | 0.77           | 0.42   |
|                  | 550                                 | 450                                   | $2.8 \pm 0.7$                                  | 6                 | 0.081 | 1.40           | 0.25   |
|                  | 700                                 | 600                                   | $1.4 \pm 0.4$                                  | 2                 | 0.28  | 0.57           | 0.14   |
|                  | 850                                 | 750                                   | $0.95 \pm 0.2$                                 | 2                 | 0.18  | 0.93           | 0.14   |
| SR-1Cand-FullDet | 175                                 |                                       | $240 \pm 20$                                   | 227               | 0.5   |                | 1.26   |
|                  | 375                                 |                                       | $17 \pm 2$                                     | 16                | 0.5   |                | 0.24   |
|                  | 600                                 |                                       | $2.2 \pm 0.2$                                  | 1                 | 0.5   |                | 0.10   |
|                  | 825                                 |                                       | $0.48 \pm 0.07$                                | 0                 | 0.5   |                | 0.08   |
| SR-2Cand-FullDet | 150                                 |                                       | $1.5 \pm 0.3$                                  | 0                 | 0.5   |                | 0.09   |
|                  | 350                                 |                                       | $0.06 \pm 0.01$                                | 0                 | 0.5   |                | 0.08   |
|                  | 575                                 |                                       | $0.007 \pm 0.002$                              | 0                 | 0.5   |                | 0.08   |
|                  | 800                                 |                                       | $0.0017 \pm 0.0009$                            | 0                 | 0.5   |                | 0.08   |

Table 5.18: The estimated and observed event yields for the 16 discovery regions, as well as the lower mass requirements to define them. Furthermore the  $p_0$ -values and the significance are given for the discovery regions where the observed number of events exceeds the estimated number of events. In the last row also the model independent upper limits are stated, with the acceptance ( $a$ ) times efficiency ( $\epsilon$ ) for the signal.

together with the obtained significance are shown in Figure 5.90 and given as numbers in Table 5.18. There also the  $p_0$ -values and the model-independent upper-limits are stated. For the values given for SR-Rhad-FullDet the two yields from the separate signal regions LOOSE and ID+CALO are added to be model independent, as a combination with separate bins would need a prior knowledge on the expected signal distribution. Small excesses are observed for SR-Rhad-MSagno and SR-Rhad-FullDet while a good agreement between estimated and observed numbers of events for SR-2Cand-FullDet and SR-1Cand-FullDet is observed. The according background and data distributions as well as exemplary signal distributions are shown in Figures 5.81 to 5.84. The largest deviation from the estimated background is found in the highest mass window for SR-Rhad-MSagno with almost  $2\sigma$ . The same two events are also visible in SR-Rhad-FullDet ID+CALO, which differs from the SR-Rhad-MSagno only by the additional single-muon trigger and by being the fall-back of the LOOSE signal region. The events are hence not promoted to SR-Rhad-FullDet LOOSE signal region. In general the surpass of data against background for the SR-Rhad-FullDet is mostly driven by the ID+CALO signal region and hence to a large extend the same events as in SR-Rhad-MSagno are seen. All events that are seen in the SR-Rhad-MSagno

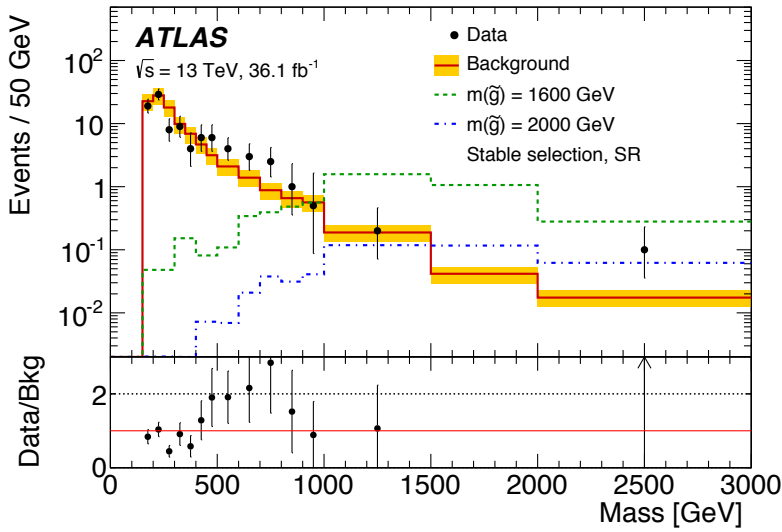


Figure 5.91: The estimated background (red) with the observed candidates (black markers) and two distributions for different signal models (dashed blue and green) superimposed for the stable  $R$ -hadron signal region. The yellow band includes both systematic and statistic uncertainties. The figure is taken from Reference. [127], where a detailed description of the signal region and the applied background estimation method can be found.

discovery region were further investigated. It was found that a large fraction of them, in particular the two candidates in the highest mass window, have no TRT hits and a low number of SCT hits and hence a poor momentum resolution. It was further observed that only one Tile Calorimeter timing measurement was used for the  $\beta_{\text{TILE}}$  for all candidates. As discussed in Sections 5.4.1 and 5.5.2, those are features that are to some extent expected to be present for HCLLPs. Nevertheless the candidates look more like muons with outliers in the respective measurements than signal candidates.

The results from this analysis can be compared to the results from the search using only the ionisation energy loss in the pixel detector to identify HCLLPs [127], which analysed the same dataset. The estimated background and the observed data as well as two different signal benchmark models are shown in Figure 5.91. The distribution is shown for the stable selection, which is targeting the stable  $R$ -hadron models. Also there two candidates are present at very high masses, which are not the same candidates as observed in SR-Rhad-MSagno or SR-Rhad-FullDet ID+CALO. The high mass candidates of SR-Rhad-MSagno are rejected due to a requirement on the momentum resolution in the pixel  $dE/dx$  analysis. The largest excess of  $2.4\sigma$  for this analysis is seen in the mass window starting at 500 GeV that is designed for a 600 GeV gluino model. This slight excess is visible as a bump of the observed data over the expected background. In the analysis described in this thesis also a slight excess of  $1.59\sigma$  can be seen in the corresponding region ( $m_{\text{TOF}}^{\text{min}} = 550$  GeV,  $m_{dE/dx}^{\text{min}} = 450$  GeV). For high masses the excesses are dominated by the two mass outliers as

| <i>R</i> -hadron | Mass [GeV] | $N_{\text{exp.}} \pm \sigma_{N_{\text{exp.}}}$ | SR-Rhad-MSagno (ID+CALO)                                 |  | $N_{\text{obs.}}$ |
|------------------|------------|--|--|--|-------------------|
|                  |            |  | $a \times \varepsilon \pm \sigma_{a \times \varepsilon}$ | $N_{\text{est.}} \pm \sigma_{N_{\text{est.}}}$ |                   |
| Gluino           | 400        | 160000±30000                                   | 0.044±0.003  | 8.0±3.0  | 8                 |
|                  | 600        | 28000±5000                                     | 0.086±0.004  | 3.0±1.0  | 7                 |
|                  | 800        | 6000±1000                                      | 0.106±0.005  | 1.8±0.6  | 4                 |
|                  | 1000       | 1300±200                                       | 0.114±0.005  | 1.0±0.3  | 2                 |
|                  | 1200       | 400±70   | 0.129±0.006  | 0.7±0.3  | 2                 |
|                  | 1400       | 140±30   | 0.148±0.007  | 0.6±0.2  | 2                 |
|                  | 1600       | 42±7   | 0.143±0.007  | 0.5±0.2  | 2                 |
|                  | 1800       | 13±2   | 0.134±0.007  | 0.4±0.1  | 2                 |
|                  | 2000       | 4.4±0.8  | 0.126±0.006  | 0.4±0.1  | 2                 |
|                  | 2200       | 1.5±0.3  | 0.114±0.004  | 0.4±0.1  | 2                 |
|                  | 2400       | 0.51±0.09                                      | 0.106±0.004  | 0.4±0.1  | 2                 |
|                  | 2600       | 0.18±0.03                                      | 0.101±0.004  | 0.4±0.1  | 2                 |
|                  | 2800       | 0.06±0.01                                      | 0.090±0.004  | 0.4±0.1  | 2                 |
|                  | 3000       | 0.023±0.004                                    | 0.090±0.004  | 0.4±0.1  | 2                 |
| Bottom squark    | 600        | 400±80   | 0.063±0.003  | 3.0±1.0  | 7                 |
|                  | 800        | 80±20  | 0.083±0.004  | 1.8±0.6  | 4                 |
|                  | 1000       | 19±3   | 0.087±0.004  | 1.0±0.3  | 2                 |
|                  | 1200       | 5.4±0.9  | 0.093±0.004  | 0.7±0.3  | 2                 |
|                  | 1400       | 1.5±0.3  | 0.093±0.004  | 0.6±0.2  | 2                 |
| Top squark       | 600        | 600±100  | 0.095±0.005  | 3.0±1.0  | 7                 |
|                  | 800        | 120±200  | 0.117±0.005  | 1.8±0.6  | 4                 |
|                  | 1000       | 28±5   | 0.128±0.005  | 1.0±0.3  | 2                 |
|                  | 1200       | 8±1  | 0.139±0.005  | 0.7±0.3  | 2                 |
|                  | 1400       | 2.4±0.4  | 0.146±0.005  | 0.6±0.2  | 2                 |

Table 5.19: The expected number of signal events ( $N_{\text{exp.}}$ ), the acceptance ( $a$ ) times efficiency ( $\varepsilon$ ) for the signal, the estimated number of background events ( $N_{\text{est}}$ ) and the observed number of events  $N_{\text{obs}}$  for all different mass hypothesis of gluino, sbottom and stop *R*-hadrons in the SR-Rhad-MSagno.

the windows are open to high masses. For the region ( $m_{\text{ToF}}^{\text{min}} = 550$  GeV,  $m_{\text{dE/dx}}^{\text{min}} = 450$  GeV) some additional candidates with a good agreement between  $m_{\text{ToF}}$  and  $m_{\text{dE/dx}}$  are found, which can be seen from Figure 5.81 (upper). These are interesting results and the next iterations of those analyses with analysing larger datasets might give answers if those small excesses are purely statistical fluctuations or if they originate from HCLLPs.

### Limit setting

As no signal was observed the data can be used to set upper limits on the production cross section, which can be translated to lower mass limits using the theoretical cross section.

**MS-agnostic** The expected number of signal events ( $N_{\text{exp.}}$ ), the acceptance ( $a$ ) times efficiency ( $\varepsilon$ ) for the signal, the estimated number of background events ( $N_{\text{est}}$ ) and the observed number of events  $N_{\text{obs}}$  for all different mass hypothesis of gluino, sbottom and stop *R*-hadrons in SR-Rhad-MSagno are given in Table 5.19. An initial increase in sensitivity is visible up to masses of 1400 GeV, while for higher masses the efficiency

is decreasing again. This efficiency is following the  $\cancel{E}_T$  trigger efficiency which is discussed in Section 5.6.1. The behaviour can be explained by the change in production mechanism. The efficiency for gluino  $R$ -hadrons is similar to the efficiency observed for stop  $R$ -hadrons. The surplus in trigger efficiency of the gluino signals is compensated by the larger fraction of charged  $R$ -hadrons after hadronisation for stops (Section 4.2). A significantly lower efficiency is obtained for the sbottom  $R$ -hadrons as they are expected to have a lower  $\cancel{E}_T$  trigger efficiency as well as the lowest rate of charged  $R$ -hadrons after hadronisation. The upper limits on the cross section are shown in Figures 5.92. For lower masses the cross-section limits are weaker due to the increased background yields, while for higher masses the decreasing signal efficiency is resulting in a weakening of the cross-section limits. The strongest limits are obtained for a mass hypothesis of 1400 GeV for all different particle types. The observed cross-section limits are weaker than the expected due to the small excesses in the low/high mass regions. The observed (expected) lower mass limits are obtained from the intersection of the theory prediction with the observed (expected) line for the upper cross-section limit. For the different models an observed (expected) lower mass limit of 1950 GeV (2060 GeV) for gluinos, 1190 GeV (1270 GeV) for sbottom and 1265 GeV (1345 GeV) for stop is obtained. Due to the lower efficiency for sbottom  $R$ -hadrons compared to stop  $R$ -hadrons also the obtained mass limits are lower.

**$R$ -hadron full-detector** The expected number of signal events ( $N_{\text{exp.}}$ ), the acceptance ( $a$ ) times efficiency ( $\varepsilon$ ) for the signal, the estimated number of background events ( $N_{\text{est}}$ ) and the observed number of events  $N_{\text{obs}}$  for all different mass hypothesis of gluino, sbottom and stop  $R$ -hadrons in SR-Rhad-FullDet LOOSE and SR-Rhad-FullDet ID+CALO are given in Table 5.20. In general the trends from the  $\cancel{E}_T$  trigger are also seen for the SR-Rhad-FullDet as also there most of the events are coming from this trigger. The fraction of  $R$ -hadrons charged in the MS is enhanced for stop compared to sbottom  $R$ -hadrons, as discussed in Section 4.5. This together with the lower fraction of charged  $R$ -hadrons after hadronisation results in an almost twice as large signal efficiency for stop  $R$ -hadrons compared to sbottom  $R$ -hadrons in SR-Rhad-FullDet LOOSE. For gluinos the signal efficiency in SR-Rhad-FullDet LOOSE is in between the one obtained for sbottom and stop, whereas the SR-Rhad-FullDet ID+CALO signal efficiency is the largest, as a higher  $\cancel{E}_T$  trigger efficiency is expected

| <i>R</i> -hadron | Mass [GeV]  | SR-Rhad-FullDet LOOSE            |  |                                  |             | SR-Rhad-FullDet ID+CALO          |  |                                  |            |
|------------------|-------------|----------------------------------|--|----------------------------------|-------------|----------------------------------|--|----------------------------------|------------|
|                  |             | $N_{exp.} \pm \sigma_{N_{exp.}}$ | $a \times \varepsilon \pm \sigma_{a \times \varepsilon}$ | $N_{est.} \pm \sigma_{N_{est.}}$ | $N_{obs.}$  | $N_{exp.} \pm \sigma_{N_{exp.}}$ | $a \times \varepsilon \pm \sigma_{a \times \varepsilon}$ | $N_{est.} \pm \sigma_{N_{est.}}$ | $N_{obs.}$ |
| Gluino           | 400         | 60000±20000                      | 0.016±0.002  | 1.5±0.5                          | 1           | 160000±3000                      | 0.044±0.003  | 9.0±2.0                          | 13         |
|                  | 600         | 11000±4000                       | 0.033±0.003  | 0.5±0.2                          | 1           | 24000±4000                       | 0.071±0.004  | 4.0±1.0                          | 9          |
|                  | 800         | 2400±600                         | 0.044±0.003  | 0.3±0.1                          | 1           | 4500±800                         | 0.083±0.004  | 2.5±0.7                          | 5          |
|                  | 1000        | 500±100                          | 0.045±0.003  | 0.14±0.05                        | 0           | 1100±200                         | 0.091±0.005  | 1.6±0.4                          | 3          |
|                  | 1200        | 160±40                           | 0.053±0.004  | 0.10±0.04                        | 0           | 300±50                           | 0.096±0.005  | 1.3±0.4                          | 2          |
|                  | 1400        | 60±10                            | 0.063±0.005  | 0.07±0.03                        | 0           | 100±20                           | 0.104±0.006  | 1.1±0.3                          | 2          |
|                  | 1600        | 17±4                             | 0.057±0.004  | 0.06±0.03                        | 0           | 30±6                             | 0.104±0.006  | 1.0±0.3                          | 2          |
|                  | 1800        | 5±1                              | 0.052±0.004  | 0.05±0.03                        | 0           | 10±2                             | 0.099±0.006  | 0.9±0.3                          | 2          |
|                  | 2000        | 1.9±0.4                          | 0.053±0.003  | 0.05±0.02                        | 0           | 2.9±0.6                          | 0.083±0.004  | 0.9±0.2                          | 2          |
|                  | 2200        | 0.6±0.1                          | 0.043±0.003  | 0.05±0.02                        | 0           | 1.0±0.2                          | 0.079±0.003  | 0.9±0.2                          | 2          |
|                  | 2400        | 0.18±0.04                        | 0.037±0.002  | 0.05±0.02                        | 0           | 0.38±0.07                        | 0.079±0.004  | 0.9±0.2                          | 2          |
|                  | 2600        | 0.07±0.01                        | 0.036±0.002  | 0.05±0.02                        | 0           | 0.13±0.02                        | 0.074±0.003  | 0.9±0.2                          | 2          |
|                  | 2800        | 0.019±0.004                      | 0.027±0.002  | 0.05±0.02                        | 0           | 0.049±0.009                      | 0.071±0.003  | 0.9±0.2                          | 2          |
| 3000             | 0.007±0.002 | 0.028±0.002                      | 0.05±0.02  | 0                                | 0.017±0.003 | 0.066±0.003                      | 0.9±0.2  | 2                                |            |
| Bottom squark    | 600         | 200±50                           | 0.032±0.002  | 0.5±0.2                          | 1           | 300±60                           | 0.047±0.003  | 4.0±1.0                          | 9          |
|                  | 800         | 38±8                             | 0.037±0.003  | 0.3±0.1                          | 1           | 60±10                            | 0.061±0.003  | 2.5±0.7                          | 5          |
|                  | 1000        | 9±2                              | 0.040±0.003  | 0.14±0.05                        | 0           | 14±3                             | 0.064±0.003  | 1.6±0.4                          | 3          |
|                  | 1200        | 2.5±0.5                          | 0.043±0.003  | 0.10±0.04                        | 0           | 3.9±0.7                          | 0.068±0.003  | 1.3±0.4                          | 2          |
| 1400             | 0.7±0.1     | 0.042±0.003                      | 0.07±0.03  | 0                                | 1.1±0.2     | 0.069±0.003                      | 1.1±0.3  | 2                                |            |
| Top squark       | 600         | 390±70                           | 0.062±0.004  | 0.5±0.2                          | 1           | 370±70                           | 0.059±0.004  | 4±1                              | 9          |
|                  | 800         | 80±20                            | 0.075±0.004  | 0.3±0.1                          | 1           | 80±20                            | 0.077±0.004  | 2.5±0.7                          | 5          |
|                  | 1000        | 18±4                             | 0.083±0.004  | 0.14±0.05                        | 0           | 18±3                             | 0.081±0.004  | 1.6±0.4                          | 3          |
|                  | 1200        | 5±1                              | 0.088±0.004  | 0.10±0.04                        | 0           | 4.9±0.9                          | 0.085±0.004  | 1.3±0.4                          | 2          |
| 1400             | 1.6±0.3     | 0.093±0.005                      | 0.07±0.03  | 0                                | 1.5±0.3     | 0.089±0.004                      | 1.1±0.3  | 2                                |            |

Table 5.20: The expected number of signal events ( $N_{exp.}$ ), the acceptance ( $a$ ) times efficiency ( $\varepsilon$ ) for the signal, the estimated number of background events ( $N_{est.}$ ) and the observed number of events  $N_{obs}$  for all different mass hypothesis of gluino, sbottom and stop *R*-hadrons in SR-Rhad-FullDet LOOSE and SR-Rhad-FullDet ID+CALO.

for gluino *R*-hadrons. Furthermore less events are promoted to the SR-Rhad-FullDet LOOSE, due to the lower charged *R*-hadron fraction in the MS compared to the stop *R*-hadrons. The upper cross-section limits are shown together with the ones obtained for the SR-Rhad-MSagno in Figures 5.92. The expected cross section limits are slightly better for SR-Rhad-FullDet for the low masses, while the difference is negligible for larger masses. The gain in signal efficiency e.g. for  $m_{\tilde{g}} = 2000$  GeV from the additional single-muon trigger is rather low (SR-Rhad-FullDet: 5.3% + 8.3% = 13.6% SR-Rhad-MSagno:12.6%) and also increases the background in SR-Rhad-FullDet ID+CALO (0.9) compared to SR-Rhad-MSagno (0.4). Therefore the main gain comes from the better background suppression in the SR-Rhad-FullDet LOOSE.

As the signal regions are almost background free for high masses, no significant gain is expected from the full-detector *R*-hadron approach. In the low-mass region significant background contributions are present, hence better upper limits are obtained with the SR-Rhad-FullDet approach. The difference between SR-Rhad-MSagno and SR-Rhad-FullDet is largest for the stop *R*-hadrons as the efficiency of the SR-Rhad-FullDet ID+CALO is best for them. The observed upper cross section limits for the SR-Rhad-MSagno are weaker due to the excess in the high mass region. For the different models an observed (expected) lower mass limit of 2000 GeV

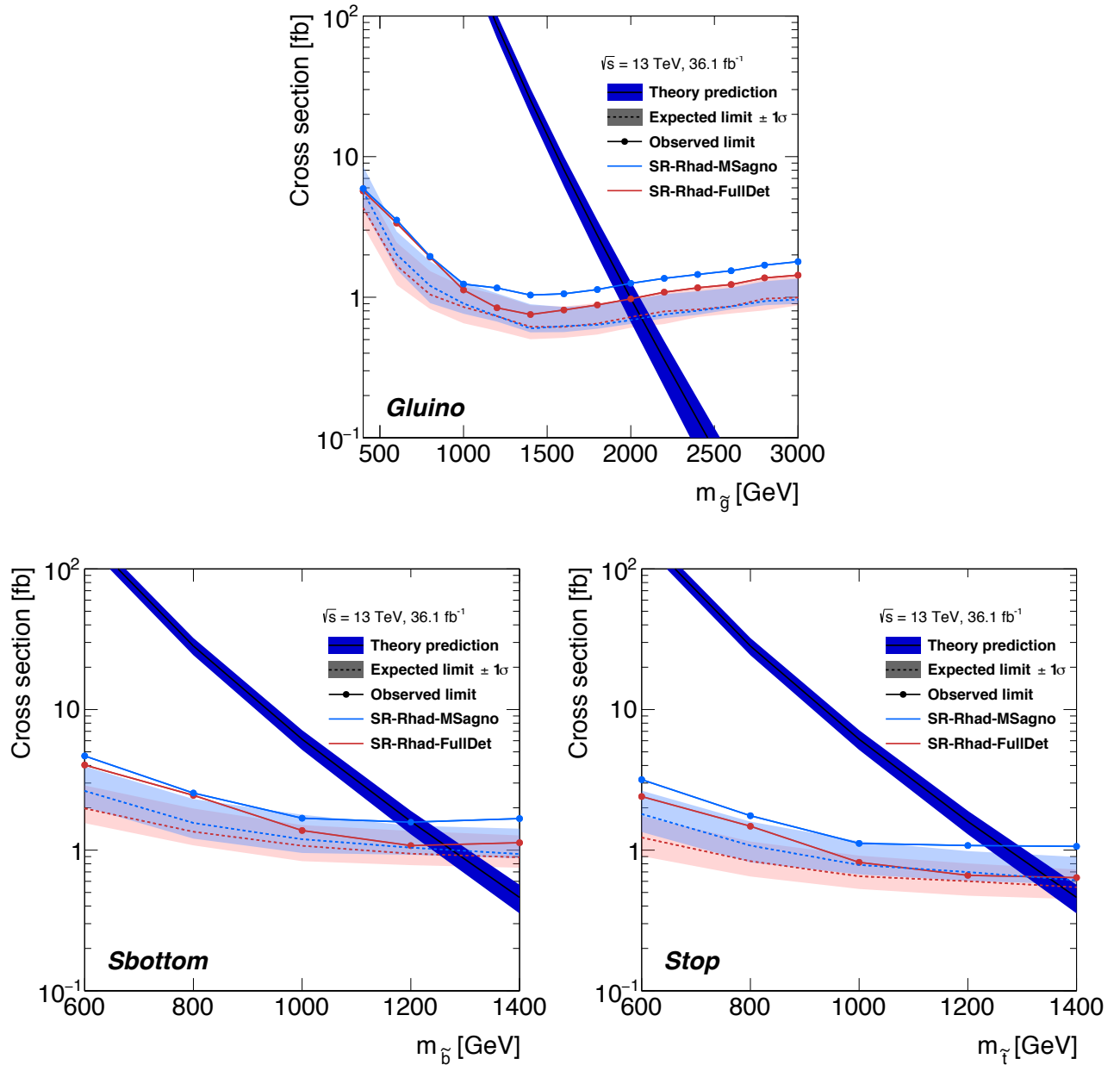


Figure 5.92: The observed and expected upper cross section limits as well as the theory prediction for the cross section of gluino (upper), sbottom (lower left) and stop (lower right)  $R$ -hadron models as function of the simulated mass. Both the limits from SR-Rhad-MSagno (blue) and SR-Rhad-FullDet (red) are shown. The dashed lines indicate the expected limits, also drawn are the  $\pm 1\sigma$  bands for the expected limit. The observed limits are shown as dots connected by a line. [5]

| Mass [GeV] | $N_{\text{exp.}} \pm \sigma_{N_{\text{exp.}}}$ | SR-2Cand-FullDet   |  |                   | SR-1Cand-FullDet                               |  |  |                   |
|------------|--|--|--|-------------------|--|--|--|-------------------|
|            |  | $a \times \varepsilon \pm \sigma_{a \times \varepsilon}$ | $N_{\text{est.}} \pm \sigma_{N_{\text{est.}}}$ | $N_{\text{obs.}}$ | $N_{\text{exp.}} \pm \sigma_{N_{\text{exp.}}}$ | $a \times \varepsilon \pm \sigma_{a \times \varepsilon}$ | $N_{\text{est.}} \pm \sigma_{N_{\text{est.}}}$ | $N_{\text{obs.}}$ |
| 287        | 13±1   | 0.167±0.005  | 0.33±0.06                                      | 0                 | 5.1±0.6  | 0.068±0.003  | 80.0±7.0                                       | 74                |
| 318        | 9±1  | 0.179±0.007  | 0.22±0.04                                      | 0                 | 3.6±0.4  | 0.073±0.004  | 56.0±5.0                                       | 52                |
| 349        | 6.1±0.7  | 0.181±0.005  | 0.15±0.03                                      | 0                 | 2.5±0.2  | 0.076±0.003  | 41.0±4.0                                       | 36                |
| 380        | 4.3±0.6  | 0.184±0.006  | 0.11±0.02                                      | 0                 | 2.1±0.2  | 0.089±0.005  | 30.0±3.0                                       | 24                |
| 411        | 3.2±0.4  | 0.196±0.005  | 0.08±0.02                                      | 0                 | 1.5±0.1  | 0.093±0.004  | 23.0±2.0                                       | 20                |
| 442        | 2.4±0.3  | 0.198±0.007  | 0.06±0.01                                      | 0                 | 1.2±0.2  | 0.096±0.005  | 17.0±2.0                                       | 16                |
| 473        | 1.8±0.3  | 0.204±0.005  | 0.045±0.009                                    | 0                 | 0.92±0.09                                      | 0.105±0.004  | 13.0±1.0                                       | 15                |
| 504        | 1.4±0.2  | 0.210±0.005  | 0.035±0.007                                    | 0                 | 0.68±0.06                                      | 0.105±0.004  | 10.1±1.0                                       | 11                |
| 536        | 1.0±0.1  | 0.208±0.005  | 0.027±0.006                                    | 0                 | 0.55±0.06                                      | 0.111±0.004  | 7.9±0.8  | 7                 |
| 567        | 0.84±0.10                                      | 0.224±0.006  | 0.027±0.006                                    | 0                 | 0.43±0.04                                      | 0.113±0.004  | 6.3±0.6  | 4                 |
| 598        | 0.65±0.09                                      | 0.227±0.006  | 0.022±0.005                                    | 0                 | 0.34±0.03                                      | 0.118±0.004  | 5.0±0.5  | 3                 |
| 629        | 0.50±0.07                                      | 0.227±0.006  | 0.017±0.004                                    | 0                 | 0.27±0.02                                      | 0.124±0.004  | 5.0±0.5  | 3                 |
| 660        | 0.40±0.05                                      | 0.234±0.006  | 0.014±0.003                                    | 0                 | 0.22±0.02                                      | 0.125±0.005  | 4.0±0.4  | 3                 |
| 692        | 0.30±0.05                                      | 0.224±0.008  | 0.011±0.003                                    | 0                 | 0.17±0.02                                      | 0.125±0.005  | 3.2±0.3  | 2                 |
| 723        | 0.24±0.03                                      | 0.229±0.007  | 0.009±0.002                                    | 0                 | 0.13±0.01                                      | 0.120±0.005  | 2.6±0.3  | 1                 |
| 754        | 0.19±0.02                                      | 0.224±0.006  | 0.008±0.002                                    | 0                 | 0.112±0.009                                    | 0.132±0.004  | 2.2±0.2  | 1                 |
| 785        | 0.15±0.02                                      | 0.222±0.006  | 0.007±0.002                                    | 0                 | 0.091±0.007                                    | 0.135±0.005  | 1.8±0.2  | 0                 |
| 817        | 0.12±0.01                                      | 0.219±0.006  | 0.007±0.002                                    | 0                 | 0.073±0.006                                    | 0.134±0.004  | 1.5±0.1  | 0                 |
| 848        | 0.09±0.01                                      | 0.215±0.005  | 0.006±0.001                                    | 0                 | 0.061±0.005                                    | 0.138±0.004  | 1.3±0.1  | 0                 |
| 879        | 0.08±0.01                                      | 0.212±0.005  | 0.005±0.001                                    | 0                 | 0.052±0.005                                    | 0.146±0.005  | 1.3±0.1  | 0                 |
| 911        | 0.065±0.007                                    | 0.225±0.006  | 0.004±0.001                                    | 0                 | 0.041±0.003                                    | 0.144±0.005  | 1.1±0.1  | 0                 |

Table 5.21: The expected number of signal events ( $N_{\text{exp.}}$ ), the acceptance ( $a$ ) times efficiency ( $\varepsilon$ ) for the signal, the estimated number of background events ( $N_{\text{est}}$ ) and the observed number of events  $N_{\text{obs}}$  for all different mass hypothesis of staus in SR-1Cand-FullDet and SR-2Cand-FullDet.

(2050 GeV) for gluinos, 1250 GeV (1280 GeV) for sbottom and 1345 GeV (1370 GeV) for stop  $R$ -hadrons is obtained from SR-Rhad-FullDet.

**Stau and chargino** The expected number of signal events ( $N_{\text{exp.}}$ ), the acceptance ( $a$ ) times efficiency ( $\varepsilon$ ) for the signal, the estimated number of background events ( $N_{\text{est}}$ ) and the observed number of events  $N_{\text{obs}}$  for all different mass hypothesis of charginos and staus in SR-1Cand-FullDet and SR-2Cand-FullDet are given in Tables 5.21 and 5.22. For SR-1Cand-FullDet and SR-2Cand-FullDet a good agreement between the estimated and the observed number of events is found for all signal regions. Two competing effects are responsible for the behaviour of the signal efficiency. The first effect is that the higher the masses of the sparticles the more central the candidates, which results in a higher acceptance. The second effect is the decrease in reconstruction efficiency for larger masses or correspondingly reduced velocities, as discussed in Section 5.4.2. For the low masses the effect of the increased acceptance is more relevant as all HCLLPs are expected to be in the plateau of the MuGirlStau reconstruction efficiency. On the other hand for high masses almost all candidates are in the acceptance window of the analysis and hence the effect from the increase in acceptance is low. Therefore first an increase in signal efficiency is expected, while for higher mass it is decreasing. This is visible for both staus and charginos, though more

| Mass [GeV] | SR-2Cand-FullDet                               |  |  |                   | SR-1Cand-FullDet                               |  |  |                   |
|------------|--|--|--|-------------------|--|--|--|-------------------|
|            | $N_{\text{exp.}} \pm \sigma_{N_{\text{exp.}}}$ | $a \times \varepsilon \pm \sigma_{a \times \varepsilon}$ | $N_{\text{est.}} \pm \sigma_{N_{\text{est.}}}$ | $N_{\text{obs.}}$ | $N_{\text{exp.}} \pm \sigma_{N_{\text{exp.}}}$ | $a \times \varepsilon \pm \sigma_{a \times \varepsilon}$ | $N_{\text{est.}} \pm \sigma_{N_{\text{est.}}}$ | $N_{\text{obs.}}$ |
| 200        | 2600±400                                       | 0.083±0.003  | 1.5±0.3  | 0                 | 1200±200                                       | 0.038±0.002  | 230±20   | 227               |
| 250        | 1200±200                                       | 0.091±0.003  | 0.51±0.10                                      | 0                 | 800±100  | 0.062±0.003  | 110±10   | 109               |
| 300        | 690±100  | 0.102±0.004  | 0.33±0.06                                      | 0                 | 490±50   | 0.073±0.003  | 79±7   | 74                |
| 350        | 360±50   | 0.101±0.004  | 0.15±0.03                                      | 0                 | 280±30   | 0.078±0.003  | 41±4   | 36                |
| 400        | 220±30   | 0.107±0.004  | 0.08±0.02                                      | 0                 | 180±20   | 0.089±0.004  | 23±2   | 20                |
| 450        | 140±20   | 0.113±0.004  | 0.06±0.01                                      | 0                 | 120±10   | 0.100±0.004  | 17±2   | 16                |
| 500        | 90±10  | 0.115±0.004  | 0.034±0.007                                    | 0                 | 77±8   | 0.100±0.004  | 10±1   | 11                |
| 550        | 59±8   | 0.119±0.004  | 0.027±0.006                                    | 0                 | 52±5   | 0.105±0.004  | 7.9±0.8  | 7                 |
| 600        | 42±6   | 0.129±0.004  | 0.021±0.004                                    | 0                 | 36±4   | 0.110±0.004  | 5.0±0.5  | 3                 |
| 650        | 27±4   | 0.123±0.004  | 0.014±0.003                                    | 0                 | 24±2   | 0.107±0.004  | 4.0±0.4  | 3                 |
| 700        | 18±3   | 0.122±0.004  | 0.011±0.003                                    | 0                 | 17±2   | 0.113±0.004  | 3.2±0.3  | 2                 |
| 750        | 12±2   | 0.113±0.004  | 0.008±0.002                                    | 0                 | 13±1   | 0.118±0.004  | 2.1±0.2  | 1                 |
| 800        | 9±1  | 0.120±0.004  | 0.007±0.002                                    | 0                 | 9.2±0.9  | 0.123±0.004  | 1.8±0.2  | 0                 |
| 850        | 6.0±0.8  | 0.112±0.005  | 0.006±0.001                                    | 0                 | 6.1±0.6  | 0.114±0.005  | 1.3±0.1  | 0                 |
| 900        | 4.2±0.6  | 0.108±0.004  | 0.004±0.001                                    | 0                 | 4.7±0.5  | 0.121±0.004  | 1.1±0.1  | 0                 |
| 950        | 3.2±0.5  | 0.112±0.004  | 0.003±0.001                                    | 0                 | 3.3±0.3  | 0.118±0.004  | 1.0±0.1  | 0                 |
| 1000       | 2.2±0.4  | 0.106±0.005  | 0.0029±0.0009                                  | 0                 | 2.5±0.2  | 0.120±0.006  | 0.84±0.10                                      | 0                 |
| 1100       | 1.2±0.2  | 0.105±0.004  | 0.0019±0.0007                                  | 0                 | 1.5±0.2  | 0.131±0.004  | 0.54±0.07                                      | 0                 |
| 1200       | 0.62±0.09                                      | 0.096±0.004  | 0.0015±0.0006                                  | 0                 | 0.74±0.07                                      | 0.115±0.004  | 0.42±0.06                                      | 0                 |
| 1300       | 0.32±0.04                                      | 0.087±0.003  | 0.0012±0.0006                                  | 0                 | 0.44±0.05                                      | 0.118±0.004  | 0.33±0.05                                      | 0                 |
| 1400       | 0.19±0.03                                      | 0.087±0.004  | 0.0009±0.0005                                  | 0                 | 0.26±0.03                                      | 0.120±0.004  | 0.27±0.04                                      | 0                 |
| 1500       | 0.10±0.02                                      | 0.077±0.003  | 0.0007±0.0005                                  | 0                 | 0.16±0.01                                      | 0.121±0.004  | 0.21±0.04                                      | 0                 |

Table 5.22: The expected number of signal events ( $N_{\text{exp.}}$ ), the acceptance ( $a$ ) times efficiency ( $\varepsilon$ ) for the signal, the estimated number of background events ( $N_{\text{est}}$ ) and the observed number of events  $N_{\text{obs}}$  for all different mass hypothesis of charginos in SR-1Cand-FullDet and SR-2Cand-FullDet.

pronounced for the latter as they span a larger range of mass hypotheses. The effect of the decrease for higher masses is not visible in the SR-1Cand-FullDet mass window, as the loss in overall efficiency is compensated by less events being promoted to SR-2Cand-FullDet. In general the signal efficiency is better for staus than for charginos as the latter are expected to be produced more in the forward direction and with lower velocities, as discussed in Section 4.1. The upper cross section limits for staus and charginos are shown in Figures 5.93. The limits are rather flat as a function of mass, but feature a slight increase for lower masses. This increase is more prominent for charginos, as the main sensitivity for the low masses originates from SR-2Cand-FullDet, where the efficiency decrease is more prominent for charginos. The observed (expected) lower mass limits are 430 GeV (420 GeV) for staus and 1090 GeV (1070 GeV) for charginos. From Table 5.22 it can be seen that a significant fraction of the sensitivity at the mass limit of charginos is originating from the SR-1Cand-FullDet, which was achieved by suppressing the background with the additional  $dE/dx$  requirement.

**Meta-stable gluinos** The breakdown of this analysis approach for lower lifetimes is tested considering gluino  $R$ -hadron signals with 10 ns, 30 ns and 50 ns. The expected number of signal events ( $N_{\text{exp.}}$ ), the acceptance ( $a$ ) times efficiency ( $\varepsilon$ ) for the signal, the estimated number of background

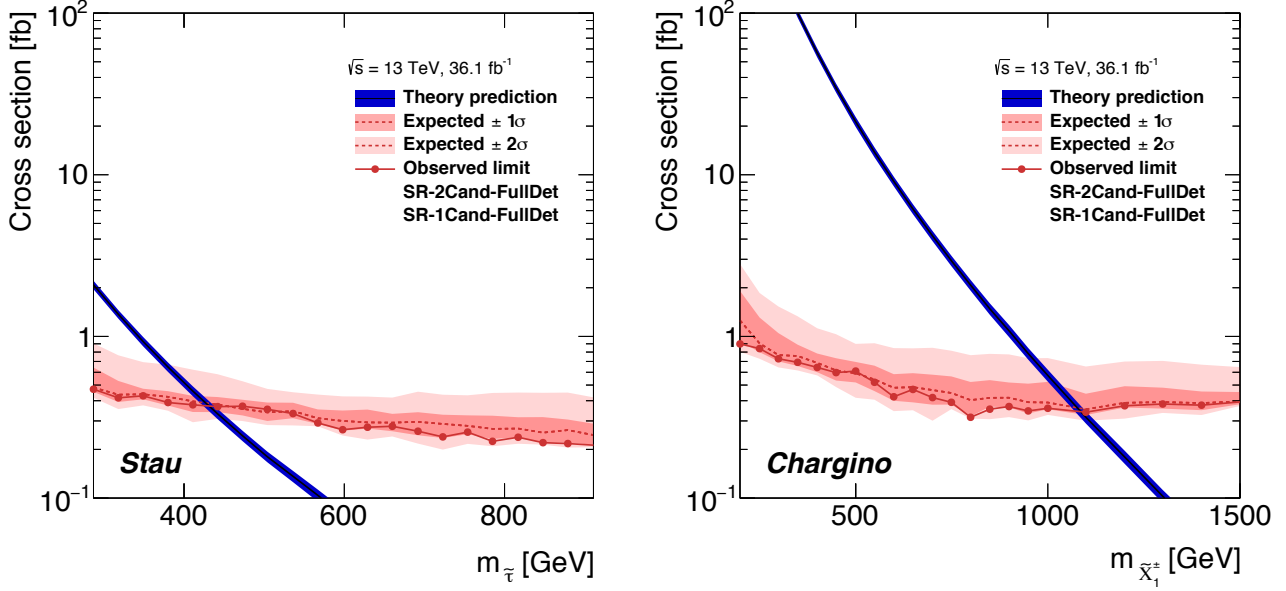


Figure 5.93: The observed and expected upper cross section limits as well as the theory prediction for the cross section of direct pair-produced staus (left) and charginos (right) as function of the simulated mass. Both limits are obtained from a combination of SR-1Cand-FullDet and SR-2Cand-FullDet. The dashed lines indicate the expected limits, while the  $\pm 1\sigma$  ( $\pm 2\sigma$ ) bands on the expected limit are drawn as dark (light) red band. The observed limits are shown as dots connected by a line. [5]

| LifETIME   | SR-Rhad-MSagno (ID+CALO)         |  |                                  |  |                                  |  |                                  |            |
|------------|----------------------------------|--|----------------------------------|--|----------------------------------|--|----------------------------------|------------|
|            | 10 ns                            |  | 30 ns                            |  | 50 ns                            |  | $N_{est.} \pm \sigma_{N_{est.}}$ | $N_{obs.}$ |
| Mass [GeV] | $N_{exp.} \pm \sigma_{N_{exp.}}$ | $a \times \epsilon \pm \sigma_{a \times \epsilon}$ | $N_{exp.} \pm \sigma_{N_{exp.}}$ | $a \times \epsilon \pm \sigma_{a \times \epsilon}$ | $N_{exp.} \pm \sigma_{N_{exp.}}$ | $a \times \epsilon \pm \sigma_{a \times \epsilon}$ |                                  |            |
| 1000       | $800 \pm 100$                    | $0.065 \pm 0.004$                                  | $1400 \pm 300$                   | $0.121 \pm 0.006$                                  | $1500 \pm 300$                   | $0.125 \pm 0.005$                                  | $1.0 \pm 0.3$                    | 2          |
| 1200       | $220 \pm 40$                     | $0.072 \pm 0.004$                                  | $400 \pm 70$                     | $0.129 \pm 0.006$                                  | $410 \pm 70$                     | $0.133 \pm 0.005$                                  | $0.7 \pm 0.3$                    | 2          |
| 1400       | $70 \pm 10$                      | $0.079 \pm 0.004$                                  | $120 \pm 20$                     | $0.132 \pm 0.005$                                  | $140 \pm 30$                     | $0.149 \pm 0.006$                                  | $0.6 \pm 0.2$                    | 2          |
| 1600       | $22 \pm 4$                       | $0.074 \pm 0.003$                                  | $41 \pm 7$                       | $0.140 \pm 0.005$                                  | $41 \pm 7$                       | $0.142 \pm 0.005$                                  | $0.5 \pm 0.2$                    | 2          |
| 1800       | $8 \pm 1$                        | $0.077 \pm 0.003$                                  | $14 \pm 2$                       | $0.139 \pm 0.005$                                  | $14 \pm 2$                       | $0.142 \pm 0.005$                                  | $0.4 \pm 0.1$                    | 2          |
| 2000       | $2.8 \pm 0.5$                    | $0.080 \pm 0.005$                                  | $4.7 \pm 0.8$                    | $0.132 \pm 0.007$                                  | $5.2 \pm 0.9$                    | $0.146 \pm 0.005$                                  | $0.4 \pm 0.1$                    | 2          |
| 2200       | $1.0 \pm 0.2$                    | $0.075 \pm 0.004$                                  | $1.7 \pm 0.3$                    | $0.132 \pm 0.005$                                  | $1.7 \pm 0.3$                    | $0.130 \pm 0.004$                                  | $0.4 \pm 0.1$                    | 2          |
| 2400       | $0.35 \pm 0.06$                  | $0.073 \pm 0.004$                                  | $0.58 \pm 0.10$                  | $0.120 \pm 0.004$                                  | $0.6 \pm 0.1$                    | $0.122 \pm 0.004$                                  | $0.4 \pm 0.1$                    | 2          |

Table 5.23: The expected number of signal events ( $N_{exp.}$ ), the acceptance ( $a$ ) times efficiency ( $\epsilon$ ) for the signal, the estimated number of background events ( $N_{est.}$ ) and the observed number of events  $N_{obs.}$  for all different mass hypothesis of gluino  $R$ -hadrons with a lifetime of 10 ns, 30 ns and 50 ns.

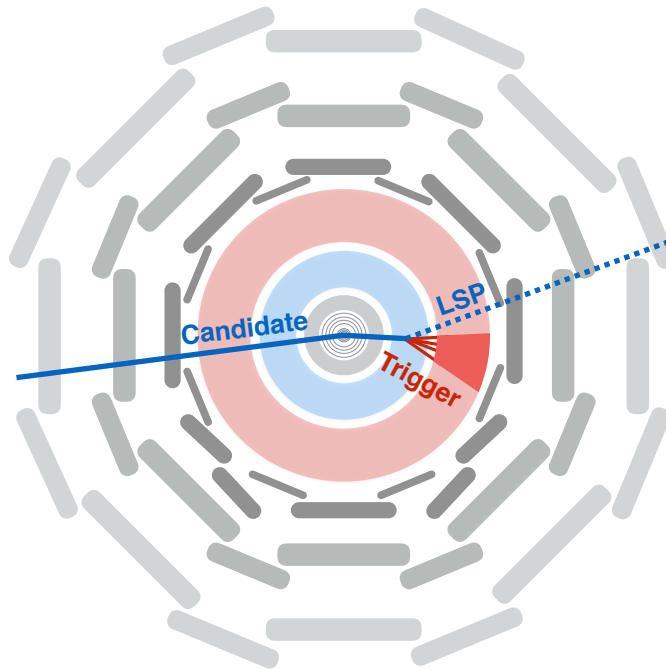


Figure 5.94: A possible constellation for pair-produced meta-stable  $R$ -hadrons, where one candidate is decaying before the calorimeters to SM quarks that are visible in the calorimeters and the LSP that is neutral. If the mass difference is significant between the  $R$ -hadron and the LSP a significant energy for the quarks is present that can lead to a  $\cancel{E}_T$  trigger accept.

events ( $N_{est}$ ) and the observed number of events  $N_{obs}$  for all different lifetimes and mass hypothesis considered for gluino  $R$ -hadrons are given in Table 5.23. Also for different lifetimes of gluino  $R$ -hadrons, two competing effects on the signal efficiency are present. On the one hand the shorter the lifetime the lower the efficiency for reconstructing HCLLPs as  $ID+CALO$  candidates as they might decay before reaching the Tile Calorimeter. On the other hand if candidates decay before or within the calorimeters, their decay products could be seen in the calorimeters and might lead to large  $\cancel{E}_T$  and hence an increase in trigger efficiency. This is in particular interesting for constellations as sketched in Figure 5.94. Such events might be selected by  $\cancel{E}_T$  triggers, without having to rely on an ISR jet and also have a HCLLP candidate in the event. For the meta-stable  $R$ -hadron signals considered in this study the decay to a neutralino ( $m_{\chi_1^0} = 100$  GeV) and two quarks is assumed, as discussed in Section 5.3. For such a large difference between the LSP and the  $R$ -hadrons masses the jets from the quarks are expected to be hard and hence most of the events that have a  $R$ -hadron decaying before the calorimeters will be accepted by the trigger. This effect can be seen as the signal efficiency is slightly increased for meta-stable  $R$ -hadrons with lifetimes of 30 ns and 50 ns compared to the stable ones. For lower lifetimes it is becoming more and more likely that both candidates decay before the calorimeters and hence give no HCLLP candidates for this analysis approach. The upper cross-section limits for

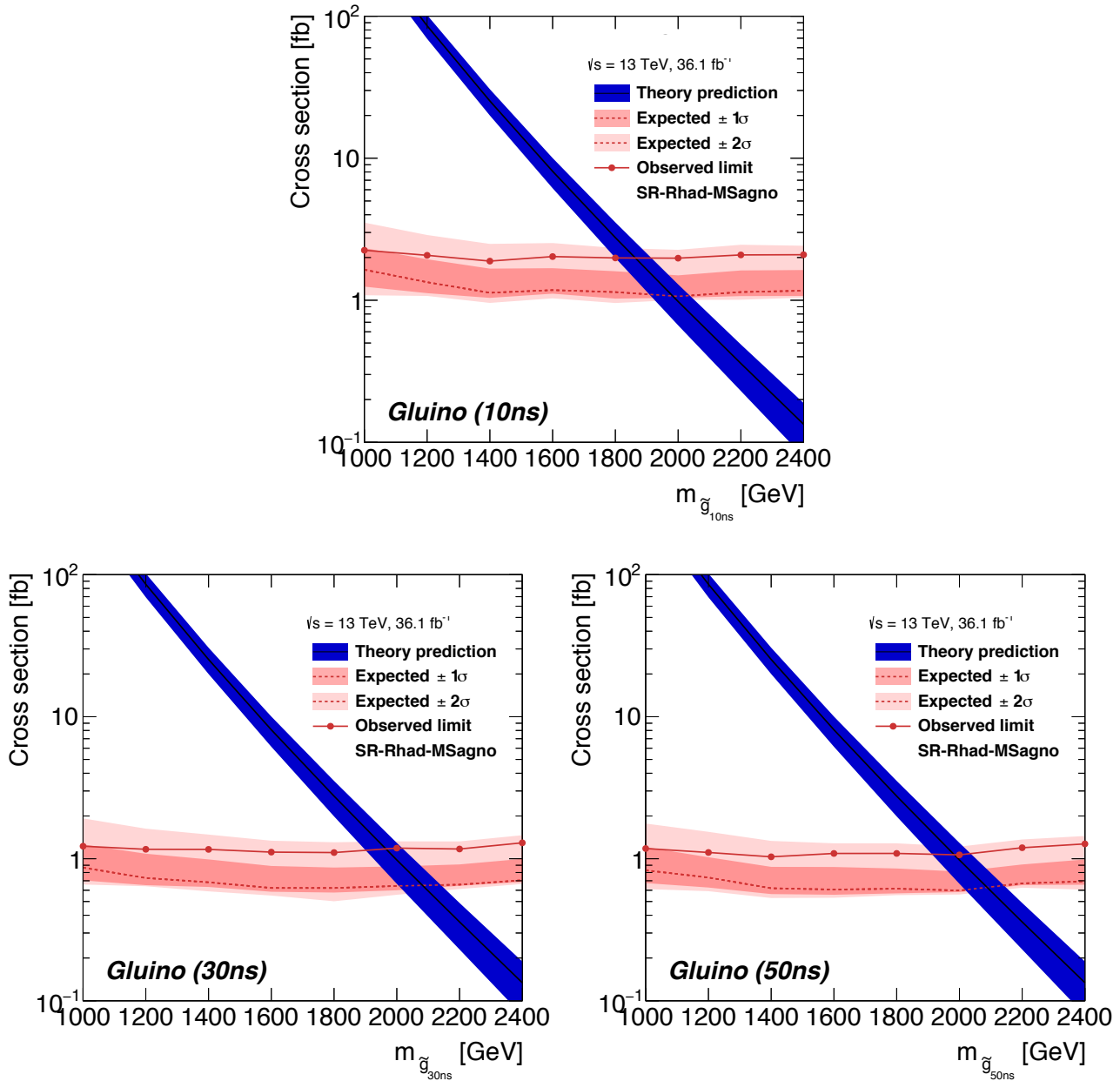


Figure 5.95: The observed and expected upper cross section limits as well as the theory prediction for the cross section of gluino  $R$ -hadrons with a lifetime of 10 ns (upper), 30 ns (lower left) and 50 ns (lower right) as function of the simulated mass. The results are obtained from SR-Rhad-MSagno. The dashed lines indicate the expected limits, while the  $\pm 1\sigma$  ( $\pm 2\sigma$ ) bands on the expected limit are drawn as dark (light) red band. The observed limits are shown as dots connected by a line. [5]

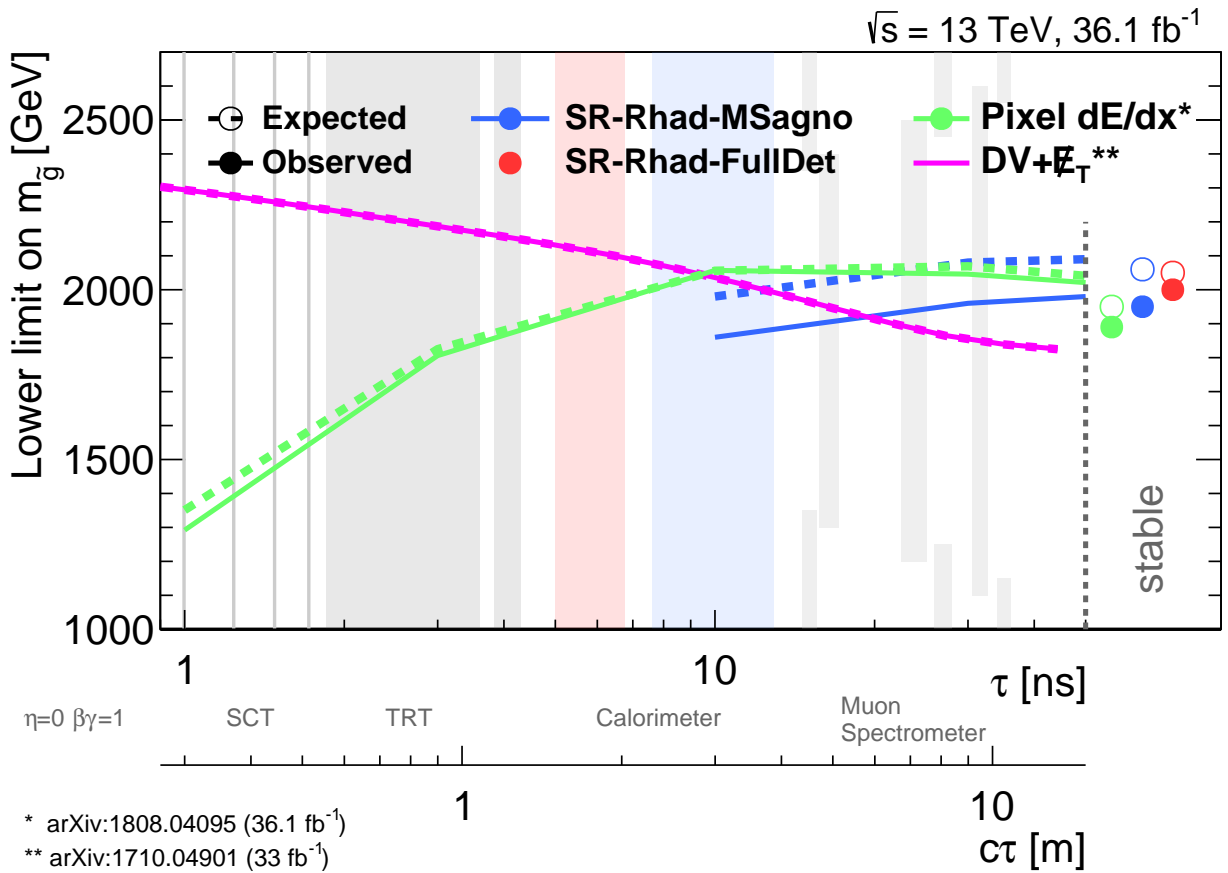


Figure 5.96: The lower mass limits obtained for pair-produced gluino  $R$ -hadron signal models for different signal regions and analysis strategies. If gluinos are generated with a lifetime the decay to two quarks and the neutralino as LSP are simulated. The mass of the neutralino is fixed to 100 GeV for all cases. For the stable cases the observed (expected) lower mass limits are shown as circles (empty circles). The observed (expected) limits for the meta-stable cases are drawn as lines (dashed lines). Besides the lifetime axis also the  $c\tau$  axis is drawn. Furthermore for  $\eta=1$  and  $\beta\gamma$  the ranges of the different sub-detectors are illustrated. The lower mass limits for the pixel  $dE/dx$  analysis are taken from Reference [127] and for the  $DV+E_T$  analysis from Reference [148].

meta-stable gluino  $R$ -hadrons are shown in Figures 5.95. It can be seen that the effect of the efficiency increase/decrease for different lifetimes is not mass dependent for the range considered, as the upper cross section limit is similarly flat for all considered lifetimes. The observed (expected) lower mass limits for meta-stable  $R$ -hadrons are 1980 GeV (1860 GeV) for 10 ns, 2080 GeV (1960 GeV) for 30 ns and 2090 GeV (1980 GeV) for 50 ns.

The lower mass limits obtained for the meta-stable  $R$ -hadron signal together with the results from the stable  $R$ -hadron signal region as well as the results from the pixel  $dE/dx$  analysis [127] and the  $DV+E_T$  analysis [148] are shown in Figure 5.96. It can be seen that for lifetimes of 30 ns and 50 ns this analysis is expected to have the best sensitivity but due to the slight excess at higher masses the observed limit is lower than for the pixel  $dE/dx$  analysis, as they do not see any excess in their meta-stable selection. For the stable case the expected limits from SR-Rhad-MSagno

and SR-Rhad-FullDet are, similar but the observed is slightly better for SR-Rhad-FullDet. The observed lower mass limit from the pixel  $dE/dx$  analysis for the stable models is about 100 GeV lower than the one obtained from SR-Rhad-FullDet. At about 10 ns lifetime the pixel  $dE/dx$  analysis has the best sensitivity, while for even lower lifetimes the DV+ $\cancel{E}_T$  analysis is taking over. The DV+ $\cancel{E}_T$  analysis looks for displaced vertices with several associated tracks and  $\cancel{E}_T$  in the event. The DV+ $\cancel{E}_T$  analysis is very sensitive to the mass difference between the LSP and the  $R$ -hadron as for small mass differences the number of charged particles in the jets as well as the total vertex mass will go down and hence decrease the reconstruction efficiencies for the displaced vertex. The scenario considered here is rather beneficial for this analysis and the picture will change significantly if scenarios with small mass splitting between the HCLLP and the LSP are considered. For the pixel  $dE/dx$  approach or the one described in this thesis no significant changes in sensitivity are expected for compressed scenarios between the HCLLP and the LSP. For even lower lifetimes prompt searches [153], which largely rely on the specific decay of the  $R$ -hadron, will take over.

**Previous results** The observed lower mass limits for this analysis as well as for the Run-1 [97] and the first Run-2 [101] analysis are summarised in Figure 5.97. For all different signal models a significant increase in the lower mass limits can be seen. The highest limits are obtained for gluino  $R$ -hadrons due to their relatively high cross section. For stop and sbottom  $R$ -hadrons the limits are now at roughly 1200 GeV to 1300 GeV and extend the results of the previous searches by 300 GeV to 400 GeV. Also a large increase (475 GeV) in the lower mass limit is visible for direct pair-produced charginos. This was achieved by the tighter definition of SR-1Cand-FullDet, compared to the Run-1 analysis, which now contributes to the sensitivity at the mass limit. The lowest mass limits are obtained for direct pair-produced staus, which are still below 500 GeV. So also for the minimal supersymmetric scenarios the moderate mass range is not yet fully ruled out. A very important remark on those mass limits is, that they are very model dependent and tend to give the illusion of the low mass range being fully ruled out. But nature does not have to be minimal and if processes are suppressed or completely different scenarios give rise to HCLLPs the cross section can be low. So the search for HCLLPs should be designed to achieve best sensitivity over the whole

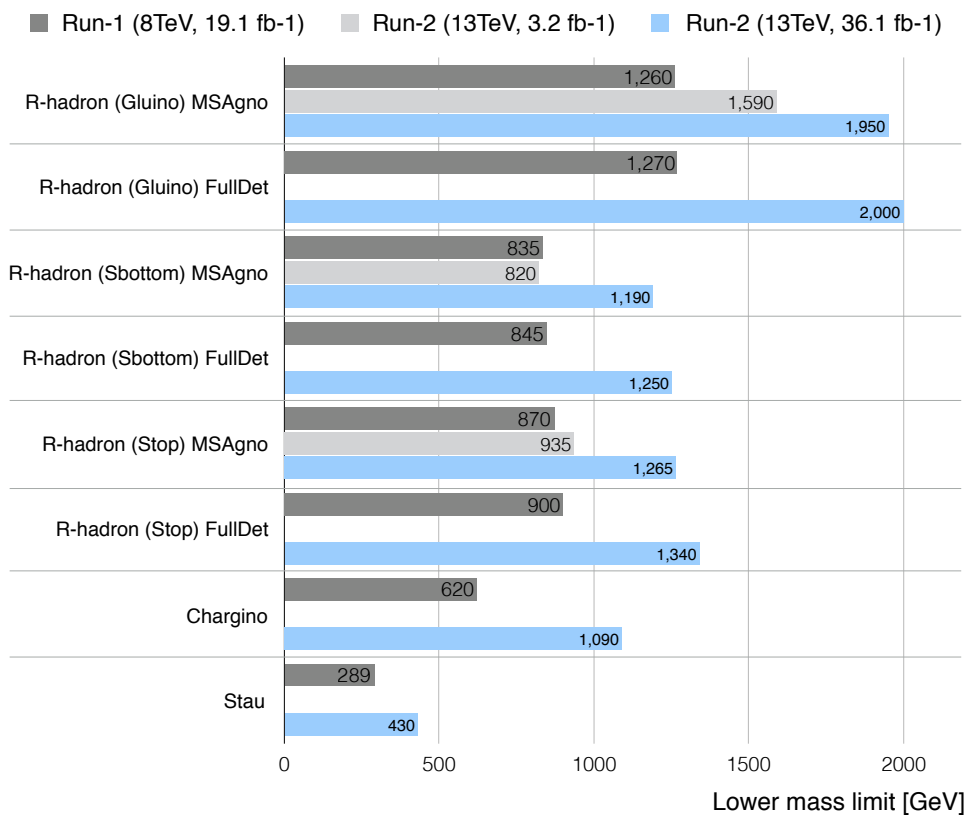


Figure 5.97: The observed lower mass limits compared to the Run-1 [97] and the first Run-2 [101] analysis. The first Run-2 analysis was only using the MS-agnostic approach and was aiming mainly for *R*-hadrons as for them the largest increase in sensitivity from 8 TeV to 13 TeV was expected. I was also working on this analysis during my Phd.

mass range.

### 5.11.3 Re-interpretation Long-Lived Multi-Charged Particles

The results of this search can be also interpreted for multi-charged particles. This can be used to study the breakdown of this analysis strategy for higher charges. Furthermore it helps to understand how multi-charged particles could appear in the signal regions of this analysis. An understanding of the  $z = 2$  multi-charged particles can be also important for the  $R$ -hadron signals as there some doubly-charged states are expected. Further details about this re-interpretation are given in Appendix A.7.

This study is based on samples used in a dedicated analysis for multi-charged particles as described in Reference [154]. The multi-charged particles are assumed to be fermions and only direct-pair production via photon exchange is considered. The mass hypotheses tested in this re-interpretation are between 400 GeV and 1400 GeV in steps of 200 GeV and charges of  $|ze|$  with  $z = 2$  and 2.5 are assumed. The samples are generated with MG5\_AMC@NLO 2.3.3 using the NNPDF23LO PDF set, the A14 set of tuned parameters and PYTHIA 8.205 for hadronisation and the underlying event.

First the most suitable of the analysis approaches presented in this work for the search for multi-charged particles has to be determined. They are charged throughout the whole detector and are therefore candidates for the SR-2Cand-FullDet SR-1Cand-FullDet approach. But this is very sensitive to inefficiencies of the LOOSE selection as for lower masses the main sensitivity originates from the SR-2Cand-FullDet. Also the SR-Rhad-FullDet approach could be used, which has the benefit of using  $\beta\gamma$ , which might be wrong, but due to the higher ionisation energy loss, rather too low, resulting in a better discrimination power. One important consequence of the higher charge of the particles is, that their momentum is wrong by  $1/z$  as for this analysis  $z = 1$  is assumed. This also affects the estimated mass, which is accordingly also off by a factor of  $1/z$ . The final mass windows that have to be chosen for multi-charged particles are therefore at low masses where a sufficient background suppression can only be achieved with SR-2Cand-FullDet. Hence, the SR-2Cand-FullDet-SR-1Cand-FullDet approach is used for the analysis of the multi-charged signals, with the mass windows selected according to the charge.

The signal efficiency as a function of the true particle mass for pair-produced charginos, and multi-charged particles with  $|2e|$  and  $|2.5e|$  is shown in Figure 5.98. The charginos are shown for comparison as

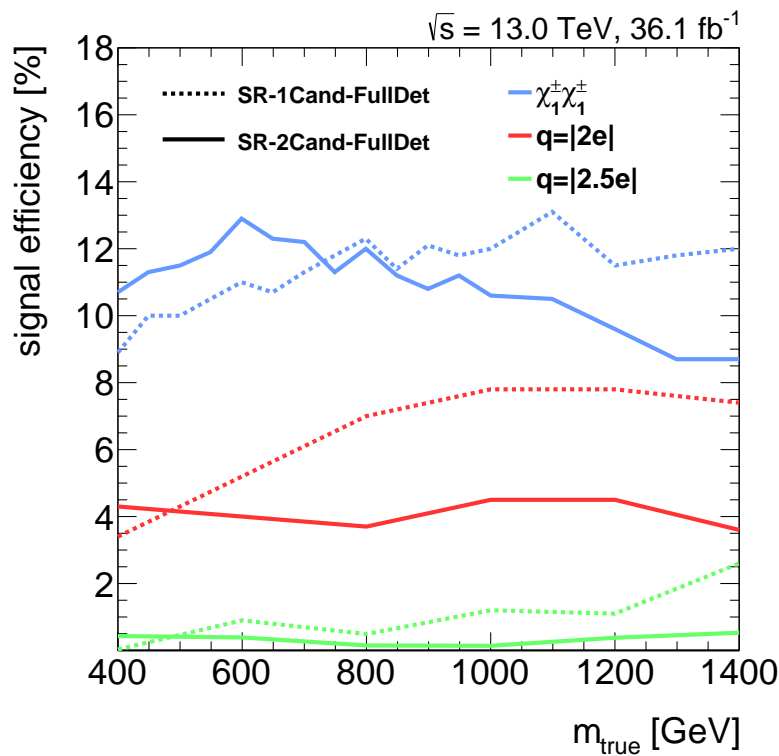


Figure 5.98: The signal efficiency as function of the true particle mass for pair-produced charginos (blue), and multi-charged particles with  $|2e|$  (red) and  $|2.5e|$  (green) in SR-1Cand-FullDet (dashed) and SR-2Cand-FullDet (solid).

they are also fermions, but with a charge  $q = |1e|$ . It can be seen that the efficiency is already for a doubly-charged particle significantly lower and completely drops for higher charges. Furthermore as discussed above mainly SR-2Cand-FullDet is contributing to the sensitivity, as SR-1Cand-FullDet is suffering from large backgrounds. Hence mainly the 4% efficiency of the SR-2Cand-FullDet are relevant. The reason why this efficiency is so low is that a significant fraction of candidates is rejected by the consistency requirement between the time-of-flight measurements. The consistency is critical as the timing in the MDT's is incorrect for multi-charged particles. This might be explained by the higher ionisation energy loss in the MDT's. The ionisation energy-loss e.g. for doubly-charged particles with  $\beta\gamma = 1$  is according to the Bethe-Bloch Equation 4.4 about six times higher than the one expected from minimum ionising particles. This could lead to a faster signal rise, resulting in smaller drift radii and accordingly to smaller  $t_0$ . This should be further investigated as  $R$ -hadrons can have doubly charged states and hence those effects might also be relevant there.

The results in SR-1Cand-FullDet and SR-2Cand-FullDet from the nominal analysis can be used to set upper cross section limits on multi-charged particles and using the theoretical prediction lower mass limits can be obtained. The observed (expected) lower mass limits for pair-produced

multi-charged particles are 715 GeV (690 GeV) for  $z = 2$  and 460 GeV (420 GeV) for  $z = 2.5$ . The lower mass limits from the dedicated analysis for multi-charged particles, which is using  $dE/dx$  measurements from the MDT, the TRT and the pixel detector as main observables to identify multi-charged stable particles. The observed limits are 980 GeV for  $z = 2$  and 1060 GeV for  $z = 2.5$ . Besides the problem with the consistency between the  $\beta$  measurements also the rather poor MuGirlStau efficiency is decreasing the sensitivity of this analysis. The dedicated approach is using the standard muon algorithms, which are, for the masses considered, almost fully efficient. Both the MuGirlStau efficiency as well as the consistency are not optimal in this analysis round and should be significantly improved in the next iteration, hence the sensitivity at least for the  $z = 2$  particles could be similar to the one achieved with the dedicated multi-charged particle analysis. The inefficiencies detected for  $z = 2$  particles can be used to improve SR-Rhad-FullDet with respect to doubly-charged  $R$ -hadron states. The argumentation could also be turned around to accept that the analysis is inefficient to doubly-charged states. As charge-flips to doubly-charged  $R$ -hadron states are the dominant source for charged  $R$ -hadron states with different charge in ID and MS, the combined ID+MS momentum instead of the ID momentum could be used for  $R$ -hadron full-detector candidates, which would significantly improve the mass resolution.

## 5.12 Ideas for the future

In this section a summary of ideas for potential improvements for the search for HCLLPs will be given. Also a personal estimate where possible on the potential and the amount of work needed will be given. The ordering of the topics follows the structure used in this work.

**HCLLPs produced in decay chains** In this analysis only models of pair produced HCLLPs are considered. Different kinematics for similar signatures are solely explored by comparing staus and charginos. A very interesting extension could be to consider models where the HCLLPs are produced in decay chains. If the available energy for the HCLLPs is low due to the decays, they might fail to be reconstructed and hence a significant decrease in signal efficiency might occur. Such decay chains could be explored e.g. using simplified models. Using those signal models also for the optimisation of the signal regions as cross-check can help to make

them more robust against the kinematics of the HCLLPs.

This could be very beneficial for the analysis and the effort needed should be manageable as people are currently working on setting up such simplified models for long-lived particles.

**MS only tracks** A rather long outstanding idea is to use MS only tracks as a new type of object. Those would mainly aim for  $R$ -hadrons were the particles undergo a chargeflip from uncharged in the ID to charged in the MS. For stops about 25% of  $R$ -hadrons are expected to have those charge flips, which is indeed a significant fraction. But this analysis is very challenging because it will suffer from huge background from cosmic-ray muons that are very hard to reject with this analysis approach. Furthermore it will be difficult to relax the  $\beta = 1$  assumption in the reconstruction and to deal with the out-of-time hits. The reconstruction efficiency will therefore drop rather rapidly as function of  $\beta$ . The effort will be very likely not in a relation to the gain for this analysis.

**Pixel  $\beta\gamma$  uncertainty** A reliable uncertainty on the  $\beta\gamma$  measured with the pixel detector could be used for a combination of all velocity measurements as well as for a more reliable consistency estimate between the  $\beta\gamma_{dE/dx}$  and  $\beta_{ToF}$ . One potential way of estimating this would be to use e.g. low-momentum protons in minimum bias data and comparing the estimated with the known mass of the proton. The uncertainty of the momentum has to be taken into account and unfolded from the resolution. Some initial studies are described in Reference [155], but some further investigation is still needed.

This first results look very promising and the gain for the analysis could be significant.

**Tile Calorimeter  $\beta$**  One potential source for improvement of the Tile Calorimeter  $\beta$  can be to re-optimize or maybe completely drop the minimum energy requirement per hit. Currently about 30% of the  $R$ -hadrons have only one Tile Calorimeter hit, used for a  $\beta$  measurement and hence no requirement on the minimum number of hits is used. But if the energy threshold per hit is lowered also less  $R$ -hadrons would be lost and a requirement on at least two hits in the Tile Calorimeter could be used. This could significantly reduce the background due to mis-measurements in the Tile Calorimeter.

This should be for sure re-optimised and tested for the next analysis round.

**Satellite-muon tagging** As described in Section 5.5.2, it was possible for the first time to identify muons from satellite-satellite collisions with the Tile Calorimeter. With more data it might even be possible to detect particles from satellites further away from the central bunches. One idea is to identify muons originating from satellite-satellite collisions with the Tile Calorimeter and tag them as satellite muons. Those can be used to validate the behaviour of other subdetectors for out-of-time signals. This could be in particular interesting for the LAr calorimeter, to check whether the slight offset, that was found for electrons, is also visible for muons, or if minimal ionising particles are measured with the correct timings. Those studies could also be expanded to validate the timing also for other subdetectors, such as the muon detectors or to validate the behaviour of the TRT for out-of-time signals.

The effort needed for those studies is rather low and in particular the validation of the LAr calorimeter timing is important as this could be potentially added as an additional time-of-flight measurement.

**Liquid Argon calorimeter  $\beta$**  Using the timing information from the LAr calorimeter to estimate  $\beta$  was tested in a bachelor project with Joschua Krink, the results are summarised in Section A.1. The basic idea is to use the calibration of single cells and the calibration over time estimated for the search for non-pointing photons, while all other calibration steps follow the guideline of this analysis, but are redone using muons, as they depend on the energy deposit or the signal distribution in the LAr calorimeter. The  $\beta$  resolution estimated from the LAr with the same minimum  $E_{hit} = 500$  MeV requirement as used for the Tile Calorimeter is not competitive, but using instead  $E_{hit} = 2$  GeV a beta resolution similar to that of the Tile Calorimeter could be achieved. A detailed tuning of this minimum requirements would be needed. To include this measurement in the analysis, studies on the out-of-time behaviour e.g. using muons from satellite-satellite collisions as discussed in the previous section are essential. It was further found that the LAr calorimeter timing even after all calibrations and with hard  $E_{hit}$  requirements, was not sufficient to resolve muons from satellite-satellite collisions in the  $33.3 \text{ fb}^{-1}$  proton-proton collisions taken in 2016. Including the LAr timing might be a significant improvement for  $ID+CALO$  candidates as the number of Tile Calorimeter

timing measurements is rather low.

**Tile Calorimeter  $dE/dx$**  Using the Tile Calorimeter to measure  $dE/dx$  for the search for HCLLPs was tested together with Manuel Ettengruber in his bachelor project. The  $dE/dx$  can be estimated for each Tile Calorimeter cell from the path length of the track in the cell and the energy deposit. Those are then combined in a similar manner as for the pixel  $dE/dx$  as a truncated mean. While for  $R$ -hadrons a separation between signal and muon background is possible this is not the case for colour singlets. The main reason is that the Tile Calorimeter is not a thin detector and hence the mean  $dE/dx$  is measured instead of the MPV. As a result high-momentum muons are releasing similar energy deposits as colour singlets with moderate velocities.  $R$ -hadrons are expected to release more energy as they also interact hadronically.

The effort that has to be put into this might be pretty substantial as all the validation and calibration would have to be done for the first time. It is only applicable for the  $R$ -hadron signal regions and is also dependent on the model used for hadronic interactions.

**$\cancel{E}_T$  using SlowMuons** In the current version of the  $\cancel{E}_T$  on analysis level the combined objects reconstructed by the standard muon algorithms are used for the calculation of the muon contribution. As these are inefficient for slow HCLLPs, they are not taken into account for the  $\cancel{E}_T$  calculation. This is in particular crucial for chargino-neutralino productions as when the chargino is not taken into account no real source for  $\cancel{E}_T$  is in the event. The implementation of this might be rather difficult but would have a substantial effect on a signal region looking for events with an HCLLP and  $\cancel{E}_T$  like used in previous analyses. Besides some technical issues the calculation of the  $\cancel{E}_T$  without SlowMuons was the main reason, why this signal region was not included this time.

**Two ID+Calo candidates signal region** One potential weak spot in sensitivity is for pair produced meta-stable colour-singlets. The lower mass as function of the lifetime for charginos decaying to a neutralino and a soft charged pion are shown in Figure 5.99. It can be seen that the new limits on charginos (1090 GeV) significantly exceed the ones from the other analysis. On the one hand the results of this analysis should be re-interpreted also for the meta-stable cases. On the other hand this analysis approach might break down rather fast as the sensitivity at lower

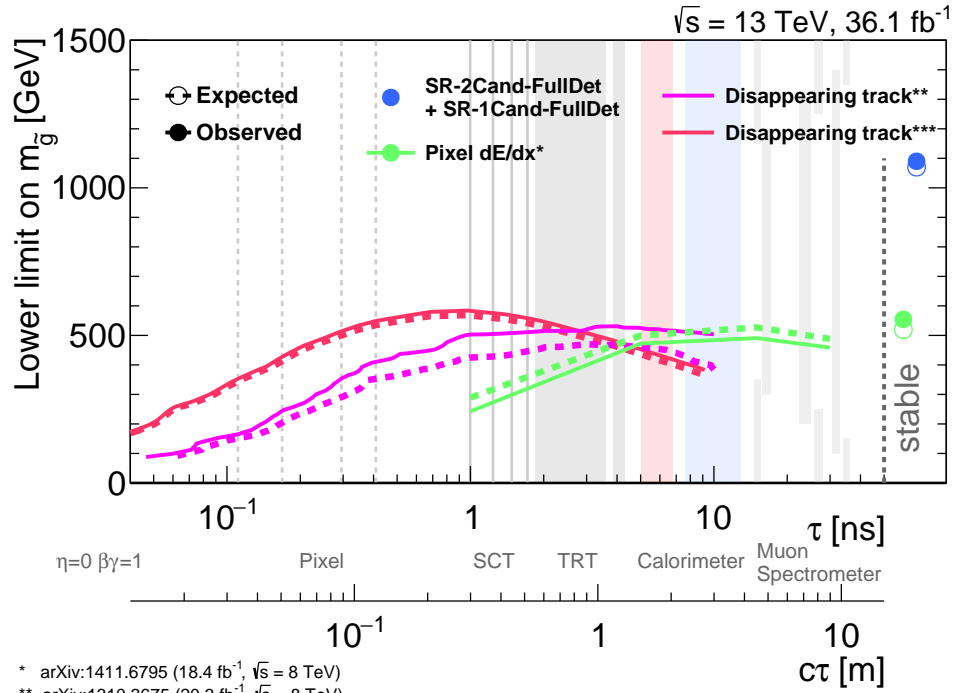


Figure 5.99: Lower mass limits for charginos decaying to a neutralino and a soft charged pion as function of the chargino lifetime in an AMSB scenario with  $\tan(\beta)=5$  and  $\mu > 0$ . The pixel-only disappearing track analysis [94] uses pixel only tracks and vetos track extensions in SCT and TRT, while the disappearing track analysis [156] uses pixel plus SCT tracks and vetos extensions in the TRT. For the limit from SR-2Cand-FullDet + SR-1Cand-FullDet only the direct pair-production of charginos is included, while the other analyses also include the chargino-neutralino production.

masses is mainly driven by the two-candidate signal region which is very sensitive to the lifetime as full-detector candidates are required. A possible new analysis approach requiring two  $\text{ID}+\text{CALO}$  candidates might be very sensitive in the regime of 10 ns to 50 ns. This could also be extended to using candidates from the pixel  $dE/dx$  analysis.

In principle it should be fairly easy to extend the analysis with such a signal region and the approach is generally applicable to pair-produced meta-stable HCLLPs. A huge gain in sensitivity for lifetimes of  $\mathcal{O}(30 \text{ ns})$  should be possible.

**Background estimation  $\eta$  templates** A modified version of the background estimate was developed using  $\eta$  templates instead of the  $\eta$  of the candidates in the control region (Appendix A.6). Combining this with a normalisation of the background in sideband control regions where the mass spectrum is estimated for a  $\beta$  sideband, could significantly stabilise the background estimate against potential signal contamination as both  $\eta$  and the normalisation are estimated in regions where any potential signal contribution is negligible compared to the background. It was shown that the  $\eta$  sampling works for the MS-agnostic approach, but is significantly more complex for the cases of the fall-back signal regions, as the  $\eta$  distribution is not independent from the prioritised signal regions.

The method is in principle very promising and is, for single-bin signal regions as e.g. the MS-agnostic approach or the pixel  $dE/dx$  analysis applicable out of the box. For the more complex signal regions used in this analysis some further investigation is needed to correctly model the dependencies of the fall-back signal regions on the prioritised ones. The gain in reliability of the background estimate would be substantial, but the effort needed is hard to estimate.

**Re-interpretation for quirks** Quirks [157] are a type of predicted particles that are charged under a new gauge group added to the SM. They are assumed to be the only particles charged under this gauge group and are hence expected to be stable. Furthermore they are assumed to be electrically charged. The new gauge group is QCD-like and the interaction gets strong at a scale  $\Lambda$  that is lower than the mass of the quirks. This has an important consequence on the phenomenology of those particles, because in contrast to the SM QCD the *strings* would not break, leading to particles oscillating through the detector. The expected oscillation length depends on the mass of the particles and  $\Lambda$  and is hence not restricted. This analysis might be sensitive to the two extreme cases. If the oscillation length is rather short they look like a single highly ionising track, where the boost of the quirk–quark system defines the velocity of the combined object seen in the detector. On the other hand if the oscillation length is very long the signatures are two separate HCLLPs and again this analysis might be applicable. Results of the corresponding search for HCLLPs with CMS were re-interpreted for the long oscillation length [158], but still no results using the full detector simulation (ATLAS/CMS) were published so far. Those results are particularly important to estimate whether a dedicated analysis approach, as for example suggested in Reference [159] is necessary. The big problem is, that currently no working detector simulation of those particles is available, and hence a substantial effort has to be made to get this in place. One interesting motivation for such quirks can be, that dark matter is composed of bound states from quirks as proposed in Reference [160].



## Chapter 6

# Summary and Conclusion

In this thesis a search for HCLLPs with the ATLAS detector analysing a data sample of  $36.1 \text{ fb}^{-1}$  proton–proton collisions, is presented. This search utilises measurements of the ionisation energy loss in the pixel detector as well as time-of-flight measurements in the Tile Calorimeter, the MDT's and RPC's to identify HCLLPs. One focus of this thesis was to elaborate the limitations of this analysis approach. This is in particular important, as HCLLPs are predicted in a variety of theories extending the SM, and therefore knowing the break down can be used to decide, if those results are applicable for other models. Furthermore it can help to spot weak spots in the experimental coverage.

Two different types of objects are used for HCLLPs, an ID track with associated Tile Calorimeter hits and a combined ID and MS track reconstructed with a dedicated muon algorithm for slow particles. The ID tracking is found to be almost fully efficient for  $\beta$  down to 0.2. For low velocities the tracking breaks down rather rapidly due to the timing window of the SCT. The momentum resolution for the high momenta of HCLLPs is found to be poor and also a bias for momenta above 1.5 TeV was found. For the combined tracks reconstructed with the MuGirlStau algorithm the efficiency is only about 75% and drops below 40% for  $\beta < 0.4$ .

The main focus for the observables was on the  $\beta$  measurement with the Tile Calorimeter. One important improvement compared to previous analyses is that the timing distributions for all single Tile Calorimeter cells were analysed for unexpected features. A distance correction was developed for the 2015 analysis and extended by an additional  $\eta$  correction which now ensures a stable timing over the full  $\eta$  range. Another important improvement compared to previous analyses is the smearing of the timing measurements in simulation, that is now performed as a function of the energy deposited in each  $\phi$ -projected cell. The  $\beta$  resolution of 0.068

is the best achieved so far with the ATLAS Tile Calorimeter. An important achievement for the reliability of the timing measurement with the Tile Calorimeter is the observation of muons from satellite–satellite collisions, which are measured with a delay that is in agreement with the expectation. For the  $\beta$  measurements a procedure to treat too small and too broad resolutions in simulation using a unified matrix method of smearing and unfolding was developed. The combined  $\beta_{\text{ToF}}$  resolution from all subsystems used for ToF measurements has a resolution of 0.021, which is also the best achieved so far.

The search utilises three different approaches, two targeting  $R$ -hadrons and one for pair-produced colour singlets. The  $R$ -hadron approaches are the MS-agnostic search which does not use any information from the MS to be less dependent on the modelling of the hadronic interactions of the  $R$ -hadrons, and the  $R$ -hadron full-detector approach, which exploits the better  $\beta_{\text{ToF}}$  resolution including the MS when possible. The approach used for pair-produced colour singlets uses the requirement of two candidates in the event to significantly reduce the background in particular in the low mass regions. An improvement for this analysis was for the one-candidate fall-back signal region as there an additional requirement on a large  $dE/dx$  is used to suppress the background, which significantly improves the sensitivity in this signal region.

The background for the different signal regions is estimated in a fully data-driven manner, by estimating templates for the key variables from sidebands and sampling the mass distribution from those templates. The background is normalised in low-mass control regions. Two assumptions that are crucial for the validity of the background estimated were carefully tested: The potential signal contamination in the low mass control regions and a potential correlation between momentum and  $\beta/\beta\gamma$ .

No significant deviations from the expected background were found for any of the signal regions used. Nevertheless the number of  $\text{ID+CALO}$  candidates is slightly higher than the background prediction in some signal regions. The largest excess of  $1.9\sigma$  was observed in  $\text{SR-Rhad-MSagno}$  in the highest mass window, but the candidates are found to have poor momentum quality and are hence believed to be outliers. Another small excess of  $1.59\sigma$  is found in the signal region designed for a 800 GeV  $R$ -hadron. This region is more interesting as the candidates are more trustworthy and in particular as the analysis using only the ionisation energy loss from the pixel detector to identify HCLLPs [127] sees an excess ( $2.4\sigma$ ) in the same region. The results are interpreted to set upper cross-section limits

as well as lower mass limits for direct pair-produced sbottom, stop and gluino  $R$ -hadrons, charginos and staus. The observed lower mass limits are 1250 GeV for sbottom, 1340 GeV for stop and 2000 GeV for gluino  $R$ -hadrons as well as 430 GeV for staus and 1090 GeV for charginos. The limits significantly extend the results from previous searches. The results were also interpreted for gluino  $R$ -hadron with different lifetimes and for multi-charged particles to estimate the sensitivity of this analysis for shorter lifetimes and higher charges of the particles. For different lifetimes the MS-agnostic has the better expected sensitivity for lifetimes of 30 ns and 50 ns compared to the pixel  $dE/dx$  analysis [127], whereas the approaches described in this work are not competitive with the dedicated analysis [154] already for doubly charged particles. The obtained lower mass limits for these signals are 1980 GeV for 50 ns, 1960 GeV for 30 ns and 1860 GeV for 10 ns lifetime of the gluino  $R$ -hadrons, while for multi-charged particles 715 GeV for  $q = |2e|$  and 460 GeV for  $q = |2.5e|$  are obtained.



# Appendix



## Appendix A

# Search for Heavy Charged Long-lived Particles

### A.1 Time-of-flight measurement in the Liquid Argon calorimeter

This study on the calibration of LAr calorimeter timing was conducted together with Joshua Krink. The calibration is very much inspired and partially the same calibration constants are used as by the late-photon analysis group. They are using electrons instead of muons as in this analysis, hence not exactly the same calibration is possible. This analysis uses so far only the cells in the second and also broadest LAr layer. The calibration constant per-cell and per-run can be directly used from the late-photon analysis as those are due to de-synchronisations between the different clocks, and hence should be independent from the particle type

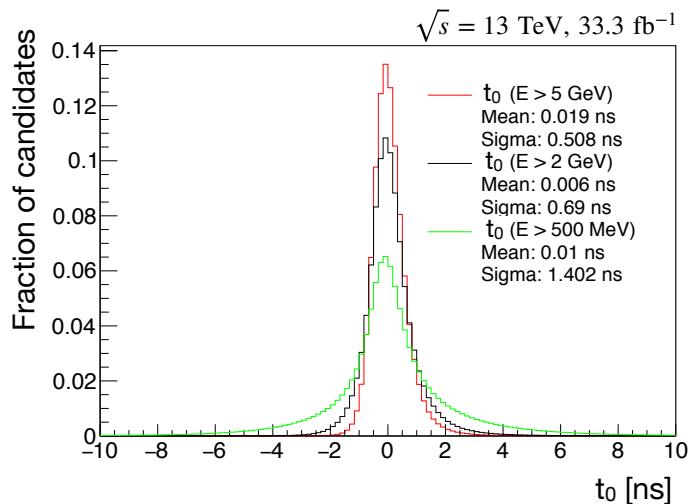


Figure A.1: The  $t_0$  distribution for the measurements in the second layer of the LAr calorimeter with different requirements on  $E_{hit}$ .

measured. All other calibrations, are conducted in a similar way as in the late-photon analysis but with muons. Those are calibrations along the energy deposit per cell, along the incident angle against the cell centre in  $\phi$  and  $\eta$ , and the relative energy fraction in the first or third LAr layer. The timing resolution achieved after calibration for different requirements on  $E_{hit}$  is shown in Figure A.1. The corresponding  $\beta$  resolutions are 0.18 for  $E_{hit} > 500$  MeV, 0.09 for  $E_{hit} > 2$  GeV and 0.07 for  $E_{hit} > 5$  GeV. The resolution for the Tile Calorimeter is 0.068, which is for a  $E_{hit} > 500$  MeV. The LAr calorimeter  $\beta$  resolution is hence only for very high energy deposits compatible to the Tile Calorimeter resolution. About 42% of the candidates in data have a LAr hit in the second layer with  $E_{hit} > 500$  MeV, while 13% have a hit with  $E_{hit} > 2$  GeV and 5% have a hit with energy  $E_{hit} > 5$  GeV. The LAr has a worse  $\beta$  resolution as expected, but it can give an additional measurement in particular as the statistics for Tile Calorimeter measurements are rather low. But as discussed earlier the LAr calorimeter timing for out-of-time signals has to be validated for muons. This can be done using the satellite tagging as mentioned in Section 5.12.

## A.2 Pre-selection Optimisation

Figures A.2–A.7 show the different optimisation studies for the quality cuts of the candidate pre-selections. Beside the respective pre-selection also some cuts of the final selection are applied as the observables are partially correlated with e.g.  $\beta$ . In particular for the consistency measurements as the measurements in the bulk of the  $\beta$  distribution are expected to be in a good agreement as roughly its close to the true value, whereas in the tails of the  $\beta$  distributions the single measurements have to be outliers and therefore a poor consistency is expected. Also the uncertainty needs to be optimised with a signal-region-like selection as it is proportional to  $\beta$ .

The distributions shown here are before the RPC bug was fixed to show how the decision on the pre-selection cuts was made. In particular for the consistency between the  $\beta$  measurements a worse discrimination power is expected.

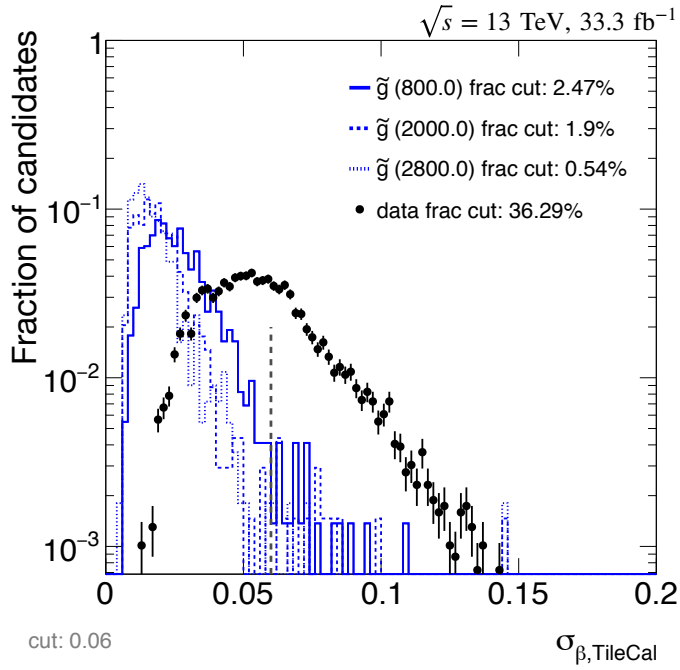


Figure A.2: The  $\sigma_\beta$  distribution for  $ID+CALO$  candidates in data overlaid by the distributions for three different gluino  $R$ -hadron models. The chosen cut is indicated by a dashed line and the fraction that gets rejected is given in the legend. Beside the candidate pre-selection also a momentum  $p_{ID} > 200$  GeV and  $\beta < 0.8$  are required.

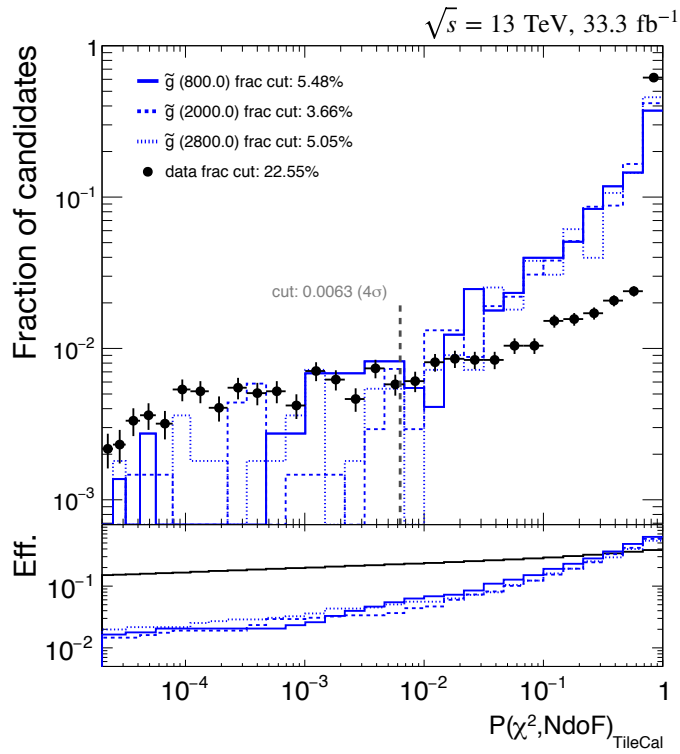


Figure A.3: The  $\beta_{TILE}$  consistency distribution for  $ID+CALO$  candidates in data overlaid by the distributions for three different stau models. The chosen cut is indicated by a dashed line and the fraction that gets rejected is given in the legend. Beside the candidate pre-selection also a momentum  $p_{ID} > 200$  GeV and  $\beta < 0.8$  are required.

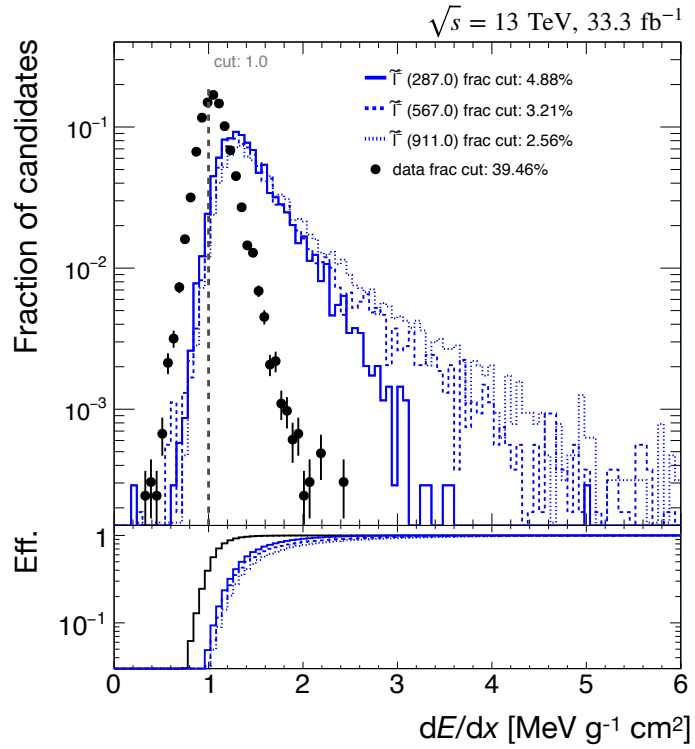


Figure A.4: The  $dE/dx$  distribution for **TIGHT** candidates in data overlaid by the distributions for three different gluino  $R$ -hadron models. The chosen cut is indicated by a dashed line and the fraction that gets rejected is given in the legend. Beside the candidate pre-selection also a momentum  $p_{Combined} > 200$  GeV and  $\beta < 0.85$  are required.

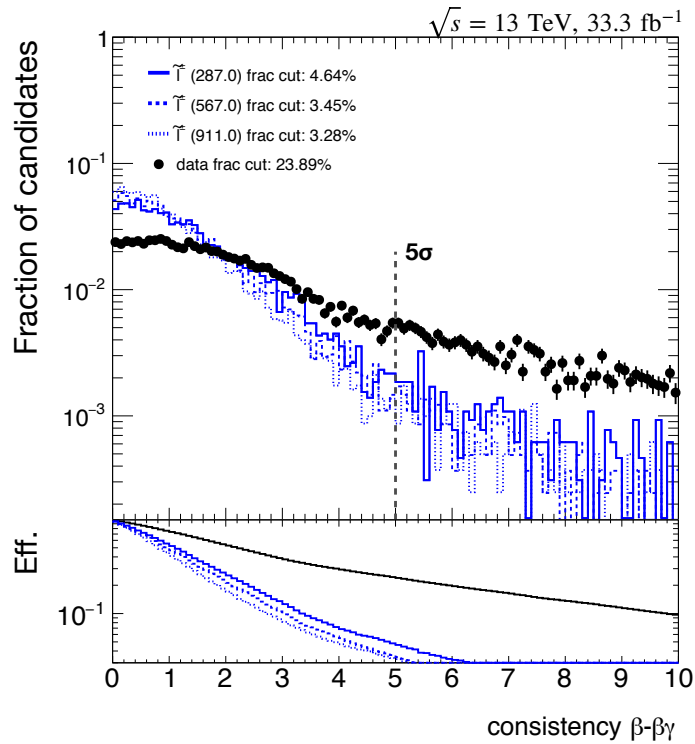


Figure A.5: The  $\beta_{ToF} - \beta_{dE/dx}$  consistency distribution for **LOOSE** candidates in data overlaid by the distributions for three different stau models. The chosen cut is indicated by a dashed line and the fraction that gets rejected is given in the legend. Beside the candidate pre-selection also a momentum  $p_{Combined} > 200$  GeV,  $\beta < 0.95$  and  $m_{\beta_{ToF}} > 200$  GeV are required.

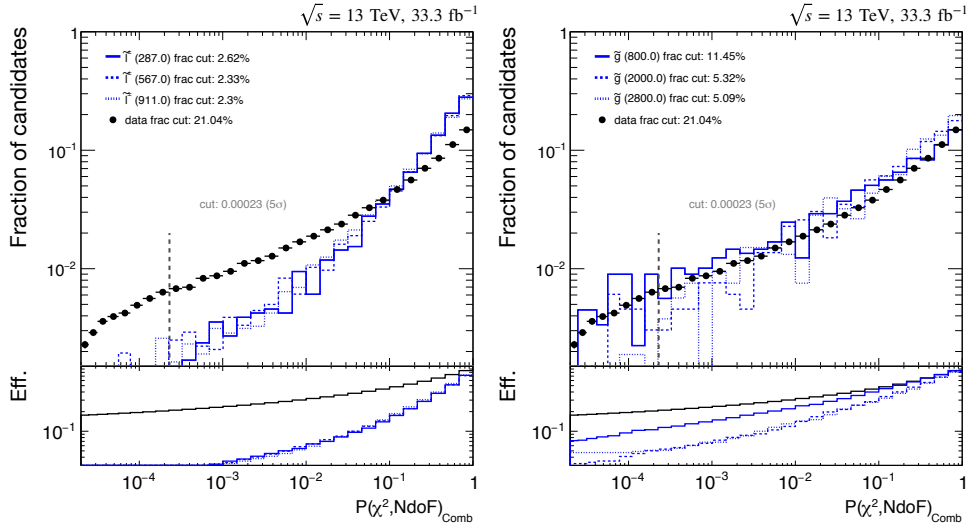


Figure A.6: The  $\beta_{\text{TOF}}$  consistency distribution for `LOOSE` candidates in data overlaid by the distributions for three different stau models (left) and three different gluino  $R$ -hadron models (right). The chosen cut is indicated by a dashed line and the fraction that gets rejected is given in the legend. Beside the candidate pre-selection also a momentum  $p_{\text{Combined}} > 200$  GeV and  $\beta_{\text{TOF}} < 0.95$  are required. Those optimisation studies were done before the bug in the RPC's was found.

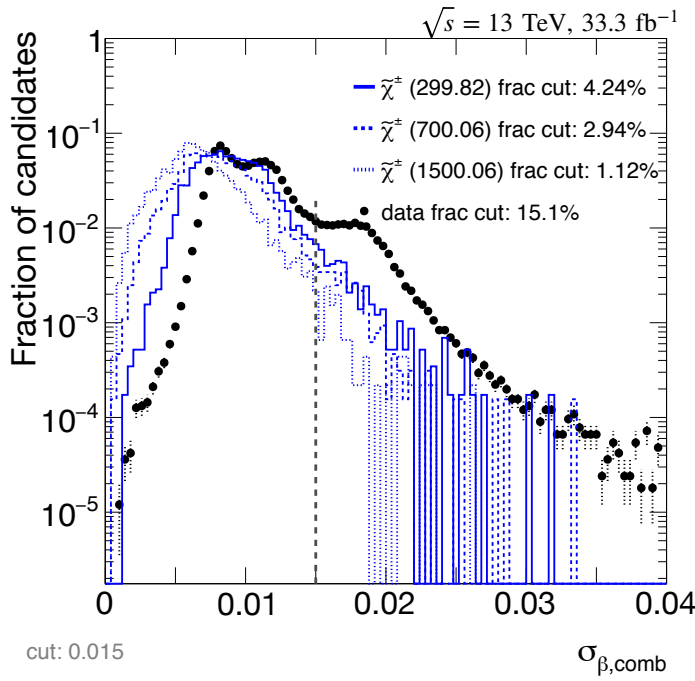


Figure A.7: The  $\sigma_{\beta_{\text{TOF}}}$  consistency distribution for `LOOSE` candidates in data overlaid by the distributions for three different chargino models. The chosen cut is indicated by a dashed line and the fraction that gets rejected is given in the legend. Beside the candidate pre-selection also a momentum  $p_{\text{Combined}} > 200$  GeV and  $\beta < 0.95$  are required.

### A.3 Templates

The template distributions, Figure A.16 and A.9, for the respective signal regions that were not shown Section 5.9.

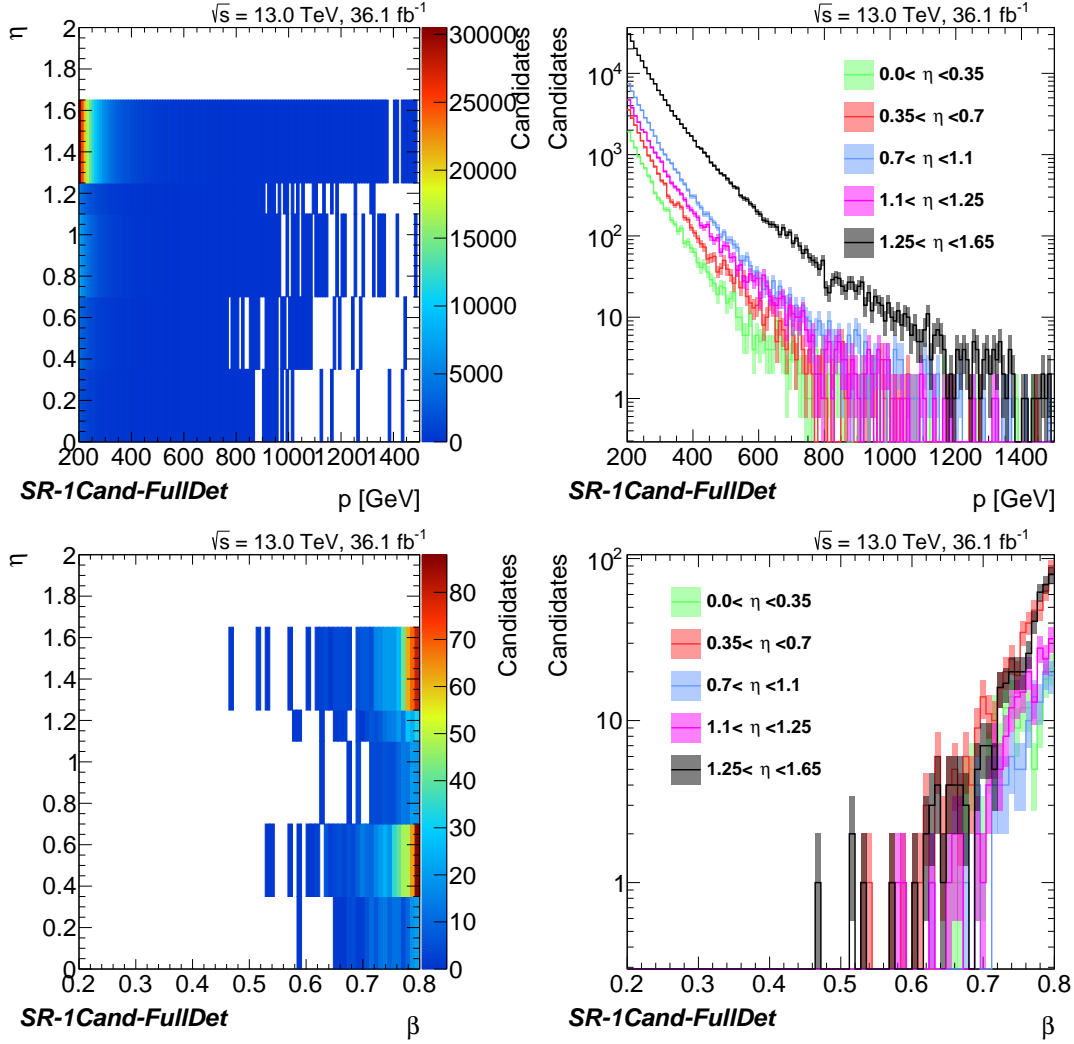


Figure A.8: The templates used for the SR-1Cand-FullDet for the momentum (upper) and  $\beta_{\text{ToF}}$  (lower). On the left the 2-dimensional distribution in  $\eta$  and the respective variable are shown, while the right plot shows the projection of each  $\eta$ -slice on the variable axis.

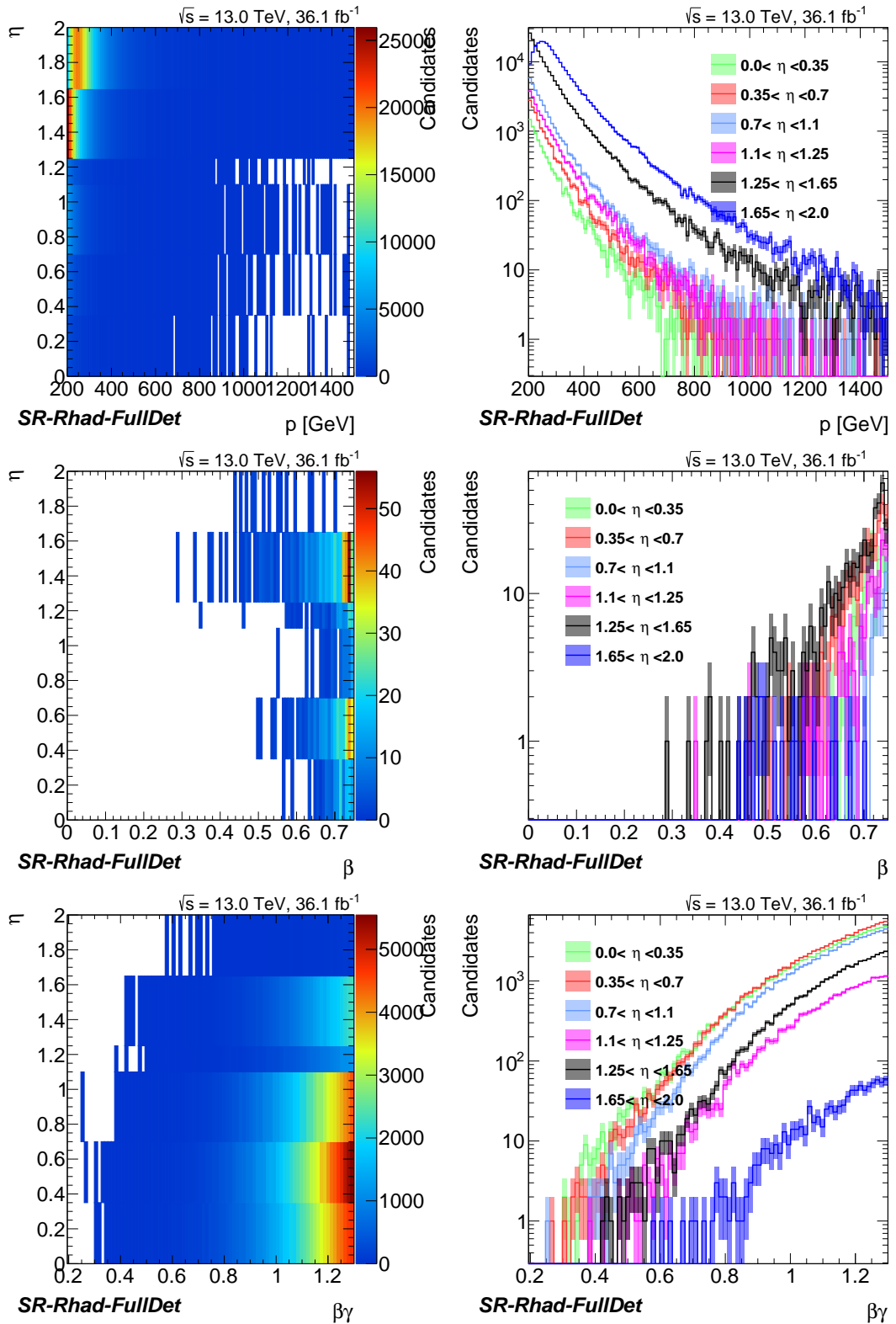


Figure A.9: The templates used for the SR-Rhad-FullDet `Loose` for the momentum (upper),  $\beta_{\text{ToF}}$  (middle) and  $\beta_{\gamma_{\text{dE/dx}}}$  (lower). On the left the 2-dimensional distribution in  $\eta$  and the respective variable are shown, while the right plot shows the projection of each  $\eta$ -slice on the variable axis.

## A.4 Signal contamination in templates

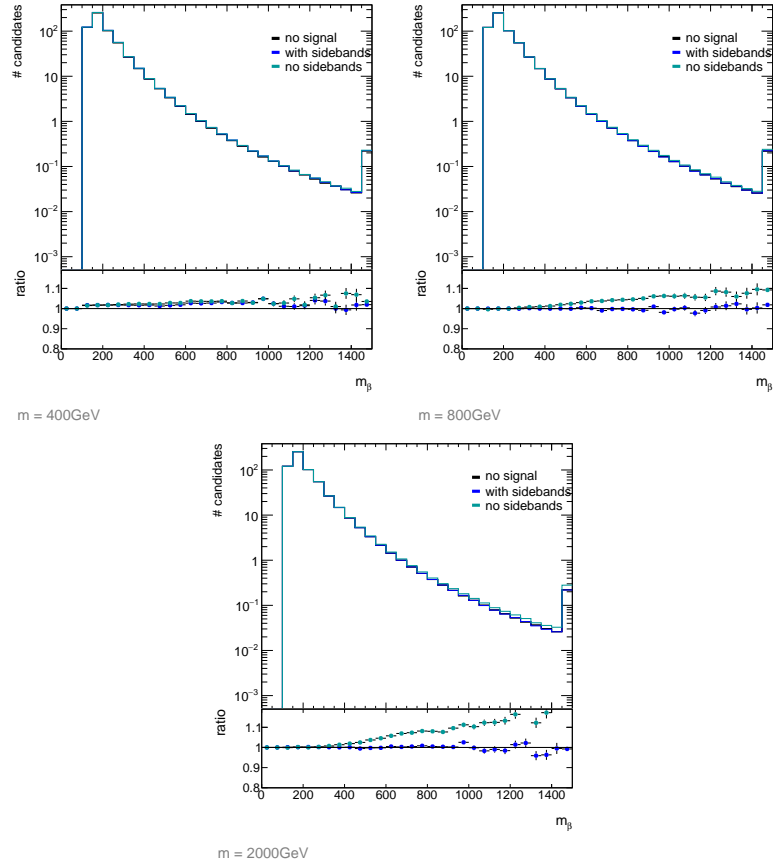


Figure A.10: Contamination of a 400 GeV (left), 800 GeV (right), and 2000 GeV signal sample in the pdfs used for the background estimate compared between no contamination (black) with sidebands (blue) and no sidebands (light blue). As cross-sections roughly the limits of the 2015 analysis are used (20 fb flat).

A generic background from all good muons is used for the  $\beta$  and momentum pdfs<sub>generic</sub> in this study. The actual templates are sampled from the generic background distributions with statistics that are seen in the actual templates used in the analysis. Three different scenarios are tested: a) no signal contamination, b) a signal contamination where the pdfs are estimated from sidebands where the momentum,  $\beta$  or  $\beta\gamma$  SR cuts are inverted, and c) without sidebands. Finally the background estimate is normalised to data in the region below 500 GeV.

The resulting distributions are shown in Figure A.10. The background estimate for the 400 GeV sample with and without sideband is performing similarly. A slight bias can be seen due to the signal contamination in the normalisation region. This bias is of the  $\mathcal{O}(2\%)$  and can be included in the low-mass SR as a systematic uncertainty. For the higher masses the signal contamination in the normalisation region is no problem, but a slope

can be seen for the background estimated without sidebands. A bias up to 10% for a 800 GeV signal and up to 20% for a 2000 GeV signal can be found. The reason being signal particles entering the pdfs, which are in the low-beta and high-momentum range. By randomly sampling from the pdfs, a slope is introduced due those contaminations. All in all, sidebands are chosen to estimate the templates where possible as it is more robust against signal contamination.

## **A.5 Signal contamination background estimate**

For this studies the influence of a potential signal contamination in the control region as well as in the templates for the sampling of the background, was tested. The cross-section assumed for the different signal models was chosen roughly at the current upper cross-section limits. For charginos and staus those were extrapolated from 8 TeV to 13 TeV. While the influence of the signal on the normalisation of the background and on the shape of the templates was included in this study, the influence of the signal on the  $\eta$  distribution of the candidates in the control region was not. This was due to technical difficulties and as the effect on the normalisation is expected to be larger this was not seen as limitation of this study. Figures ??–5.84 show the results of the signal contamination studies for the different signal regions. For all regions a good agreement between signal contaminated and nominal background within the uncertainties was found.

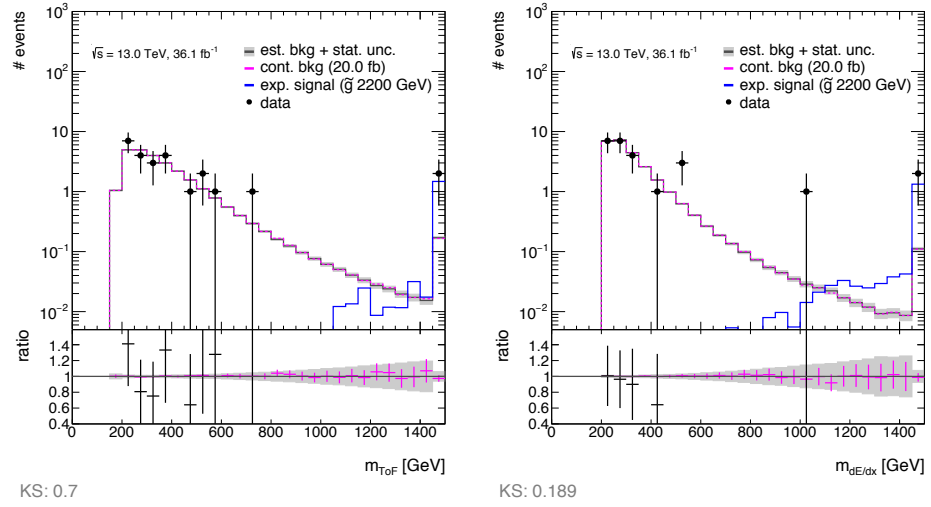


Figure A.11: Background estimate for MS-agnostic analysis with and without signal contamination aiming at gluino  $R$ -hadrons (SR-Rhad-MSagno). Left:  $m_{\text{ToF}}$ -projection, Right:  $m_{dE/dx}$ -projection. The last bin(s) include the overflow. Only the statistical uncertainty is shown for the background estimate. This Figures correspond to Figures 5.81 in the main body. The dotted pink line illustrates the expected background given signal contamination as described in the text.

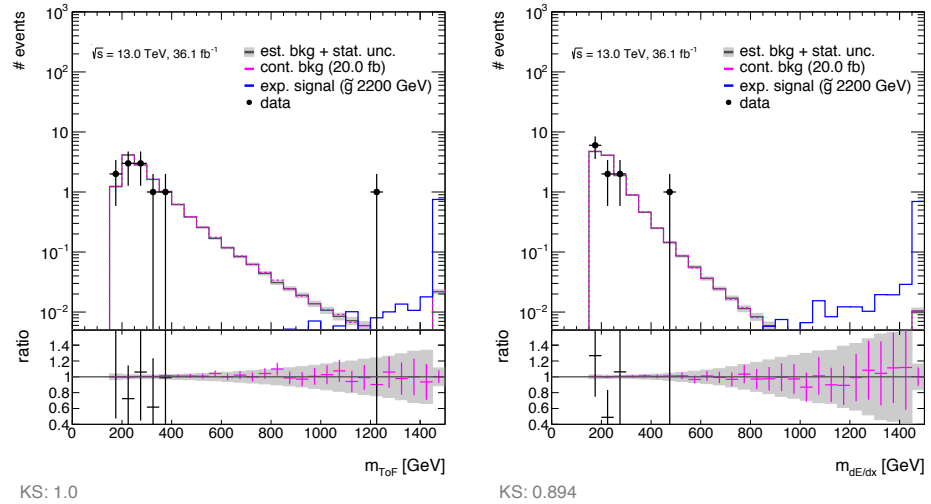


Figure A.12: Background estimate for full-detector analysis (Loose part) with and without signal contamination aiming at gluino  $R$ -hadrons (SR-Rhad-FullDet). Left:  $m_{\text{ToF}}$ -projection, Right:  $m_{dE/dx}$ -projection. The last bin(s) include the overflow. Only the statistical uncertainty is shown for the background estimate. The dotted pink line illustrates the expected background given signal contamination as described in the text.

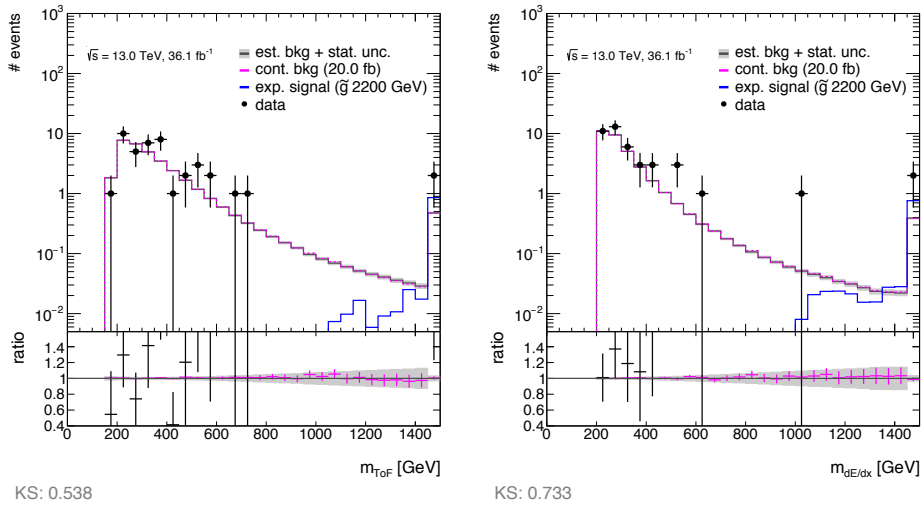


Figure A.13: Background estimate for full-detector analysis ( $\text{ID}+\text{CALO}$  part) with and without signal contamination aiming at gluino  $R$ -hadrons (SR- $\text{Rhad-FullDet}$ ). Left:  $m_{\text{TOF}}$ -projection, Right:  $m_{dE/dx}$ -projection. The last bin(s) include the overflow. Only the statistical uncertainty is shown for the background estimate. The dotted pink line illustrates the expected background given signal contamination as described in the text.

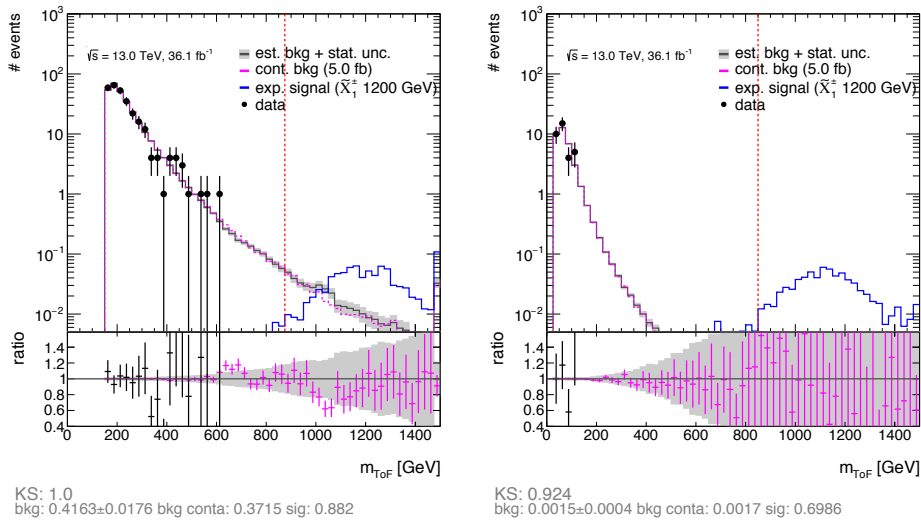


Figure A.14: Background estimate with and without signal contamination for analysis aiming at pair-produced C1C1. Left: one  $\tau_{1\text{GH1}}$  candidate SR, Right: two  $\text{LOOSE}$  candidates SR. The last bin(s) include the overflow. The dotted red lines indicated the lower bounds of the signal regions. The dotted pink line illustrates the expected background given signal contamination as described in the text. Only the statistical uncertainty is shown for the background estimate.

## A.6 Background estimate from $\eta$ template

The current version of the background estimate needs a very careful tuning of the control regions to avoid any larger effects of potential signal contamination on the background estimate. A new method was developed to reduce the effects of signal contamination by estimating  $\eta$  templates. But also a new treatment of the normalisation is needed to achieve a more robust background estimate. For the normalisation new dedicated sideband regions might be applicable. Both methods will be introduced in the following.

To estimate the expected  $\eta$  distribution in the signal region, first the  $\eta$  distribution for the low- $\beta/\beta\gamma$  and the high- $p$  have to be estimated. Here the final requirements on  $\beta(\beta\gamma)$  and momentum have to be used. One important remark those should not be obtained in sidebands as the sideband definition could have a correlation with the  $\eta$  distribution. Even if signal is present it has a negligible fraction, due to the large backgrounds, and hence has no influence on the final  $\eta$  distribution. The  $\eta$  distribution in the final signal region where both low- $\beta/\beta\gamma$  and high- $p$  are required is then obtained as illustrated in Figure A.15. The distributions are bin-by-bin multiplied and then normalised. Those  $\eta$  templates can then be used to sample the  $\eta$  values of the candidates instead of using the  $\eta$  from the candidate. This has beside the lower influence of potential signal contamination a further benefit as the  $\eta$  used for the background does not rely on the very low statistics in the control region, where partially  $\eta$  slices are not even populated. Both methods were applied to a loose MS-agnostic signal region and the results are shown in Figure A.16. It can be seen that the background estimated with this new  $\eta$  template method can nicely reproduce the results with the candidate  $\eta$  version. It was decided to not use this method as it had some limitations for the more complex scenarios with the fall-back signal regions. There the  $\eta$  distribution in the fall-back signal region is not independent of the prioritised signal region. In particular in the SR-2Cand-FullDet/SR-1Cand-FullDet there is more investigation needed on how to treat those. Therefore the old method with using the  $\eta$  of the candidates in the control region was used similarly for all signal regions to have a common approach. Nevertheless with some more investigation e.g. by sampling SR-2Cand-FullDet/SR-1Cand-FullDet together and simulating the efficiency, the method could be extended also to the other signal regions.

With the  $\eta$  templates only the problem of potential signal changing the  $\eta$

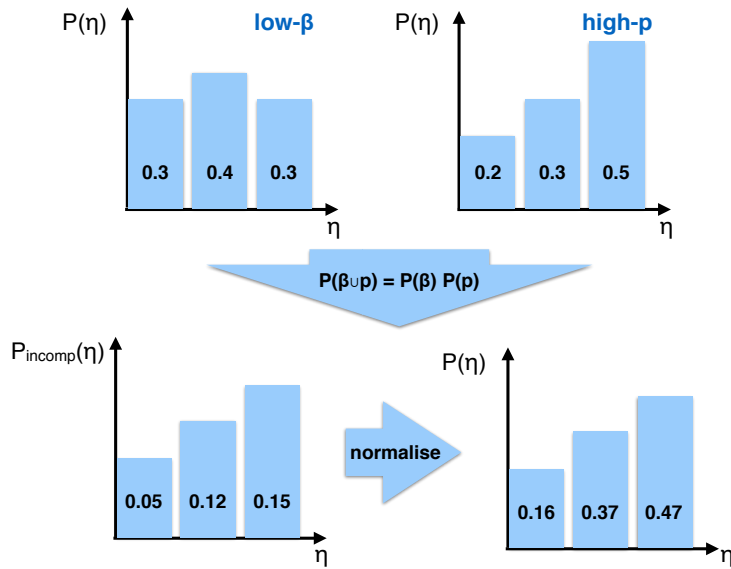


Figure A.15: Schematic drawing of the estimation of the  $\eta$  templates from the  $\eta$  distributions of the single observables.

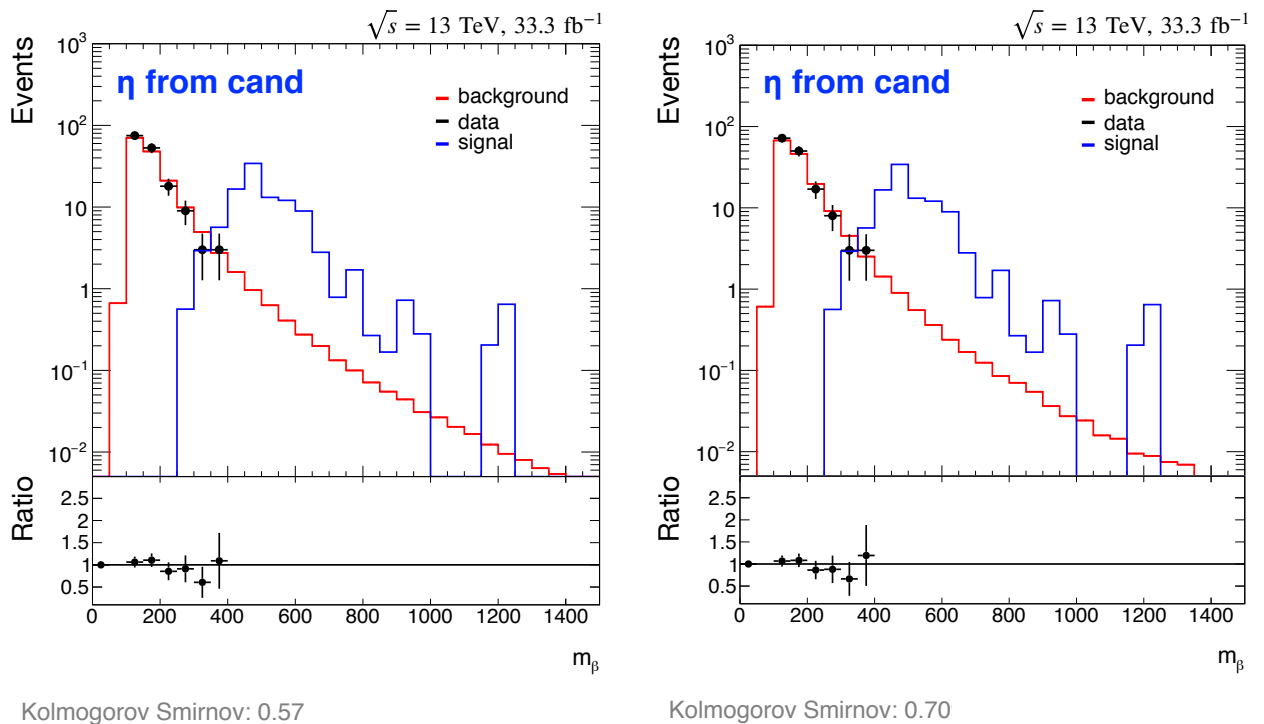


Figure A.16: The estimated background with the  $\eta$  from the candidates (left) and with the  $\eta$  templates (right) in a MS-agnostic signal region but with looser cuts as in the nominal selection and everything above 400 GeV is blinded. The Kolmogorov-Smirnov test is used as measure for the agreement between data and the estimated background in the low mass control region.

composition is solved but still the more prominent effect of signal contamination via the normalisation is present. A potential solution to this might be to use sideband normalisation regions where the backgrounds are by far more dominant. The idea is to invert the final cuts of  $\beta(\beta\gamma)$  and maybe use also some upper bounds, e.g.  $0.95 > \beta > 0.8$  but use the final momentum requirement,  $P > 200$  GeV. For this region the same methods as in the nominal signal regions are applied to estimate the background there. As this region is largely dominated by background the normalisation of the background can be made there and also used for the nominal signal region. In principle this means that the parts of the mass distributions that are cut away by the strong final requirements are re-cycled for the normalisation of the background. This method was so far not tested and therefore some further investigation might be needed.

Both methods described could be as a combination significantly reduced potential effects from low-mass signal contamination on the background estimate. The normalisation with the sidebands was not tested so far, but similar approaches are commonly used e.g. in the pixel  $dE/dx$  analysis, and hence should be applicable also in this analysis. For a simple signal region as e.g. MS-agnostic also the  $\eta$  template method is rather simple and was shown to work properly. But the difficulty are the 2-bin signal regions. There some detailed investigation and new ideas are needed.

## A.7 Re-interpretation Long-Lived Multi-Charged Particles

In this section the procedure for the reinterpretation for multi-charged particles will be described. The study is based on the samples from the dedicated multi-charged particle analysis [154] and are described in detail in Section 5.11.3. Both was tested using the SR-Rhad-FullDet approach and the SR-2Cand-FullDet/SR-1Cand-FullDet approach. For the SR-Rhad-FullDet no sensitivity was achieved at all and therefore only the SR-2Cand-FullDet/SR-1Cand-FullDet approach will be discussed in this section.

The samples are treated in the same way as the charginos and stau signal samples. First a re-weighting is applied to match the pile-up distribution as observed in data. Afterwards the same pre-selections are applied. The resulting cutflow for the LOOSE selection is shown in Figure A.17. The main steps in the cutflow are the requirement of at least one SlowMuon per event, the  $\eta$  range and the  $\beta_{\text{TOF}}$  consistency. For the SlowMuon

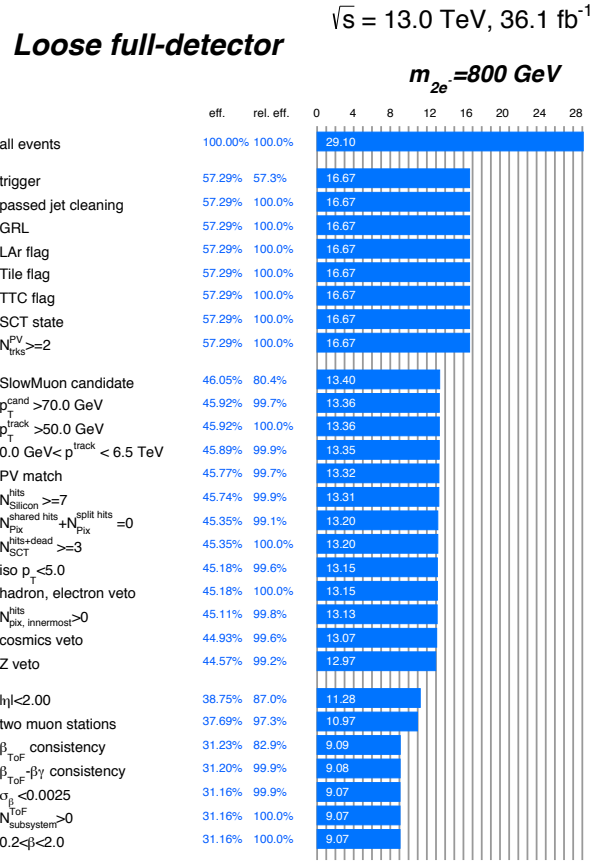


Figure A.17: The `Loose` selection applied on a signal sample of doubly-charged particles with a mass of 800 GeV. A multi-charged particle mass hypothesis close to the expected mass limit is chosen. The selection requirements are grouped into blocks. The first block are the event selection requirements, the second the common track preselection and the third the `Loose` requirements. Beside the (expected) event yields also the efficiency and the relative efficiency are stated. The corresponding cutflow for data is shown in Figure 5.70.

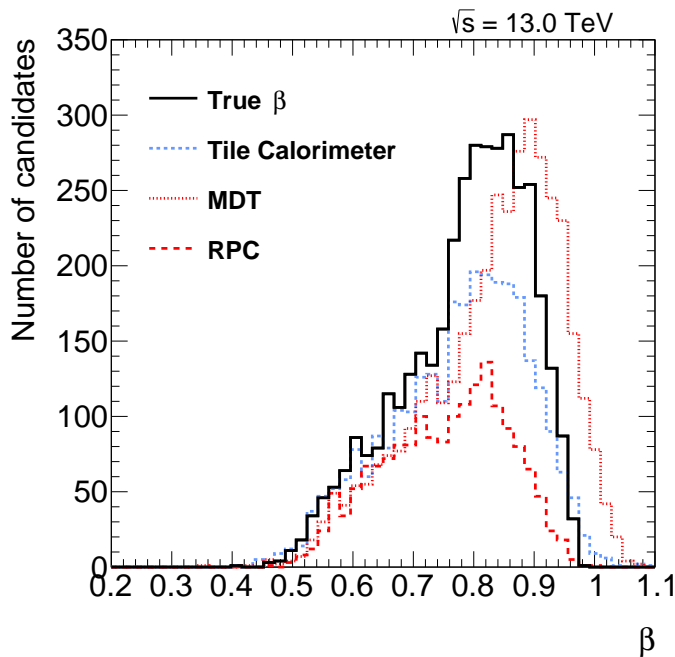


Figure A.18: The true  $\beta$  distribution overlaid by the reconstructed  $\beta$  in the different subsystems. A sample of direct pair-produced doubly-charged particles with a mass of 800 GeV is used.

| Mass [GeV] | $m_{\text{ToF}}$ min. [GeV] |                  |
|------------|-----------------------------|------------------|
|            | SR-2Cand-FullDet            | SR-1Cand-FullDet |
| 400        | 150                         | 175              |
| 600        | 225                         | 250              |
| 800        | 325                         | 350              |
| 1000       | 400                         | 425              |
| 1200       | 450                         | 500              |
| 1400       | 525                         | 550              |

Table A.1: The lower mass requirements on  $m_{\text{ToF}}$  for SR-1Cand-FullDet and SR-2Cand-FullDet for multi-charged particles with  $z = 2$  and 2.5.

reconstruction efficiency beside the fiducial volume its also the rather poor reconstruction eff. of the MuGirlStau algorithm in the Athena 20.7 version. Those particles are assumed to be fermions, accordingly they are produced rather in the forward direction comparable to charginos and therefore the step for the  $\eta$  range. The reason for the step due to the  $\beta_{\text{ToF}}$  consistency can be seen in Figure A.18. The reconstructed  $\beta$  with the MDT is shifted to higher values of  $\beta$ , while the Tile Calorimeter is in rather good agreement with the true spectrum. For the RPC's the distribution is slightly to low in  $\beta$ . This can be understood as the RPC's only cover the central region where the  $\beta$  of the particles is lower, as can be seen in Figure 5.12. The bias seen for the MDT's was discussed with the experts and might be due to the faster signal rise due to the significantly higher energy loss for multi-charged particles, roughly six times higher for  $z = 2$  particles with  $\beta\gamma = 1$  then for a minimum ionising particle with  $z = 1$ . The standard procedure for the estimation of the masses assumes  $|q|=1e$ . For a  $q = 2e$  particle the momentum is off by a factor two and hence also the mass. To account for this the final mass windows for the charginos/staus with half the mass of the multi-charged particle is used. In principle the  $z = 2.5$  particles should have the mass windows corresponding to  $m/2.5$ , but as the sensitivity for those cases is found to be very low for simplicity the same mass windows as applied for the  $z = 2$  particles are also used. A summary of the lower mass requirements used for the different mass hypotheses and signal regions is given in Table A.1. The systematic uncertainties on the signal yield are re-evaluated for most of the sources, only for small contributions and for the trigger the same as for charginos were used. Using the uncertainty for charginos on the

| Charge | $q = 2e$    |                                  | SR-2Cand-FullDet<br>$q = 2.5e$                           |                                  | $N_{est.} \pm \sigma_{N_{est.}}$ | $N_{obs.}$ |
|--------|-------------|----------------------------------|--|----------------------------------|----------------------------------|------------|
|        | Mass [GeV]  | $N_{exp.} \pm \sigma_{N_{exp.}}$ | $a \times \varepsilon \pm \sigma_{a \times \varepsilon}$ | $N_{exp.} \pm \sigma_{N_{exp.}}$ |                                  |            |
| 400    | 32.0±5.0    | 0.043±0.003                      | 5.0±1.0  | 0.0043±0.0007                    | 1.5±0.3                          | 0          |
| 600    | /±/         | /±/                              | 0.7±0.3  | 0.0039±0.0006                    | 0.33±0.06                        | 0          |
| 800    | 1.0±0.2     | 0.037±0.002                      | 0.07±0.04  | 0.0015±0.0006                    | 0.08±0.02                        | 0          |
| 1000   | 0.36±0.06   | 0.045±0.003                      | 0.018±0.009  | 0.0014±0.0004                    | 0.034±0.007                      | 0          |
| 1200   | 0.12±0.02   | 0.045±0.002                      | 0.015±0.005  | 0.0038±0.0006                    | 0.022±0.005                      | 0          |
| 1400   | 0.033±0.007 | 0.036±0.003                      | 0.007±0.003  | 0.0053±0.0010                    | 0.011±0.003                      | 0          |

Table A.2: The expected number of signal events ( $N_{exp.}$ ), the acceptance ( $a$ ) times efficiency ( $\varepsilon$ ) for the signal, the estimated number of background events ( $N_{est}$ ) and the observed number of events  $N_{obs}$  in SR-2Cand-FullDet for all different mass hypothesis of multi-charged particles considered in this work with  $q = 2e$  and  $2.5e$ .

| Charge | $q = 2e$    |                                  | SR-1Cand-FullDet<br>$q = 2.5e$                           |                                  | $N_{est.} \pm \sigma_{N_{est.}}$ | $N_{obs.}$ |
|--------|-------------|----------------------------------|--|----------------------------------|----------------------------------|------------|
|        | Mass [GeV]  | $N_{exp.} \pm \sigma_{N_{exp.}}$ | $a \times \varepsilon \pm \sigma_{a \times \varepsilon}$ | $N_{exp.} \pm \sigma_{N_{exp.}}$ |                                  |            |
| 400    | 25.0±4.0    | 0.034±0.002                      | 0.3±0.4  | 0.0003±0.0002                    | 230.0±20.0                       | 227        |
| 600    | /±/         | /±/                              | 1.7±0.5  | 0.009±0.001                      | 79.0±7.0                         | 74         |
| 800    | 2.0±0.2     | 0.070±0.003                      | 0.2±0.1  | 0.0049±0.0008                    | 23.0±2.0                         | 20         |
| 1000   | 0.62±0.08   | 0.078±0.003                      | 0.15±0.05  | 0.012±0.002                      | 10.1±1.0                         | 11         |
| 1200   | 0.20±0.03   | 0.078±0.003                      | 0.04±0.01  | 0.011±0.001                      | 5.0±0.5                          | 3          |
| 1400   | 0.067±0.008 | 0.074±0.003                      | 0.036±0.005  | 0.026±0.002                      | 3.2±0.3                          | 2          |

Table A.3: The expected number of signal events ( $N_{exp.}$ ), the acceptance ( $a$ ) times efficiency ( $\varepsilon$ ) for the signal, the estimated number of background events ( $N_{est}$ ) and the observed number of events  $N_{obs}$  in SR-1Cand-FullDet for all different mass hypothesis of multi-charged particles considered in this work with  $q = 2e$  and  $2.5e$ .

trigger efficiency is reasonable as they are also fermions and hence a similar kinematic is expected, which is the main source of differences, as the events are mainly coming from the single-muon trigger. All uncertainties on the observables ( $\beta_{\gamma dE/dx}$  and  $\beta_{ToF}$ ) as well as the contribution from pile-up are re-evaluated with the procedures as described in Section 5.10. The dominant sources of systematic uncertainties are found to be the SlowMuon efficiency (5%–15%) and the MS  $\beta$  uncertainties (2%–11.5%) for  $z = 2$  particles. The overall systematic uncertainty on the signal efficiency for  $z = 2$  is between 11% and 19%. For  $z = 2.5$  particles the systematic uncertainties are very much dominated by the very low signal statistic in the final signal regions. The systematic uncertainty is 125% from the 400 GeV mass window in the SR-1Cand-FullDet signal region and between 15% and 50% for all other mass windows in SR-1Cand-FullDet and SR-2Cand-FullDet.

The expected number of signal events ( $N_{exp.}$ ), the acceptance ( $a$ ) times efficiency ( $\varepsilon$ ) for the signal, the estimated number of background events ( $N_{est}$ ) and the observed number of events  $N_{obs}$  for all different mass hypothesis of the multi-charged particles considered in this work are given in Table A.2 for SR-2Cand-FullDet and in Table A.3 for SR-1Cand-FullDet. It can be seen that basically all the sensitivity comes from SR-2Cand-FullDet as the SR-1Cand-FullDet is for all but the very

Figure A.19: The observed and expected upper cross section limits as well as the theory prediction for the cross section of direct pair-produced multi-charged particles ( $q = 2e$ ) as function of the simulated mass. Both limits are obtained from a combination of SR-1Cand-FullDet and SR-2Cand-FullDet. The dashed lines indicate the expected limits, while the  $\pm 1\sigma$  ( $\pm 2\sigma$ ) bands on the expected limit are drawn as dark (light) red band. The observed limits are shown as dots connected by a line.

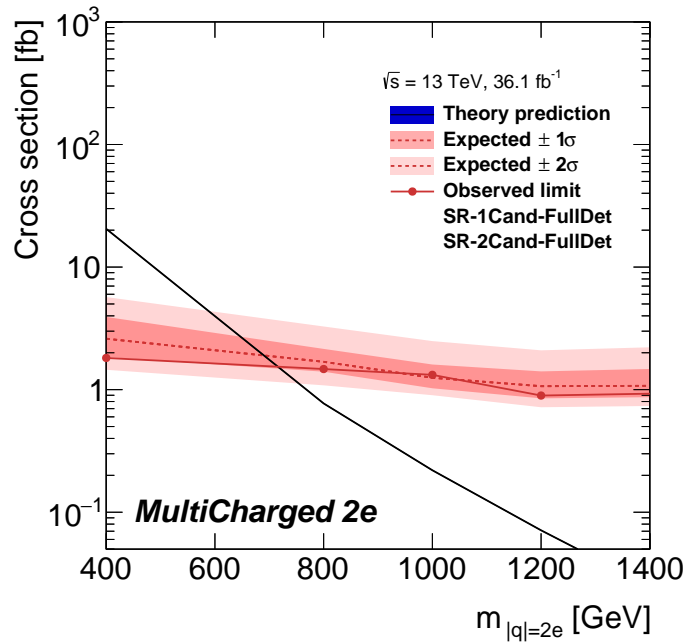
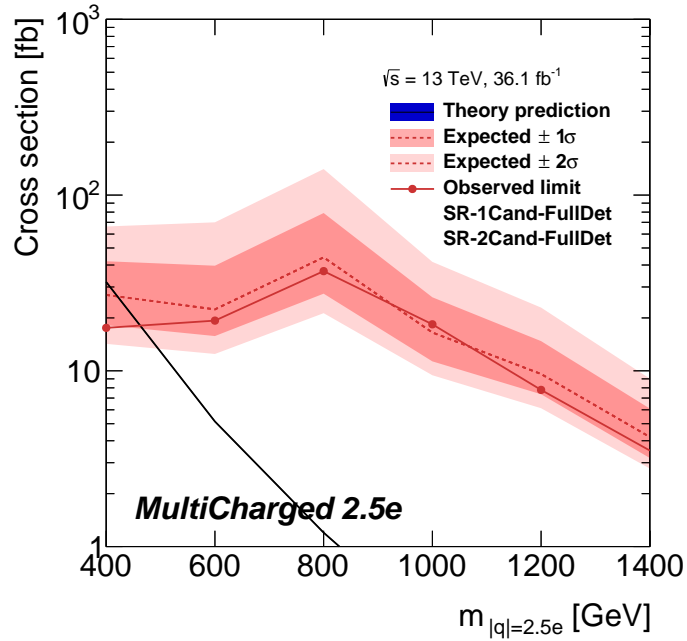


Figure A.20: The observed and expected upper cross section limits as well as the theory prediction for the cross section of direct pair-produced multi-charged particles ( $q = 2.5e$ ) as function of the simulated mass. Both limits are obtained from a combination of SR-1Cand-FullDet and SR-2Cand-FullDet. The dashed lines indicate the expected limits, while the  $\pm 1\sigma$  ( $\pm 2\sigma$ ) bands on the expected limit are drawn as dark (light) red band. The observed limits are shown as dots connected by a line.



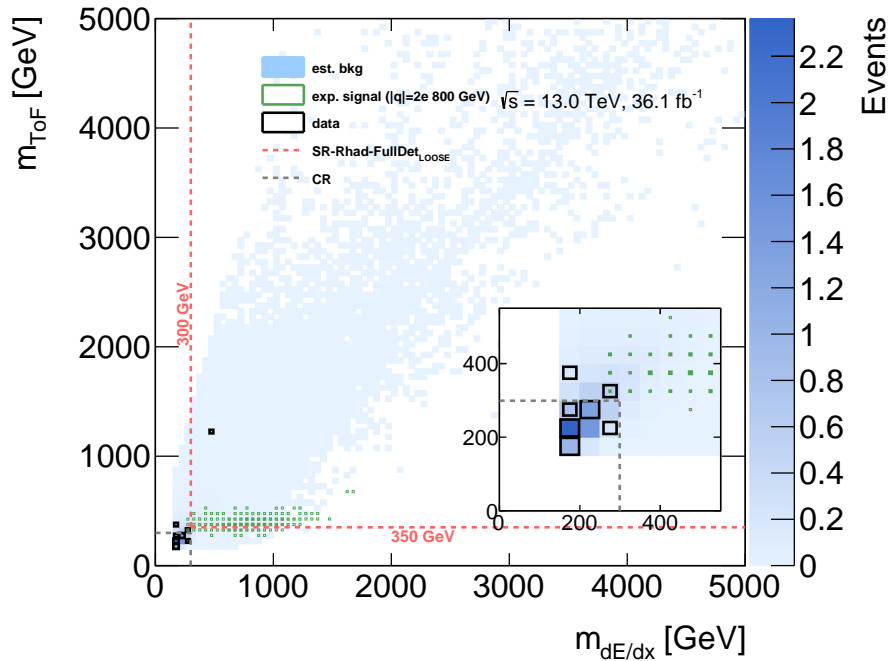


Figure A.21: The estimated background for the SR-Rhad-FullDet<sub>LOOSE</sub> signal region in the  $m_{\text{ToF}}-m_{dE/dx}$  plane. The distribution is overlaid by the data points and the distribution for a multi-charged particles model with  $m_{2e} = 800$  GeV with  $q = 2e$ . The overflow is included in the last bin of each distribution. The lower mass requirements of the signal region for the given mass hypothesis is indicated by the dotted red lines, while the dotted grey lines are illustrating the upper bound for the control region. The inlay shows a zoomed version of the low-mass region. The statistical uncertainty on the background estimate is illustrated with the shaded grey area.

high masses suffering from large backgrounds. With those yields and the estimated systematic uncertainties upper cross-section limits are estimated for the different charge hypotheses and masses. The upper cross-section limits as well as the theoretical prediction of the cross section are drawn in Figure A.19 for  $q = 2e$  and in Figure A.20 for  $q = 2.5e$ . The observed (expected) lower mass limits for pair-produced multi-charged particles are 715 GeV (690 GeV) for  $z = 2$  and 460 GeV (420 GeV) for  $z = 2.5$ .

Whilst no sensitivity is achieved from the SR-Rhad-FullDet it is nevertheless interesting to study the signal distribution for those regions, as two a small fraction doubly-charged  $R$ -hadron states are possible. The final SR-Rhad-FullDet<sub>LOOSE</sub> mass distributions in the two-dimensional  $m_{dE/dx}-m_{\text{ToF}}$  plane for data, estimated background and pair-produced doubly-charged particles with a mass of 800 GeV are shown in Figure A.21. The form of the signal is very different to the results for the  $R$ -hadron samples in Figure 5.82. The signal is oriented rather parallel to the  $m_{dE/dx}$  axis and not along the diagonal. For the  $m_{\text{ToF}}$  the estimated values are about half the true mass of the particles, which can be explained as for the mass estimation  $q = 1e$  is assumed as discussed before. For  $m_{dE/dx}$  a large spread is visible up to rather high masses. The reason is that for a multi-charged particle the estimated  $dE/dx-\beta\gamma$  relations are no longer valid and using the Bethe-Bloch formula the expected mean  $dE/dx$  should be off

by roughly a factor  $z^2$ . Furthermore for the significantly larger  $dE/dx$  the pixel detector is likely to be in saturation. So the estimate  $\beta\gamma$  is tending to be reconstructed to high while the distribution gets washed out due to the saturation effects in the pixel detector, as can be seen in Figure A.21.

# Acronyms

**AMSB** Anomaly Mediated Supersymmetry-breaking

**BSM** Beyond the Standard Model

**CSC** Cathode Strip Chamber

**CMSSM** Constrained Supersymmetric Standard Model

**CL** Confidence Level

**DxAOD** Derived Analysis Object Data

**DV** Displaced Vertex

**EM** Electromagnetic

**ESD** Event Summary Data

**EW** Electroweak

**FSR** Final State Radiation

**GMSB** Gauge Mediated Supersymmetry Breaking

**GUT** Grand Unified Theory

**GRL** Good Runs Lists

**HCLLP** Heavy Charged Long-Lived Particle

**HLT** High-Level Trigger

**IBL** Insertable B-Layer

**ID** Inner Detector

- IP** Interaction Point
- ISR** Initial State Radiation
- KK** Kaluza–Klein
- LAr** Liquid Argon
- LEP** Large Electron-Positron Collider
- LHC** Large Hadron Collider
- LSP** Lightest Supersymmetric Particle
- MDT** Monitored Drift Tube
- MS** Muon Spectrometer
- MC** Monte Carlo Simulation
- MPV** Most Probable Value
- NdoF**  $N$  degrees of freedom
- OFA** Optimal Filtering Algorithm
- PDF** Parton Density Functions
- PV** Primary Vertex
- QFT** Quantum Field Theory
- ROC** Receiver Operating Characteristic
- RPC** Resistive Plate Chamber
- SM** Standard Model of Particle Physics
- SCT** Semiconductor Tracker
- SUSY** Supersymmetry
- TGC** Thin Gap Chamber
- TRT** Transition Radiation Tracker
- ToF** Time-of-Flight

**TTC** Timing and Trigger System

**xAOD** Analysis Object Data



# Bibliography

- [1] The ATLAS Collaboration. Observation of a new particle in the search for the Standard Model Higgs boson with the ATLAS detector at the LHC. *Phys.Lett. B716* 1-29, *arXiv:1207.7214*, 2012.
- [2] The CMS Collaboration. Observation of a new boson at a mass of 125 GeV with the CMS experiment at the LHC. *Phys. Lett.*, B716:30–61, 2012.
- [3] Richard Massey, Thomas Kitching, and Johan Richard. The dark matter of gravitational lensing. *Rept. Prog. Phys.*, 73:086901, 2010.
- [4] N. Aghanim et al. Planck 2018 results. VI. Cosmological parameters. 2018.
- [5] The ATLAS collaboration. Search for heavy long-lived charged particles with the ATLAS detector in  $36.1 \text{ fb}^{-1}$  of proton–proton collision data at  $\sqrt{s} = 13 \text{ TeV}$ .
- [6] D. Griffiths. *Introduction to Elementary Particles*. WILEY-VCH Verlag GmbH Co. KGaA, 1987.
- [7] K. Oliv et al. (Particle Data Group). Review of Particle Physics. *Chin. Phys. C*, 38, 090001, 2014.
- [8] V. A. Bednyakov, N. D. Giokaris, and A. V. Bednyakov. On Higgs mass generation mechanism in the Standard Model. *Phys. Part. Nucl.*, 39:13–36, 2008.
- [9] Makoto Kobayashi and Toshihide Maskawa. Cp-violation in the renormalizable theory of weak interaction. *Progress of Theoretical Physics*, 49(2):652–657, 1973.
- [10] Sheldon L. Glashow. The renormalizability of vector meson interactions. *Nucl. Phys.*, 10:107–117, 1959.

- [11] Abdus Salam and J. C. Ward. Weak and electromagnetic interactions. // *Nuovo Cimento (1955-1965)*, 11(4):568–577, Feb 1959.
- [12] Steven Weinberg. A Model of Leptons. *Phys. Rev. Lett.*, 19:1264–1266, 1967.
- [13] A. D. Sakharov. Violation of CP invariance, C asymmetry, and baryon asymmetry of the universe. *Journal of Experimental and Theoretical Physics* 5: 24–27., 1967.
- [14] G. F. Giudice and R. Rattazzi. Theories with gauge mediated supersymmetry breaking. *Phys. Rept.*, 322:419–499, 1999.
- [15] Lisa Randall and Raman Sundrum. Out of this world supersymmetry breaking. *Nucl. Phys.*, B557:79–118, 1999.
- [16] Thomas Appelquist, Hsin-Chia Cheng, and Bogdan A. Dobrescu. Bounds on universal extra dimensions. *Phys. Rev.*, D64:035002, 2001.
- [17] Hsin-Chia Cheng, Konstantin T. Matchev, and Martin Schmaltz. Radiative corrections to Kaluza-Klein masses. *Phys. Rev.*, D66:036005, 2002.
- [18] Nausheen R. Shah and Carlos E. M. Wagner. Gravitons and dark matter in universal extra dimensions. *Phys. Rev.*, D74:104008, 2006.
- [19] Rabindra N. Mohapatra and Jogesh C. Pati. Left-right gauge symmetry and an "isoconjugate" model of CP violation. *Phys. Rev. D*, 11:566–571, Feb 1975.
- [20] A. Hrynevich. Performance of the ATLAS Tile Calorimeter. *JINST*, 12(06):C06021, 2017.
- [21] Christoph A. Stephan. Almost-commutative geometries beyond the standard model. *J. Phys.*, A39:9657, 2006.
- [22] <http://www.damtp.cam.ac.uk/user/db275/Cosmology/Lectures.pdf>, Jul 2018.
- [23] M. Fairbairn, A.C. Kraan, D.A. Milstaed, T. Sjöstrand, P. Skands, T. Sloan. Stable Massive Particles at Colliders. *arXiv:hep-ph/0611040v2*, 2006.
- [24] Malcolm Fairbairn and Louise M Griffiths. Large extra dimensions, the galaxy power spectrum and the end of inflation. *JHEP*, 02:024, 2002.
- [25] Alain Coc, Jean-Philippe Uzan, and Elisabeth Vangioni. Standard Big-Bang Nucleosynthesis after Planck. 2013.

- [26] Motohiko Kusakabe, Grant J. Mathews, Toshitaka Kajino, and Myung-Ki Cheoun. Review on Effects of Long-lived Negatively Charged Massive Particles on Big Bang Nucleosynthesis. *Int. J. Mod. Phys.*, E26(08):1741004, 2017.
- [27] Joe Sato, Takashi Shimomura, and Masato Yamanaka. A Solution to Lithium Problem by Long-Lived Stau. *Int. J. Mod. Phys.*, E26(08):1741005, 2017.
- [28] E. Komatsu, K. M. Smith, J. Dunkley, C. L. Bennett, B. Gold, G. Hinshaw, N. Jarosik, D. Larson, M. R.olta, L. Page, D. N. Spergel, M. Halpern, R. S. Hill, A. Kogut, M. Limon, S. S. Meyer, N. Odegard, G. S. Tucker, J. L. Weiland, E. Wollack, and E. L. Wright. Seven-year Wilkinson Microwave Anisotropy Probe (WMAP) Observations: Cosmological Interpretation. *apjs*, 192:18, February 2011.
- [29] M. Citron, J. Ellis, F. Luo, J. Marrouche, K. A. Olive, and K. J. de Vries. End of the CMSSM coannihilation strip is nigh. *Phys. Rev.*, D87(3):036012, 2013.
- [30] Gordon L. Kane, Christopher F. Kolda, Leszek Roszkowski, and James D. Wells. Study of constrained minimal supersymmetry. *Phys. Rev.*, D49:6173–6210, 1994.
- [31] John R. Ellis, Keith A. Olive, Yudi Santoso, and Vassilis C. Spanos. Supersymmetric dark matter in light of WMAP. *Phys. Lett.*, B565:176–182, 2003.
- [32] Graham D. Kribs and I. Z. Rothstein. Bounds on longlived relics from diffuse gamma-ray observations. *Phys. Rev.*, D55:4435–4449, 1997. [Erratum: *Phys. Rev.* D56,1822(1997)].
- [33] Wayne Hu and Joseph Silk. Thermalization constraints and spectral distortions for massive unstable relic particles. *Phys. Rev. Lett.*, 70:2661–2664, May 1993.
- [34] T. Yamagata, Y. Takamori, and H. Utsunomiya. Search for anomalously heavy hydrogen in deep sea water at 4000-m. *Phys. Rev.*, D47:1231–1234, 1993.
- [35] D. Javorsek, D. Elmore, E. Fischbach, D. Granger, T. Miller, D. Oliver, and V. Teplitz. New experimental limits on strongly interacting massive particles at the tev scale. *Phys. Rev. Lett.*, 87:231804, Nov 2001.

- [36] Asimina Arvanitaki, Chad Davis, Peter W. Graham, Aaron Pierce, and Jay G. Wacker. Limits on split supersymmetry from gluino cosmology. *Phys. Rev.*, D72:075011, 2005.
- [37] P. Gambino, G. F. Giudice, and P. Slavich. Gluino decays in split supersymmetry. *Nucl. Phys.*, B726:35–52, 2005.
- [38] Graham D. Kribs, Tuhin S. Roy, John Terning, and Kathryn M. Zurek. Quirky composite dark matter. *Phys. Rev. D*, 81:095001, May 2010.
- [39] Brüning, Oliver Sim and Collier, Paul and Lebrun, P and Myers, Stephen and Ostojic, Ranko and Poole, John and Proudlock, Paul. *LHC Design Report*. CERN Yellow Reports: Monographs. CERN, Geneva, 2004.
- [40] The CMS collaboration. CMS Physics : Technical Design Report Volume 1: Detector Performance and Software. 2006.
- [41] The LHCb collaboration. LHCb technical design report: Reoptimized detector design and performance. 2003.
- [42] The ALICE collaboration. The ALICE experiment at the CERN LHC. *JINST*, 3:S08002, 2008.
- [43] Esma Mobs. The CERN accelerator complex. Complexe des accélérateurs du CERN. Jul 2016. General Photo.
- [44] Michael Benedikt, Paul Collier, V Mertens, John Poole, and Karlheinz Schindl. *LHC Design Report*. CERN Yellow Reports: Monographs. CERN, Geneva, 2004.
- [45] The LEP collaboration. *LEP design report*. CERN, Geneva, 1984. Copies shelved as reports in LEP, PS and SPS libraries.
- [46] Laurent Ducimetire, N Garrel, M J Barnes, and G D Wait. The LHC injection kicker magnet. (LHC-Project-Report-655. CERN-LHC-Project-Report-655):4 p, Jun 2003.
- [47] <https://twiki.cern.ch/twiki/bin/view/AtlasPublic/LuminosityPublicResults>, Aug 2018.
- [48] J. Pumplin, D. R. Stump, J. Huston, H. L. Lai, Pavel M. Nadolsky, and W. K. Tung. New generation of parton distributions with uncertainties from global QCD analysis. *JHEP*, 07:012, 2002.

- [49] The ATLAS collaboration. The ATLAS Experiment at the CERN Large Hadron Collider. *JINST*, 3:S08003, 2008.
- [50] A. Yamamoto, Y. Makida, R. Ruber, Y. Doi, T. Haruyama, F. Haug, H. ten Kate, M. Kawai, T. Kondo, Y. Kondo, J. Metselaar, S. Mizumaki, G. Olesen, O. Pavlov, S. Ravat, E. Sbrissa, K. Tanaka, T. Taylor, and H. Yamaoka. The atlas central solenoid. *Nuclear Instruments and Methods in Physics Research Section A: Accelerators, Spectrometers, Detectors and Associated Equipment*, 584(1):53 – 74, 2008.
- [51] The ATLAS collaboration. ATLAS barrel toroid: Technical design report. 1997.
- [52] The ATLAS collaboration. ATLAS endcap toroids: Technical design report. 1997.
- [53] The ATLAS collaboration. *ATLAS detector and physics performance: Technical Design Report, 1*. Technical Design Report ATLAS. CERN, Geneva, 1999.
- [54] Karolos Potamianos. The upgraded Pixel detector and the commissioning of the Inner Detector tracking of the ATLAS experiment for Run-2 at the Large Hadron Collider. *PoS, EPS-HEP2015*:261, 2015.
- [55] The ATLAS collaboration. *ATLAS pixel detector: Technical Design Report*. Technical Design Report ATLAS. CERN, Geneva, 1998.
- [56] M Capeans, G Darbo, K Einsweiler, M Elsing, T Flick, M Garcia-Sciveres, C Gemme, H Pernegger, O Rohne, and R Vuillermet. ATLAS Insertable B-Layer Technical Design Report. Technical Report CERN-LHCC-2010-013. ATLAS-TDR-19, Sep 2010.
- [57] The ATLAS collaboration. Atlas pixel detector electronics and sensors. *Journal of Instrumentation*, 3(07):P07007, 2008.
- [58] The ATLAS collaboration. The atlas transition radiation tracker (trt) proportional drift tube: design and performance. *Journal of Instrumentation*, 3(02):P02013, 2008.
- [59] N J Buchanan, L Chen, D M Gingrich, Shutian Liu, Hungwei Chen, J Farrell, James Kierstead, Francesco Lanni, D Lissauer, Hong Ma, D Makowiecki, Veljko Radeka, Sergio Rescia, Helio Takai, Hamid Ghazlane, A Hoummada, H G Wilkens, J Bán, S Boettcher, and P K Teng. Design and implementation

- of the front end board for the readout of the atlas liquid argon calorimeters. 3:P03004, 03 2008.
- [60] The ATLAS collaboration. ATLAS liquid argon calorimeter: Technical design report. 1996.
- [61] W.E. Cleland and E.G. Stern. Signal processing considerations for liquid ionization calorimeters in a high rate environment. *Nuclear Instruments and Methods in Physics Research Section A: Accelerators, Spectrometers, Detectors and Associated Equipment*, 338(2):467 – 497, 1994.
- [62] The ATLAS Collaboration. Search for nonpointing and delayed photons in the diphoton and missing transverse momentum final state in 8 TeV  $pp$  collisions at the LHC using the ATLAS detector. *Phys. Rev.*, D90(11):112005, 2014.
- [63] The ATLAS Collaboration. The Laser calibration of the Atlas Tile Calorimeter during the LHC run 1. *JINST*, 11(10):T10005, 2016.
- [64] The ATLAS Collaboration. *ATLAS tile calorimeter: Technical Design Report*. Technical Design Report ATLAS. CERN, Geneva, 1996.
- [65] Giulio Usai. Signal reconstruction of the ATLAS Hadronic Tile Calorimeter: implementation and performance. *J. Phys. Conf. Ser.*, 293:012056, 2011.
- [66] T Davidek. Atlas tile calorimeter time calibration, monitoring and performance. 928:012003, 11 2017.
- [67] E. Diehl. Calibration and Performance of the ATLAS Muon Spectrometer. In *Particles and fields. Proceedings, Meeting of the Division of the American Physical Society, DPF 2011, Providence, USA, August 9-13, 2011*, 2011.
- [68] The ATLAS Collaboration. ATLAS muon spectrometer: Technical design report. 1997.
- [69] The ATLAS Collaboration. ATLAS first level trigger: Technical design report. 1998.
- [70] The ATLAS Collaboration. ATLAS high-level trigger, data acquisition and controls: Technical design report. 2003.
- [71] [https://indico.in2p3.fr/event/8870/contributions/47421/attachments/38106/47054/CRSG-ATLAS\\_Request-2014-2015.pdf](https://indico.in2p3.fr/event/8870/contributions/47421/attachments/38106/47054/CRSG-ATLAS_Request-2014-2015.pdf), Aug 2018.

- [72] Andy Buckley et al. General-purpose event generators for LHC physics. *Phys. Rept.*, 504:145–233, 2011.
- [73] GEANT4 Collaboration. GEANT4: A simulation toolkit. *Nucl. Instrum. Meth. A* 506 250-303, 2003.
- [74] Zachary Marshall and the Atlas Collaboration. Simulation of pile-up in the atlas experiment. *Journal of Physics: Conference Series*, 513(2):022024, 2014.
- [75] A Buckley, T Eifert, M Elsing, D Gillberg, K Koeneke, A Krasznahorkay, E Moyses, M Nowak, S Snyder, and P van Gemmeren. Implementation of the atlas run 2 event data model. *Journal of Physics: Conference Series*, 664(7):072045, 2015.
- [76] James Catmore, Jack Cranshaw, Thomas Gillam, Eirik Gramstad, Paul Laycock, Nurcan Ozturk, and Graeme Andrew Stewart. A new petabyte-scale data derivation framework for atlas. *Journal of Physics: Conference Series*, 664(7):072007, 2015.
- [77] B. Andersson et al. *Phys.Rept.* 97 31, 1983.
- [78] T. Sjostrand, S. Mrenna, and P. Skands. PYTHIA 6.4 Physics and Manual. *JHEP* 05 026, *arXiv:hep-ph/0603175*, 2006.
- [79] OPAL, G. Alexander et al. *Z. Phys.* C69 543, 1996.
- [80] Rasmus Mackeprang. *Stable Heavy Hadrons in ATLAS*. PhD thesis, Bohr Inst., 2007.
- [81] W. Beenakker, R. Hopker, M. Spira, and P. M. Zerwas. Squark and gluino production at hadron colliders. *Nucl. Phys.*, B492:51–103, 1997.
- [82] Daniel Stump, Joey Huston, Jon Pumplin, Wu-Ki Tung, H. L. Lai, Steve Kuhlmann, and J. F. Owens. Inclusive jet production, parton distributions, and the search for new physics. *JHEP*, 10:046, 2003.
- [83] Y. R. de Boer, A. B. Kaidalov, D. A. Milstead, and O. I. Piskounova. Interactions of Heavy Hadrons using Regge Phenomenology and the Quark Gluon String Model. *J. Phys.*, G35:075009, 2008.
- [84] Rasmus Mackeprang and David Milstead. An Updated Description of Heavy-Hadron Interactions in GEANT-4. *Eur. Phys. J.*, C66:493–501, 2010.

- [85] Aafke Christine Kraan. Interactions of heavy stable hadronizing particles. *Eur. Phys. J.*, C37:91–104, 2004.
- [86] Glennys R. Farrar and Pierre Fayet. Phenomenology of the Production, Decay, and Detection of New Hadronic States Associated with Supersymmetry. *Phys. Lett.*, 76B:575–579, 1978.
- [87] M. Foster and Christopher Michael. Hadrons with a heavy color adjoint particle. *Phys. Rev.*, D59:094509, 1999.
- [88] Nathan Isgur and Mark B. Wise. Weak Decays of Heavy Mesons in the Static Quark Approximation. *Phys. Lett.*, B232:113–117, 1989.
- [89] P. D. B. Collins. *An Introduction to Regge Theory and High Energy Physics*. Cambridge Monographs on Mathematical Physics. Cambridge University Press, 1977.
- [90] G. Aad et al. (ATLAS Collaboration). Search for long-lived stopped R-hadrons decaying out of time with pp collisions using the ATLAS detector. *Phys. Rev. D* 88, 112003, 2013.
- [91] The CMS collaboration, Sirunyan, A.M., Tumasyan, A. et al. Search for decays of stopped exotic long-lived particles produced in proton-proton collisions at  $\sqrt{s}=13$  TeV. *J. High Energ. Phys. (2018)* 2018: 127. [https://doi.org/10.1007/JHEP05\(2018\)127](https://doi.org/10.1007/JHEP05(2018)127), 2018.
- [92] The ATLAS Collaboration. Search for metastable heavy charged particles with large ionization energy loss in pp collisions at  $\sqrt{s} = 13$  TeV using the ATLAS experiment. *Phys. Rev.*, D93(11):112015, 2016.
- [93] Vardan Khachatryan et al. Search for long-lived charged particles in proton-proton collisions at  $\sqrt{s} = 13$  TeV. *Phys. Rev.*, D94(11):112004, 2016.
- [94] Morad Aaboud et al. Search for long-lived charginos based on a disappearing-track signature in pp collisions at  $\sqrt{s} = 13$  TeV with the ATLAS detector. *JHEP*, 06:022, 2018.
- [95] Yu L Dokshitzer, V A Khoze, and S I Troyan. On specific qcd properties of heavy quark fragmentation ('dead cone'). *Journal of Physics G: Nuclear and Particle Physics*, 17(10):1602, 1991.

- [96] J. Abdallah et al. Search for supersymmetric particles in light gravitino scenarios and sleptons NLSP. *Eur. Phys. J.*, C27:153–172, 2003.
- [97] The ATLAS Collaboration. Searches for heavy long-lived charged particles with the ATLAS detector in proton-proton collisions at  $\sqrt{s} = 8$  TeV. *JHEP*, 01:068, 2015.
- [98] G. Abbiendi et al. Search for stable and longlived massive charged particles in  $e^+ e^-$  collisions at  $s^{*(1/2)} = 130$ -GeV to 209-GeV. *Phys. Lett.*, B572:8–20, 2003.
- [99] Victor Mukhamedovich Abazov et al. Search for charged massive long-lived particles at  $\sqrt{s} = 1.96$  TeV. *Phys. Rev.*, D87(5):052011, 2013.
- [100] A. Heister et al. Search for stable hadronizing squarks and gluinos in  $e^+ e^-$  collisions up to  $s^{*(1/2)} = 209$ -GeV. *Eur. Phys. J.*, C31:327–342, 2003.
- [101] The ATLAS Collaboration. Search for heavy long-lived charged  $R$ -hadrons with the ATLAS detector in  $3.2 \text{ fb}^{-1}$  of proton-proton collision data at  $\sqrt{s} = 13$  TeV. *Phys. Lett.*, B760:647–665, 2016.
- [102] The ATLAS Collaboration. Search for stable hadronising squarks and gluinos with the ATLAS experiment at the LHC. *Phys. Lett.*, B701:1–19, 2011.
- [103] The ATLAS Collaboration. Searches for heavy long-lived sleptons and  $R$ -Hadrons with the ATLAS detector in  $pp$  collisions at  $\sqrt{s} = 7$  TeV. *Phys. Lett.*, B720:277–308, 2013.
- [104] Simone Alioli, Paolo Nason, Carlo Oleari, and Emanuele Re. A general framework for implementing NLO calculations in shower Monte Carlo programs: the POWHEG BOX. *JHEP*, 06:043, 2010.
- [105] Torbjorn Sjostrand, Stephen Mrenna, and Peter Z. Skands. A Brief Introduction to PYTHIA 8.1. *Comput. Phys. Commun.*, 178:852–867, 2008.
- [106] D. J. Lange. The EvtGen particle decay simulation package. *Nucl. Instrum. Meth.*, A462:152–155, 2001.
- [107] The ATLAS Collaboration. Measurement of the  $Z/\gamma^*$  boson transverse momentum distribution in  $pp$  collisions at  $\sqrt{s} = 7$  TeV with the ATLAS detector. *JHEP*, 09:145, 2014.

- [108] Torbjorn Sjostrand, Stephen Mrenna, and Peter Z. Skands. PYTHIA 6.4 Physics and Manual. *JHEP*, 05:026, 2006.
- [109] Further ATLAS tunes of PYTHIA6 and Pythia 8. Technical Report ATL-PHYS-PUB-2011-014, CERN, Geneva, Nov 2011.
- [110] J. Alwall, R. Frederix, S. Frixione, V. Hirschi, F. Maltoni, O. Mattelaer, H. S. Shao, T. Stelzer, P. Torrielli, and M. Zaro. The automated computation of tree-level and next-to-leading order differential cross sections, and their matching to parton shower simulations. *JHEP*, 07:079, 2014.
- [111] A. Kulesza and L. Motyka. Threshold resummation for squark-antisquark and gluino-pair production at the LHC. *Phys. Rev. Lett.*, 102:111802, 2009.
- [112] A. Kulesza and L. Motyka. Soft gluon resummation for the production of gluino-gluino and squark-antisquark pairs at the LHC. *Phys. Rev.*, D80:095004, 2009.
- [113] Wim Beenakker, Silja Brensing, Michael Kramer, Anna Kulesza, Eric Laenen, and Irene Niessen. Soft-gluon resummation for squark and gluino hadroproduction. *JHEP*, 12:041, 2009.
- [114] W. Beenakker, S. Brensing, M. n Kramer, A. Kulesza, E. Laenen, L. Motyka, and I. Niessen. Squark and Gluino Hadroproduction. *Int. J. Mod. Phys.*, A26:2637–2664, 2011.
- [115] ATLAS Run 1 Pythia8 tunes. Technical Report ATL-PHYS-PUB-2014-021, CERN, Geneva, Nov 2014.
- [116] Richard D. Ball et al. Parton distributions with LHC data. *Nucl. Phys.*, B867:244–289, 2013.
- [117] W. Beenakker, R. Hopker, and M. Spira. PROSPINO: A Program for the production of supersymmetric particles in next-to-leading order QCD. 1996.
- [118] Summary of ATLAS Pythia 8 tunes. Technical Report ATL-PHYS-PUB-2012-003, CERN, Geneva, Aug 2012.
- [119] A. D. Martin, W. J. Stirling, R. S. Thorne, and G. Watt. Parton distributions for the LHC. *Eur. Phys. J.*, C63:189–285, 2009.

- [120] S. Tarem, S. Bressler, H. Nomoto, and A. Di Mattia. Trigger and reconstruction for heavy long-lived charged particles with the atlas detector. *The European Physical Journal C*, 62(2):281–292, Jul 2009.
- [121] The ATLAS Collaboration. Performance of the atlas track reconstruction algorithms in dense environments in lhc run 2. *The European Physical Journal C*, 77(10):673, Oct 2017.
- [122] R. Frühwirth. Application of kalman filtering to track and vertex fitting. *Nuclear Instruments and Methods in Physics Research Section A: Accelerators, Spectrometers, Detectors and Associated Equipment*, 262(2):444 – 450, 1987.
- [123] <https://twiki.cern.ch/twiki/bin/view/AtlasPublic/SCTPublicResults>, Sep 2018.
- [124] The ATLAS Collaboration. Performance of the atlas transition radiation tracker in run 1 of the lhc: tracker properties. *Journal of Instrumentation*, 12(05):P05002, 2017.
- [125] The ATLAS Collaboration. Performance of the ATLAS Transition Radiation Tracker in Run 1 of the LHC: tracker properties. *JINST*, 12(05):P05002, 2017.
- [126] The Atlas Collaboration. Muon reconstruction performance of the ATLAS detector in proton-proton collision data at  $\sqrt{s} = 13$  TeV. *The European Physical Journal C*, 76(5):292, May 2016.
- [127] The ATLAS Collaboration. Search for heavy charged long-lived particles in proton-proton collisions at  $\sqrt{s} = 13$  TeV using an ionisation measurement with the ATLAS detector. 2018.
- [128] Jochen Jens Heinrich. *Search for Charged Stable Massive Particles with the ATLAS Detector*. PhD thesis, LMU Muinch, 2018.
- [129] The ATLAS Collaboration. Search for heavy long-lived multi-charged particles in pp collisions at  $\sqrt{s} = 8$  TeV using the ATLAS detector. *Eur. Phys. J.*, C75:362, 2015.
- [130] Corentin Allaire. A High-Granularity Timing Detector (HGTD) in ATLAS : Performance at the HL-LHC. Technical Report ATL-LARG-PROC-2018-003, CERN, Geneva, Feb 2018.

- [131] The ATLAS Collaboration. Search for nonpointing and delayed photons in the diphoton and missing transverse momentum final state in 8 tev  $pp$  collisions at the LHC using the ATLAS detector. *Phys. Rev. D*, 90:112005, Dec 2014.
- [132] Esteban Fullana, J Castelo, V Castillo, C Cuenca, A Ferrer, E Higon, C Iglesias, A Munar, J Poveda, A Ruiz-Martinez, et al. Digital signal reconstruction in the ATLAS hadronic tile calorimeter. *IEEE transactions on nuclear science*, 53(4):2139–2143, 2006.
- [133] Michael Adersberger. Studies on Velocity Measurements with the ATLAS Calorimeters for the Search for Heavy Long-Lived Particles, Master thesis, LMU Munich, 2015.
- [134] T Davidek and J Montejo. Cell time resolution as a function of cell energy in the collision data at  $\sqrt{s} = 7$  TeV. Oct 2011.
- [135] P. Baudrenghien, E. Bracke, T. Linnekar, H. Marty, J. Molendijk, Y. Pilchen, U. Wehrle, and F. Weierud. The New RF control system for the CERN SPS accelerator. *Conf. Proc.*, C960610:1757–1759, 1996. [1757(1996)].
- [136] B Cleland, N Nikiforou, and J Parsons. Observation, Using Liquid Argon Calorimeter Timing, of Satellite-Satellite Collisions in the 2012  $pp$  Dataset. Technical Report ATL-COM-LARG-2014-008, CERN, Geneva, Apr 2014.
- [137] Adam Jeff, Carsten Welsch, and Andrea Boccardi. A Longitudinal Density Monitor for the LHC, Dec 2012. Presented 11 Dec 2012.
- [138] Tim Adye. Unfolding algorithms and tests using RooUnfold. In *Proceedings, PHYSTAT 2011 Workshop on Statistical Issues Related to Discovery Claims in Search Experiments and Unfolding, CERN, Geneva, Switzerland 17-20 January 2011*, pages 313–318, Geneva, 2011. CERN, CERN.
- [139] G. D’Agostini. A Multidimensional unfolding method based on Bayes’ theorem. *Nucl. Instrum. Meth.*, A362:487–498, 1995.
- [140] The ATLAS collaboration. Selection of jets produced in 13TeV proton-proton collisions with the ATLAS detector. 2015.
- [141] M. Baak, G.J. Besjes, D. Cote, A. Koutsman, J. Lorenz, D. Short. HistFitter software framework for statistical data analysis. *arXiv:1410.1280 [hep-ex]*, 2014.

- [142] Schmidt M., Lipson H. Distilling Free-Form Natural Laws from Experimental Data. *Science*, Vol. 324, no. 5923, pp. 81 - 85., 2009.
- [143] Eilam Gross and Ofer Vitells. Trial factors for the look elsewhere effect in high energy physics. *Eur. Phys. J.*, C70:525–530, 2010.
- [144] S. S. AbdusSalam et al. Benchmark Models, Planes, Lines and Points for Future SUSY Searches at the LHC. *Eur. Phys. J.*, C71:1835, 2011.
- [145] Borschensky, Christoph and Krämer, Michael and Kulesza, Anna and Mangano, Michelangelo and Padhi, Sanjay and Plehn, Tilman and Portell, Xavier. Squark and gluino production cross sections in pp collisions at  $\sqrt{s} = 13, 14, 33$  and 100 TeV. *Eur. Phys. J.*, C74(12):3174, 2014.
- [146] S. Catani, F. Krauss, R. Kuhn, and B. R. Webber. QCD matrix elements + parton showers. *JHEP*, 11:063, 2001.
- [147] Leif Lonnblad and Stefan Prestel. Matching Tree-Level Matrix Elements with Interleaved Showers. *JHEP*, 03:019, 2012.
- [148] The ATLAS Collaboration. Search for long-lived, massive particles in events with displaced vertices and missing transverse momentum in  $\sqrt{s} = 13$  TeV pp collisions with the ATLAS detector. *Phys. Rev.*, D97(5):052012, 2018.
- [149] Gemme C. private communications.
- [150] The ATLAS collaboration. Luminosity determination in pp collisions at  $\sqrt{s} = 8$  TeV using the ATLAS detector at the LHC. *Eur. Phys. J.*, C76(12):653, 2016.
- [151] A L Read. Modified frequentist analysis of search results (the  $CL_s$  method). (CERN-OPEN-2000-205), 2000.
- [152] Alexander L. Read. Presentation of search results: The CL(s) technique. *J. Phys.*, G28:2693–2704, 2002. [,11(2002)].
- [153] The ATLAS collaboration. Search for squarks and gluinos in final states with jets and missing transverse momentum using 36.1 fb<sup>-1</sup> of  $\sqrt{s} = 13$  TeV pp collision data with the ATLAS detector. *Phys. Rev.*, D97(11):112001, 2018.
- [154] The ATLAS collaboration. Search for heavy long-lived multi-charged particles in proton–proton collisions at  $\sqrt{s} = 13$  TeV using the ATLAS detector.

- [155] Mike Lauge. *dE/dx Measurements in the ATLAS Detector*, Master thesis, Niels Bohr Institute, University of Copenhagen, 2017.
- [156] The ATLAS Collaboration. Search for charginos nearly mass-degenerated with the lightest neutralino based on a disappearing-track signature in  $pp$  collisions at  $\sqrt{s} = 8$  TeV with the ATLAS detector. *Phys. Rev. D* 88, 112006, 2013.
- [157] Junhai Kang and Markus A. Luty. Macroscopic Strings and 'Quirks' at Colliders. *JHEP*, 11:065, 2009.
- [158] Marco Farina and Matthew Low. Constraining Quirky Tracks with Conventional Searches. *Phys. Rev. Lett.*, 119(11):111801, 2017.
- [159] Simon Knapen, Hou Keong Lou, Michele Papucci, and Jack Setford. Tracking down Quirks at the Large Hadron Collider. *Phys. Rev.*, D96(11):115015, 2017.
- [160] Graham D. Kribs, Tuhin S. Roy, John Terning, and Kathryn M. Zurek. Quirky Composite Dark Matter. *Phys. Rev.*, D81:095001, 2010.

# Danksagungen

Zu guter Letzt darf ich auch noch bei einer Reihe von Personen ein herzliches Dankeschön sagen, ohne die diese Arbeit nicht möglich gewesen wäre.

- Ein besonderer Dank geht an Prof. Dr. Dorothee Schaile für die Betreuung meiner Arbeit und das angenehmen Arbeitsumfeld am Lehrstuhl
- Ein ganz herzliches Dankeschön geht an Dr. Sascha Mehlhase für die Betreuung über die letzten Jahre. Nachdem die anfänglichen sprachlichen Barrieren dank intensivem Training überwunden werden konnten, hatten wir eine verdammt gute Zeit! Auch wenn ich bis heute nicht ganz verstehe, warum man Gurken grillen sollte?
- Mein Dank gilt auch Prof. Dr. Martin Fässler für das Erstellen des Zweitgutachtens und die viel damit verbundene viele Arbeit.
- Mein herzlicher Dank geht auch an die weiteren Mitglieder der Prüfungskommission: Prof. Dr. Gerhard Buchalla, Prof. Dr. Thomas Preibisch, Prof. Dr. Ralf Bender und Dr. Alexander Mann
- Ein Dankeschön geht an alle SMPLer Martin Habedank, Jochen Jens Heinrich und Vincent Kitali mit denen ich über die Jahre am Lehrstuhl zusammenarbeiten durfte, für die unzähligen fruchtbaren Diskussionen und natürlich auch die Dart Turniere.
- Thanks also to Shlomit Tarem and Troels Petersen from the ATLAS SMP group for all your support over the last years, was a pleasure to work with you.
- Ein Dank geht auch an Elke Grimm-Zeidler für die Hilfe bei allen bürokratischen Hürden.

- Mein besonderer Dank gilt allen Softi-Kollegen. Man muss echt sagen, der Name ist nur bedingt passend, wenn ich an die vielen lustigen Abendstunden bei so mancher Konferenz denke.
- Ein herzliches Dankeschön geht auch an unsere Hardware-Gruppe für die Unterstützung während meiner Qualifikation als ATLAS Autor. Im Speziellen geht mein Dank an Prof. Ottmar Biebel, Dr. Ralf Hertenberg und an Dr. Philipp Lösel. Auch allen anderen aus der Hardware-Gruppe will ich für ihre aufopferungsvolle Performance in den Abendstunden so mancher Konferenz danken.
- Mein Dank gilt auch meiner Ersatz-WG, Anna-Maria Bachmann, Fabian Batsch und Mathias Hüther für die tolle Zeit am CERN.
- Mein Dank geht auch an Andrea Matic die mich während meiner Zeit am Cern mit den neusten Entwicklungen am Lehrstuhl auf dem laufenden gehalten hat.
- Many thanks to all the lectors of (parts of) my thesis: Sascha Mehlhase, Anna-Maria Bachmann, Emmy Gabriel, Cindi Langley, Mathias Hüther, Benedikt Lippert, Serverin Lüst and Christoph Langley.
- Many thanks also to all the lovely people i met during my Phd at conferences, schools, CERN or wherever.
- An dieser Stelle will ich auch all meinen Freunden danken, dafür dass ihr immer ein offenes Ohr und ein kühles Bier für mich habt.
- Zu guter Letzt geht mein spezieller Dank an meine Familie für die wahnsinnige Unterstützung! Allen voran meinen Eltern Astrid und Josef Adersberger, meinen Geschwistern Maria und Josef und ihren Liebsten Florian und Nina und der damit verbundenen Rasselbande Amelie, Emma, Vinzi und Maxi und meinen Grosseltern Anna und Emil.

Allen oben Genannten (und denen die ich vergessen habe im Speziellen zu erwähnen) ein ganz herzliches Dankeschön für die Unterstützung während meiner Promotion, ohne euch hätte ich das bestimmt nicht geschafft.